Multifunctional Electrodeposited Nanocrystalline Cu-Ni Films

Doctoral Thesis presented by **Aïda Varea Espelt**

Supervised by

Dr. Jordi Sort Viñas

Dra. Eva Pellicer Vilà

and

Prof. M. Dolors Baró Mariné

Bellaterra, November 2012

Grup de Física de Materials II

Departament de Física

El Dr. Jordi Sort Viñas, Professor d'Investigació ICREA i professor de la Universitat Autònoma de Barcelona, la Dra. Eva Pellicer Vilà, investigadora post-doctoral de la Universitat Autònoma de Barcelona i la Dra. M. Dolors Baró Mariné, Catedràtica de Física Aplicada de la Universitat Autònoma de Barcelona, com a directors de la tesi doctoral realitzada per Aïda Varea Espelt i que porta per títol **"Multifunctional Electrodeposited Nanocrystalline Cu-Ni Films"**.

FAN CONSTAR:

Que l'aportació de la doctoranda al treball que es presenta ha estat fonamental tant pel que fa a la síntesi de les mostres, la seva caracterització, l'anàlisi de les dades i la discussió i elaboració dels resultats.

I perquè així consti, a petició de la interessada i als efectes oportuns, signen la present:

Bellaterra, el 22 de novembre del 2012

AÏDA VAREA ESPELT

JORDI SORT VIÑAS

EVA PELLICER VILÀ

M. DOLORS BARÓ MARINÉ

Agraïments

Voldria donar els més sincers agraïments a totes aquelles persones que amb el seu suport han fet possible la realització d'aquest treball.

En primer lloc, agraeixo a Dr. Jordi Sort per haver-me donat l'oportunitat, ara farà casi 4 anys, d'entrar en el món de la investigació. A la Prof. M. Dolors Baró i al Prof. Santiago Suriñach, haver fet possible la meva continuïtat en el *Grup de Física de Materials II*. A tots tres directors d'aquesta Tesis, Dr. Jordi Sort, Prof. M. Dolors Baró i Dra. Eva Pellicer, els vull agrair tot el que m'han ensenyat, l'ajuda que m'han ofert i els consells que he rebut durant la seva direcció. A la Dra. Eva Pellicer vull agrair-li especialment, la meticulosa i exhaustiva correcció d'aquest treball i l'especial dedicació que ha tingut en el transcurs de la redacció d'aquest manuscrit.

Al Dr. Enric Menéndez i al Dr. Josep Nogués m'agradaria també agrair tots els coneixements sobre magnetisme que m'han aportat en tots aquests anys. Al Dr. Salvador Pané i al Dr. Bradley J. Nelson la seva col·laboració i aportació en els treballs que aquí es presenten.

Als meus companys de *Física de Materials II*: Pau, Jordina, Alberto, Patxi, Anna, Sergio i Miguel vull agrair els bons moments que m'han fet passar, els grans consells que m'han donat i el fort recolzament que he rebut en moments difícils. Als meus companys de *Física de Materials I* agrair-los les bones estones que hem passat dinant i prenent cafè.

Donar les gràcies al *Servei de Microscòpia* de la Universitat Autònoma de Barcelona per tot el suport tècnic que m'han ofert durant tota la meva recerca, en especial a la Dra. Emma Rossinyol i a Onofre Castell. A tot el servei tècnic de la Universitat Autònoma de Barcelona, gràcies per les ràpides i eficients solucions donades quan ho he necessitat.

Als meus amics, moltes gràcies! En especial vull agrair a en Manel tots els magnífics i genials moments que hem compartit des del primer dia que ens vam trobar en una classe de la carrera de Física, gràcies per escoltar-me i estar al meu costat des de fa 12 anys. Als professors i als alumnes de *MATFIS*, gràcies per donar-me tantes bones estones compartint coneixements.

A la meva família, en especial a la meva mare i a l'Eva, moltes gràcies per mostrar la fortalesa que heu tingut en moments molt durs i com heu aixecat al cap i m'heu dedicat el millor dels vostres somriures. Agrair al meu pare tot el que em va ensenyar, sempre serà el millor professor.

Finalment vull donar-li les gràcies a en Jose per estar al meu costat en tots els moments, bons i dolents, escoltar-me, fer-me somriure cada dia i fer que la meva vida sigui una vida plena d'alegria i il·lusions! Moltes gràcies!

Als meus pares, a l'Eva i a en Jose

Resum

Aquesta Tesi engloba la fabricació mitjançant electrodeposició de capes nanocristal·lines de Cu-Ni en tot el rang de composicions, així com la seva caracterització morfològica (microscòpia electrònica de rastreig i de forces atòmiques), microestructural (difracció de raigs X i microscòpia electrònica de transmissió), mecànica (nanoindentació), magnètica (emprant els magnetòmetres d'efecte Kerr magneto-òptic i superconducting quantum interference device – SQUID-), de resistència a la corrosió (mètode de polarització potenciodinàmica), així com la seva estabilitat tèrmica. El procés d'electrodeposició s'ha realitzat en corrent continu en una cel·la convencional de tres elèctrodes. Els banys utilitzats contenen el mateix tipus de sals metàl·liques (sulfats de Cu i Ni) i additius (citrat, dodecilsulfat de sodi i sacarina), però s'ha variat la relació de concentracions [Cu(II)]/[Ni(II)] per tal d'obtenir capes en tot el rang de composicions ($Cu_{1-x}Ni_x$). Convé destacar l'important paper que fa la sacarina com a agent refinador de gra, ja que la seva presència en el bany permet obtenir capes llises i nanocristal·lines (mida de cristall ~30 nm) amb propietats mecàniques notablement superiors a capes de composició anàloga amb mides de cristall més grans (~400 nm). Per a tots els banys, un augment en el valor absolut de la densitat de corrent comporta un augment del sobrepotencial i, de retruc, un increment del contingut de Ni en els dipòsits. D'aquesta manera, dins de la sèrie de capes nanocristal·lines fabricades, s'observa que la duresa, la resistència al desgast i a la deformació plàstica i la recuperació elàstica milloren en augmentar el contingut en Ni de l'aliatge. S'han assolit valors de duresa de $H = 8.2$ GPa en capes amb composició $Cu_{0.13}Ni_{0.87}$, que són força elevats si es comparen amb els valors de duresa que poden trobar-se a la literatura per a capes de naturalesa similar. Tot i així la presència de Cu també pot ésser beneficiosa per a certes aplicacions on s'hagi de sotmetre el material a temperatures elevades, ja que la seva presència contribueix a augmentar l'estabilitat tèrmica de l'aliatge bo i desplaçant l'inici del creixement de gra i, de retruc, el deteriorament de les propietats mecàniques, cap a temperatures de recuit superiors (p.e. $T = 575$ K per a $Cu_{0.44}Ni_{0.56}$) en comparació amb aquelles capes amb continguts més baixos de Cu (p.e. $T = 525$ K per a $Cu_{0.12}Ni_{0.88}$ i $T = 425$ K per a Ni pur). Pel que fa a les propietats magnètiques s'ha observat comportament ferromagnètic modulable en capes amb un contingut de Ni superior al 70 at% i s'han estudiat els canvis en els cicles d'histèresi magnètica amb la temperatura de recuit. Quant a la resistència a la corrosió en medi clorur, aquesta augmenta en incrementar el contingut de Ni dels dipòsits. També s'observa que el procés de nanoestructuració no deteriora de forma significativa la resistència a la corrosió del material. Així doncs queda demostrat que, gràcies a l'elevat grau de modulació que s'aconsegueix en les propietats mecàniques i magnètiques, el Cu-Ni és un bon candidat per a la seva implementació en sistemes electromecànics tant a escala micromètrica com nanomètrica. I per aquest mateix motiu, el treball de Tesi finalitza amb la presentació dels resultats derivats de la miniaturització d'aquest aliatge utilitzant el mateix concepte sintètic, de manera que es demostra la fabricació de matrius ordenades de nanocolumnes de diàmetres compresos entre 100 nm i 200 nm així com la seva composició i caracterització magnètica.

Abstract

This Thesis dissertation encompasses the fabrication of nanocrystalline Cu-Ni films in all range of compositions by means of electrodeposition and their morphological (using scanning electron and atomic force microscopies), microstructural (by X-ray diffraction and transmission electron microscopy), mechanical (by nanoindentation) and magnetic (using magneto-optical Kerr effect and superconductor quantum interferometer device –SQUID- magnetometers) characterization, as well as their corrosion resistance (by potentiodynamic polarization method) and thermal stability. The electrodeposition process has been carried out by direct current in a conventional three-electrode cell configuration. The baths used throughout the work contain the same metallic salts (Cu and Ni sulphates) and additives (citrate, sodium dodecylsulphate and saccharine), but the [Cu(II)]/Ni(II)] concentration ratio in solution has been changed to obtain Cu-Ni films in all range of compositions ($Cu_{1-x}Ni_x$). Saccharine exerts a key role as a grain-refining agent since its addition to the bath leads to smooth, nanocrystalline films (crystallite size ~30 nm) with markedly improved mechanical performance compared to films with similar composition but larger crystallite sizes (~400 nm). For all the baths, an increase of the absolute value of the current density causes an increase in the overpotential which, in turns, yields to the deposits with larger Ni contents. Within the fabricated nanocrystalline films series, larger hardness, improved wear resistance and resistance to plastic deformation and larger elastic recovery are observed as the Ni content in the alloy increases. Hardness values around 8.2 GPa have been achieved for $Cu_{0.13}Ni_{0.87}$ films, which are larger than those found in the literature for films of similar nature. Even so, the presence of Cu can be beneficial for certain applications where the material has to operate at high temperatures. Namely, the presence of Cu increases the thermal stability by delaying grain growth toward higher annealing temperatures (T = 575 K for $Cu_{0.44}Ni_{0.56}$) as compared to films with lower Cu contents (T = 525 K for $Cu_{0.12}Ni_{0.88}$ and T = 425 K for pure Ni). Accordingly, a delay in the deterioration of the mechanical properties is seen. Regarding magnetic behaviour, tuneable ferromagnetic behaviour for Ni contents beyond 70 at% has been found and the changes in the magnetic hysteresis loops with the annealing temperature have been explored. Concerning the corrosion resistance in chloride environments, it improves as the Ni content increases in the deposits. It is also shown that the nanostructuring process does not significantly worsen the corrosion resistance of the material. It is thus demonstrated that, owing to their tuneable mechanical and magnetic properties, Cu-Ni alloys are good candidates for their implementation in electromechanical systems both at micro- and nanoscales. For this reason, this Thesis dissertation ends up with the presentation of the results about the miniaturization of this alloy using the same synthetic concept. In this sense, the fabrication of arrays of ordered nanopillars of 100 and 200 nm in diameter is demonstrated and their composition and magnetic properties are disclosed.

Table of contents

List of Figures 5

List of Tables 7

Preface 9

Chapter 1 : Introduction 11

1.1. Nanomaterials 11

1.2. Electrodeposition as a fabrication technique 14

1.3. Copper-Nickel system 18

1.3.1. Overview on Cu-Ni electrodeposition 20

1.4. Motivation 22

Schedule 23

References 26

Chapter 2 : Theoretical Concepts 29

2.1. Electrodeposition 29

2.1.1. Faraday laws 30

2.1.2. Electrode cell 31

2.1.3. Electrodeposition methods 32

2.1.4. Codeposition of two metals in aqueous solutions 33

2.1.5. Electrodeposition parameters 34

2.2. Mechanical properties 38

2.2.1. Mechanical properties in nanocrystalline materials 40

2.3. Magnetic behaviour of materials 41

2.3.1. Magnetization curves 42

2.3.2. Magnetic behavior in nanocrystalline materials 44

2.4. Corrosion behaviour 45

2.4.1. Corrosion behavior in nanocrystalline materials 48

References 50

Chapter 3 : Experimental Techniques **53**

3.1. Preparation of nanocrystalline Cu-Ni films by electrodeposition 53

3.1.1. Bath formulation 53

3.1.2. Substrates 55

3.2. Electrochemical analysis methods 56

3.2.1. Cyclic voltammetry 56

3.2.1.a. Working conditions 56

3.2.2. Corrosion test: potentiodynamic polarization method 56

3.2.2.a. Tafel extrapolation 57

3.2.2.b. Working conditions 60

3.2.3. Polarization method: porosity evaluation 60

3.3. Structural and morphological analysis techniques 61

3.3.1. X-ray diffraction (XRD) 61

3.3.1.a. XRD pattern fitting. Rietveld method 62

3.3.1.b. Working conditions 63

3.3.2. Scanning electron microscope 63

3.3.2.a. Working conditions 66

3.3.3. Transmission electron microscope 66

3.3.3.a. High resolution transmission electron microscope (HRTEM) 71

3.3.3.b. Sample preparation 71

3.3.3.c. Working conditions 72

3.3.4. Atomic force microscopy 72

3.3.4.a. Working conditions 74

3.4. Mechanical measurements 75

3.4.1. Nanoindentation 75

3.4.1.a. Indentation size effect 77

3.4.1.b. Working conditions 77

3.4.1.c. Data analysis 78

3.5. Magnetic measurements 78

3.5.1. Magneto-optical Kerr effect magnetometer (MOKE) 78

3.5.1.a. Working conditions 79

3.5.2. Superconductor quantum interferometer device (SQUID) 80

3.5.2.a. Working conditions 81

3.6. Other techniques 81

3.6.1. Film thickness measurements 82

3.6.2. Heat treatments 82

References 83

Chapter 4 : Self-Background on Copper-Nickel Electrodeposition **85**

4.1. Previous work on Cu-Ni alloy 85

4.1.1. Introduction 85

4.1.2. Experimental 86

4.1.3. Results and discussion 87

4.1.1. Conclusions 101

References 102

Chapter 5 : Results and Discussion: Compilation of Articles **105**

5.1. A comparison between fine-grained and nanocrystalline electrodeposited Cu-Ni films. Insights on mechanical and corrosion performance. 107

5.2. Grain boundary segregation and interdiffusion effects in nickel-copper alloys: an effective means to improve the thermal stability of nanocrystalline nickel. 135

5.3. Mechanical properties and corrosion behaviour of nanostructured Cu-rich CuNi electrodeposited films. 165

Chapter 6 : Template-Assisted Electrodeposition of Cu-Ni Nanopillars **187**

6.1. Introduction. Miniaturization of Cu-Ni layers 187

6.2. Experimental conditions 189

6.2.1. Substrate fabrication and sample preparation 189

6.2.2. Nanopillars electrodeposition 190

6.2.3. Characterization 190

6.3. Results and discussion 191

6.3.1. Morphological characterization 191

6.3.2. Magnetic behaviour 196

6.4. Conclusions 198

References 199

Chapter 7 : General Conclusions **201**

Chapter 8 : Future Perspectives **203**

Scientific Curriculum **205**

Publications 205

List of Figures

Figure 1.1: Calculated Cu-Ni phase diagram assessed by 1992Mey (NIMS) (27). 19
Figure 2.1: Schematic representation for reduction and oxidation processes in an electrode. 30
Figure 2.2. Scheme of two and three-electrodes configurations. 31
Figure 2.3: Typical representation of current-time waveform for pulse plating (PP) and reverse pulse plating (RPP) applied signals. 32
Figure 2.4: Deposition of component A at the limiting diffusion current; the two curves represent the partial currents for components A and B (adapted from (2)). 33
Figure 2.5: Change in partial current curves for components A and B after introduction of SASs: the subscript (a) designates curves in the absence of SASs; subscript (b) curves in the presence of SASs (adapted from (2)). 34
Figure 2.6: Variation of the partial current curve of component A upon complex formation (adapted from (2)). 34
Figure 2.7: Magnetic moment configuration for a) ferromagnetic, b) antiferromagnetic and c) ferrimagnetic materials (17). 42
Figure 2.8: Magnetic response under application of magnetic field for the various types of magnetic materials. 43
Figure 2.9: Dependence of the coercivity on the crystallite size, <d>, for a FM material (adapted from (19)). 45
Figure 2.10: Important points to take into account when a corrosion resistant material is to be designed. 48
Figure 2.11: Schematic representation of the three behaviours that a metallic material immersed in a solution can experiment. 48
Figure 3.1. Scheme of electrodeposition cell used to prepare the Cu-Ni films. 54
Figure 3.2: Molecular structure of the additives used as complexing agent (citric acid and sodium citrate), as grain refiner (saccharine) and as wetting agent (sodium dodecyl sulphate). 55
Figure 3.3. Schematic representation of Cu (400 nm)/Ti (15 nm)/Si (100) substrates used for Cu-Ni alloy electrodeposition. 55
Figure 3.4: Semilogarithmic representation of polarization curves for a corrosion system under activation control (Tafel behaviour). 59
Figure 3.5. Schematic representation of the conditions for constructive interference, according to Bragg's law. 62
Figure 3.6: Scheme of an X-ray diffractometer in Bragg-Brentano configuration. 63
Figure 3.7. Types of electrons and radiation generated after the interaction between the primary electron beam and the sample. 65
Figure 3.8: Schematic representation of the generation of the electron signal in TEM. 67
Figure 3.9: a) Schematic diagram showing the geometry of the formation of an electron diffraction pattern and illustrating the parameter camera length *L*. b) Schematic diagram of the formation of a diffraction pattern from a single crystal in the electron microscope. The beam is parallel to a zone axis, with two planes of that zone shown. Note that the angle φ between the spots is equal to the angle between the normal to the planes themselves [adapted from (13)]. 69
Figure 3.10: Types of diffraction pattern for a) single crystal, b) a small number of grains, and c) a large number of randomly oriented grains. 70

Figure 3.11: Schematic illustration of the working principle of an atomic force microscope. A sharp tip is scanned over the surface of the assessed material (16). 73
Figure 3.12: a) Load and unload sequence curve for a nanoindentation test. b) Schematic illustration of the unloading process showing the parameters characterizing the contact geometry (20). 77
Figure 3.13: MOKE setup used to measure the hysteresis loops of Cu-Ni samples. 80
Figure 3.14: Schematic representation of SQUID working principle. 81
Figure 4.1: Galvanostatic curves for Cu-Ni deposition onto Cu/Ti/Si substrate at i) -10, ii) -20, iii) -30, and iv) -40 mA/cm^2. 87
Figure 4.2: Stabilized potential (left y-axis) and Ni percentage (right y-axis) in the films achieved as a function of the applied current density. 88
Figure 4.3: a) XRD patterns of $Cu_{1-x}Ni_x$ thin films in the 38°-56° 2θ region. The dashed lines indicate the position of (111) fcc reflection for pure copper and pure nickel. Peaks denoted by § and * belong to the Cu seed layer and the Cu-Ni phase, respectively. b) Cell parameter variation with Ni amount in the alloy. The line is a fit of the data using the Vegard's law (linear correlation coefficient, R, of 0.996). 90
Figure 4.4: XRD patterns of selected Cu-Ni films in the 38°-56° 2θ region collected under grazing incidence α=2.2°. 91
Figure 4.5: (a) Bright-field TEM image of the $Cu_{0.55}Ni_{0.45}$ film and (b) the corresponding SAED pattern. (c) HRTEM image showing the existence of some nanotwins (as the one indicated by the white arrow) inside a nanometre-sized grain and (d) detail of a twin boundary (white solid line) with the crystalline planes visible at each side. 92
Figure 4.6: Topographical AFM image of the film surface corresponding to $Cu_{0.30}Ni_{0.70}$ specimen. 93
Figure 4.7: (a) Load-unload nanoindentation curves (applied load, P, vs. penetration depth, h) corresponding to $Cu_{0.55}Ni_{0.45}$, $Cu_{0.21}Ni_{0.79}$ and $Cu_{0.13}Ni_{0.87}$ films. The following panels show the dependences of (b) the nanoindentation hardness H, (c) reduced elastic modulus E_r, (d) H/E_r, (e) H^3/E_r^2 and (f) elastic recovery (i.e., W_{el}/W_{tot} ratio, where W_{el} and W_{tot} denote, respectively, the elastic and total energies during nanoindentation), on the thin film composition. 95
Figure 4.8: (a) MOKE hysteresis loops of various $Cu_{1-x}Ni_x$ films. (b) Dependence of the saturation magnetisation (M_S) (▲, left y-axis) and Kerr signal (○, right y-axis) on the Ni percentage in the films. 100
Figure 6.1: Layered structure of the substrates used for nanopillars electrodeposition. 189
Figure 6.2: In-plane SEM image of a) Cu-Ni nanopillars electrodeposited directly onto 15 nm-thick upper Ti layer. As shown, most of the structures are detached from the substrate due to the poor adherence after the resin stripping; b) Overplated nanopillars. Inset: side-wide of one of these overplated entities featuring a mushroom-like appearance. 193
Figure 6.3: SEM image of a forest of nano-trees obtained due to exceedingly large overpotential and deposition time. 193
Figure 6.4: a) Potentiostatic curves for Cu-Ni alloy nanopillars deposition onto Au/Ti/Si substrates. b) Ni percentages in the nanopillars as a function of applied potential. 194
Figure 6.5: FE-SEM images of $Cu_{0.66}Ni_{0.34}$ nanopillars: a) planar view of 200 nm-diameter, and b-c) 70° tilted images in which the periodicity and uniformity of 200 and 100 nm-diameter nanopillars, respectively, can be appreciated. 195
Figure 6.6: a) FESEM image of a couple of 200 nm-diameter nanopillars and b) the corresponding EDX mapping analysis along their length. 196
Figure 6.7: Room-temperature MOKE hysteresis loops for: (a) Cu-Ni nanopillar arrays with diameter of 100 nm, measured in longitudinal configuration, (b) Cu-Ni nanopillar arrays with diameter of 100 nm, measured in polar configuration and (c) continuous (unpatterned) films, measured in longitudinal configuration. 197

List of Tables

Table 1.1. Classification of nanomaterials and synthesis methods (3) 12
Table 1.2. Classification of nanomaterials production process (1, 3) 16
Table 1.3. Synthesis of nanomaterials (18) 16
Table 1.4 Classification of electrodeposited alloys as a function of the application field (21) 17
Table 2.1 Tragedies caused by corrosion during last fifty years (27, 28) 47
Table 3.1 Electrolytic solution composition and electrodeposition parameters 54
Table 3.2 Corrosion test parameters 60
Table 3.3 Control parameters used for ion milling 72
Table 4.1 Global structural parameters obtained after Rietveld refinement of the XRD data of Cu-Ni films 91
Table 6.1 Electrodeposition conditions for the deposition of pure Ni and Cu, and for Cu-Ni nanopillars (concentration of Ni and Cu salts and additives in solution, applied potential, time, stirring rate and temperature) 194

Preface

The contents of this thesis have been organized in different chapters as follows:

- Chapter 1: the introduction sets out the aim of this thesis and the main goals pursued. An overview of Cu-Ni electrodeposition and a schedule of the work are presented.
- Chapter 2: deals with the theoretical concepts related to the basics of electrodeposition and to the physical and chemical properties of nanocrystalline metallic films. Special emphasis is laid on the description of the effects of nanostructuring on the mechanical and magnetic properties and the corrosion performance of these materials (i.e., size effects).
- Chapter 3: focusses on the electrodeposition set-up and the experimental conditions used to fabricate the samples. The various techniques for the morphological, structural, mechanical and magnetic characterization of the samples and the assessment of their corrosion resistance and thermal stability are described.
- Chapter 4: summarizes the previous works on Cu-Ni electrodeposition undertaken during my master degree. Though they are not formally included in the results section, they serve to better contextualize the results presented in Chapter 5.
- Chapter 5: presents the obtained results and their discussion as a compilation of articles. A brief introductory abstract is included before each article.
- Chapter 6: highlights the main results achieved on the template-assisted electrodeposition of Cu-Ni nanopillars.
- Chapter 7: points out the main conclusions of this doctoral thesis.
- Chapter 8: future perspectives are briefly outlined.

Chapter 1 : Introduction

1.1. Nanomaterials

Nanomaterials belong to a group of materials that have exterior dimensions or constituent phases (at least in one dimension) of less than 100 nm; however, most of their unique properties occur in dimensions less than 50 nm (1). Nanomaterials can be classified in a number of ways depending on the selected criteria. Two of the possible classifications take into account i) the exterior material dimension and ii) the internal structural dimension. The former is currently the most used and it is based on the number of dimensions which are not confined at the nanoscale. According to this, nanomaterials can be categorized as follows (Table 1.1):

- **Zero-dimensional (0D):** all the dimensions fall within the nanoscale (e.g., nanoparticles).
- **One-dimensional (1D):** one dimension is outside the nanoscale (e.g., nanotubes, nanopillars, and nanowires).
- **Two-dimensional (2D):** two dimensions are not confined at the nanoscale; as a result these materials exhibit plate-like shapes (e.g., nanolayers, nanoribbons and nanocoatings).
- **Three-dimensional (3D):** also termed bulk nanomaterials; these materials are not confined at the nanoscale in any dimension and, therefore, they are characterized by having three arbitrary dimensions above 100 nm. Despite their "large" dimensions, these materials either possess a nanocrystalline structure or involve the presence of features at the nanoscale (e.g., nanoparticles-metal matrix composites, bundles of nanowires and nanotubes, multi-nanolayers and micron-thick nanocrystalline films).

Usually, the 3D-nanomaterials showing an internal structure composed of crystals with nanoscale dimensions are called nanocrystalline materials (2). More specifically, nanocrystalline materials can be defined as single phase or multi-phase polycrystalline materials made up of crystallites with nanometric size (i.e., nanocrystals) (3). Some authors distinguish between submicrocrystalline materials (with a mean grain size between 300 and 40 nm) and nanocrystalline materials (with a mean grain size of less than 40 nm) (3). A more precise classification has been proposed by other researchers (4):

- **Nanocrystalline materials (nc):** The average crystallite size and the entire range of grain sizes is typically finer than 100 nm.
- **Ultrafine grained materials (ufg):** The grain sizes are of the order of 100 nm – 1 µm. For grain sizes between 500 nm and 1 µm, the term fine-grained (fg) can be used.
- **Microcrystalline materials (mc):** Also termed as coarse-grained (cg) materials are those materials with grain sizes greater than 1 µm.

Table 1.1. Classification of nanomaterials and synthesis methods (3)

Dimensionality	Designation	Typical method(s) of synthesis
0D	Nanoparticles	Sol-gel method
1D	Filamentary	Chemical vapour deposition
2D	Layered (lamellar)	Vapour deposition Electrodeposition
3D	Nanostructured bulk materials	Gas condensation Mechanical alloying

At this point, it should be mentioned that the difference between "grain size" and "crystallite size" is not clear as we are approaching the nanoscale. Many times, these terms are used at random in the literature. Strictly speaking, a grain is composed of crystallites with dissimilar orientations. Only when a grain is composed of a single crystallite, are the terms "grain" and "crystallite" synonymous. However, since grain refining usually implies a reduction in crystallite size, many authors use both terms indistinctly.

Nanocrystalline materials are known to benefit from enhanced and sometimes novel physical and chemical properties compared with their coarse-grained analogues. In

general, the optical features improve; enhancement in catalytic properties can be found; tensional strength, semiconductor's band gap and coercivity of magnetic materials increase, the melting point and electrical resistance decrease, and superplastic behaviour can be found (4–7), among others (1). Interestingly, some of the mechanical characteristics of nanocrystalline materials were theoretically predicted by Gleiter et al. two decades ago (8) and have since then been experimentally verified by a number of researchers (lower elastic moduli than for coarse-grained conventional materials, very large hardness and strength, and increased ductility that it is believed to be caused by grain boundary diffusional deformation mechanisms). Likewise, the magnetic properties of ferromagnetic materials, which depend on the domain structure and, therefore, on interatomic distances, grain size, and constituents undergo an important change when their dimensions are decreased toward the nanoscale. When the grain size is reduced, both saturation magnetization and Curie temperature decrease whereas coercivity increases (1), provided the size remains sufficiently large to avoid the occurrence of superparamagnetism.

Different reasons account for the observed improved/novel characteristics of nanomaterials in general and of nanocrystalline materials in particular:

- Material size (or crystallite size) approaching molecular and atomic scale ranges.
- High surface-to-volume ratio: the large surface area exhibited by nanomaterials (compared to their volume) causes an increase of the free surface energy of the material, which plays a key role in dictating the properties of nanomaterials.
- An increase in the volume fraction of grain boundaries due to the decrease in grain size which, in turn, affects materials physical features and can confer special attributes to the materials (3).
- A significant portion of the atoms is located at interfaces such as free surfaces, grains boundaries, and interphases.

In order to understand the relationship between structure and properties, nanocrystalline materials need to be characterized on both atomic and nanometre scale. The microstructural features of importance include i) grain size, distribution, and morphology, ii) the nature and morphology of grain boundaries and interphase defects, iii) nature of intergrain defects, iv) composition profiles across grains and interfaces, and v) identification of residual trapped species from processing (3).

Within the nanocrystalline type materials, the fabrication of nc-metals and metallic alloys is of great interest to obtain mechanically hard, corrosion-resistant coatings and for the implementation of components in micro/nano-electromechanical systems (MEMS/NEMS) (thin-film technology). Nowadays, MEMS/NEMS are usually fabricated from either pure silicon or silicon-based compounds, such as silicon nitride or silicon carbide (9). Silicon oxide and aluminium oxide are used as passivation and/or insulating layers. However, these materials are not suitable for magnetic applications or devices requiring high electrical conductivity. In turn, silicon compounds, like SiC, suffer from some tribological and fabrication shortcomings (10). Diamond thin films are also of interest for the implementation of MEMS since their hardness and Young's modulus are exceptional (11). However, fabrication of MEMS/NEMS from diamond requires rather complex lithographic procedures. For these reasons, pure metals and metallic alloys are emerging as potential candidates to replace Si compounds in certain MEMS/NEMS applications, particularly in magnetic MEMS/NEMS, which have the added value that they can be remotely actuated (12, 13). In fact, metallic films exhibit more ductility and fracture toughness than silicon. The main drawbacks are that their strength is usually lower than for silicon and surface roughness is often exceedingly large. This precludes conventional metallic films from being used in advanced structural components for NEMS (12). Hence, intensive research is currently pursued to produce nc-metallic films with outstanding mechanical and magnetic performance and low roughness.

1.2. Electrodeposition as a fabrication technique

There are several physical and chemical methods utilized for the production of nanomaterials. A nanomaterial can be built up from the gas, the liquid (or melt), and even from the solid phase. Table 1.2 shows some of the main processes depending on the starting phase. Each of these processes has their pros and cons. The selection of the production method depends on a variety of factors such as the characteristics of the final structure (grain size, phase morphology, etc.), the purity of the final product and, most importantly, the application for which it has been designed. One has to take into account that the processing route often determines the behaviour of the material. In a broad sense, the synthetic methods used to produce nanomaterials can be classified into two categories (see Table 1.3): top-down approach, in which one begins from a bulk material that is processed to convert it into a nanomaterial, and bottom-up approach, in which the nanomaterial is built up from fine (i.e., atomic) scales. Indeed, nanomaterials found in

nature are formed through bottom-up approaches (14). The top-down approaches begin with larger starting materials and, in a more or less controlled fashion (depending on the technique), remove material until the desired structure is achieved. It often uses the traditional workshop or microfabrication methods where externally controlled tools are used to cut, mill, and shape materials into the desired shape and order. Bottom-up approaches, in contrast, begin with smaller subunits that are assembled, again with varying levels of control, depending on the technique, into the final product (15). It uses the chemical properties of single molecules to make single-molecule components to i) self-organize or self-assemble into some useful conformation, or ii) rely on positional assembly.

Electrodeposition can be classified as a bottom-up method of preparation of nanomaterials with different dimensionality, including nanoparticles, nanowires and 3D nanocrystalline materials (i.e., micron-thick nanocrystalline metallic films). Electrodeposition is a process of coating a conductive substrate with another material which is present in its ionized form in an electrolyte. Electrodeposition occurs by the nucleation of crystallites on the substrate surface and their consequent growth along with the continuous nucleation of fresh crystallites (16). To obtain fine grains, nucleation events should be favoured over growth. The variables in electrodeposition include bath composition, bath pH, temperature, overpotential, bath additives, and direct current vs. pulse electrodeposition. It has been stated (17) that the two most important mechanisms that are rate-determining steps for the formation of nanoscale grains in electrodeposition are charge transfer at the electrode surface and surface diffusion of ad-ions (and/or ad-atoms) on the crystal surface. One method to inhibit the growth of nucleated crystallites is by reducing the surface diffusion of ad-ions by adsorption of foreign species (which may be referred to as “grain-refiners”) on the growing surface. Because high overpotentials favor extensive nucleation, pulse plating, a powerful method to achieve high overpotentials, is frequently used as a technique to obtain a nanocrystalline structure without the use of additives.

Electrodeposition can be considered a rather simple technique that has been used for many years for protective and decorative purposes. Nowadays it is one of the most cost-effective techniques being used in a wider range of technological fields. Overall, electrodeposition is used in many diverse industrial areas including home appliances, jewellery, automotive, aircraft/aerospace, and electronics. The purpose of decorative plating is to provide a durable, pleasant finishing to the surfaces of manufactured articles, so the corrosion characteristics of the deposits and their ability to protect the substrates

are important factors. Other properties like hardness, wear resistance, ductility and stress are also important to the engineering applications of plated coatings.

Table 1.2. Classification of nanomaterials production process (1, 3)

Production from	Production process
Vapour	Physical and chemical deposition of the vapour, sputtering, plasma processing, inert gas condensation
Liquid (or melt)	Sol-gel, electrochemical deposition (electrodeposition), rapid solidification
Solid	Mechanical alloying, severe plastic deformation, mechanochemical process, crystallization of the amorphous phase, sliding wear, spark erosion

Table 1.3. Synthesis of nanomaterials (18)

Top-down	Bottom-up
Mechanical alloying	Chemical vapour deposition
Lithography	Gas phase agglomeration
Erosion	Electrodeposition

The recent upsurge of interest in electrodeposition is due to four main issues (19): (i) metal deposition for the fabrication of integrated circuits; (ii) deposition of magnetic patterned media (in heads, discs); (iii) deposition of multilayered structures; (iv) integration of electrodeposited components MEMS/NEMS devices. The latter has particularly experienced a renaissance. MEMS (characteristic length of less than 1 mm but more than 100 nm) and NEMS (characteristic length less than 100 nm) are systems where electrical and mechanical constituents are present and mobile and fixed elements are combined. In practice, a uniform, compact and bright deposit is desired and in most cases, the success of commercial process depends to a large extent on the addition of agents to the plating electrolytes (19). These will be discussed in Section 2.1.5.

The electrodeposition of pure metal films offers several advantages compared to physical fabrication techniques (sputtering, evaporation, molecular beam epitaxy, focused ion beam…). First, electrodeposition does not require vacuum system; it can work at ambient pressure and room temperature; a wide variety of substrate shapes can be coated

provided that they are conductive, which is particularly useful for template-assisted deposition (i.e., patterned substrates); pore-free relatively thick coatings (up to several hundreds of micrometers in thickness) can be obtained (which can be further used for example as magnetron sputtering targets (Ag, Cr, Au, Fe, Ni, Co and alloys) (20)), and high deposition rates are attainable. All these features make electrodeposition a less-time consuming and cost-effective technique for the production of metallic coatings.

The codeposition of metals is also of paramount interest, as the current trend in engineering and technology supports the replacement of individual metals by their alloys, which usually feature a wider spectrum of properties. Moreover, the properties and performances are several times better than those of individual components. This is particularly valid with regard to wear resistance, hardness, corrosion resistance and thermal stability (21). The scope for application of alloy electroplating is extremely diverse. According to their fields of application, electrodeposited alloys can be classified as shown in Table 1.4.

Table 1.4 Classification of electrodeposited alloys as a function of the application field (21)

Application	Alloy
Protective-decorative	Ni-Zn, Ni-Au, Ni-Cd, Ni-Sn, Au-Cu, Au-Ag, Cu-Sn
Corrosion resistance	Zn-Cd, Zn-Sn, Cd-Sn, Cr-Ni, Cr-Re, Cu-Ni
Soldered coatings	Sn-Pb, Sn-Bi, Sn-Sb, Sn-Ni, In- and Bi-based alloys
Heat-resistance alloys	Ni-Co, Ni-Fe, Ni-Fe-Co, Co-W, Co-Pt, Fe-Pt, Cr-Mn, Cr-W, Cr-Mo, W-Fe
Magnetic alloys	Ni-Co, Ni-Fe, Ni-Fe-Co, Co-W, Co-Pt, Fe-Pt
Coatings replacing individual noble metals in electronics and jewellery	Pd-Ni, Au-Ni, Au-Co
Antifriction alloys	Pb-Ag, In-Pb, Pb-Cu, Ag-Sn
Adhesion coatings	Cu-Zn
Electric contact coatings	Ag-Sb, Ag-Pd, Au-Pd, Pd-Ni, Au-Ni, Au-Sb, Pd-In, Ph-In

1.3. Copper-Nickel system

Copper (Cu) and nickel (Ni), the latter belonging to the so-called iron-group metals, have been used for a wide range of applications for years. Cu is mechanically soft and shows better ductility than many other metals, which is advantageous in terms of mechanical workability. Furthermore, copper is a good thermal and electrical conductive material being used in heat transfer and electronic devices (e.g., circuitry, wiring, contacts and cables (22)), and as a metallization material of integrated circuits (23). Nanocrystalline Cu can experiment, under certain conditions, superplastic behaviour (4–7).

On the other hand, Ni is mechanically harder, malleable, ductile, and resistant to corrosion in alkaline media. Moreover, it is soft ferromagnetic at ambient temperature. In alloys, Ni imparts strength, magnetic properties, hardness and resistance to corrosion and oxidation. Its chemical properties allow its use in dyes, catalysts and batteries. The most important industrial use of nickel is that of an alloying element in ferrous alloys (stainless steels, cast irons). Nickel is also used as an alloying element in nonferrous alloys, most notably copper alloys. Other important uses for nickel include nickel-base alloys for corrosion and heat resistant applications, nickel coatings and nickel powders in coinage, electrodes in battery systems, and filters (24). The role of nickel as a catalyst in chemical processes is perhaps the least known of its uses (25).

Cu-Ni is a substitutional type alloy (26) like Fe-Ni or Fe-Co, among others (21). Since Cu and Ni are mutually soluble in the overall compositional range (27), a Cu-Ni solid solution forms (26), in which one atom type can randomly substitute the other in the crystalline lattice. The complete solubility can be explained by the fact that both Cu and Ni possess the same face-centred cubic crystal structure (26), identical atomic radii, similar electronegativity and same valence. The Cu-Ni system is considered isomorphic due to the complete solubility of the two components in liquid and solid states (Figure 1.1). Substitutional alloys exhibit a crystal lattice constant close to the lattice constant of the main component. The change in the interplanar distance (d) can be used to assess the fraction N of the dissolved component. A linear dependence between d and N is usually observed; such relationship is called Vegard's law. The Vegard's law is an experimental rule which holds that a linear relation exists, at fixed temperature, between the lattice constant of an alloy and the concentration of the constituent elements (28).

It has been demonstrated that Cu-Ni alloys can synergistically combine the properties of both pure metals. In fact, this alloy has attracted the attention of electroplaters due to their anticorrosion, antifouling (29–33) and electrocatalytic properties, as well as their high

tensile strength and reasonably good wear resistance (32, 34). This combination of properties makes Cu-Ni films well suited for many applications, such as resistive and thermoelectric devices, MEMS (35, 36), heat exchanges and sea water condenser tubes (37). Moreover, either ferromagnetic or nonmagnetic behaviour is possible in this alloy by properly tuning the composition of the Cu-Ni solid solution (38). While ferromagnetic Cu-Ni films find applications in magnetic sensors and actuators, the nonmagnetic compositions can serve as nonmagnetic gap in recording write heads. For instance, the $Cu_{0.55}Ni_{0.45}$ alloy, so-called Constantan in industrial environments, is characterised to be nonmagnetic and can be used as substrate for coated conductor wires (39).

Amongst the materials for magnetic MEMS/NEMS applications, pure Ni, $Ni_{19}Fe_{81}$ (permalloy) and Co-Fe based alloys have received attention due to their soft magnetic character (13). However, some of their mechanical properties (e.g. hardness in fine-grained Ni or Young's modulus in $Ni_{19}Fe_{81}$ thin films) are worse than those of silicon, the most widely used material in MEMS devices (40, 41). Most of these detrimental issues could be overcome with the search for advanced routes to obtain nc-metallic thin films that combine ferromagnetic behaviour with good mechanical properties and low surface roughness. Electrodeposited nc-Cu-Ni alloy films emerge as good candidates to meet all the current technological demands.

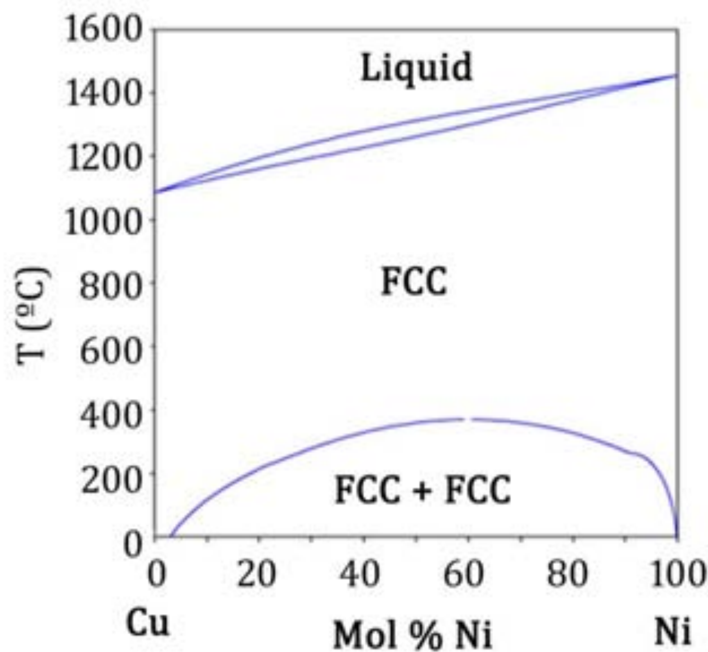

Figure 1.1: Calculated Cu-Ni phase diagram assessed by 1992Mey (NIMS) (27).

1.3.1. Overview on Cu-Ni electrodeposition

Cu-Ni alloy coatings had earlier been used mainly for decorative purposes. The eletrodeposition of Cu-Ni alloys has been studied in depth since 1912, and much of the early work in the field has been summarized by Brenner (42) in 1963 and reviewed some years later by Roos (43) et al. in 1984. Cu-Ni electrodeposition has been demonstrated from a variety of electrolytes such a citrate (44), cyanide (45), sulfamate (46), sulphate-oxalate (47), and pyrophosphate (48).

Concerning the utilization of citrate as a complexing agent, Priscott (44) was able to prepare Cu-Ni deposits from a citrate bath and studied the dependence of the composition on the current density, temperature and agitation of the solution. However, alloys with high Ni content could only be obtained with low current efficiencies. In 1987 Yahalom and Zadok (49) described the production of composition-modulated alloys by electrodeposition, initially for the Cu-Ni system. The role of citrate ion as a leveling, brightening and buffering agent was studied by Despic et al. (50), Ishikawa et al. (51) and Pushpavanam et al. (52), respectively. These studies supported Brenner's (42) belief that citrate-containing baths are the best suited to electrodeposit good quality Cu-Ni alloy deposits. Ying (53) proposed a mathematical model for Cu-Ni electrodeposition from a citrate bath for citrate concentrations larger than the total amount of metal concentration. Under these conditions $NiCit^-$ and $CuCit^-$ are the predominant electroactive species involved in deposition. Citrate baths developed by Roos et al. (43) and more recently by Chaisssang et al. (54) enabled Ni-rich Cu-Ni alloys to be obtained more readily. Quang et al. (55) showed that the addition of sodium citrate to the Cu-Ni plating baths improved the quality of the deposits by ensuring stable potential values during deposition. Madore (56) formulated a citrate bath capable of electrodepositing Cu-Ni alloys with current efficiencies approaching 100%. However, the major difficulty regarding the use of most of the citrate-containing baths is their instability (43, 53) since precipitates appear in the bulk of the solution after a few days of use. Green et al. (57) determined the optimal pH value (pH = 6) to have stable citrate baths for periods in excess of a month for the electrodeposition of Cu-Ni alloys at high current efficiency.

Concerning the preparation of nanocrystalline Cu-Ni films, Ghosh et al. (34) determined the current efficiency involved in the preparation of nc-Cu-Ni alloys by direct and pulse current methods. Yang et al. (58) investigated the galvanostatic

and potentiostatic deposition of compositionally modulated nc-Cu-Ni alloys from a Watts' bath containing nickel sulfate, nickel chloride and copper sulfate. Saccharine has also been studied as grain-refiner in Cu-Ni electrodeposition. In fact, it works as an efficient inhibitor of crystal growth in Watts and sulphamate nickel plating baths (59) as well as in copper electroplating baths (60). In Cu-Ni alloys, a low concentration of saccharine in the bath (0.5g/L) has been demonstrated as sufficient to lead to dendrite-free Cu-Ni coatings (61). Cu-Ni system is still one the most studied when it comes to electrochemically produced multilayered structures (composite structures consisting of alternated Cu/Ni layers). The reasons for this are quite compelling. There is a sufficient difference in the reduction potentials of the two metals. Their crystal structure is the same (fcc) and the lattice parameters are close to each other, ensuring good lattice matching between layers. In the last decades, Cu-Ni multi nanolayers have received growing attention because of their exciting mechanical properties, their improved resistance to pitting corrosion (62) and their catalytic, electric, and giant magnetoresistance properties (63–66) which are important primarily for sensor applications.

In spite of the literature related to Cu-Ni electrodeposits, studies about the physical (mechanical, magnetic and thermal stability) and chemical (corrosion behaviour) properties of nanocrystalline Cu-Ni alloys are still scare and there is much room for investigation in this field. Likely because of the historical decorative and protective function of Cu-Ni films, the corrosion behaviour is one of the issues that has received greater attention. Alloying Ni with Cu is known to improve the corrosion resistance of pure Ni metal in solutions containing chloride ions. Milosev et al. (30) determined that the corrosion behaviour of nc-Cu-Ni films was strongly influenced by the chloride ion concentration. Ghosh et al. (62) compared pulsed and direct current plated nanocrystalline Cu-Ni deposits with the commercial Monel-400 ($Cu_{33}Ni_{67}$), concluding that the pulse plated films exhibited superior corrosion resistance than both direct current plated deposits and Monel-400.

1.4. Motivation

The motivation of this Thesis is to perform a comprehensive investigation on the electrodeposition of Cu-Ni films with variable morphology, composition and crystallite size (fine-grained vs. nanocrystalline) and correlate the observed features with the mechanical and magnetic properties of the films (a Pert diagram of the tasks is shown below). Nanocrystalline layers in all range of compositions have been fabricated to obtain tunable physical properties in view of the potential applications of this alloy. Besides the magnetic and mechanical properties, the thermal stability and corrosion resistance of the developed films are also explored to reveal the synergies achieved through alloying. For this reason, the response of the Cu-Ni alloy films is compared to that of the pure metals. This Thesis is also aimed at having a better knowledge of the effects of nanostructuring in electrodeposited films to further provide a valuable roadmap for other systems. Finally, the preparation of Cu-Ni nanopillars through template-assisted electrodeposition is explored as a means toward the full integration of the alloy in MEMS/NEMS devices.

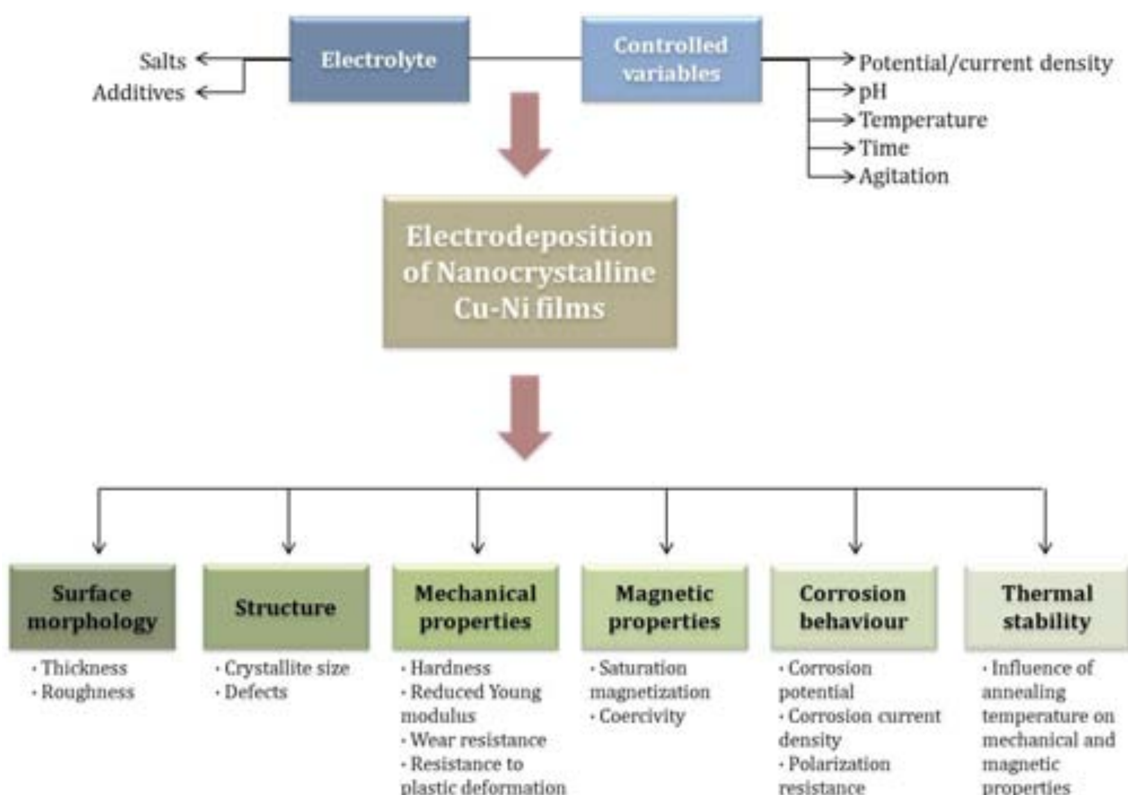

Schedule

A schedule of the work is chronologically shown in the following tables

		2009						2010						2011						2012					
		J F	M A	M J	J A	S O	N D	J F	M A	M J	J A	S O	N D	J F	M A	M J	J A	S O	N D	J F	M A	M J	J A	S O	N D
EXPERIMENTS	› Nanocrystalline Cu-Ni samples received from ETH-Zurich.																								
	› Morphological, structural, mechanical and magnetic characterization of the samples.																								
	› Installation of potentiostat/galvanostat Autolab in our laboratory																								
	› Installation of home-made oven in our laboratory																								
	› Fabrication of nanocrystalline and fine-grained Ni and Ni-rich Cu-Ni samples.																								
	› Morphological, structural, mechanical and magnetic characterization of the Ni-rich samples.																								
	› Thermal stability study.																								
	› Initial studies about corrosion.																								
	› Fabrication of nanocrystalline Cu-rich Cu-Ni samples.																								
	› Morphological, structural, and mechanical characterization of the Cu-rich samples.																								
	› Corrosion behaviour study of Cu-rich samples.																								
	› Electron-Beam Lithography process in CT-ISOM (Madrid).																								
	› Template-assisted electrodeposition of Cu-Ni nanopillar																								
	› Morphological, structural, mechanical and magnetic characterization of Cu-Ni nanopillars.																								

		2009						2010						2011						2012					
		J F	M A	M J	J A	S O	N D	J F	M A	M J	J A	S O	N D	J F	M A	M J	J A	S O	N D	J F	M A	M J	J A	S O	N D
DISSEMINATION OF THE WORK	**› Posters and talks where I have been the presenting author**																								
	· *Magnetic Patterning based on Indentation-Induced Nanocrystallization of a Metallic Glass.* IWNCS 10 (Barcelona, April). Poster.								■																
	· *From micro to nano: improving the properties of electrodeposited Cu-Ni alloys.* BCN-b (Bellaterra, July). Poster.																■								
	· *Nanocrystalline CuNi alloys: improvement of mechanical properties and thermal stability*. BcNano'11 (September 2011). Poster.																	■							
	· *Electrodeposition of Cu, Ni and Cu-Ni nanopillars*. Invited talk in ISMANAM 2012 (Moscow, June).																					■			
	› Publications directly related to the thesis work where I am co-author																								
	· *Nanocrystalline Electroplated Cu-Ni: Metallic Thin Films with Enhanced Mechanical Properties and Tunable Magnetic Behaviour* (Adv. Funct. Mater., vol.20 (March 2010) p.983).								■																
	· *A comparison between fine-grained and nanocrystalline electrodeposited Cu-Ni films. Insights on mechanical and corrosion performance* (Surf. Coat. Technol., vol. 205 (June 2011) p. 5285).															■									
	· *Grain Boundary Segregation and Interdiffusion Effects in Nickel-Copper Alloys: An Effective Means to Improve the Thermal Stability of nanocrystalline Nickel* (ACS Appl. Mat. Interfaces, vol. 3 (June 2011) p. 2265.															■									
	· *Mechanical Properties and Corrosion Behaviour of Nanostructured Cu-rich CuNi Electrodeposited Films* (Int. J. Electrochem. Sci., vol. 7 (February 2012) p. 1288).																			■					
	› Publications not related to the thesis work where I am co-author																								
	· *Out-of-plane Magnetic Patterning Based on Indentation-Induced Nanocrystallization of a Metallic Glass* (Small, vol.6 (2010), p. 1543).							■																	
	· *Tuneable magnetic patterning of paramagnetic $Fe_{60}Al_{40}$ (at.%) by consecutive ion irradiation through pre-lithographed shadow masks* (J. Appl. Phys., vol.109 (May 2011), p. 093918).															■									
	· *Enhanced mechanical properties and in vitro corrosion behaviour of amorphous and devitrified $Ti_{40}Zr_{10}Cu_{38}Pd_{12}$ metallic glass* (J. Mech. Behav.. Biomed. Mat., vol. 4 (May 2011), p. 1709).															■									
	· *Cuando el desorden genera magnetismo* (Rev. Esp. Fis., vol. 26 (2012) p. 16).																				■				
ACADEMIC RECORD	Physics degree	■	■	■	■	■																			
	Master CITEM (Ciència I Tecnologia dels Materials)					■	■	■	■	■															
	Materials Engineering Degree										■	■	■	■	■	■	■	■							
	Thesis Registration														■										
	Thesis Submission																								■

References

1. **M. Aliofkhazraei, N. Ali.** *Two-Dimensional Nanostructures.* Boca Raton : CRC Press, 2012.

2. **M. F. Ashby, P. J. S. G. Ferreira, D. L. Schodek.** *Nanomaterials, Nanotechnologies and Design: An Introduction for Engineers and Architects.* Oxford : Butterworth-Heinemann, 2009.

3. **C. Suryanarayana.** 1995, Int. Mater. Rev., Vol. 40, p. 41.

4. **M. Dao, L. Lu, R. J. Asaro, J. T. M. De Hosson, E. Ma.** 2007, Acta Mater., Vol. 55, p. 4041.

5. **C. C. Koch, K. M. Youssef, R. O. Scattergood, K. L. Murty.** 2005, Adv. Eng. Mater., Vol. 7, p. 757.

6. **K. S. Kumar, H. Van Swygenhoven, S. Suresh.** 2003, Acta Mater., Vol. 51, p. 5743.

7. **K. S. Kumar, S. Suresh, M. F. Chisholm, J. A. Horton, P. Wang.** 2003, Acta Mater., Vol. 51, p. 387.

8. **H. Gleiter.** 1989, Prog. Mater. Sci., Vol. 33, p. 223.

9. **M. Gupta, V. K. Rathi, R. Thangaraj, O. P. Agnihotri, K. S. Chari.** 1991, Thin Solid Films, Vol. 204, p. 77.

10. **Z. Rymuza, Z. Kusznierewicz, M. Misiak, K. Schmidt-Szalowski, Z. Rzanek-Boroch, J. Sentek.** *Tribology Issues and Opportunities in MEMS.* [ed.] B. Bhushan. Dordrecht : Kluwer Academic Publishers, 1998.

11. **A. R. Krauss, O. Auciello, D. M. Gruen, A. Jayatissa, A. Sumant, J. Tucek, D. C. Mancini, N. Moldovan, A. Erdemir, D. Ersoy, M. N. Gardos, H. G. Busmann, E. M. Meyer, M. Q. Ding.** 2001, Diam. Relat. Mater., Vol. 10, p. 1952.

12. **E. Luber, R. Mohammadi, C. Ophus, Z. Lee, N. Nelson-Fitzpatrick, K. Westra, S. Evoy, U. Dahmen, V. Radmilovic, D. Miltin.** 2008, Nanotechnol., Vol. 19. 125705.

13. **N. V. Myung, D.-Y. Park, B.-Y. Yoo, P. T. A. Sumodjo.** 2003, J. Magn. Magn. Mater., Vol. 265, p. 189.

14. **K. T. Ramesh.** *Nanomaterials: Mechanics and Mechanisms.* New York : Springer, 2009.

15. **B. Bhushan, [ed.].** *Handbook of Nanothecnology.* Würzburg : Springer, 2007.

16. **W. A. Goddard III, D. W. Brenner, S. E. Lyshevski, G. J. Iafrate, [ed.].** *Handbook of Nanoscience, Engineering, and Technology.* Third Edition. Boca Raton : CRC Press, 2012.

17. **A. F. Zimmerman, D. G. Clark, K. T. Aust, U. Erb.** 2002, Mater. Lett., Vol. 52, p. 85.

18. **V. Rajendran.** *Engineering Physics.* New Delhi : Tata McGraw-Hill, 2009.

19. **M. Nuñez.** *Metal Electrodeposition.* New York : Nova Science Publishers, 2005.

20. **R. F. Bunshah, [ed.].** *Handbook of deposition technologies for films and coatings.* Second Edition. New Jersey : Noyes Publications, 1994.

21. **Y. D. Gamburg, G. Zangari.** *Theory and Practice of Metal Electrodeposition.* New York : Springer, 2011.

22. **D. R. Askeland, P. P. Fulay, W. J. Wright.** *The Science and Engineering of Materials.* Stanford : Cengage Learning, 2011.

23. **S. H. Hong, K. S. Kim, Y. M. Kim, H. H. Hahn, C. S. Lee, J. H. Park.** 2005, Compos. Sci. Technol, Vol. 65, p. 1401.

24. **N. Anyadike.** *Nickel: An Industry on the Brink of Expansion.* Cambrige : Woodhead Publishing, 2002.

25. **J. R. Davis, [ed.].** *Nickel, Cobalt, and Their Alloys.* Ohio : ASM International, 2000. Vol. 8.

26. **L. C. Melo P. de Lima-Neto, A. N. Correia.** 2011, J. Appl. Electrochem., Vol. 41, p. 415.

27. NIMS. [Online] National Institute of Materials Science. [accessed June, 2012] http://www.nims.go.jp/.

28. **A. R. Denton, N. W. Ashcroft.** 1991, Phys. Rev. A, Vol. 43, p. 3161.

29. **M. Metikos-Hukovic, R. Babic, I. Skugor-Roncevic, Z. Grubac.** 2011, Desalination, Vol. 276, p. 228.

30. **I. Milosev, M. Metikos-Hukovic.** 1997, Electrochim. Acta, Vol. 42, p. 1537.

31. **J. Crousier, A. M. Beccaria.** 1990, Werks. Korr., Vol. 41, p. 185.

32. **I. G. Casella, M. Gatta.** 2002, J. Electrochem. Soc., Vol. 149, p. B465.

33. **A. M. Beccaria, Y. Z. Wang, G. Poggi.** 2004, Surf. Interf. Anal., Vol. 21, p. 442.

34. **S. K. Ghosh, A. -K. Grover, G. K. Grey, M. K. Totlal.** 2000, Surf. Coat. Technol., Vol. 126, p. 48.

35. **S.-G. Hur, D.-J. Kim, B.-D. Kang, S.-G. Yoon.** 2004, J. Vac. Sci. Technol., Vol. 22, p. 2698.

36. **Y. W. Huang, T.-Y. Chao, C. C. Chen, Y.T. Cheng.** 2007, Appl. Phys. Lett., Vol. 90. 244105.

37. **W. A. Badawy, K. M. Ismail, A. M. Fathi.** 2005, Electrochim. Acta, Vol. 50, p. 3603.

38. **J. C. Ododo, B. R. Coles.** 1977, J. Phys. F: Met. Phys., Vol. 7, p. 2393.

39. **A. Girard, C. E. Bruzek, J. L. Jorda, L. Ortega, J. L. Souberyoux.** 2006, J. Phys.: Conf. Ser., Vol. 43, p. 341.

40. **X. Li, G. Ding, T. Ando, M. Shikida, K. Sato.** 2008, Microsyst. Technol, Vol. 14, p. 131.

41. Physical properties of permalloy materials. [Online] [accessed August, 2012] http://www.metanix.co.jp/metanix/english/product/permally/index.html.

42. **A. Brenner.** *Electrodeposition of Alloys.* New York : Academic Press, 1963. Vol. I.

43. **J. R. Roos, J. P. Celis, C. Buelens, D. Goris.** 1984, Proc. Metall., Vol. 3, p. 177.

44. **B. H. Priscott.** 1959, Trans. Inst. Met. Finish., Vol. 36, p. 93.

45. **H. D. Hineline, W. B. Cooley.** 1925, Trans. Inst. Met. Finish., Vol. 61, p. 48.

46. **P. Bradley, S. Roy, D. Landolt.** 1996, J. Chem. Soc. Faraday Trans., Vol. 92, p. 4015.

47. **R. B. P. Crawford, R. D. Snyder.** *1,750,092* U.S., 1930. Patent.

48. **S. K. Panikkar, T. L. Rama-Char.** 1957, J. Electrochem. Soc. Jp, Vol. 25, p. E121.

49. **J. Yahalom, O. Zadok.** 1987, J. Mat. Sci., Vol. 22, p. 499.

50. **A. R. Despic, V. D. Jovic, S. Spaic.** 1989, J. Electrochem. Soc., Vol. 136, p. 1651.

51. **M. Ishikawa, H. Enomoto, M. Matsuoka, C. Iwakura.** 1995, Electrochim. Acta, Vol. 40, p. 1663.

52. **M. Pushpavanam, K. Balakrishnan.** 1996, J. Appl. Electrochem., Vol. 26, p. 1065.

53. **R. Y. Ying.** 1988, J. Electrochem. Soc., Vol. 135, p. 2957.

54. **E. Chassaing.** 2001, J. Electrochem. Soc., Vol. 148, p. C690.

55. **K. V. Quang, E. Chassaing, B. L. Viet.** 1985, Met. Finish., Vol. 85, p. 25.

56. **C. Madore.** PhD. Thesis. *Analyse théorique et réalisation pratique de nouveaux dispositifs expérimentaux pour l'étude de la distribution des courants partiels lors de l'électrodéposition d'alliages.* Switzerland : École Polytechnique Fédérale de Lausanne, 1993.

57. **T. A. Green, A. E. Russell, S. Roy.** 1998, J. Electrochem. Soc., Vol. 145, p. 875.

58. **C. C. Yang, H. Y. Cheh.** 1995, J. Electrochem. Soc., Vol. 142, p. 3034.

59. **A. M. Rashidi, A. Amadeh.** 2009, Surf. Coat. Technol., Vol. 204, p. 353.

60. **M. Troyon, L. Wang.** 1996, Appl. Surf. Sci., Vol. 103, p. 517.

61. **X. Cui, W. Chen.** 2008, J. Electrochem. Soc., Vol. 155, p. K133.

62. **S. K. Ghosh, G. K. Dey, R. O. Dusane, A. K. Grover.** 2006, J. Alloys Comp., Vol. 426, p. 235.

63. **I. Kazeminezhad, W. Schwarzacher.** 2004, J. Solid State Electrochem., Vol. 8, p. 187.

64. **I. Bakonyi, E. Tóth-Kádár, J. Tóth, T. Becsei, T. Tarnóczi, P. Kamasa.** 1999, J. Phys.: Condens. Matter., Vol. 11, p. 963.

65. **I. Bakonyi, J. Tóth, L. Goulau, T. Becsei, E. Tóth-Kádár, W. Schwarzacher, G. Nabiyouni.** 2002, J. Electrochem. Soc., Vol. 149, p. C195.

66. **I. Bakonyi, L. Péter, Z. Rolik, K. Kiss-Szabó, Z. Kupay, J. Tóth, L. F. Kiss, J. Pádár.** 2004, Phys. Rev. B, Vol. 70. 054427.

Chapter 2 : Theoretical Concepts

In this chapter the basics of electrodeposition and some of the physical and chemical properties of nanocrystalline metallic films are introduced. Special emphasis is laid on the description of the effects of nanostructuring on the mechanical and magnetic properties and the corrosion performance of materials (i.e., size effects).

2.1. Electrodeposition

Electrodeposition is a process of coating a working electrode with another material which is present in its ionized form in the electrolyte. Thermodynamically, it is not possible to achieve movement of charges in the presence of solitary electrode-electrolyte interface. Hence, electrochemical experiments are always conducted in electrochemical cells. An electrochemical cell is a device capable of either deriving electrical energy from chemical reactions, or facilitating chemical reactions through the introduction of electrical energy. There are two types of electrochemical cells. Spontaneous reactions occur in galvanic (voltaic) cells; non-spontaneous reactions occur in electrolytic cells. Both types of cells contain electrodes where the oxidation and the reduction reactions occur. Oxidation occurs at the electrode termed anode and reduction occurs at the electrode called cathode. The potential represents the energy available to drive charges between the electrodes and its magnitude controls the direction and the rate at which charges are transferred between the two interfaces. In an electrolytic cell, a direct current (DC) source (power supply), usually a rectifier or motor generator, supplies a current flowing in one direction through the external portion of the circuit when a potential difference is imposed across the system. The current flow is that of electrons in the external connecting wires (external circuit). The mechanism of electrical transfer in the solution is by means of electrically charged “particles” called ions (ionic conduction). Positive ions (cations) travel toward the negative electrode (cathode) and negative ions (anions) travel toward the positive

electrode (anode) when the potential is applied, thus completing the electrical circuit. The deposition of the materials can happen either due to oxidation (anodic electrodeposition) or due to reduction (cathodic electrodeposition) (Figure 2.1).

In cathodic electrodeposition metal species reduce onto conductive substrates used as working electrode. For bivalent species the overall reduction reaction is:

$$M^{2+} + 2e^{-} \rightarrow M^{0}$$

In electrodeposition from aqueous solutions, hydrogen evolution may consume part of the current density input as a secondary reaction, reducing the current efficiency:

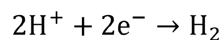

$$2H^{+} + 2e^{-} \rightarrow H_2$$

The H_2 bubbles formed may incorporate into the deposit, causing an embrittlement of the coating (1).

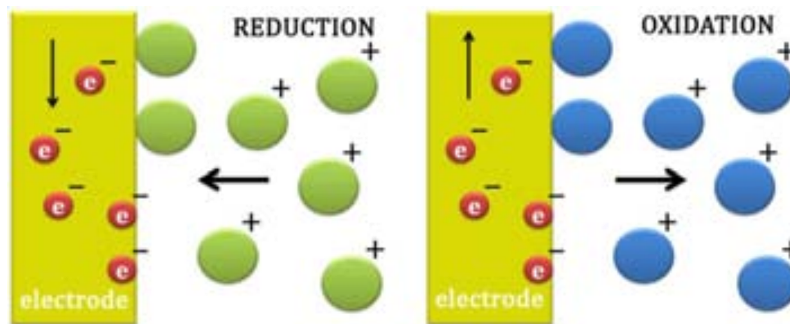

Figure 2.1: Schematic representation for reduction and oxidation processes in an electrode.

2.1.1. Faraday laws

Faraday's Laws of electrolysis (1833) are basic to electrodeposition (2). They relate the current flow, time and the equivalent weight of the metal with the weight of the deposit and can be summarized as follows:

i) The mass of the substance produced by electrolysis is proportional to the quantity of electricity passing through the electrode.

ii) The amount of electricity in coulombs required to produce 1 mole of a substance is a simple whole number multiple of a constant F = 96485 C/mol.

The laws are mathematically expressed as:

$$W = \frac{Q \cdot A}{n \cdot F} \qquad \text{[Eq. 2.1]}$$

where W is the weight of the deposited mass (g), Q is the total charge (C) which is related with time through $Q = \int I \cdot dt$ (I is the current and t the duration of the electrolysis), A is the molar weight (g/mol), n is the valence of the ions, and F the Faraday's constant. The Faraday's Laws assume a current efficiency of 100% (i.e., hydrogen evolution and other secondary reactions are not taken into account). Thus, the Faraday's Laws constitute an approximation to determine the weight of the deposited mass.

2.1.2. Electrode cell

In electrodeposition one can work with two main cell configurations:

- Two-electrodes cell (Figure 2.2. left): It is formed by the working electrode (WE) and the counter electrode (CE) (which must be inert at the required potential or serve as sacrificial anode). The CE acts as an anode whenever the WE functions as a cathode and vice versa. This configuration is used when a precise control of the potential across the electrochemical interface in not critical.

- Three-electrodes cell (Figure 2.2 right): It is formed by the WE, the CE and an extra electrode called reference electrode (RE) (which must have a known potential, furthermore it must balance the electron added or removed by the working electrode). The potential is measured between WE and RE, and the current flows between WE and CE.

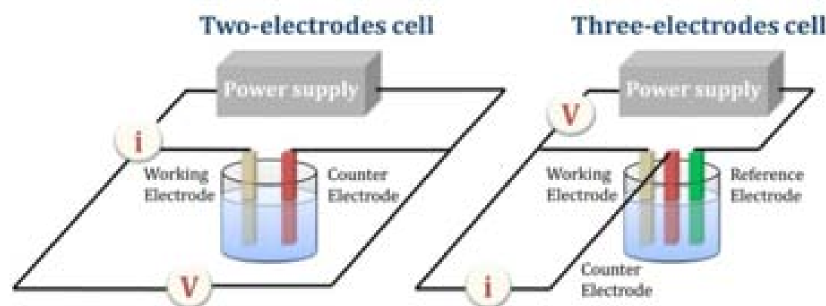

Figure 2.2. Scheme of two and three-electrodes configurations.

2.1.3. Electrodeposition methods

The electrodeposition of a metallic material onto a conductive substrate can be done by either direct or pulsed methods:

- Direct:
  - Potentiostatic: the potential is applied by an external source between WE and RE and it is held constant while the current passing through the WE is measured as a function of time.
  - Galvanostatic: a constant current is applied between the WE and the CE, the potential is measured between the WE and the RE.
- Pulsed: the applied signal (potential or current) is periodically pulsed.
  - Pulse plating (PP): the potential or current is alternated swiftly between two different values. This results in a series of pulses of equal amplitude, duration and polarity, separated by zero current. Each pulse consists of an on-time (t_{on}) during which potential or current is applied, and an off-time (t_{off}) during which zero current is applied (3) (Figure 2.3).
  - Reverse Pulse Plating (RPP): the plating current is periodically interrupted and a stripping time is introduced into the plating cycle (Figure 2.3). RPP has the same effect of replenishing the diffusion layer as PP and selectively dissolves the protrusions of the metal surface to ensure a uniform deposit (3).

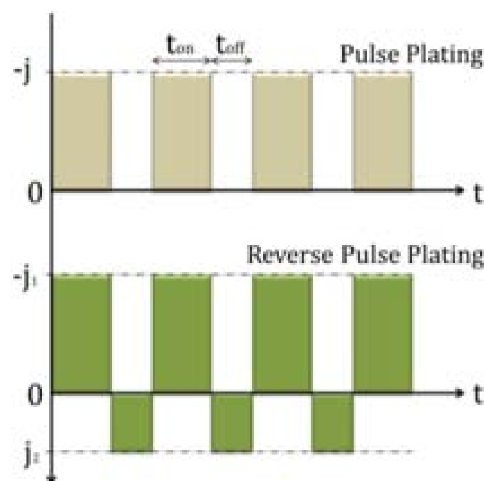

Figure 2.3: Typical representation of current-time waveform for pulse plating (PP) and reverse pulse plating (RPP) applied signals.

2.1.4. Codeposition of two metals in aqueous solutions

Alloy electrodeposition is technically a more complicated process compared to the deposition of individual metals, as it requires a more stringent control of the composition of the electrolyte and the deposition conditions, as well as closer monitoring of these parameters (2).

One has to take into account some issues to successfully codeposit two metals, A and B, A being the nobler one, depending on their partial current profiles (2):

1. Deposition of component A at the limiting diffusion current (Figure 2.4). The potential required for the deposition of component B is reached by depleting the cathodic solution layer of ions of component A, i.e., by generating a concentration polarization and simultaneously an increase in the charge transfer overpotential for A. Unfortunately, dendrites or powders are generally formed at the limiting current. In addition, the fraction of element A incorporated in the alloy is limited by the concentration of A. In these conditions, dendritic growth may be avoided for example if the solution contains surface-active substances (SASs), able to inhibit such growth mode.

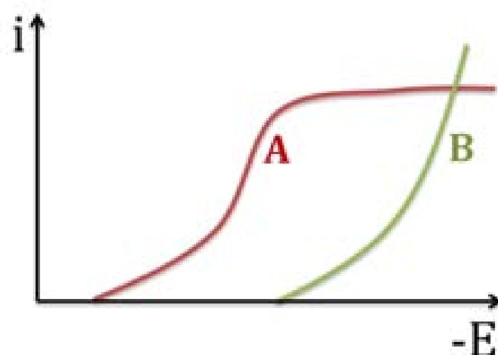

Figure 2.4: Deposition of component A at the limiting diffusion current; the two curves represent the partial currents for components A and B (adapted from (2)).

2. The simple addition of SASs may be sufficient to make alloy formation possible (Figure 2.5).

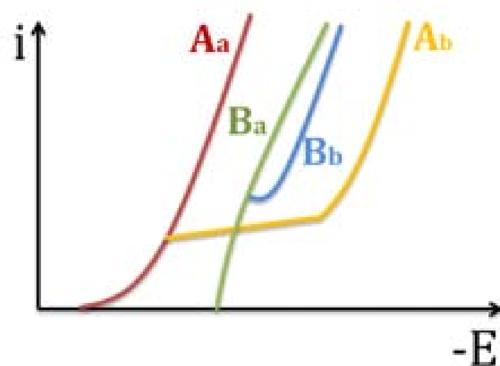

Figure 2.5: Change in partial current curves for components A and B after introduction of SASs: the subscript (a) designates curves in the absence of SASs; subscript (b) curves in the presence of SASs (adapted from (2)).

3. Complex formation between A (or both A and B) and ligands introduced into the solution (Figure 2.6). The most widely used ligands are cyanides, ammoniates, pyrophosphate, tripolyphosphates, aminoacetic and other organic acids, trilon B, gluconates, citrates, etc. Complex compounds of the electropositive metals generally have high stability constants and feature higher polarizability, and consequently tend to draw the deposition potentials of the two components closer.

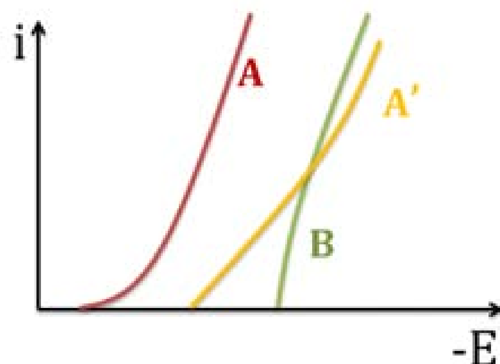

Figure 2.6: Variation of the partial current curve of component A upon complex formation (adapted from (2)).

4. Use of solutions concentrated in B but diluted in A. It requires dilution by approximately two orders of magnitude or more.

2.1.5. Electrodeposition parameters

One of the most important steps in any electrodeposition process is the bath formulation (i.e., solution composition). Although the influence and effects of the operating variables are somewhat dependent upon the solution composition, there are a few rational trends that allow predicting their impact on the morphology,

composition, structure and properties of the deposits. Nevertheless, they are not always predictable and the optimum ranges are usually empirically established.

- Current density: an increase in the overpotential (which is usually related to higher current density) commonly results in an increase of the content of the less noble metal in the deposited alloy.

- Temperature: an increase in temperature causes a decrease of the cathode polarization. Activation polarization decreases with increasing temperature because the exchange current density (j_0) rises rapidly with temperature. In turn, concentration polarization drops as a result of the increase of the metal concentration in the diffusion layer at cathode surface. Lower cathode polarization brings about an increase in the content of the more noble metal in the alloy.

- pH: it is the measure of the activity of the (solvated) hydrogen ion related to the hydrogen ion concentration. During electrolysis of an aqueous solution, hydrogen ions are discharged together with the ions of the metal/s being deposited. The hydrogen evolved has often unfavourably effects on the structure and properties of the electrodeposits, causing spongy or powdery deposits. Also a change in pH value considerably affects the cathodic current efficiency of the electrodeposition process (4). To minimize hydrogen evolution during electrodeposition, one may work at higher pH values or add wetting agents to the bath (see additives classification listed below).

- Mechanical agitation: it reduces the thickness of the cathode diffusion layer, which causes a decrease in the concentration polarization. Lower cathode polarization in agitated cathode or electrolyte results in an increase of the content of the more noble metal in the alloy. An appropriate agitation system can greatly improve the plating performance since it provides sufficient mixing of the chemicals in the electrolyte.

- Air agitation (O_2, N_2, Ar): air agitation by low pressure blowers is used to enhance the removal of the hydrogen bubbles discharged at the cathode.

- Additives: as it has been already mentioned, one of the most important electrodeposition parameters is the chemical composition of the electrolyte to produce deposits with well-defined properties. Apart from

the electroactive species, the presence of SASs (or simply additives) significantly affects the properties of the deposit. In most electrodeposition process from additive-free solutions, the overpotentials corresponding to the different elementary steps automatically adjust themselves to such values as to provide unacceptable cathodic deposits from the technological point of view (dendritical, non-adherent, etc.) (5). Organic additives result in better surface finish and lower internal stresses in the deposits by preventing the nuclei from further growth (6). Metals differ in their susceptibility to the effect of additives (7). Additives act as grain refiners and levellers because of their effects on i) electrokinetics and ii) the structure of the electrical double layer at the plating surface (7). The effects of additives are often manifested by changes in the polarization characteristics of the cathode. Many are thought to operate by adsorption on the substrate or by forming complexes with the metal. This results in the development of a cathodic overpotential that is maintained at a level that allows the production of smooth, non-dendritic deposits having the desired grain size and structure (7). Additives are generally consumed in the deposition process. One of the structural effects that additives impart on deposits is the generation of microtwin faults in metallic deposits, which eventually influences deposit morphology and its mechanical performance. Different interpretations have been put forward concerning their formation. Most theories explain them as caused by the blocking of one of the crystal growth directions by the additive (5). Others assume that the additive molecule, if similar in size to the metal atom to be deposited, allows an advancing growth step and permit the crystal layers to pile up continuously in a correct stacking sequence; in this case, no faults will be produced (5). However, if the adsorbed foreign molecule is considerably larger than the metal atom, an advancing growth step is forced by this obstacle to change its growth direction, and the growth layers continue to pile up in a stacking sequence in reverse to the former until the molecule is covered; thus, a fault is created (5).

Additives can be classified as:

- Complexing agents: electrodeposition of an alloy composed of metals with different electrode potentials results in preferential deposition of the more noble metal. In order to obtain an alloy with the composition

similar to the ratio of the metal concentrations in the electrolyte their potentials should be brought closer together. The difference between the standard electrode potential of Cu and Ni is around 0.6 V. Therefore, Cu and Ni ions should be complexed in aqueous solutions to facilitate their codeposition (8).

- Grain refiners: the dimensions of the grains are determined by the number of grain-dislocations as well as by the number of nuclei which appear during the electrodeposition of metal. In electrodeposition, there are two main ways to obtain nanocrystalline metallic deposits: i) by the addition of organic additives like saccharin (6), coumarin (9) or thiourea (10) among others, which induce disorder during the incorporation of ad-atoms into the lattice of the growing metallic deposit or inhibit surface diffusion of ad-atoms towards growing centres, ii) using a pulsed deposition method (PP or RPP) (6) or iii) using high overpotentials and/or current densities, leading to a high degree of supersaturation of the surface by adatoms (5). However, it should be mentioned that grain refinement is a necessary, but not sufficient condition for the production of bright deposits (6).

- Dendrite and roughness inhibitors: absorb onto the surface and cover it with a thin layer which serves to inhibit the growth of dendrite precursors. These additives can be organic or inorganic substances with the latter typically being more stable. Polyacrylamide is an organic roughness inhibitor used for Cu electrodeposition (11).

- Levelling agents: normal electrodeposition accentuates roughness by putting more deposit in the peaks than in the valleys of the cathode. The current density is highest at the peaks because the electric field strength is greatest in this region. In order to produce a smooth and shiny surface, more metal has to be deposited in the valleys than in the peaks, which is the opposite of the normal effect. Levelling agents are absorbed preferentially on the peaks of the substrate and inhibit deposition, (i.e., they act as an insulator). Therefore, levelling agents improve the throwing power of the plating solution mostly by increasing the slope of the activation potential curve. For example, coumarin or butynediol are typical levelling agents in nickel plating

solutions. The necessary conditions to produce levelling in thick metal film deposition is that the exchange current density is smaller than the limiting diffusion current density in the considered system and that the deposition current density is a little bit larger than the one corresponding to the end of the Tafel linearity (6).

- Brightening agents: a bright deposit is one that has a high degree of specular reflection (i.e., it has a mirror-like finish), in the as-plated condition. Although brightening and levelling are closely related, many solutions capable of producing bright deposits have no levelling ability.
- Wetting agents or surfactants: prevent pits or pores in the deposit because they favour H_2 bubbles detachment from the cathode.

2.2. Mechanical properties

The interest in the mechanical properties of metallic materials lies in that often these materials are subjected to loads during their life cycle. The applied loads can cause deformation or even the fracture of the material making it not useful for the required function. For this reason, the mechanical properties of metallic materials have been investigated for centuries by different means (tension and compression tests, scratching test, indentation test, and Charpy test, among others). The classical mechanical properties typically characterized are the following (12):

- **Hardness:** is the measure of how resistant a solid material is to various kinds of permanent shape change when a force is applied. Tests: scratch hardness, indentation hardness, and rebound hardness. Hardness, and also strength, are measures of material's resistance to localized plastic deformation.
- **Young's modulus:** also called tensile modulus or elastic modulus is a measure of the stiffness of an elastic material.
- **Yield strength:** is the stress at which a material begins to deform plastically. Prior to the yield point the material will deform elastically and will return to its original shape when the applied stress is removed. Once the yield point is passed, some fraction of the deformation will be permanent and non-reversible.

- **Wear resistance:** wear is related to interactions between surfaces and more specifically the removal and deformation of material on a surface as a result of mechanical action of the opposite surface. The definition of wear may include loss of dimension from plastic deformation if it is originated at the interface between two sliding surfaces. Wear resistance is the ability of a metal to resist the wearing away caused by abrasion and friction.

- **Elastic recovery:** is a period of slight rebound in a material after a load has been removed.

- **Resilience:** is the ability of a material to absorb energy when it is deformed elastically, and release that energy upon unloading.

There are some routes or methods aimed at increasing the strength or hardness of a metallic material. The selection of the strengthening method has to take into account both the nature and the final application of the material. The main strengthening routes are (13):

- **Grain-boundary strengthening** (or Hall-Petch strengthening): is a method of strengthening materials by changing their average crystallite (grain) size. It is based on the observation that grain boundaries impede dislocation movement and that the number of dislocations within a grain have an effect on how easily dislocations can traverse grain boundaries and travel from grain to grain.

- **Work hardening** (or strain hardening or cold working): is the strengthening of a metal by plastic deformation at temperature below the melting point. This strengthening occurs because of dislocation movements and dislocation generation within the crystal structure of the material. Cu and Al can be strengthened by work hardening.

- **Solid solution strengthening:** in this case alloying is used to improve the strength of a pure metal. It consists of adding atoms of one element (the alloying element, which is harder) to the crystalline lattice of another element (the base material, which is softer). The alloying element diffuses into the matrix, forming a solid solution.

- **Precipitation hardening** (or age hardening): is a heat treatment technique used to increase the yield strength of malleable materials, including most structural alloys of Al, Mg, Ni, Ti, and some stainless steels. Precipitation hardening relies on

changes in solid solubility with temperature to produce fine particles of an impurity phase, which impede the movement of dislocations, or defects in crystal's lattice. Since dislocations are often the dominant carriers of plasticity, this serves to harder the material. The impurities play the same role as the particle substances in particle-reinforced composite materials. Unlike ordinary tempering, alloys must be kept at elevated temperature for hours to allow precipitation to take place. This period is called aging.

- **Martensitic transformation:** the martensitic transformation is a diffusionless first order phase transformation in the solid state, which proceeds by nucleation and growth of the new phase. The strengthening caused by martensitic transformation arises from various factors such as solid solution hardening, precipitation hardening, order hardening and hardening due to lattice defects and fine crystallite size.

2.2.1. Mechanical properties in nanocrystalline materials

As already mentioned, one of the methods for hardening a material is via the reduction of the crystallite (or grain) size. To explore the mechanical behaviour of nanocrystalline layers with small lateral dimensions and thicknesses in the range from hundreds of nanometres to a few microns, conventional tensile and macroindentation tests are not applicable. This has made necessary to either develop new techniques to assess the mechanical properties of these materials at the nanoscale or adapt the macrotesting tools to the submicro/nanoworld.

Many factors including phase shape, distribution, size, impurities, and also density of crystalline defects influence the mechanical behaviour of nanocrystalline nanomaterials. For polycrystalline materials the empirical Hall-Petch equation provides the relationship between yield strength and grain size (14):

$$\sigma_y = \sigma_0 + kd^{-1/2} \quad \text{[Eq. 2.2]}$$

where σ_y is the yield stress, σ_0 is the innate yield stress for generating a single dislocation, d is the grain diameter, and k is a constant related to the grain boundaries effect on dislocations. In the same way, equation 2.2 shows the effect of grain size on the hardness of polycrystalline materials (14)

$$H_y = H_0 + kd^{-1/2} \qquad \text{[Eq. 2.3]}$$

where H and H_0 are the hardness and innate hardness (hardness of a single crystal) respectively. In nanocrystalline metals with grain sizes of about 10 nm, the hardness and the yield strength are about two to seven times larger than for their coarse-grained counterparts (with grain sizes of more than 1 μm (14)). In aqueous electrodeposition, there are several ways to promote reduction in the grain size (15):

- Current density increases
- Cathode potential increases
- Solution agitation increases
- Solution temperature decreases
- Metal ion concentration decreases
- Additives are added to the electrolyte solution

Of course, not all the strategies work fine for all systems and their suitability need to be explored in each particular case.

2.3. Magnetic behaviour of materials

Magnetism is a macroscopic phenomenon with its origin in quantum mechanics. Materials can be classified depending on the response to an applied field as:

- **Diamagnetic:** its origin is found in the precession of the electron orbit in the presence of an applied magnetic field. Diamagnetic materials do not present permanent magnetic moment and their response is opposed to the applied magnetic field (Faraday-Lenz law (16)).

- **Paramagnetic (PM):** its origin is due to electron spin and to orbital magnetic moment. Paramagnetic materials present permanent magnetic moments but due to thermal activation the spins are randomly orientated (not exchange coupled).

- **Ferromagnetic (FM):** the spins of electrons that belong to ferromagnetic materials are oriented parallel to an applied field as a result of first neighbour interaction (Figure 2.7.a). Temperature plays an important role in ferromagnetic materials. Ferromagnetic behaviour disappears due to thermal agitation when the

temperature surpasses a critical value called Curie temperature (T_C), beyond which the material becomes PM.

- **Antiferromagnetic (AFM):** the magnetic moments are aligned in antiparallel manner, cancelling the total magnetic moment (Figure 2.7.b). Like ferromagnetism, there is a temperature above which antiferromagnetism disappears, the Néel temperature (T_N).
- **Ferrimagnetic:** the magnetic moments present an antiferromagnetic arrangement, but the net magnetic moment is not zero because the antiparallel moment sublattices do not have the same magnitude (Figure 2.7.c).

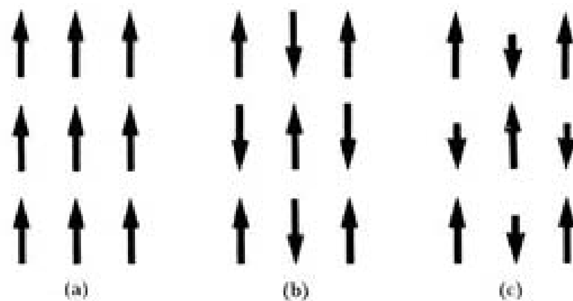

Figure 2.7: Magnetic moment configuration for a) ferromagnetic, b) antiferromagnetic and c) ferrimagnetic materials (17).

2.3.1. Magnetization curves

In Figure 2.8 the magnetic response (M) of diamagnetic, paramagnetic, antiferromagnetic, ferromagnetic and ferrimagnetic materials to an applied field (H) are shown. These curves are called magnetization curves. For ferromagnetic (and ferrimagnetic) materials the magnetization curve defines a cycle called hysteresis curve, from which the following parameters can be extracted:

- Saturation magnetization (M_S): is the value of the magnetization when all the magnetic moments are aligned to the applied magnetic field.
- Remanent magnetization (M_R): after removing the applied magnetic field some magnetic moments remain oriented; the value of that magnetization is the remanent magnetization.
- Coercivity (H_C): is the negative magnetic field needed in order to obtain zero net magnetization.

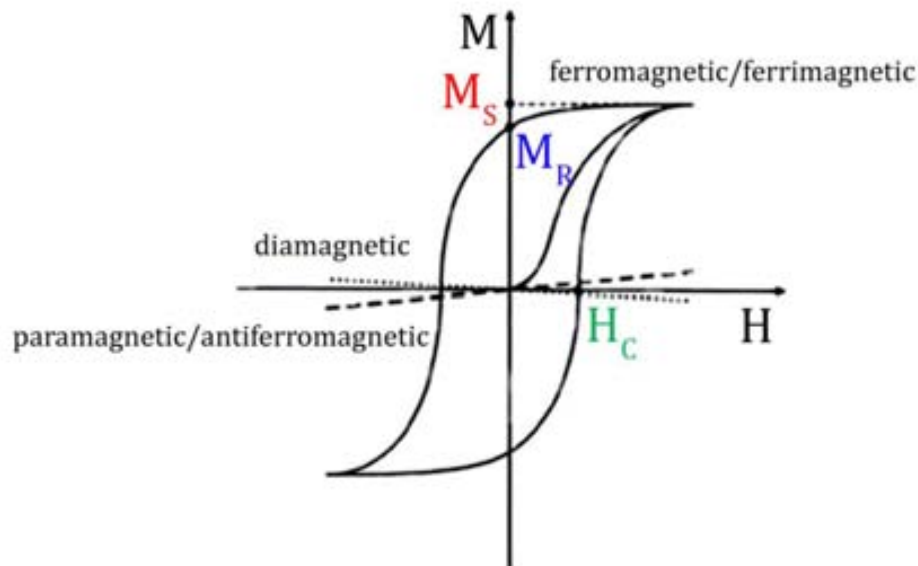

Figure 2.8: Magnetic response under application of magnetic field for the various types of magnetic materials.

Both FM and ferrimagnetic materials differ widely from the other magnetic materials in that they can be magnetized. If a small applied field is enough to produce saturation, the material is said to be magnetically soft. Soft magnetic materials are characterized by low values of *Hc*, typically lower than 10 Oe, and large values of *Ms*, usually higher than 100 emu/g. Some examples of soft FM materials are Fe, Ni or permalloy ($Fe_{20}Ni_{80}$) and they are used in, for example, electromagnets or transformers cores. Hard magnetic materials are characterized by high values of *Hc*, typically larger than 350 Oe, and usually smaller values of *Ms* than soft magnetic materials, i.e. wide hysteresis loops. Some examples of hard magnetic materials are $SmCo_5$, Al-Ni-Co alloys and $Nd_2Fe_{14}B$. Hard magnetic materials are known as permanent magnets. They are used, for example, in motors and generators, in telecommunications, in high-density magnetic recording media and in synchrotrons (18).

There are several factors that affect the properties of magnetic materials: crystallite size, magnetic anisotropy, orientation, particle shape, and exchange interactions (19).

Concerning magnetic anisotropies, the magnetic dipolar anisotropy (also known as shape anisotropy) plays a predominant role in thin films and it is mediated by the dipolar interaction. This is a long range interaction, so its contribution is dependent upon the shape of the sample. Hence shape anisotropy often produces in plane alignment of moments in thin films. In a thin film considered as a magnetic continuum the dipolar anisotropy energy per unit volume is given by:

$$E = \frac{1}{2}\mu_0 M_S \cos^2\theta \quad \text{[Eq. 2.4]}$$

where M_S is the saturation magnetisation, assumed to be uniform throughout the layer. The magnetization subtends an angle, θ, to the plane normal. The dipolar anisotropy energy is thus minimised for an angle of 90° i.e., moments lying in the plane of the layer.

The preference of magnetic moments to align along a given crystallographic direction is called magnetocrystalline anisotropy. In a crystal lattice, certain directions are preferred directions, or easy axes, for the magnetization; the crystal is easier to magnetise in these directions and requires more energy to be magnetised in other directions. The interactions between the crystal field and spin-orbit coupling are the primary source of magnetocrystalline anisotropy. Magnetocrystalline anisotropy has a great influence on industrial uses of ferromagnetic materials. Materials with high magnetic anisotropy usually have high coercivity; that is they are hard to demagnetise. Magnetocrystalline anisotropy is intrinsic to a given material and is independent of a particle shape, although it does depend on temperature. In the case of hexagonal close packed (hcp) cobalt, the easy axis of magnetization is the c axis. In a cubic lattice, symmetry creates multiple easy axes; typically, at room temperature the easy magnetization axes of cubic Ni and Fe are <111> and <100>, respectively (20).

2.3.2. Magnetic behavior in nanocrystalline materials

The magnetic properties are influenced by the interatomic distances, and thereby by the crystallite size. As can be seen in

Figure 2.9 the curve H_C versus crystallite size $<d>$ presents a maximum value for $<d>_C$. For large values of $<d>$, when the direction of H is reversed, the magnetization changes from positive to negative values, due to the formation and motion of domain walls. However, if the crystallite size is reduced to $<d>_C$, the formation of domain walls becomes energetically unfavourable, so that the particles are in a single-domain state. Consequently, the magnetization reverses by means of coherent rotation of spins, resulting in a high value of H_C. If $<d>$ is further reduced below $<d>_C$, thermal fluctuations cause some magnetic disorder in the FM and H_C is progressively reduced. Finally, if $<d>$ is low enough the system becomes superparamagnetic and no hysteresis is observed.

The saturation magnetization (M_S) in nanocrystalline materials can be considerably lower compared with microcrystalline materials of the same composition. For example, the M_S of 6 nm in diameter Fe nanoparticles is 130 emu/g, while that of microcrystalline α-Fe is 220 emu/g (21). Similarly, the Curie temperature (T_C) decreases as crystallite size decreases. For example, a reduction of T_C of Ni by about 40 K was reported if the crystallite size was reduced to 70 nm (22). These changes all come from the decrease of the grain size toward the nanometric range, as each grain can act like an independent unit.

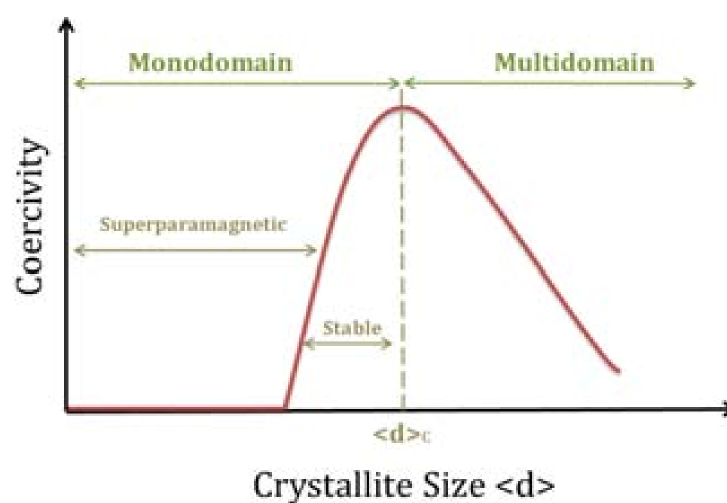

Figure 2.9: Dependence of the coercivity on the crystallite size, <d>, for a FM material (adapted from (19)).

2.4. Corrosion behaviour

Corrosion can be defined as the destruction or deterioration of a material by chemical or electrochemical reaction with its environment (7). The study of the corrosion of materials is of great economical importance, accounting for losses of tens of billions euros a year.

There are many reasons to study the corrosion phenomena and some of them are based on societal issues regarding (23):

- **Human life and safety:** There are several examples during the last fifty years, which corrosion together with other factors have become a misfortune for human life and safety. Some examples are listed in table 2.1.

- **The cost of corrosion:** The damage induced by corrosion throughout European industries costs approximately 270 billion euro per year, the equivalent to 4% of the gross domestic product (GDP) of the European Union, in terms of repair, maintenance and loss of production capacity. Economic losses are divided in directs and indirect losses. Direct losses include the costs of replacing corroded structures and machinery of their components, including necessary labour. Indirect losses are more complex to define, but some examples are: shutdown (loss of production hours to replace a corroded component), loss of product (oil, gas, and water), loss of efficiency (diminished heat transfer, combustion gases), contamination of product, overdesign (commonly equipment is designed many times heavier than corrosion behaviour allows).

- **Conservation of materials:** Statues show corrosion caused by industrial pollution, which after have to be replaced or cleaned.

- **Not well understood corrosion phenomena:** Corrosion science and corrosion engineering must work together to understand and reinforce each other to get better knowledge of the corrosion factors applying in each situation.

There are several factors affecting the corrosion resistance of a metal. Namely, chemical, electrochemical, physical, metallurgical and thermodynamic factors (7). Corrosion is an important aspect associated with coatings. A variety of factors determine the corrosion performance of a metallic coating. These include structure, grain size, porosity, metallic impurity content, interactions involving metallic underplates and cleanliness or freedom from processing contaminants (7).

The corrosion behaviour of materials and coatings can be assessed by different means (24, 25): immersion testing, salt spray/fog testing, electrochemical methods, high velocity flow testing and environmental cracking test methods. Electrochemical testing (including potentiodynamic polarization, potentiostatic polarization, galvanostatic polarization, Tafel extrapolation, polarization resistance determinations, electrochemical impedance spectroscopy and electrochemical noise) is by far one of the most used, especially for coatings. Polarization techniques have been widely used in assessing the resistance to localized corrosion of stainless steels and other iron, nickel, or cobalt-based alloys (26).

Table 2.1 Tragedies caused by corrosion during last fifty years (27, 28)

Date	Consequences	Causes
December 15, 1967	The "Silver Bridge" over the Ohio River linking Point Pleasant, West Virginia, and Kanauga, Ohio, collapsed carrying 46 people to their deaths.	Combined effect of stress and corrosion.
June 23, 1983	A 100-ft long section of a bridge span on a major US Interstate highway collapsed. Three people died and three more were seriously injured.	Corrosion of a support pin.
April 28, 1988	The cabin of a commercial airliner en route from Hilo to Honolulu, Hawaii, suddenly disintegrated, and a flight attendant was tragically lost and 65 passengers were injured.	Combined effects of metal fatigue and corrosion.
February 2001	A nuclear power plant in Ohio was operating on the brink of a potentially devastating nuclear accident.	"Pineapple-sized hole" caused by corrosion in the reactor's lid.
November 19, 2002	The Prestige ship, an oil tanker, split in half, releasing over 76,000 m^3 of heavy fuel oil into the Atlantic ocean. The consequence was the pollution of the sea bed and the contamination of the coastline, especially along the territory of Galicia.	Corrosion in the ballast tanks.
Winter 2004	Toxic levels of dissolved lead ions were found in the drinking water in Washintong DC homes which were serviced by lead pipes.	Change in water treatment procedure which inadvertently disturbed the protective oxide film on lead, thus allowing the underlying metal to corrode and discharge lead ions into drinking water.
July 2005	A 50-ft pedestrian bridge at a shopping mall collapsed on top of a box truck, which was demolished. The collapsed occurred after normal business hours, so no one was injured.	Corrosion of large metal bolts which connected the bridge to a parking garage and to the stores in the mall.
December 2008	A massive water main break in suburban Washintong DC, unleashed a torrent of water that forced dramatic rescues of trapped motorists.	

In fact, the growth of protective metallic coatings is one method of preventing corrosion. Deposits obtained by electrodeposition protect the substrate underneath in three different ways: i) cathodic protection (or galvanic protection); ii) barrier action; and iii) environmental modification or control (7). As is shown in Figure 2.10, when thinking about corrosion, it is important to consider the combination of the material and the environment (29). The corrosion behaviour of a material cannot be described unless the environment in which the material is to be exposed is identified.

Figure 2.10: Important points to take into account when a corrosion resistant material is to be designed.

When a metal is immersed in a solution, it can behave in one of the three ways illustrated in Figure 2.11. These three ways are: immune behaviour (there is no reaction of the metal and thereby no corrosion), active behaviour (the metal dissolves in solution producing a high weight loss of metal) and passive behaviour (metal corrodes but a state of passive behaviour is observed, so that an insoluble, protective corrosion-product film is formed referred to as passive film) (29).

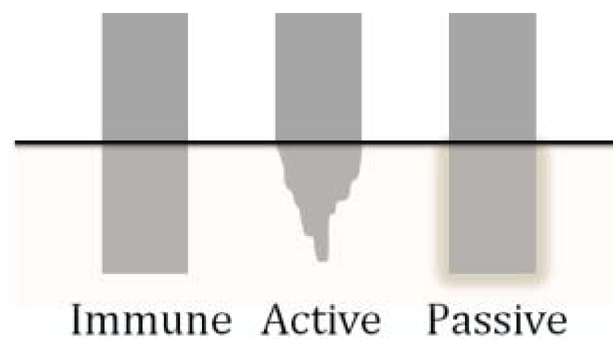

Figure 2.11: Schematic representation of the three behaviours that a metallic material immersed in a solution can experiment.

2.4.1. Corrosion behavior in nanocrystalline materials

In many cases the industrial application of novel materials, such as nanocrystalline materials, will ultimately depend on their corrosion resistance over extended periods of service. For this reason, corrosion problems must be considered at an appropriate stage of material development. In general, the corrosion resistance of nanocrystalline materials in aqueous solutions is of major importance when assessing a wide range of future applications.

An increasing number of investigations are currently focused on the corrosion of nanocrystalline materials. Rofagha et al. studied nanocrystalline Ni and Ni-P produced by electrodeposition technique whereupon the observed behaviour was considered to be consistent with substantial contributions to the bulk electrochemical behaviour from the intercrystalline regions (i.e. grain boundaries and triple junctions) of these materials (30).

Inturi and Szklarska-Smialowska have observed improved localised corrosion resistance in HCl media for sputtered-deposited nanocrystalline type 304 stainless steel in comparison with the coarse-grained counterpart, and attributed this to the fine grain size and homogeneity of the former (31).

Thorpe et al. (32) studied the corrosion behaviour of nanocrystalline $Fe_{32}Ni_{36}Cr_{14}P_{12}B_6$ alloy obtained by the crystallization of the melt-spun amorphous ribbon. These authors determined that the corrosion resistance of this material was significantly greater than that of its amorphous counterpart, and attributed the improvement to the observed greater Cr enrichment of the electrochemical surface via rapid interphase boundary diffusion. Likewise, Fornell et al. (33) also observed an improvement of the corrosion resistance of $Ti_{40}Zr_{10}Cu_{38}Pd_{12}$ metallic glass upon devitrification (i.e., formation of a nanocrystalline structure).

It is difficult to predict the corrosion behaviour of nanocrystalline materials. Some authors have pointed out that nanocrystalline materials exhibit enhanced oxidation and corrosion resistance compared to their coarse-grained counterparts. In contrast, results obtained by other researchers show that nanocrystalline materials possess higher rates of dissolution and corrosion.

Grain size reduction in nanocrystalline materials has been shown to considerably improve the corrosion performance for a wide range of electrochemical conditions. Many of these studies indicate that this is mainly due to the elimination of the localized attack at grain boundaries, which is one of the most detrimental mechanisms of degradation in polycrystalline materials. Several explanations have been put forward for this effect, including: i) the solute dilution effect by grain size refinement; ii) crystallographic texture changes with decreasing grain size, and iii) grain size-dependent passive layer formation.

References

1. **I. M. Robertson, H. K. Birnbaum.** 1986, Acta Metall., Vol. 34, p. 353.

2. **Y. D. Gamburg, G. Zangari.** *Theory and Practice of Metal Electrodeposition.* New York : Springer, 2011.

3. **M. S. Chandrasekar, M. Pushpavanam.** 2008, Electrochim. Acta, Vol. 53, p. 3313.

4. **C. H. Siah, N. Aziz, Z. Samad, N. Noordin, M. N. Idris, M. A. Miskam.** ebookbrowse. *A Review Of The Fundamentals Studies For The Electroplating Process.* [Online] [accessed September, 2012] www.ebookbrowse.com.

5. **M. Nuñez.** *Metal Electrodeposition.* New York : Nova Science Publishers, 2005.

6. **M. Bhardwaj, K. Balani, R. Balasubramaniam, S. Pandey, A. Agarwal.** 9, 2011, Surf. Eng., Vol. 27, p. 642.

7. **J. W. Dini.** *Electrodeposition. The Materials Science of Coatings and Substrates.* New Jersey : Noyes Publications, 1993.

8. **E. Beltowska-Lehman, P. Ozga.** 1998, Electrochim. Acta, Vol. 43, p. 617.

9. **M. Mouanga, L. Ricq, G. Douglade, J. Douglade, P. Berçot.** 2006, Surf. Coat. Technol., Vol. 201, p. 762.

10. **A. C. Mishra.** 2012, Phys. B, Vol. 407, p. 923.

11. **C. Fabian, M. J. Ridd, M. Sheehan.** 2006, Hydromet., Vol. 84, p. 256.

12. **W. D. Callister, D. G. Rethwisch.** *Fundamentals of Materials Science and Engineering: An Integrated Approach.* Fourth Edition. New York : John Wiley & Sons, 2012.

13. **D. R. Askeland, P. P. Fulay, W. J. Wright.** *The Science and Engineering of Materials.* Stanford : Cengage Learning, 2011.

14. **K. T. Ramesh.** *Nanomaterials: Mechanics and Mechanisms.* New York : Springer, 2009.

15. **R. F. Bunshah, [ed.].** *Handbook of deposition technologies for films and coatings.* Second Edition. New Jersey : Noyes Publications, 1994.

16. **W. Saslow.** *Electricity, magnetism, and light.* Toronto : Thomson Learning, Inc, 2022.

17. La ciencia para todos. [Online] [accessed July, 2012] http://bibliotecadigital.ilce.edu.mx/sites/ciencia/menu.htm.

18. **J. Nogués, I. K. Schuller.** 1999, J. Magn. Magn. Mater., Vol. 192, p. 203.

19. **J. Sort.** *Magnetic hardening induced by ferromagnetic-antiferromagnetic coupling.* Bellaterra, Barcelona, Spain : PhD Thesis, UAB, 2002.

20. **G. Schmid, [ed.].** *Nanoparticles: From Theory to Applications.* Weinheim : Wiley-VCH, 2010.

21. **R. Birringer, U. Herr, H. Gleiter.** 1986, Suppl. Trans. Jpn. Inst. Met. Suppl., Vol. 27, p. 43.

22. **R. Z. Valiev, R. R. Mulyukov, K. Y. Mulyukov, V. I. Novikov, L. I. Trusov.** 1989, Pis'ma Zh. Tekh. Fiz., Vol. 15, p. 78.

23. **E. McCafferty.** *Introduction to Corrosion Science.* London : Springer, 2010.

24. **R. Baboian.** *Corrosion Tests and Standards: Applications and Interpretation.* Baltimore : ASTM International, 2005.

25. **A. Eftekhar,** *Nanostructured Materials in Electrochemistry.* Weinheim : John Wiley & Sons, 2008.

26. **F. Mansfeld.** *Electrochemical Corrosion Testing: A Symposium.* Baltimore : ASTM International, 1981. Vol. 727.

27. **E. McCafferty.** *Introduction to Corrosion Science.* New York : Springer, 2010.

28. El Periodico. *El capitán del "Prestige" admite "corrosión" en los tanques del buque.* [Online] [accessed November, 2012] www.elperiodico.es.

29. **J. R. Davis.** *Corrosion. Understanding the basics.* Ohio : ASM International, 2000.

30. **R. Rofagha, U. Erb, D. Ostrander, G. Palumbo, K. T. Aust.** 1993, Nanostr. Mat., Vol. 2, p. 1.

31. **R. B. Inturi, Z. Szklarska-Smialowska.** 1993, Corr. Sci., Vol. 34, p. 1973.

32. **S. J. Thorpe, B. Ramaswami, K. T. Aust.** 1988, J. Electrochem. Soc., Vol. 135, p. 2162.

33. **J. Fornell, N. Van Steenberge, A. Varea, E. Rossinyol, E. Pellicer, S. Suriñach, M. D. Baró, J. Sort.** 2011, J. Mech. Behav. Biomed. Mat., Vol. 4, p. 1709.

Chapter 3 : Experimental Techniques

In this chapter, the experimental details for Cu_xNi_{1-x} electrodeposition and the fundamentals of the techniques used to study the morphology, structure, physical (mechanical, magnetic and thermal stability) and chemical (corrosion) properties of the deposits will be explained.

3.1. Preparation of nanocrystalline Cu-Ni films by electrodeposition

The theoretical concepts about electrodeposition have been already explained in Section 2.1, and the experimental details concerning the preparation of the Cu-Ni films can be found in the articles presented in Chapter 5. Nevertheless, we deem appropriate to briefly indicate common experimental details related to the electrodeposition of Cu-Ni alloy films.

In all experiments a three-electrodes cell configuration has been employed to have a better control of applied potential and current density. As it is shown in Figure 3.1 a double junction Ag|AgCl (E=+0.210 V versus standard hydrogen electrode (SHE)) reference electrode (Metrohm AG) was used with 3 M potassium chloride inner solution and 1 M sodium sulphate as outer solution. A platinum sheet served as counter electrode and metallized silicon substrates as working electrode.

3.1.1. Bath formulation

The bath contained Cu and Ni sulphate salts, citrate as complexing agent and some other additives (Figure 3.2). In particular, saccharine was added to the bath as a grain-refining agent. The [Ni(II)]/[Cu(II)] molar ratio was varied between 11 and 95.2. All bath formulations are specifically detailed in each article included in this Thesis. Also, the temperature, pH, and stirring were maintained constant in all

depositions as shown in Table 3.1. The pH was adjusted to 4.5 by adding NaOH diluted in ultra-pure MQ water (18 MΩ· cm).

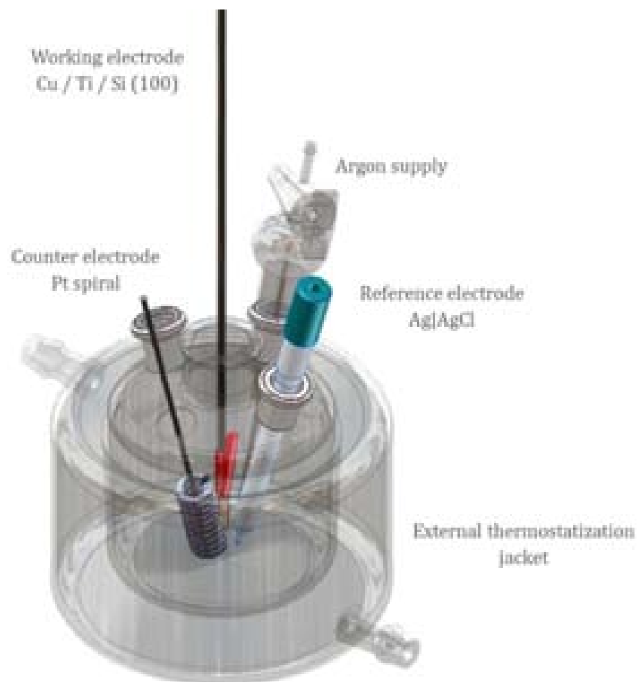

Figure 3.1. Scheme of electrodeposition cell used to prepare the Cu-Ni films.

Table 3.1 Electrolytic solution composition and electrodeposition parameters

Electroactive species	Cu and Ni sulphate salts
Complexing agent	Citric acid monohydrate ($C_6H_8O_7 \cdot H_2O$) Sodium citrate ($NaC_6H_7O_7$)
Wetting agent	Sodium dodecyl sulphate ($NaC_{12}H_{25}SO_4$)
Grain refinement agent	Saccharine ($C_7H_5NO_3S$)
Temperature	30°C
pH	4.5
Agitation	200 rpm using a magnetic stirrer bar

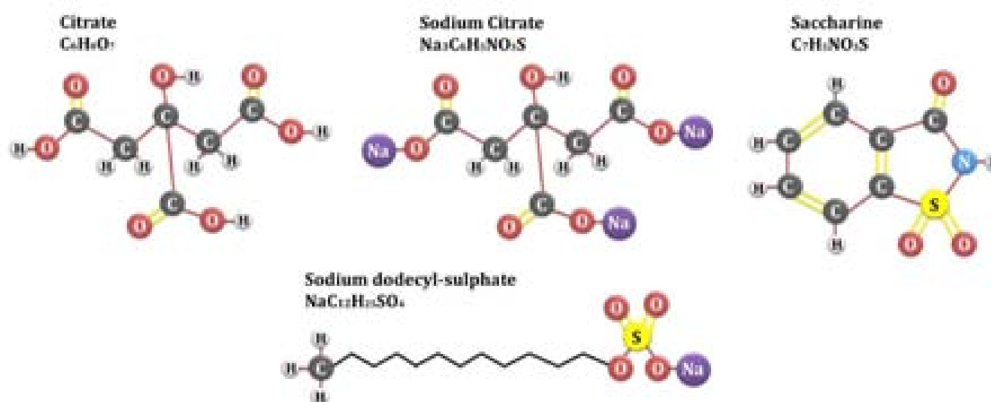

Figure 3.2: Molecular structure of the additives used as complexing agent (citric acid and sodium citrate), as grain refiner (saccharine) and as wetting agent (sodium dodecyl sulphate).

3.1.2. Substrates

The continuing trend of technological evolution has led to the implementation of silicon-based technology combined with other materials to achieve multifunctional devices. Because one of the key application of Cu-Ni alloy films is in the MEMS/NEMS field, silicon based substrates have been used. Direct electrodeposition onto silicon typically requires large applied potentials and/or current densities because silicon is a semiconductor. This poses some restrictions in terms of surface finishing and overall quality of the deposit. To overcome this issue, metallic thin layers are usually sputtered or evaporated onto silicon. Herein Cu-Ni alloy films have been grown onto Si (100) substrates with evaporated Cu (400 nm) and Ti (15 nm) layers (Figure 3.3). The Ti and Cu layers work as adhesion and seed-layers, respectively. Before each deposition, the Cu seed-layer was first degreased with acetone and subsequently dipped in diluted sulphuric acid (10% vol.) to remove any oxides present on the substrate. The working areas have been set between (0.25 ± 0.01) cm^2 and (0.30 ± 0.01) cm^2.

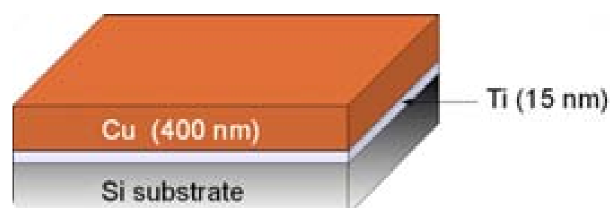

Figure 3.3. Schematic representation of Cu (400 nm)/Ti (15 nm)/Si (100) substrates used for Cu-Ni alloy electrodeposition.

3.2. Electrochemical analysis methods

3.2.1. Cyclic voltammetry

Voltammetry is a powerful technique that electrochemists use in their daily work to investigate electrolysis mechanisms. Cyclic voltammetry (CV) refers to the technique where the potential is ramped between two potential limits at fixed scan rate; upon reaching the lower limit, the scan is reversed back to the lower limit. In our case, CV was used to determine both the effect of complexing agents (i.e., citrate) on Cu_xNi_{1-x} deposition and the optimum range of working current densities from each bath.

3.2.1.a. Working conditions

CVs were recorded/acquired using a PGSTAT 30 or 120 AutoLab potentiostat/galvanostat (Ecochemie). A platinum sheet was used as a CE, a double junction Ag|AgCl as a RE (with 3 M KCl as inner solution and 1 M Na_2SO_4 as outer solution), and vitreous carbon cylindrical rod with $\pi \cdot 10^{-2}$ cm^2 surface area was used as working electrode. A single cycle was run in each experiment, at a scan rate of 50 mV/s. The potential was swept from 0.25 V towards different cathodic limits, and then the scan was reversed towards the positive direction.

3.2.2. Corrosion test: potentiodynamic polarization method

Potentiodynamic polarization methods have been used to investigate the corrosion performance of electrodeposited Cu_xNi_{1-x} films in all range of compositions. E_{OCP}, E_{corr}, j_{corr} and R_P parameters have been determined by Tafel analysis of potentiodynamic polarisation curves.

3.2.2.a. Tafel extrapolation

The Tafel extrapolation method can be used to assess the corrosion rate of a metal when metallic dissolution is under activation control (1). The most common application is for metals immersed in de-aerated acid solutions for which the anodic reaction for a bivalent metal is:

and the cathodic reaction is

The semi-logarithmic plot in Figure 3.4 is not linear near the open-circuit potential (i.e. near zero overpotential). This is because the other half-cell reaction is still appreciable and contributes to the total current. However, at sufficiently high overpotentials, the contribution of the reverse reaction becomes negligible. In this linear Tafel region, the straight lines shown in Figure 3.4 can be extrapolated back to zero overpotential (i.e., back to E_0) to give the open-circuit exchange current density j_0, as shown below.

The well-known Tafel equation follows from the Butler-Volmer equation:

$$\vec{j}_{net} = j_0[e^{\frac{\alpha nF(E-E_0)}{RT}} - e^{\frac{-(1-\alpha)nF(E-E_0)}{RT}}] \quad \text{[Eq. 3.1]}$$

At sufficiently high overpotentials, the rate of the reverse reaction becomes negligible so that Eq. 3.1 can be written as

$$\vec{j}_{net} = j_0[e^{\frac{\alpha nF(E-E_0)}{RT}}] \quad \text{[Eq. 3.2]}$$

or simply

$$j = j_0[e^{\frac{\alpha nF(E-E_0)}{RT}}] \quad \text{[Eq. 3.3]}$$

Taking logarithms in Eq. 3.3:

$$\log j = \log j_0 + \frac{\alpha nF\cdot(E-E_0)}{2.303\cdot RT} \quad \text{[Eq. 3.4]}$$

Thus, a plot of log *|j|* vs. the overpotential (E-E_0) (or of log *|j|* vs. the electrode potential *E*) gives a straight line, as shown in Figure 3.4. From Eq. 3.4 when E=E_0, then $j = j_0$. Thus, the Tafel region can be extrapolated back to $E = E_0$ to give the exchange current density j_0, as shown in Figure 3.4.

Equation 3.4 can also be written as:

$$\eta_a = b_a \log \frac{j}{j_0} \qquad \text{[Eq. 3.5]}$$

Which is one form of the Tafel equation, where η_a is the anodic overpotential and b_a is the anodic Tafel slope given by:

$$b_a = \frac{2.303 \cdot RT}{\alpha nF} \qquad \text{[Eq. 3.6]}$$

Similar considerations also hold for the cathodic branch of the polarization curve. For the cathodic direction, when the back reaction (now the anodic reaction) becomes negligible, Eq. 3.1 produces a cathodic Tafel region which can also be extrapolated back to $E = E_0$ to give the exchange current density j_0, as also shown in Figure 3.4. Moreover Eq. 3.1 leads to

$$\eta_b = b_b \log \frac{j}{j_0} \qquad \text{[Eq. 3.7]}$$

Where η_c is the cathodic overpotential and b_c is the cathodic Tafel slope

$$b_c = \frac{2.303 \cdot RT}{(1-\alpha)nF} \qquad \text{[Eq. 3.8]}$$

From Figure 3.4, it can be easily seen that cathodic Tafel slopes have negative signs and the anodic Tafel slopes have positive signs. Tafel slopes have the units of volts or millivolts per decade of current density. The Tafel slope is always defined as *dE/d log |j|*.

If a well-defined Tafel region exists, as in Figure 3.4, the anodic and cathodic Tafel regions can be extrapolated back to zero overpotential. The intersection of the anodic and cathodic Tafel slopes gives the corrosion potential E_{corr} and the corrosion current density j_{corr} as indicated in Figure 3.4. Linear Tafel regions are usually observed for overpotentials 59 – 120 mV away from the open-circuit potential.

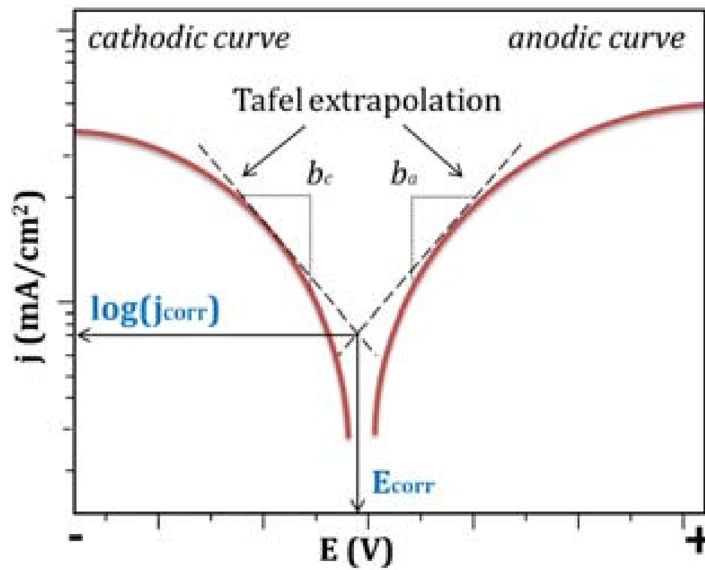

Figure 3.4: Semilogarithmic representation of polarization curves for a corrosion system under activation control (Tafel behaviour).

If the Tafel slopes are known, one can calculate a qualitative parameter which is related to corrosion resistance, the so-called polarization resistance (R_P):

$$R_P = 2.303 \frac{b_a b_b}{b_a + b_c} \cdot \left(\frac{1}{j_{corr}} \right) \qquad \text{[Eq. 3.9]}$$

The polarization resistance can be used in turn to evaluate the porosity of a coating (see Section 3.2.3).

The Tafel extrapolation method is valid if the following conditions apply:

i) Both the anodic and the cathodic branches of the polarization curves are under activation control (stirring the solution can minimize concentration polarization effects).

ii) Well-defined anodic and cathodic Tafel regions exist (over at least one decade of current).

iii) The anodic and cathodic reactions at the corrosion potential are also the only reactions taking place during determination of the polarization curves. (This also means that corrosion product films are not formed at anodic potentials).

iv) Corrosion is general (i.e., uniform) in nature, and localized corrosion does not occur.

3.2.2.b. Working conditions

The corrosion tests were performed in de-aerated NaCl solutions since Cu-Ni alloys have been traditionally used in marine environments where large concentrations of chloride ions are present. Once the sample was introduced in the electrolyte, the open circuit potential (E_{OCP}) was typically achieved after 3 – 4h. The potential was considered to be stabilized when fluctuations smaller than 10 mV/h were observed. The potentiodynamic polarization scans were performed scanning the potential from E_{OCP} – 300 to E_{OCP} + 300 mV (Table 3.2).

Table 3.2 Corrosion test parameters

Electrolyte	De-aerated 3.5 wt% NaCl
Temperature	Room temperature: (22 ± 1)°C
Scanned potential	(E_{OCP} – 300 < E < E_{OCP} + 300) mV
Scan rate	0.1 mV/s
Exposed area	(0.25 – 0.30) cm^2

3.2.3. Polarization method: porosity evaluation

Polarization methods can provide indirect information on the porosity degree of a coating. Specifically, the porosity of a film can be estimated as follows (2):

$$P = \frac{R_{P,S}}{R_P} \quad \text{[Eq. 3.10]}$$

where $R_{P,S}$ and R_P are the polarization resistance of the substrate and the deposited layer respectively. This equation has been applied to estimate the porosity degree of Cu-rich Cu-Ni electrodeposits onto Cu/Ti/Si substrates.

3.3. Structural and morphological analysis techniques

3.3.1. X-ray diffraction (XRD)

The interaction of X-rays with matter can be grouped in two types: absorption and scattering phenomena. X-ray wavelengths are comparable with inter-atomic distances in crystals and, therefore, are an excellent probe for this length scale since X-rays can be diffracted (3). The regular arrangement of the atoms in a crystal structure involves the interference between X-ray beams scattered by atoms. This interference is caused by the existence of specific phase shifts between the waves emitted by the different atoms and this, in turn, is a consequence of the specific distances between the atoms. The resulting wave interference pattern is the basis of diffraction analysis (3). To obtain constructive interference in X-ray diffraction (XRD) experiments, the phase shift should be proportional to 2π or the difference in the length of the path for rays reflected from successive planes should be equal to an integer number of wavelengths, as illustrated in Figure 3.5.

Thus, the peak of the crystallographic planes characterized by the interplanar distance d, will appear in the diffraction pattern if for a certain wavelength λ of the X-ray radiation and a certain incident angle θ Bragg's law is obeyed, given by:

$$n\lambda = 2d \cdot \sin(\theta) \quad \text{[Eq. 3.11]}$$

The integer n, which gives the number of wavelengths in the path difference for waves coming from successive planes, is the *order of reflections*.

To roughly determine the crystallite size of a specimen, <*d*>, the Scherrer's (4) formula can be used:

$$\langle d \rangle = \frac{k\lambda}{\beta\cos(\theta)} \quad \text{[Eq. 3.12]}$$

where λ is the wavelength, k is the instrumental correction, θ is the diffraction angle, and β is the full width at half maximum (FWHM) of the diffraction peak. However, this equation does not take into account the contribution of lattice strain and/or stacking faults on the peaks width and therefore, biased crystal size values can be obtained upon direct application of the formula. For this reason, to have more realistic crystallize size values, the Rietveld method has been applied.

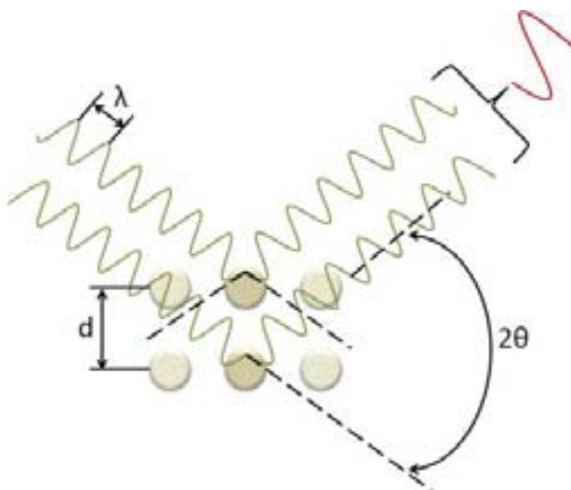

Figure 3.5. Schematic representation of the conditions for constructive interference, according to Bragg's law.

3.3.1.a. XRD pattern fitting. Rietveld method

The overall microstructural parameters, such as lattice cell parameters (*a*), crystallite sizes (*<d>*, average coherently diffracting domain sizes), microstrains ($<\varepsilon^2>^{1/2}$, atomic level deformations), can be precisely evaluated by fitting the full XRD patterns using the "Materials Analysis Using Diffraction" (MAUD) Rietveld refinement program (5, 6).

The Rietveld method uses a least square approach to refine a theoretical line profile until it matches the measured pattern (5). MAUD fits the XRD profiles deconvoluting the "pure" material profile from the instrumental broadening (5).

Specifically, the MAUD program fits the diffraction XRD patterns by describing the peaks using pseudo-Voigt analytical functions having both Lorentzian and Cauchy components (6, 7). For deconvoluting size and strain contributions to line broadening, once the instrumental broadening is extracted, MAUD uses the Williamson-Hall like formalism (8). From the integral width of each components (Cauchy and Gaussian) corresponding to the "pure" profile, the crystallite size and the microstrains are obtained respectively.

This software also includes a formalism to quantitatively evaluate the stacking fault probability (α_{SF}) (6, 9) from the anomalous peak broadening and the relative variations in intensity of some of the XRD peaks (9), thus allowing an

accurate assessment of these planar defects. A stacking fault (SF) is a defect in a faced-cantered cubic or hexagonal close-packed crystal in which there is a change from the regular sequence of positions of atomic planes. According to Warren's description of stacking faults, $1/\alpha_{SF}$ designates the average number of planes between two consecutives stacking faults.

3.3.1.b. Working conditions

The X-ray diffraction patterns have been recorded on a *Philips X'Pert* Diffractometer in Bragg-Brentano geometry (Figure 3.6) using Cu K_α radiation (note that both wavelengths $\lambda(K_{\alpha1})$ = 1.5406 Å and $\lambda(K_{\alpha2})$ = 1.5443 Å have been used in an intensity proportion of $I(K_{\alpha2})/I(K_{\alpha1})$ = 0.5) in the 38°-110° 2θ range (0.03° step size, and 10 s holding time).

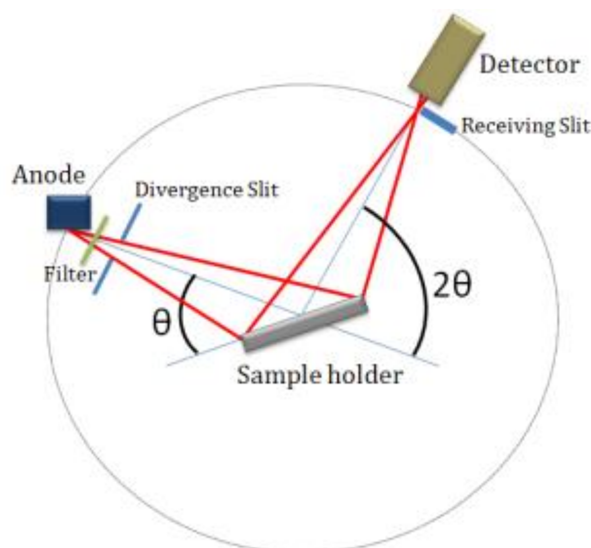

Figure 3.6: Scheme of an X-ray diffractometer in Bragg-Brentano configuration.

3.3.2. Scanning electron microscope

The working principle of a scanning electron microscope (SEM) is based on the utilisation of a focused electron beam (in vacuum) to scan the surface of a material. From the interaction products between the electron beam and the sample, information about topography or composition can be obtained upon collection of either emitted electrons and radiation of the sample or primary electrons which have already interacted with the material (Figure 3.7) (10). The main images

produced in the SEM are of three types: secondary electron (SE) images, backscattered electron (BE) images and elemental X-ray maps. Secondary and backscattered electrons are separated according to their energies.

As is shown in Figure 3.7, several signals are produced when the electrons interact with the sample, and they can provide different information. Specifically the SE and BE signals useful for imaging can be classified taking into account the production mechanism:

- **Elastic scattering:** when high-energy primary electrons interact with the atomic nucleus. When an electron beam penetrates into the sample, part of these primary electrons will immediately be reflected back without any significant loss of energy (< 1 eV), and only a change in direction occurs due to the interaction with the atomic nuclei of the sample. These electrons are called backscattered electrons (BE) and come from elastic incoherent scattering. Backscattered electrons are considered to be the electrons that exit the specimen with energy greater than 50 eV (including Auger electrons). These backscattered electrons have a typical energy between 15 and 30 keV, depending on the primary beam energy.
  - *Imaging:* Because BE are strongly related to the Z-number of the specimen, BE can provide information about the distribution of different elements in the sample. Heavy elements (high Z-number) backscatter electrons more strongly than light elements (low Z-number), and thus appear brighter in the image. The BE signal can be used to detect areas with different chemical compositions.
- **Inelastic scattering:** when high-energy primary electrons interact with atomic electrons.
  - *Imaging:* In an inelastic collision with an electron, some amount of energy is transferred to another electron. If the energy transfer is very small (less than 1 eV), the emitted electrons will probably not have enough energy to exit the surface. If the energy transferred exceeds the work function of the material, the emitted electron can exit the surface. When the energy of the emitted electron is less than 50 eV, by convention it is referred to as a secondary electron. Most of the emitted secondary electrons are produced within the first few nanometres (depending on the material) from the

surface. Secondary electrons produced much deeper in the material suffer additional inelastic collisions, which lower their energy and trap them in the interior of the solid.

– *Composition:* When an incident electron beam hits one atom of the sample inducing the emission of another electron, the corresponding hole is immediately occupied by a third electron located in a more external electronic shell. As a consequence, some energy in the frequency range of X-rays, is emitted. The wavelengths of the emitted X-rays are characteristics of the atoms that compose the sample. Thus, the resulting spectrum is often used to make compositional analyses of the material. This process is usually denoted as Energy Dispersive X-ray Spectroscopy (EDXS). If some regions of the sample are scanned selecting the part of the X-ray spectra corresponding to one of the elements in the sample, it is possible to obtain the distribution of this element at the surface. This technique is commonly known as X-ray Mapping. Therefore regions with higher densities of this element will appear as bright or coloured in the image, while lack of this element will result in a dark area. It has to be mentioned that the accuracy of this technique is commonly nearer ±2% and also, it excels at identifying the heavier elements.

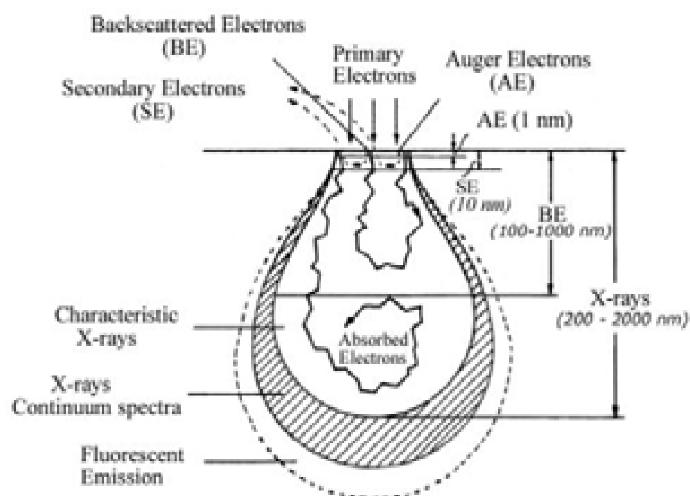

Figure 3.7. Types of electrons and radiation generated after the interaction between the primary electron beam and the sample.

The resolution of the SEM depends on the size of the electron beam, which in turn depends on both the wavelength of the electrons and the electro-optical system that produces the scanning beam. Also, the resolution depends on the size of the interaction volume, or to the extent to which the material interacts with the electron beam.

3.3.2.a. Working conditions

The SEM images corresponding to the surface morphology of Cu-Ni films have been taken on a *JEOL JSM 6300, Zeiss EVO* and field emission *Zeiss MERLIN* microscopes, all of them equipped with EDX data acquisition system for compositional analysis of the samples. All these microscopes are located at the Servei de Microscòpia of the Universitat Autònoma de Barcelona.

3.3.3. Transmission electron microscope

In the transmission electron microscope (TEM) the electron beam is transmitted through an ultra-thin (less than 200 nm) specimen (e.g. nanofilms, nanoparticles), interacting with the specimen as it does so (Figure 3.8). A series of magnetic lenses at and below the sample position are responsible for delivering the signal to a detector, usually a fluorescent screen or a video camera. Accompanying this signal transmission is a magnification of the spatial information of the signal by as little as 50 times to as much as a factor 106. This remarkable magnification range is facilitated by the small wavelength of the incident electrons, and it is the key to the unique capabilities associated with TEM analysis. The probe's source is an electron gun designed to emit highly coherent beam of monoenergetic electrons with exceedingly small wavelength. The wavelength for 200 keV electrons is 0.0025 nm, much smaller than that of light, X-rays, or neutrons used in other analytical techniques. The high spatial resolution of TEM is due to both, electron wavelength and highly focused electron beam, and it is given by

$$R = \frac{0.61 \cdot \lambda}{\alpha} \qquad \text{[Eq. 3.13]}$$

Where λ is the wavelength of incident electrons, and α is the semi-angle of the objective lens aperture. However, the use of larger apertures to increase resolution

is limited by several aberration errors in lenses. As a result, an optimum aperture equilibrating minimum aberration and maximum resolution exists (11, 12).

Like SEM, with TEM analysis one can obtain several signals used to determine different aspects of the sample. Electrons interact primarily with the potential field of an atomic nucleus, and to some extent the electron cloud surrounding the nucleus. In this case one can differentiate between elastic and inelastic scattering signals.

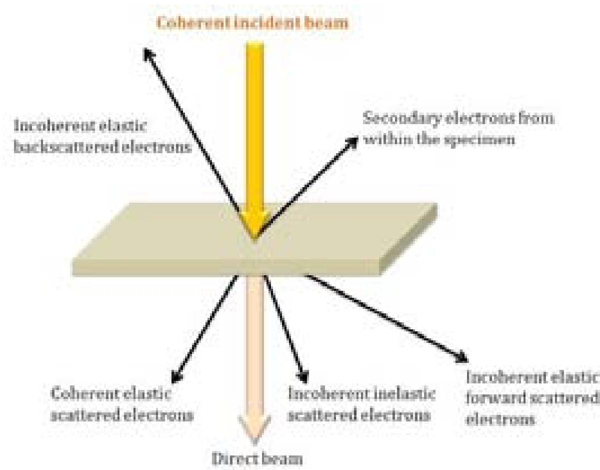

Figure 3.8: Schematic representation of the generation of the electron signal in TEM.

- **Elastic scattering:** is formed by coherently scattered electrons, i.e., scattered in the forward direction, nearly parallel to the incident beam direction.
  - *Imaging:* elastic scattering of electrons by the Coulomb potential of the nucleus is the most important of the interactions that contributes to image contrast. The contribution of different parameters to the elastic scattering are expressed by the atomic scattering factor $f(\theta)$, which is the measure of the amplitude of an electron wave, scattered from an isolated atom, and $|f(\theta)|^2$ is proportional to the scattered intensity:

$$f(\theta) = \frac{1+(E/E_0)}{8\pi^2 a_0} \cdot \left(\frac{\lambda}{\sin(\theta/2)} \right)^2 \cdot (Z - f_x) \qquad \text{[Eq. 3.14]}$$

with θ the angle of scattering, E_0 is the rest energy of a single electron ($E_0 = m_0c^2$), E the beam energy (in keV), a_0 the Bohr radius of the scattering atom, λ the wavelength, Z the atomic number and f_x the scattering factor for

X-ray. Eq. 3.14 shows that elastic scattering increases for higher Z (i.e., heavier elements), but decreases when both θ and λ increases (i.e., high accelerating voltage).

The transmitted and scattered electrons leaving the TEM sample pass through the objective lens (which is placed behind the sample, contrary to the SEM) and a diffraction spectrum is formed in the back focal plane of this objective lens. Recombination of the diffracted electron waves results in the formation of an image in the image plane. The image built up in this way is called bright field image. Alternatively, dark field image is formed by excluding all beams, except for a particular diffracted beam of interest (11, 12). Dark field image reveals the regions contributing to the diffracted beam intensity selected, which can be useful in the characterization of complex microstructures.

- *Diffraction:* when no aperture is placed in the back focal plane of the objective lens, the diffraction pattern itself can be observed and recorded. By inserting an aperture at the image plane of the objective lens, the field from which the diffracted information is obtained is limited; this is referred to as selected area electron diffraction (SAED). The use of such an aperture makes it possible to obtain diffraction from small portions of the specimen. In this way, a direct correlation can be made between the morphological information obtained by imaging and the crystallographic information obtained by diffraction from very small areas. Typical intermediate aperture sizes range from 50 μm to 5 μm. As explained already for X-ray diffraction, the necessary condition to obtain diffraction is represented by the Bragg's law [Eq. 3.11]. This equation can be simplified taking into account the small wavelength for electrons in TEM as:

$$n\lambda = 2d\cdot\theta \qquad \text{[Eq. 3.15]}$$

Planes that are parallel (with a few degrees) to the incident beam will be represented in the diffraction pattern by a diffraction spot located along the normal of the crystallographic plane it represents and at a distance $\lambda L/d$ from the center of the diffraction pattern. L is the camera length and λL is the camera constant (Figure 3.9), as is shown in Figure 3.9, for small angles $2\theta=R/L$. Substituting this expression in [Eq. 3.15], $Rd=L\lambda$ is obtained.

Then, R is inversely proportional to d spacing so, simply by measuring R on the pattern d can be obtained.

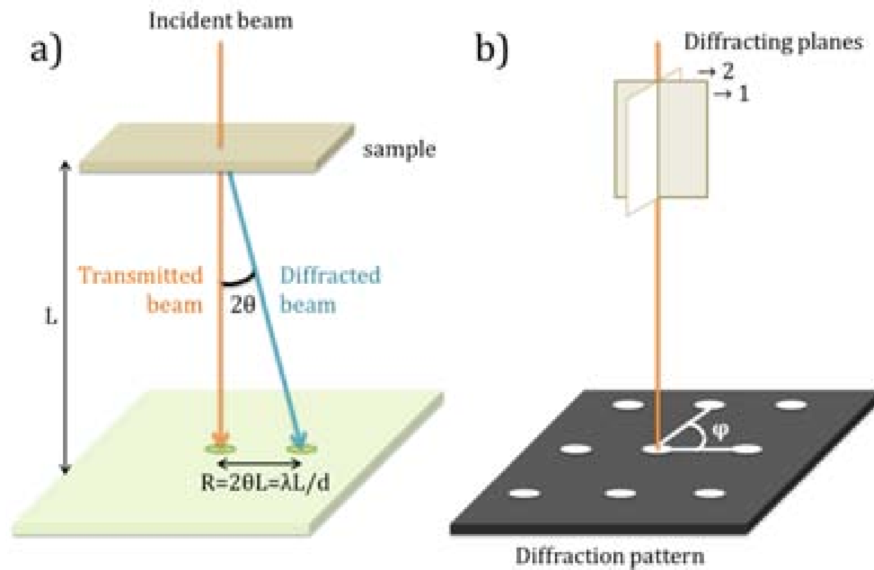

Figure 3.9: a) Schematic diagram showing the geometry of the formation of an electron diffraction pattern and illustrating the parameter camera length *L*. b) Schematic diagram of the formation of a diffraction pattern from a single crystal in the electron microscope. The beam is parallel to a zone axis, with two planes of that zone shown. Note that the angle φ between the spots is equal to the angle between the normal to the planes themselves [adapted from (13)].

A single crystal specimen (Figure 3.10.a) will give rise to a diffraction pattern consisting of a regular array of spots. If the specimen contains several crystals of different orientations, then the diffraction pattern will be the sum of the individual patterns (Figure 3.10.b). Figure 3.10.c shows the case for a specimen containing many crystals oriented randomly. In this case, the spots on the rings are so close to each other that the rings appear continuous.

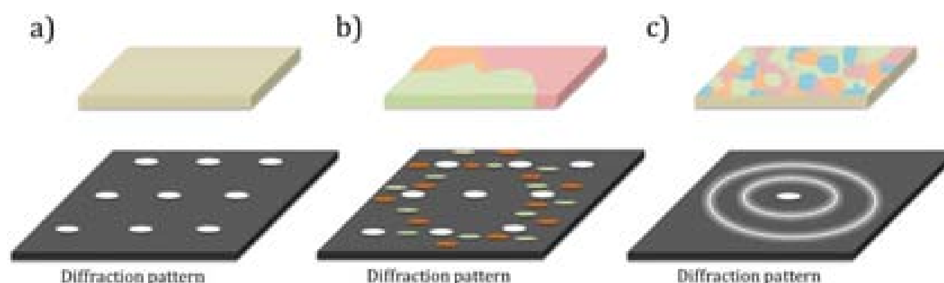

Figure 3.10: Types of diffraction pattern for a) single crystal, b) a small number of grains, and c) a large number of randomly oriented grains.

- **Inelastic scattering:** is concentrated within smaller scattering angles, and the excitation of energy states results in energy losses. The dominant mechanisms are plasmon and interband excitations, which can be described by the dielectric theory. These inelastic scattering processes are less localized than elastic scattering and cannot contribute to high resolution. Inner-shell ionizations result in edge-shaped structures in the electron energy-loss spectrum (EELS) which can be used for analytical electron microscopy at high spatial resolution (14).

  – *EDX:* the way by which characteristic X-ray are generated and what they are useful for has already been explained in detail in Section 3.3.2.

  – *EELS:* EELS signal is the result of the inner-shell ionisation of atoms by the primary electrons. The electron that ionized the atom is deviated only through a small angle (≤ 10 mrad), since its loss in energy is quite small, and it is likely to pass through the sample. These inelastically scattered electrons with a characteristic energy of $E=E_0-E_{binding}$ are measured by EELS microanalysis. EELS detects electrons, in a range of 0.1 to 10 keV, which have passed through the material. EELS tends to work best at relatively low Z-number atoms. Specimen thickness is very crucial for EELS analysis and should be less than 50 nm. With EELS, atomic composition, chemical bonding, valence and conduction band electronic properties, surface properties and element-specific pair distance functions can be studied. EELS has the ability to determine local electronic structures for the extraction of local chemical bonding by analysing near-edge and to extend fine structures of ionization edges.

The measured quantity in EELS is the electron intensity as a function of sample position and energy loss. EELS has better spatial resolution than EDX because the sample volume which provides the information can be defined by apertures confining the collection angle of the spectrometer.

3.3.3.a. High resolution transmission electron microscope (HRTEM)

For high resolution transmission electron microscopy (HRTEM) several beams of the back focal plane are selected, by using a large objective aperture. The image results from multiple beam interference and is based on the phase difference between the transmitted and diffracted beams. It is therefore called the phase contrast image (12). HRTEM can be used to determine structural models, which should however be refined by other high-resolution diffraction techniques using X-rays or neutrons. However, the strength of HRTEM lies in determining disordered and defect structures, which is often difficult to do by other methods.

An interesting tool implemented in HRTEM is the Fast Fourier Transform (FFT) option. FFT is an important image processing tool which uses a complex algorithm that allows measuring interplanar distances.

3.3.3.b. Sample preparation

Probably the most difficult, yet at the same time, most important aspect of the TEM technique is the preparation of high-quality thin specimens for observation. This is an old, ever-expanding, complicated, an intricate field of both materials science and art.

In our case, the 3 μm-thick Cu-Ni films deposited onto Cu/Ti/Si substrates were first subjected to mechanical grinding to remove the substrate. Afterwards, ion milling (with argon ions) was used to produce a hole at the centre of the thinned films. This process consists of bombarding the specimen with energetic ions in order to sputter the material, while is usually rotated, until it is thin enough to be studied in TEM. The controlling parameters are the ion energy, the angle of incidence, the attack from the top and/or backside of the specimen, and the time (Table 3.3).

3.3.3.c. Working conditions

TEM and FFT images and SAED patterns were carried out on a 200 kV *JEOL-JEM-2011*, located at the Servei de Microscòpia of the Universitat Autònoma de Barcelona. EELS analyses were performed using a *JEOL-JEMF-2012* TEM, operated at 200 kV, with a spot size of 0.5 nm, located at the Serveis Cientifico-Tècnics of Universitat de Barcelona.

Table 3.3 Control parameters used for ion milling

Ions	Argon
Energy	4 kV
Incident angle	4° - 4.5°
Attack	Bottom and top
Time	~ 5 h

3.3.4. Atomic force microscopy

In atomic force microscopy (AFM), a probe consisting of a sharp tip arranged near the end of a cantilever is scanned across a sample surface (Figure 3.11), using a piezoelectric positioning device, at distances where the tip-sample atomic interactions are significant. Qualitatively, while keeping the tip-sample interaction constant upon scanning, the topography of the sample can be assessed by measuring the vertical deflection of the cantilever. To achieve this, most atomic force microscopes use laser beam which is reflected from the backside of the cantilever, often coated by a thin metal layer to increase reflectivity, onto a position-sensitive photodetector consisting of two side-by-side photodiodes. In this arrangement, a small deflection of the cantilever will tilt the reflected beam and change the position of the beam on the detector. The difference between the two photodiode signals indicates the position of the laser spot on the detector, and, hence, the angular deflection of the cantilever (15).

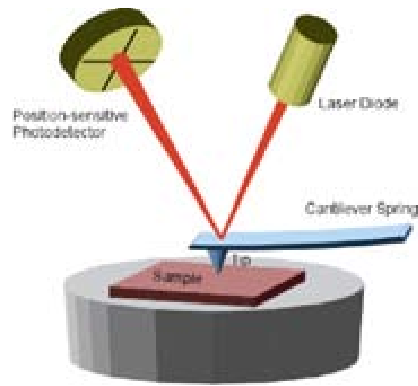

Figure 3.11: Schematic illustration of the working principle of an atomic force microscope. A sharp tip is scanned over the surface of the assessed material (16).

In general, imaging types are divided into:

- **Static** (also called contact or DC mode): the probe is essentially dragged across the sample surface, leading to a repulsive overall force. During scanning, a constant bend in the cantilever is maintained, which constitutes the feedback signal. As the topography of the sample changes, the piezoelectric device moves the relative position of the tip with respect to the sample to keep the set deflection of the cantilever. Using the feedback signal mechanism, the topography of the sample in thus mapped during scanning since the motion of the piezoelectric scanner corresponds directly to the sample topography. Regrettably, when the combination of the applied forces and the contact areas involved results in high contact stresses, tips can be extremely damaged. For this reason the DC mode is usually used to scan very flat surfaces.

- **Dynamic** (usually known as *TappingMode*, name registered by *Veeco Instruments* (17), or AC mode): to reduce or eliminate the damaging forces associated with contact mode, the cantilever can be oscillated near its first bending mode resonance frequency (normally of the order of 100 kHz) as the probe is scanned above the surface in either non-contact mode or intermittent contact mode (i.e., *TappingMode*). In non-contact dynamic mode, the cantilever is externally oscillated at or close to its resonance frequency. The oscillation amplitude, phase and resonance frequency are modified by tip-sample interaction forces. In effect, these changes in oscillation with respect to the external reference provide the feedback

signal and therefore information about the sample. Since under ambient conditions most samples develop a liquid meniscus layer due to the atmospheric humidity, keeping the probe close enough to maintain short-range forces detectable, but without touching the sample, presents major impediment for the non-contact dynamic mode in ambient conditions (15). Nevertheless, to circumvent this, the so-called intermittent dynamic regime is used (*TappingMode*) where the cantilever is driven to oscillate up and down at near its resonance frequency by a small piezoelectric element mounted in the AFM tip holder. The amplitude of the oscillation is greater than in non-contact regime due to the interaction of forces acting on the cantilever when the tip gets closer to the sample. Furthermore, using the changes in phase angle of the cantilever probe, a second image, called a phase image or phase contrast image, can be collected. This image has been shown to be sensitive to material surface properties like chemical composition (17).

AFM surface analysis is typically used to assess the surface roughness (determined by the root-mean-square (RMS) value) and the peak-to-valley of thin films and coatings. The RMS value is given by the standard deviation of the z-values in the scanned sample area, as given by the following equation (18):

$$\mathrm{RMS} = \sqrt{\sum_{n=1}^{N} \frac{(z_n - \bar{z})^2}{N}} \qquad \text{[Eq. 3.16]}$$

where z indicates the vertical height of the surface. The peak-to-valley describes the maximum observed range in a sample area and is given by the distance between the highest peak (z_{max}) and the lowest valley (z_{min}) on the measured surface (18).

$$\mathrm{PTV} = z_{max} - z_{min} \qquad \text{[Eq. 3.17]}$$

3.3.4.a. Working conditions

A *Dual Scope™ C-26* system (Danish Micro Engineering) working in AC mode (*TappingMode*) has been used to evaluate the RMS and peak-to-valley values of the deposits surface. A commercial silicon tip (50-100 kHz resonance frequency) has been used to scan surface areas of 5 x 5 μm^2.

3.4. Mechanical measurements

3.4.1. Nanoindentation

Early hardness tests were based on natural minerals with a scale constructed solely on the ability of one material to scratch another that was softer. A qualitative and somewhat arbitrary hardness indexing scheme was devised, termed Mohs scale, which ranged from 1 on the soft end to 10 for diamond. Quantitative hardness techniques have been developed over the years, for example indentation tests. Indentation testing is a mechanical properties measure technique that consists of touching the material of interest with another whose values of hardness (H_i) and Young's modulus (E_i) are known. In conventional macro-indentation testing, the dimensions of the residual impression left on the sample surface have to be measured to determine H. Rockwell and Brinell hardness tests are examples of macro-indentation test in which spherical indenters are used. For Rockwell the minor applied load is 10 kg, and for Brinell loads are ranging between 500 kg and 3000 kg. Other two testing techniques are Knoop and Vickers microindentation.

The nanoindentation technique is a powerful method to determine mechanical properties of thin films. The penetration depth (h) is of the order of nanometers rather than microns or millimetres due to the small forces involved (in the range of mN with a resolution of nN) (19). It has to be noticed that previous sample preparation is not needed to assess the mechanical properties of films by nanoindentation.

The test procedure involves a loading sequence followed by an unloading; both load (P) and displacement (h) of the tip are recorded during the test (Figure 3.12.a). The attractiveness of nanoindentation tests to measure the mechanical properties of thin films or micro- and nanometric structures stems largely from that they can be determined directly from the loading and displacement curves without the need to image the hardness impression (20) left behind. The Oliver and Pharr method (20) can be used to calculate the hardness:

$$H = \frac{P_{max}}{A} \qquad \text{[Eq. 3.18]}$$

where P_{max} and A are the maximum applied load and contact area respectively. Various shapes of indenter tips can be used to investigate the mechanical behaviour of films. For a Berkovich triangular pyramid tip (Figure 3.12.b) the contact area can be calculated as:

$$A = 25.56 h_c^2 \qquad \text{[Eq. 3.19]}$$

Where h_c is related to h_{max} through:

$$h_c = h_{max} - 0.75 \frac{P_{max}}{S} \qquad \text{[Eq. 3.20]}$$

Where S is the contact stiffness and is determined from the initial unloading slope (Figure 3.12):

$$S = \frac{dP}{dh} \qquad \text{[Eq. 3.21]}$$

This value depends on the geometry (β) and the reduced Young's modulus (E_r) of the indenter as:

$$S = \beta \frac{2}{\sqrt{\pi}} E_r \sqrt{A} \qquad \text{[Eq. 3.22]}$$

For a Berkovich indenter and metallic materials, β=1.034. The reduced Young's modulus is related to the Young's modulus through:

$$\frac{1}{E_r} = \frac{1 - \nu^2}{E} + \frac{1 - \nu_i^2}{E_i} \qquad \text{[Eq. 3.23]}$$

Where E and υ are the Young's modulus and Poisson's ratio, respectively, of the sample, and E_i and υ_i are the values for the indenter (for a diamond indenter Young's modulus and Poisson's ratio are E_i=1140 GPa and υ_i=0.07, respectively) (19).

The value of reduced Young's modulus may be affected greatly by the material behavior. For this reason one has to take care when comparing the Young's modulus of materials obtained by different techniques and on different types of specimens.

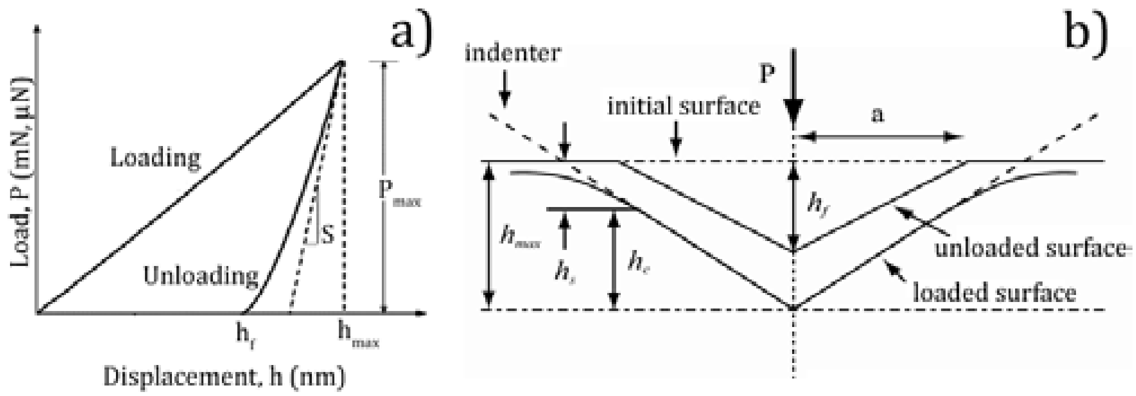

Figure 3.12: a) Load and unload sequence curve for a nanoindentation test. b) Schematic illustration of the unloading process showing the parameters characterizing the contact geometry (20).

3.4.1.a. Indentation size effect

The hardness values obtained by nanoindentation tests are usually higher than those obtained from Vickers microhardness tests. This discrepancy, which can be ranged between 10% and 30% (depending on the material being tested), is often related to the so-called indentation size effect (ISE), which refers to the inversely proportional relationship between H and the indentation applied load P. The ISE has been ascribed to a variety of factors, such as surface effects, friction between the indenter and the sample, or strain gradient hardening (21).

3.4.1.b. Working conditions

Hardness and reduced Young's modulus have been evaluated by nanoindentation, operating in the load control mode, using an *Ultra-Micro Indentation System* (UMIS) device from Fischer-Cripps Laboratories equipped with a Berkovich pyramidal-shaped diamond tip.

The value of maximum applied force was chosen to be 10 mN to ensure that the maximum penetration depth during the test was kept below one tenth of the overall film thickness. This is considered as a necessary condition to avoid having an influence of the substrate on the measured mechanical properties of the film (22). The thermal drift during the nanoindentation was kept below

0.05 nm/s. Corrections for the contact area (calibrated with a fused quartz specimen), instrument compliance, and initial penetration depth were applied.

3.4.1.c. Data analysis

Using Oliver and Pharr method, explained in this section, not only hardness and reduced Young's modulus values were obtained, but also other parameters like H/E_r and H^3/E_r^2 which are proportional to the wear resistance and resistance to plastic deformation respectively (23). The elastic recovery was also evaluated as the ratio between elastic, W_{el}, and total, W_{tot} (elastic + plastic) energies during nanoindentation. These energies were calculated from the nanoindentation experiments as the areas between the unloading curve and the x-axis (W_{el}) and between the loading curve and x-axis (W_{tot}) (19). The results presented here represent the statistical average of a set of 100 indentations for each sample.

3.5. Magnetic measurements

3.5.1. Magneto-optical Kerr effect magnetometer (MOKE)

Magnetic-optical Kerr effect (MOKE) is the net rotation and elliptically polarization of incident vertically linearly polarized light (e.g., laser) as it is reflected off a magnetized sample (24). This effect is due to the interaction of the electric and magnetic fields of the laser with the spin of the electrons of the sample.

MOKE systems are a class of magneto-optical characterization setup increasingly used nowadays for the investigation of the vectorial direction of magnetization at the surface of thin magneto-optical films, or of magnetic nanostructures in different growth configurations. Depending on the details of system design, these instruments are at least capable of in situ qualitative evaluations of magnetization direction (they not provide a quantitative measure of magnetization). The basic principles of operation of a MOKE system consist of focussing shining polarized light onto a magnetic sample under an applied magnetic field, passing the reflected and rotated polarized light through an analyser, before collecting it by a

photodetector. The Kerr rotation is measured by the relative change in intensity, and is proportional to the magnetization of the sample. The output of the analysing setup consisting of the Kerr rotation measurements in either longitudinal, transverse, or polar geometry versus applied magnetic field can be plotted on a graph in order to obtain a MOKE hysteresis loop. It should be noted that hysteresis loops in longitudinal or transverse geometry involve an in-plane magnetizing field, perpendicular to the light plane of incidence, and are therefore sensitive to an in-plane magnetization. On the other hand, polar Kerr rotation hysteresis loops are acquired when the magnetic field is perpendicular to the sample surface, responding to an out-of-plane sample magnetization (perpendicular to the sample surface) (25). Thus, MOKE systems have established themselves as high-resolution spatial tools for measuring the three magnetization components in many magnetic systems.

For homogeneous ferromagnetic materials, magneto-optical effects can be considered as linear against magnetization (26). Then, by measuring the change in rotation or elliptical changes one can probe the magnetic hysteresis loop as a function of the applied magnetic field. This technique is surface sensitive because the reflected light is from about the upper 15-30 nm penetration depth for metals in the visible wavelength.

3.5.1.a. Working conditions

The MOKE measurements have been performed in longitudinal and polar configurations by means of a *Durham Magneto-Optics* magnetometer from the Institut Català de Nanotecnologia. An image of our experimental MOKE set-up is displayed in Figure 3.13.

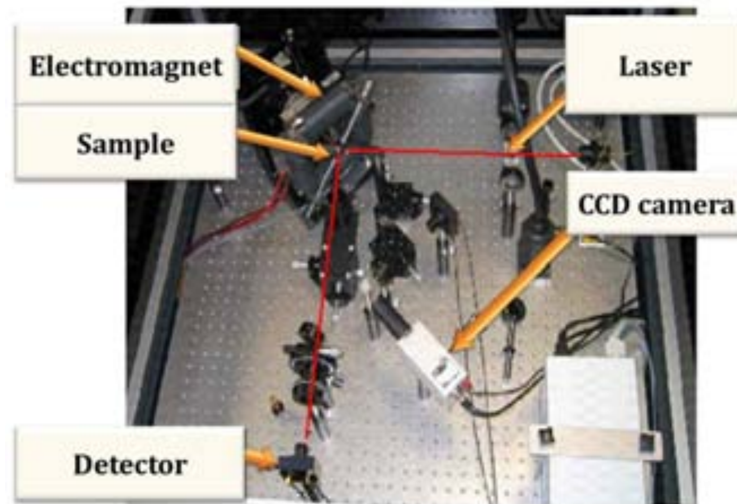

Figure 3.13: MOKE setup used to measure the hysteresis loops of Cu-Ni samples.

3.5.2. Superconductor quantum interferometer device (SQUID)

Since MOKE measurements offer a qualitative study of magnetization, the *Superconductor Quantum Interferometer Device* (SQUID) is typically used to provide quantitative measurements of magnetization. The SQUID is the most sensitive type of detector available at present (27) and its working principle is based on the Josephson junction.

Josephson junction: is made of two superconductors, separated by a non-superconducting (insulating) layer sufficiently thin, so that electrons can pass through (tunnelling) the insulating barrier. Electrons flow between two superconducting junctions which are separated by an insulating layer by means of tunnelling even in absence of an applied voltage. When a voltage is applied, then the current flow stops and the current begins to oscillate (Josephson effect). The Josephson Effect is influenced by magnetic fields in the vicinity. This enables the Josephson junction to be used as buildings blocks in devices that measure extremely weak magnetic fields, such as superconducting quantum interference devices (SQUIDs).

- **Direct current** (DC) SQUID (Two – Junction): consists of two Josephson junctions connected in parallel (Figure 3.14). In practice, the circuit consists of two bulk superconductors, which, together with the Josephson

junctions, form a ring. The flux through the loop of the SQUID is generated by a magnetic coil placed in the interior of the ring.

- **Radio frequency** (RF) SQUID (Single – Junction): the basic element of a single-junction SQUID is a superconducting ring containing a Josephson junction.

3.5.2.a. Working conditions

The magnetic field dependence of the magnetization *M(H)* in DC measurements have been performed using a *MPMS-XL7 SQUID* magnetometer of the Institut Català de Nanotecnologia. The experiments have been carried out by measuring the magnetic moment of the sample (i.e., emu in cgs units), with the applied field parallel to the film plane, and after, scaled to the volume of the sample to obtain the magnetization (i.e., emu/cm^3).

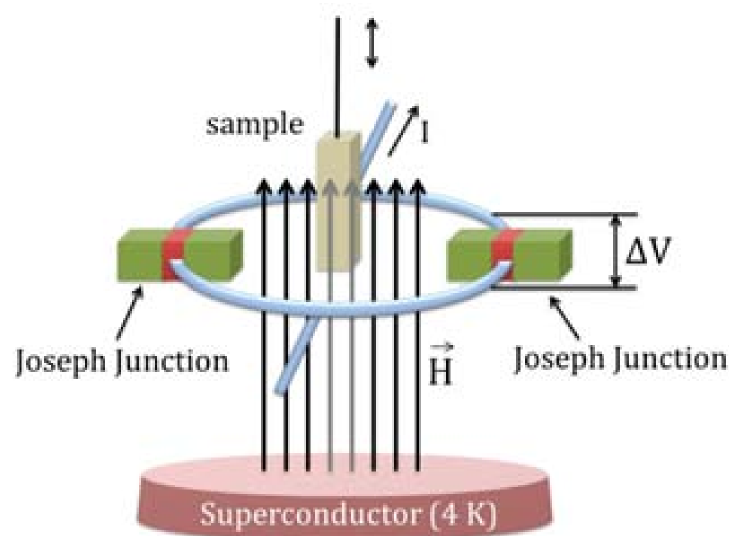

Figure 3.14: Schematic representation of SQUID working principle.

3.6. Other techniques

At this point, the main experimental techniques used along this thesis have been thoroughly explained. In this section the equipment utilized to determine film thickness and to perform annealing treatments are briefly outlined

3.6.1. Film thickness measurements

The average film thickness has been determined from four point measurements at the coating/substrate interface by means of an interferometric profilometer, which is equipped with an optical probe whose principal approach is based on implementing two-beam interferometry architecture, directly derived from the Michelson interferometer. The constructive/destructive interference effect observed at each pattern point is due to the difference in the lengths of the paths followed by the corresponding light rays traveling within two split beams (they are called the *reference path* and the *measurement path*). Such a difference in the path lengths can be converted into a height measure for the corresponding specimen surface point, as long as the position of the corresponding point on the reference mirror (i.e., the length of the reference path) is known (28). Film thickness measurements have been performed a *Tencor P10 (KLA-Tencor Corporation)* profilometer located at the Institute of Robotics and Intelligent Systems (IRIS), ETH Zurich.

3.6.2. Heat treatments

Thermal stability is an important issue when a material is subjected to heating under working conditions because can induce deterioration of mechanical and/or magnetic material properties. In an extreme situation, the material might become useless for the end application. In other cases heat treatments can have a beneficial effect on preserving the nc character of the material, particularly when segregation of one of the constituent elements to the grain boundaries occurs during annealing. This effect is particularly exacerbated in alloys composed of elements with large positive enthalpy of mixing. Heat treatments have been performed at annealing temperatures, T_{ANN}, ranging from 425 to 625 K under vacuum conditions ($< 10^{-5}$ mbar), on a home-made oven located at Unitat de Física de Materials II at Universitat Autònoma de Barcelona.

References

1. **E. McCafferty.** *Introduction to Corrosion Science.* London : Springer, 2010.

2. **J. Creus, H. Mazille, H. Idrissi.** 2000, Surf. Coat. Technol., Vol. 130, p. 224.

3. **W. L. Bragg.** 1913, Proc. Camb. Phil. Soc., Vol. 17, p. 43.

4. **W. Song, R. E. Justice, C. A. Jones, V. H. Grassian, S. C. Larsen.** 2004, Langmuir, Vol. 20, p. 4696.

5. **R. A. Young [ed.].** *The Rietveld Method.* Oxford : Union of Crystallografy, Oxford University Press, 1995.

6. **L. Lutterotti, P. Scardi.** 1990, J. Appl. Crystallogr., Vol. 23, p. 246.

7. **S. Enzo, G. Fagherazzi, A. Benedetti, S. Polizzi.** 1988, J. Appl. Crystallogr., Vol. 21, p. 536.

8. **G. K. Williamson, W. H. Hall.** 1953, Acta Metall., Vol. 1, p. 22.

9. **B. E. Warren.** *X-ray Diffraction.* New York : Addison-Wesley, 1969.

10. **J. Goldstein.** *Scanning Electron Microscopy and X-Ray Microanalysis.* New York : Plenum Publishers, 2003.

11. **D. B. Williams, C. B. Carter.** *Transmission Electron Microscopy - A Textbook for Materials Science- Part 1.* New York : Springer, 2009.

12. **G. Thomas, M. J. Goringe.** *Transmission Electron Microscopy of Materials.* New York : TechBooks, 1979.

13. **P. E. Champness.** *Electron diffraction in the Transmission Electron Microscope.* Oxford : Taylor & Francis Group: BIOS , 2001.

14. **L. Reimer, H. Kohl.** *Transmission Electron Microscopy.* New York : Springer, 2008.

15. **E. Meyer, H. J. Hug, R. Bennewitz.** *Scanning Probe Microscopy: The Lab on a tip.* New York : Springer-Verlag, 2003.

16. Biophysics and Soft Matter. *University Greifswald.* [Online] [accessed September, 2012] http://www3.physik.uni-greifswald.de/method/afm/eafm.htm.

17. [Online] [accessed June, 2012] www.veeco.com.

18. The Membranes Research Environment. [Online] [accessed August, 2012] http://membranes.edu.au/wiki/index.php/Surface_Roughness.

19. **A. C. Fisher-Cripps.** *Nanoindentation.* Second Edition. New York : Springer, 2004.

20. **W. C. Oliver, G. M. Pharr.** 1992, J. Mater. Res., Vol. 7, p. 1564.

21. **M. Dao, L. Lu, R. J. Asaro, J. T. M. De Hosson, E. Ma.** 2007, Acta Mater., Vol. 55, p. 4041.

22. **X. Zhang, A. Misra, H. Wang, M. Nastasi, J. D. Embury, T.E. Mitchell, R. G. Hoagland, J. P. Hirth.** 2004, Appl. Phys. Lett., Vol. 84, p. 1096.

23. **T. Y. Tsui, G. M. Pharr, W. C. Oliver, C. S. Bathia, C. T. White, S. Anders, A. Anders, I. G. Brown.** 1995, Mater. Res. Soc. Symp. Proc., Vol. 383, p. 447.

24. **Z. Q. Qiu, S. D. Bader.** 2000, Rev. Sci. Instrum., Vol. 71, p. 1243.

25. **C. G. Stefanita.** *Magnetism. Basics and Applications.* Berlin : Springer, 2012.

26. **W. J. Geerts.** PhD. Thesis. *Magnetization distribution at the surface of Co-Cr films: Magneto-Optical, Chemical, and Structural Characterization.* The Netherlands : University of Twente, 1992.

27. **C. Shadrach, S. Vadivelu.** *Engineering Physics.* Chennai : Pearson, 2007.

28. **B. M. Colosimo, N. Senin, [ed.].** *Geometric Tolerances: Impact on Product Quality Inspection and Statistical Process Monitoring.* London : Springer-Verlag, 2011.

Chapter 4 : Self-Background on Copper-Nickel Electrodeposition

In this chapter we present our previous work entitled: "***Nanocrystalline electroplated Cu-Ni: metallic thin films with enhanced mechanical properties and tuneable magnetic behavior***" published in Advanced Functional Materials, 2010, Vol. 20, p. 983. This article was written by the end of my master degree, previously to the registration of my Thesis, and thereby it cannot be formally included in the compendium of publications. This work serves to better contextualize the background and motivation of this Thesis and the articles included in Chapter 5.

4.1. Previous work on Cu-Ni alloy

4.1.1. Introduction

Nanocrystalline 3 μm thick $Cu_{1-x}Ni_x$ ($0.45 \leq x \leq 0.87$) films were electrodeposited galvanostatically onto Cu/Ti/Si (100) substrates, from a citrate- and sulphate-based bath containing sodium lauryl sulphate and saccharine as additives. The films exhibit large values of reduced Young's modulus and hardness, both of which can be tailored by varying the composition. The outstanding mechanical properties of these metallic films can be ascribed to their nanocrystalline nature – as evidenced by X-ray diffraction, transmission electron microscopy, and atomic force microscopy – along with the occurrence of stacking faults and the concomitant formation of intragranular nanotwins during the film growth. Due to their nanocrystalline character, films also show very low surface roughness (root mean square deviation of around 2 nm). Furthermore, tuneable magnetic behaviour, are observed when the Ni percentage is increased. This combination of properties,

together with the simplicity of the fabrication method, makes this system attractive for widespread technological applications, including hard metallic coatings or magnetic micro/nano-electromechanical devices.

4.1.2. Experimental

Cu-Ni alloys were obtained by direct current ED in one-compartment thermostatized three-electrode cell (Figure 4.1) using a *PGSTAT30 Autolab* potentiostat/galvanostat (Ecochemie). Silicon (100) substrates with e-beam evaporated Ti (100 nm)/Cu (500 nm) adhesion/seed layers were used as the working electrode (WE), which was positioned vertically within the electrolyte. The working area was 0.3 cm^2. Prior to deposition, the copper surface was first degreased with acetone and subsequently dipped in diluted sulphuric acid to remove any oxides present on the copper surface. Silicon substrate backside was insulated by painting it with a nonconductive ink to ensure only the copper surface was conductive. A standard Ag/AgCl (E = +0.210V/SHE) electrode (EcoChemie) and a platinum spiral were used as reference and counter electrodes respectively. The bath employed to prepare Cu-Ni samples is based on Green's formulation (1). This bath is sulphate-based and contains citrate as complexing agent. The role of the citrate is to reduce the large difference between the reduction potentials of Cu and Ni, thereby allowing their co-deposition. With the aim to refine the grain size and suppress dendrite growth in our electrodeposited thin films saccharine was added (2). The electrolyte contained 184 g/L $NiSO_4 \cdot 6H_2O$, 6.24 g/L $CuSO_4 \cdot 5H_2O$, 62.2 g/L $C_6H_8O_7.H_2O$ (citric acid monohydrate), 0.2 g/L $NaC_{12}H_{25}SO_4$ (sodium lauryl sulphate) and 0.5 g/L $C_7H_5NO_3S$ (saccharine). Analytical grade reagents and ultrapure water (18 MΩ cm) were used to prepare the plating solution. The bath pH was brought to 4.5 and the temperature was set at 30°C. Cu-Ni films were obtained galvanostatically by applying a constant current density in the range from -10 mA/cm^2 to -40 mA/cm^2. Deposition was conducted under gentle stirring (200 rpm) using a magnetic stirrer bar. A similar electrical charge flowed in all experiments, yielding film thickness of about 3.0 µm. Before each deposition, the electrolyte (100 mL) was de-aerated with nitrogen gas flow and a blanket of nitrogen was kept on top of the solution during Cu-Ni growth.

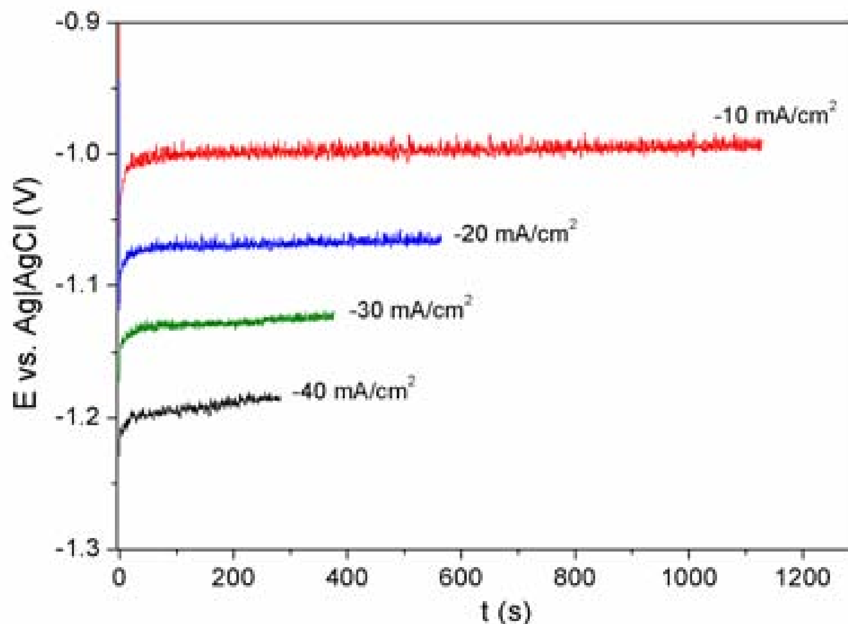

Figure 4.1: Galvanostatic curves for Cu-Ni deposition onto Cu/Ti/Si substrate at i) -10, ii) -20, iii) -30, and iv) -40 mA/cm^2.

4.1.3. Results and discussion

Galvanostatic curves recorded for Cu-Ni deposition onto Cu/Ti/Si (100) substrates are shown in Figure 4.1. These curves are characterized by a very short initial spike followed by a relaxation of the potential towards a stationary value. The value of the stabilised potential decreased as the applied current density was made more negative. The used current densities yielded Cu-Ni deposits with large variation in composition. The nickel percentage obtained from energy dispersive X-ray spectroscopy (EDXS) increased from 45 to 87 at% as the absolute value of the current density was increased (Figure 4.2). It is known that in citrate-containing electrolytic solutions, copper deposition is mass-transfer-controlled whereas that of nickel is charge-transfer-controlled. Upon decreasing the current density, Ni deposition is enhanced while the concentration of electroactive Cu species at the electrolyte/working-electrode interface becomes depleted, thus providing nickel-richer deposits.

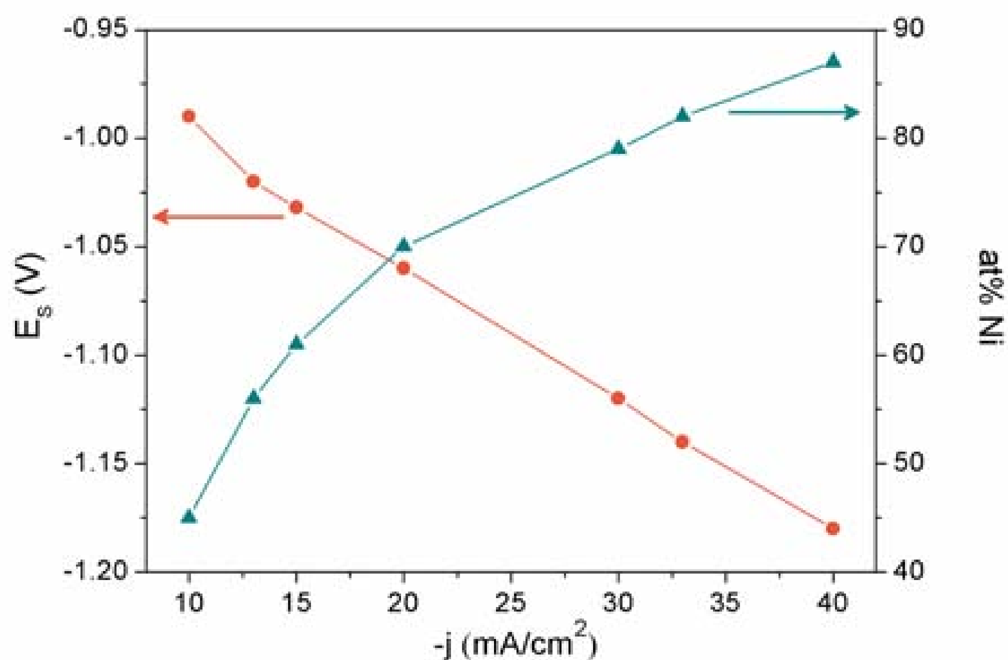

Figure 4.2: Stabilized potential (left y-axis) and Ni percentage (right y-axis) in the films achieved as a function of the applied current density.

The stirring rate ensured homogeneous composition both on surface and across the thickness of films. Only for the copper-richest films, slight composition inhomogeneities were detected at the opposite edges from the electrical contact. All Cu-Ni films were silvery-bright and showed good adherence to the copper surface. Importantly, the films did not peel off from the substrate even at the highest overpotentials, a feature that is easily encountered in additive-free baths due to the high tensile stress caused by hydrogen evolution (3). Measured film thickness was (3.0 ± 0.2) μm.

The X-ray diffraction (XRD) patterns of the Cu-Ni films consist of broad diffraction peaks, which match those of copper (seed-layer) and face-centred cubic (fcc) Cu-Ni phase. The 38°-56° 2θ range, covering the (111) and (200) reflections, is shown in Figure 4.3.a. A progressive shift in the Cu-Ni peak positions, towards larger 2θ angles, is observed as the Ni percentage is increased while Cu seed-layer peaks are not shifted in angle. Indeed, such reflections do not appear when acquiring the XRD patterns under grazing incidence conditions (see Figure 4.4: The patterns consisted of broad diffraction peaks related to the face-centered cubic (fcc) Cu-Ni alloy. No other reflections were observed. Particularly, the response of the copper

seed-layer, which was collected by conventional XRD, vanished.).The above mentioned shift towards higher angles indicates a decrease in the cell parameter (see Table 4 and Figure 4.3.b), as predicted by Vegard's law (4).

Note that direct application of the Scherrer's formula to the Cu-Ni fcc (111) peak width underestimated the true crystallite size, since this formula does not take into account microstrains and stacking faults that contribute on peak's width. Furthermore, a clear difference in the width of the (111) and (200) Cu-Ni peaks is observed, which is indicative of the existence of stacking faults. Rietveld refinement analysis of the XRD patterns (using MAUD software) evidences that the crystallite size is kept at around 30 nm for the complete range of compositions (Table 4.1). MAUD software includes a formalism to deconvolute the contributions from crystallite size and microstrains on the XRD peaks width, as well as to quantitatively evaluate the stacking fault probability (5). The grain size small values can be ascribed to the crystal size refinement promoted by saccharine (2, 6). However, no clear trends related to the current density were observed. In general and within certain limits, smaller crystallite sizes would be expected for higher current densities (7). As this tendency was not observed here, presumably the effect of saccharine overcomes any possible influence of the current density. The microstrain associated with electrodeposits is usually small, about one order of magnitude lower than that in ball-milled and consolidated nc-metals (8). Similarly, α_{SF} is lower than the stacking fault probability evaluated using MAUD in ball-milled cobalt powders consolidated using high pressure torsion (9). According to Warren's description of stacking faults, $1/\alpha_{SF}$ designates the average number of planes between two consecutive stacking faults. Taking into account that α_{SF} lies within 0.007-0.008, there are ca. 130 planes between two consecutive stacking faults. Nevertheless, α_{SF} can be regarded as relatively high, keeping in mind that it refers only to growth twins (created during film deposition) and does not include deformation-induced planar defects. According to these values and taking the crystallite size into account, it can be roughly estimated that approximately half of the grains contain planar defects.

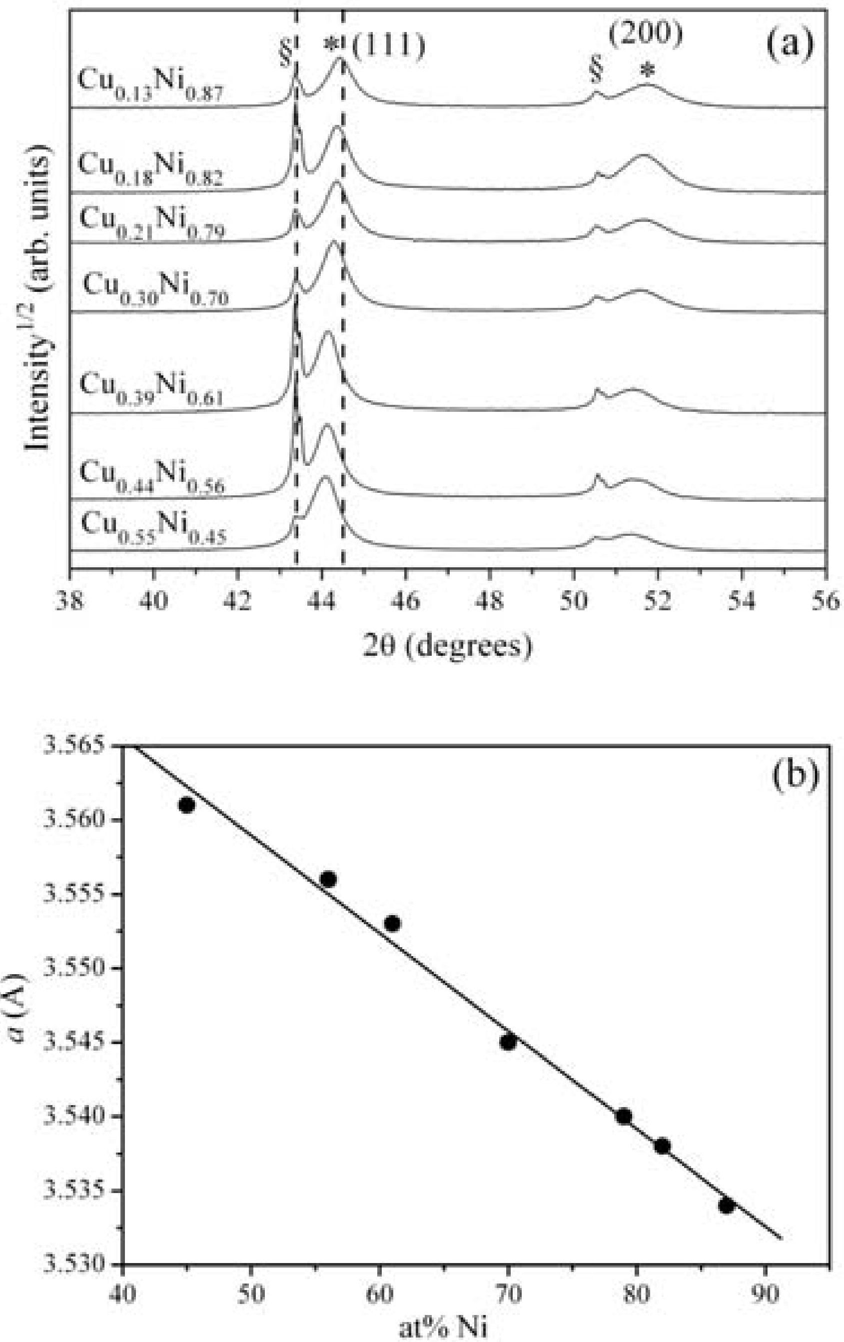

Figure 4.3: a) XRD patterns of $Cu_{1-x}Ni_x$ thin films in the 38°-56° 2θ region. The dashed lines indicate the position of (111) fcc reflection for pure copper and pure nickel. Peaks denoted by § and * belong to the Cu seed layer and the Cu-Ni phase, respectively. b) Cell parameter variation with Ni amount in the alloy. The line is a fit of the data using the Vegard's law (linear correlation coefficient, R, of 0.996).

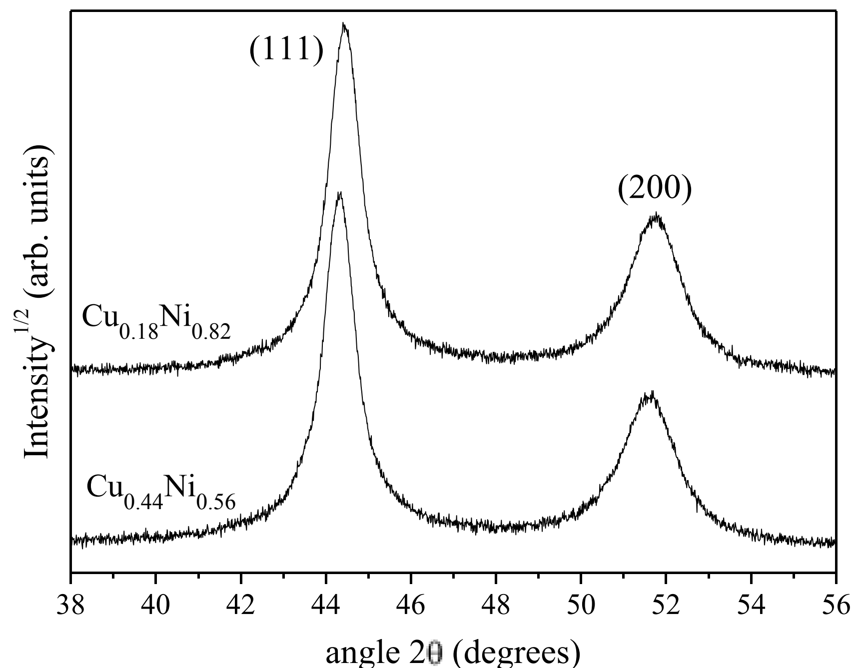

Figure 4.4: XRD patterns of selected Cu-Ni films in the 38°-56° 2θ region collected under grazing incidence α=2.2°.

Table 4.1 Global structural parameters obtained after Rietveld refinement of the XRD data of Cu-Ni films

Specimen composition	Lattice cell parameter a (± 10^{-3} Å)	Crystallite size <*D*> (± 3 nm)	Microstrain $<\varepsilon^2>^{1/2}$ (±10^{-4})	Stacking fault probability α_{SF} (± $5x10^{-4}$)
$Cu_{0.55}Ni_{0.45}$	3.561	26	0.0002	0.0075
$Cu_{0.44}Ni_{0.56}$	3.555	32	0.0002	0.0080
$Cu_{0.39}Ni_{0.61}$	3.553	33	0.0002	0.0078
$Cu_{0.30}Ni_{0.70}$	3.544	28	0.0002	0.0071
$Cu_{0.21}Ni_{0.79}$	3.539	28	0.0001	0.0069
$Cu_{0.18}Ni_{0.82}$	3.538	30	0.0001	0.0084
$Cu_{0.13}Ni_{0.87}$	3.534	29	0.0002	0.0071

In order to further confirm the structural features observed from the XRD study, the Cu-Ni specimens were observed by transmission electron microscopy (TEM). Figure 4.5.a shows a representative plane-view TEM image of the films, in which the nanometre-sized crystallites appear to be homogeneously distributed and randomly oriented. The corresponding Selected Area Electron Diffraction (SAED) pattern shows continuous rings indicating the existence of tiny crystals (Figure 4.5.c). Indexing of the primary rings is consistent with the lattice structure of fcc Cu-Ni. Enlarged views of the crystallites unveil the existence of intragranular nanotwins (Figure 4.5.c and d), in agreement with the assessment of planar defects by XRD. The twin domain thickness is of about 4-5 nm.

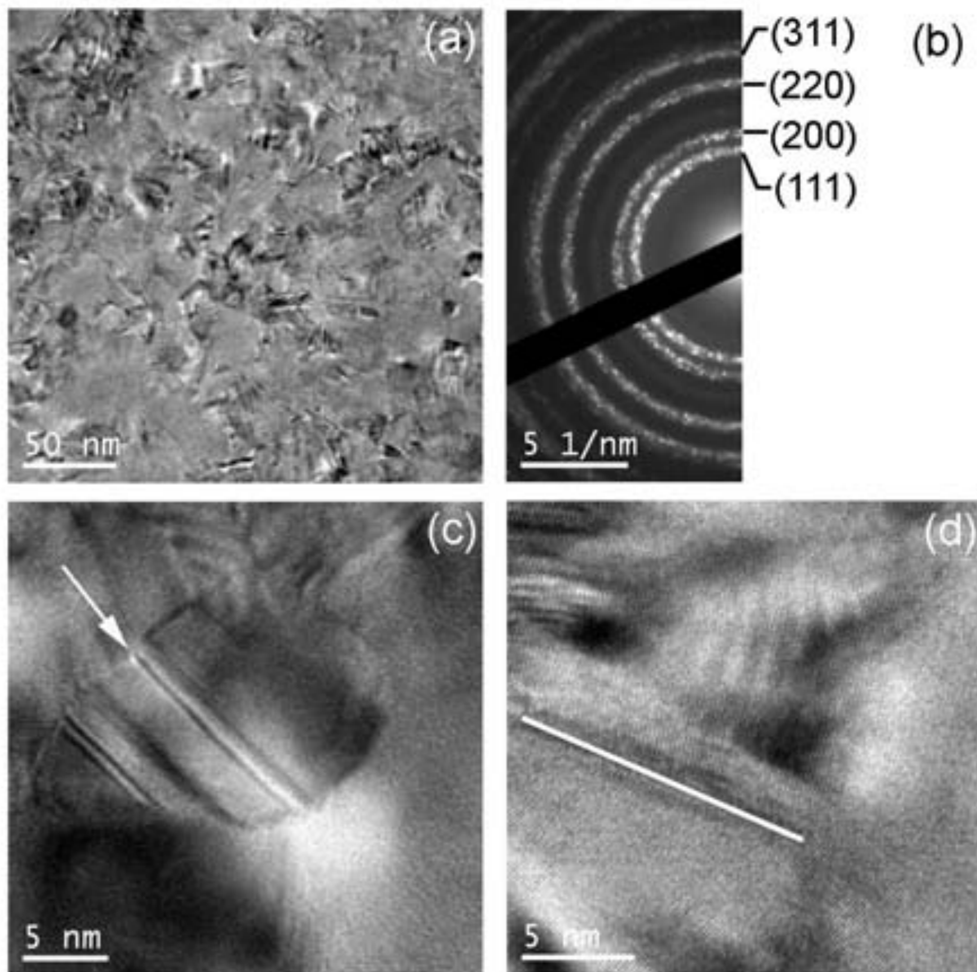

Figure 4.5: (a) Bright-field TEM image of the $Cu_{0.55}Ni_{0.45}$ film and (b) the corresponding SAED pattern. (c) HRTEM image showing the existence of some nanotwins (as the one indicated by the white arrow) inside a nanometre-sized grain and (d) detail of a twin boundary (white solid line) with the crystalline planes visible at each side.

Atomic force microscopy (AFM) topographical images further confirmed the nanocrystalline nature of the films (Figure 4.6). From these images, the peak-to-valley distance values were estimated to be at around 20 nm over 1x1 μm^2 area for all films and the root mean square (RMS) values were also found to be very low, of about 2-3 nm. Such small values can be ascribed to the nanocrystalline nature of the films (10) since microcrystalline electrodeposited alloys usually exhibit much rougher surfaces, with peak-to-valley distances that can reach several hundreds of nanometres (11, 12). The low roughness accounts for the mirror-bright finish of the Cu-Ni films, in contrast to the grey appearance of deposits prepared from saccharine-free baths, which are coarse-grained (showing 1-3 μm nodules) (1).

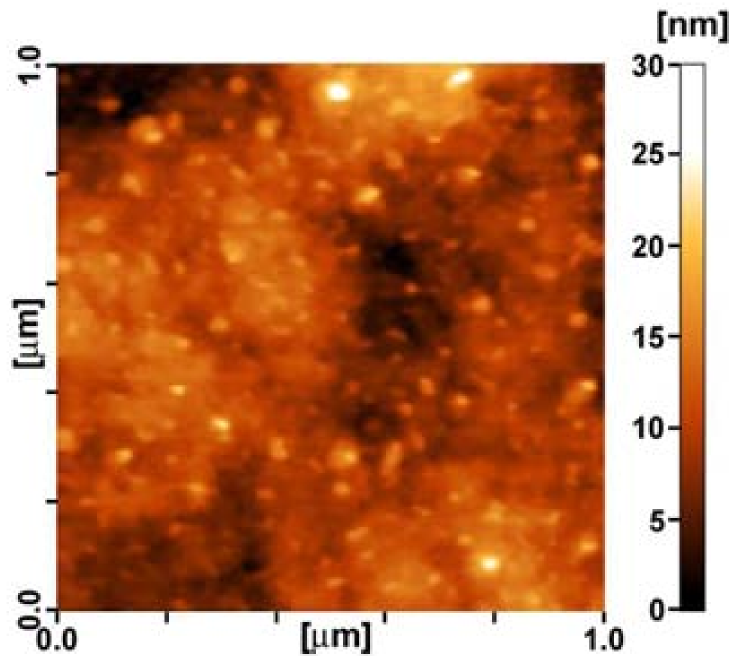

Figure 4.6: Topographical AFM image of the film surface corresponding to $Cu_{0.30}Ni_{0.70}$ specimen.

Figure 4.7.a shows three typical nanoindentation curves corresponding to $Cu_{1-x}Ni_x$ films with x = 0.45, 0.79 and 0.87. The penetration depth achieved at the end of the loading segment is lower for larger Ni percentages, suggesting that alloys with larger Ni content are mechanically harder. The overall dependence of the hardness, *H*, on the Ni percentage, shown in

Figure 4.7.b, indicates that *H* increases from 6.4 GPa (for x = 0.45) to 8.2 GPa (for x = 0.87). These values are much higher than those reported in other metallic thin film systems. Indeed, the hardness values obtained from nanoindentation at low loads (e.g. 10 mN) are usually larger than those evaluated from Vickers microhardness, where the maximum applied load is of the order of 500 mN or more (13). This discrepancy, which can range between 10 to 30 % depending on the material being tested, is often related to the so-called indentation size effect (ISE), which refers to the inversely proportional relationship between *H* and the indentation applied load. The ISE has been ascribed to a variety of factors, such as surface effects, friction between the indenter and the sample or, more recently, strain gradient hardening, which is related to the creation of geometrically necessary dislocations required to accommodate plastic flow in very small indentations (14, 15). It should be noted that the ISE in polycrystalline metals, particularly when the grain size is much smaller than the size of the indented regions, is not very pronounced or even inexistent (14). Therefore, since the lateral size of our indentations is of about 1 μm, the ISE is probably small in our case.

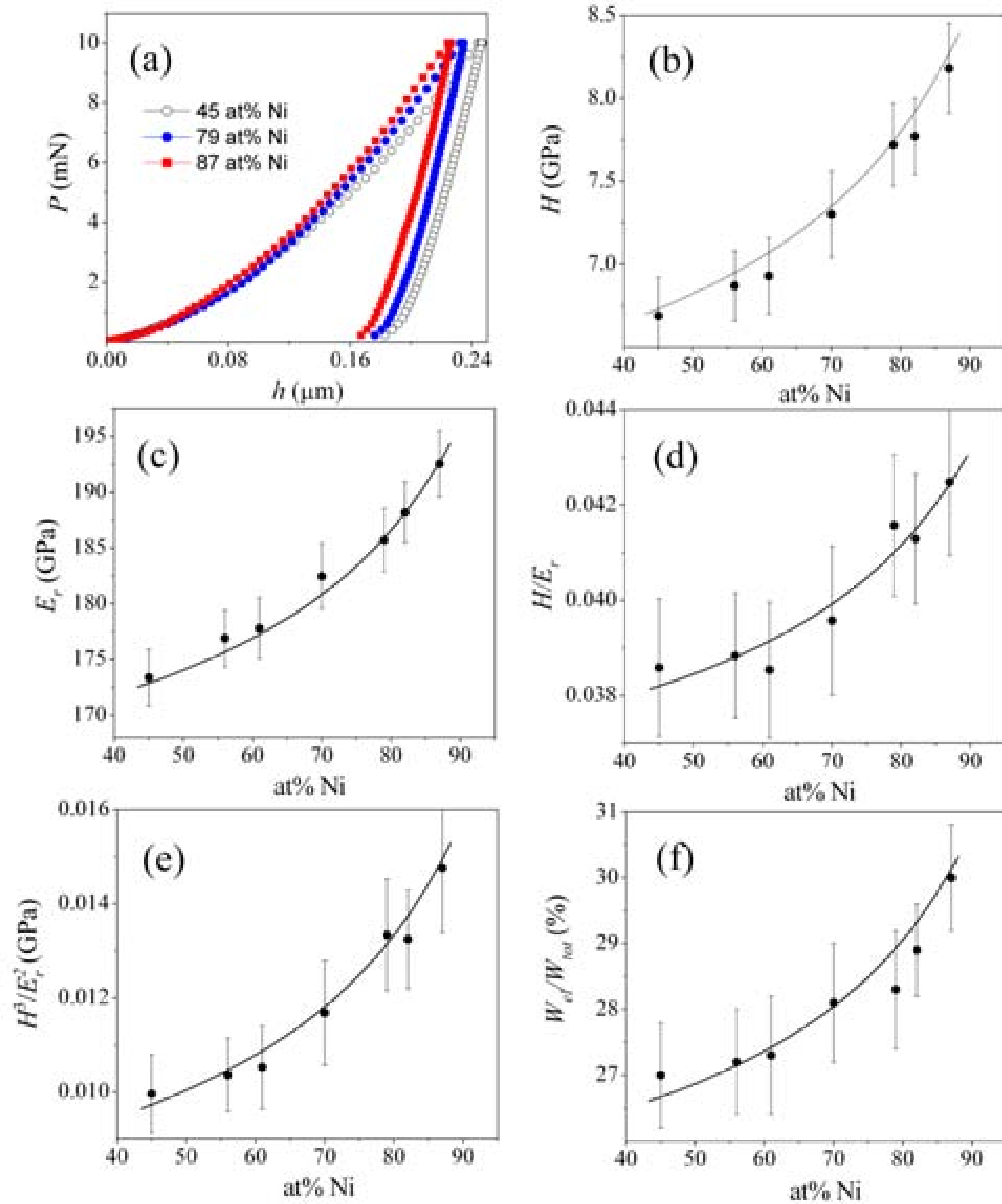

Figure 4.7: (a) Load-unload nanoindentation curves (applied load, *P*, vs. penetration depth, *h*) corresponding to $Cu_{0.55}Ni_{0.45}$, $Cu_{0.21}Ni_{0.79}$ and $Cu_{0.13}Ni_{0.87}$ films. The following panels show the dependences of (b) the nanoindentation hardness *H*, (c) reduced elastic modulus E_r, (d) H/E_r, (e) H^3/E_r^2 and (f) elastic recovery (i.e., W_{el}/W_{tot} ratio, where W_{el} and W_{tot} denote, respectively, the elastic and total energies during nanoindentation), on the thin film composition.

Remarkably, even if an ISE of 10-30% is taken into account, the hardness values obtained in the $Cu_{1-x}Ni_x$ thin films investigated here are clearly much larger than those of microcrystalline or nanocrystalline Cu thin films (16) in concordance with the larger hardness of pure Ni with respect to Cu (17). The hardness of $Cu_{1-x}Ni_x$ films is also considerably larger than in electrodeposited micro-sized pure Ni (18) coarse-grained Co-Ni alloys (19), as-deposited ultra-nanocrystalline Ni-P, Ni-W-P or Ni-W-Cu-P films (20) or Ni-P-W multilayered structures (21). Hardness values similar to the ones of the present study have been achieved, for example, in electroplated nanocrystalline Ni-W alloys (22) nano-multilayered Ni-Cu films (23), or nanocrystalline Ni-Co films (24). Pure nc-Cu and nc-Ni with crystal sizes comparable to the Cu-Ni films were also prepared by electrodeposition in our laboratory and indented using the same set-up, giving rise to hardness values of 2.0 and 8.2 GPa, respectively. In addition to the obvious interest of mechanically hard thin films for surface coating technology, a large hardness is also desirable in order to use thin films as structural components in NEMS, for example in cantilevers, where plastic deformation during resonance is undesirable. It should be noted that some ceramic thin films (e.g., cubic BN or TiB_2) are mechanically much harder (with H exceeding 60 GPa) than nanocrystalline metallic films (25). However, these films suffer from the drawback that, when deposited onto softer substrates, they are unable to accommodate the strains occurring when the substrate is subject to deflection or bending, because of both their intrinsic brittleness and their very high Young's modulus. This precludes the use of ultra-hard ceramic coatings in some technological applications.

The main reason for the large hardness displayed by the electrodeposited $Cu_{1-x}Ni_x$ alloys is the saccharine-assisted crystallite size refinement during thin film growth. For small crystallite sizes, the role of grain boundaries in hindering dislocation motion is enhanced, resulting in increased stress concentration at grain boundaries due to dislocation pile-up. This leads to the so-called Hall-Petch relationship, which postulates that H is inversely proportional to the square root of grain size (16). In addition, it has been reported that the occurrence of intragranular nano-twins also enhances the material strength (6, 26, 27). Actually, twin boundaries can act in an analogous manner as high-angle grain boundaries in terms of disrupting dislocation motion and have been shown to be particularly effective in impeding the propagation of single dislocations (27). At this point it should be noted that, from a mechanical point of view, the saccharine

concentration used in the present study seems to be close to the optimum, since larger saccharine concentrations have been reported to result in slightly larger grain sizes and a reduced density of twin boundaries (6). Figure 4.7.c shows the dependence of reduced Young's modulus, E_r, on the Ni percentage. Since the Young's modulus of Ni is higher than for Cu, a progressive increase of E_r is observed for higher Ni contents. Interestingly, although the hardness values of nanocrystalline Cu-Ni are slightly lower than for Si, the latter exhibits a Young's modulus of 130 GPa (28), hence lower than for the metallic films investigated here. In turn, the measured Young's modulus of permalloy (96.4 GPa) – one of the typical alloys used for soft magnetic MEMS – is also much lower than for Cu-Ni (29). If one assumes a Poisson's ratio for Cu-Ni of 0.34 (30), the real Young's modulus of the $Cu_{1-x}Ni_x$ nanocrystalline films would vary between 180.2 and 204 GPa for x = 0.45 and 0.87, respectively. These values are somewhat larger than the Young's modulus of pure nickel. Indeed, the Young's modulus of fcc Ni electrodeposited on copper substrate at current densities comparable to the ones used in this work (i.e. -10 and -20 mA/cm^2) was reported to be of about 180 GPa (31). Hence, it is likely that the nanocrystalline character of the $Cu_{1-x}Ni_x$ films can also lead to an increase in the Young's modulus, as it was reported long ago in the literature (32).

It is worth mentioning that the wear resistance of a thin film not only depends on its hardness (typically harder materials exhibit a higher wear resistance) but also on the reciprocal of the Young's modulus. Namely, the elastic strain to failure, which is related to the ratio H/E_r, has been shown to be a suitable parameter to describe the wear resistance of a coating, even more than the hardness alone (33, 34). In Cu-Ni films, the ratio H/E_r increases with the Ni percentage (as shown in Figure 4.7.d). Another parameter which is related to the wear characteristics is H^3/Er^2, which is indicative of the resistance of the film to plastic deformation in loaded contact, i.e., the so-called yield pressure (16) (35). The H^3/Er^2 ratio, plotted in Figure 4.7.e as a function of the Ni atomic percentage, also increases with the Ni content. These trends indicate that the wear resistance of Cu-Ni films is larger for higher Ni contents. Finally, Figure 4.7.f shows the dependence of the elastic recovery, W_{el}/W_{tot}, on the film composition. It indicates how much energy is released from the material after being loaded. It has been demonstrated that there is no general correlation between hardness and elastic recovery (35). However, in the $Cu_{1-x}Ni_x$ films, W_{el}/W_{tot} is also found to increase with the Ni percentage. This is

expected since W_{plast}/W_{tot} (where $W_{plast} = W_{tot} - W_{el}$) has been shown to be inversely proportional to the H/E_r ratio (36).

The MOKE results indicate that the $Cu_{1-x}Ni_x$ films with x < 0.6 are nonmagnetic, whereas clear ferromagnetic behaviour was observed for $Cu_{0.30}Ni_{0.70}$ films and for higher Ni percentages (see Figure 4.8.a). As can be seen in Figure 4.8.b the saturation magnetization, M_S, (and the Kerr signal) of the alloys increases monotonically as the amount of Ni becomes larger. This trend is similar to the one experimentally and theoretically observed in bulk Cu-Ni alloys (37–40). Moreover, the threshold for ferromagnetic behaviour of the $Cu_{1-x}Ni_x$ films (x ~ 0.70) is consistent with the Curie temperatures, T_C, observed in bulk, where x ~ 0.70 is need to obtain T_C around room temperature (37, 38). Note that the SQUID hysteresis loops indicated weak ferromagnetism even for x < 0.6 films, in contrast to MOKE observations. This can be explained as a result of small amounts of ferromagnetic impurities in the Si substrate or by taking into account slight composition inhomogeneities in the low x films. Note that MOKE measures rather locally (a few tens of μm^2 spot), while SQUID probes the whole sample (several mm^2). In fact, in the $Cu_{0.55}Ni_{0.45}$ films the regions far from the electrical contact were characterized by EDXS to be slightly richer in Ni and are thus probably responsible for the weak ferromagnetic signal observed by SQUID. For this sample, the SQUID loop (not shown) displayed a clear paramagnetic contribution superposed to the weak ferromagnetic component.

The coercivity (H_C) of the films also varied as a function of alloy composition, giving rise to values in the range from 11 Oe to 26 Oe as the Ni percentage increases. A similar trend was observed for the saturation magnetic field. Note that such increase of coercivity cannot be simply attributed to changes in the film thickness or the crystallite size, as both remained virtually constant for the overall range of alloy composition. Since both the coercivity and saturation magnetisation increase with the Ni content, changes in coercivity are probably due to variations in the magnetocrystalline anisotropy. Actually, an increase of the magnetocrystalline anisotropy with the Ni percentage in $Cu_{1-x}Ni_x$ alloys has been reported in the literature (41). Moreover, for lower Ni contents the Curie temperature should be closer to room temperature (37) which should further reduce the anisotropy.

It is noteworthy that both the mechanical and magnetic properties of the Cu-Ni films remain unchanged after vacuum annealing of the specimens at 200°C. Moreover, no grain size increase was detected by XRD analyses. Thermal stability is also an important requirement for MEMS/NEMS applications as film oxidation, the development of internal stresses and/or the formation of precipitates within the Cu-Ni matrix on heating may degrade device performance. Although more data should be collected to assess the thermal stability of the here-prepared Cu-Ni thin films, it is expected that changes (particularly with respect to grain growth) may occur beyond 200°C. Actually, it has been reported for sputter-deposited Cu-Ni films on heating in oxidizing atmosphere that noticeable oxidation starts at 350°C and that the surface becomes coarse-grained only above 450°C (42).

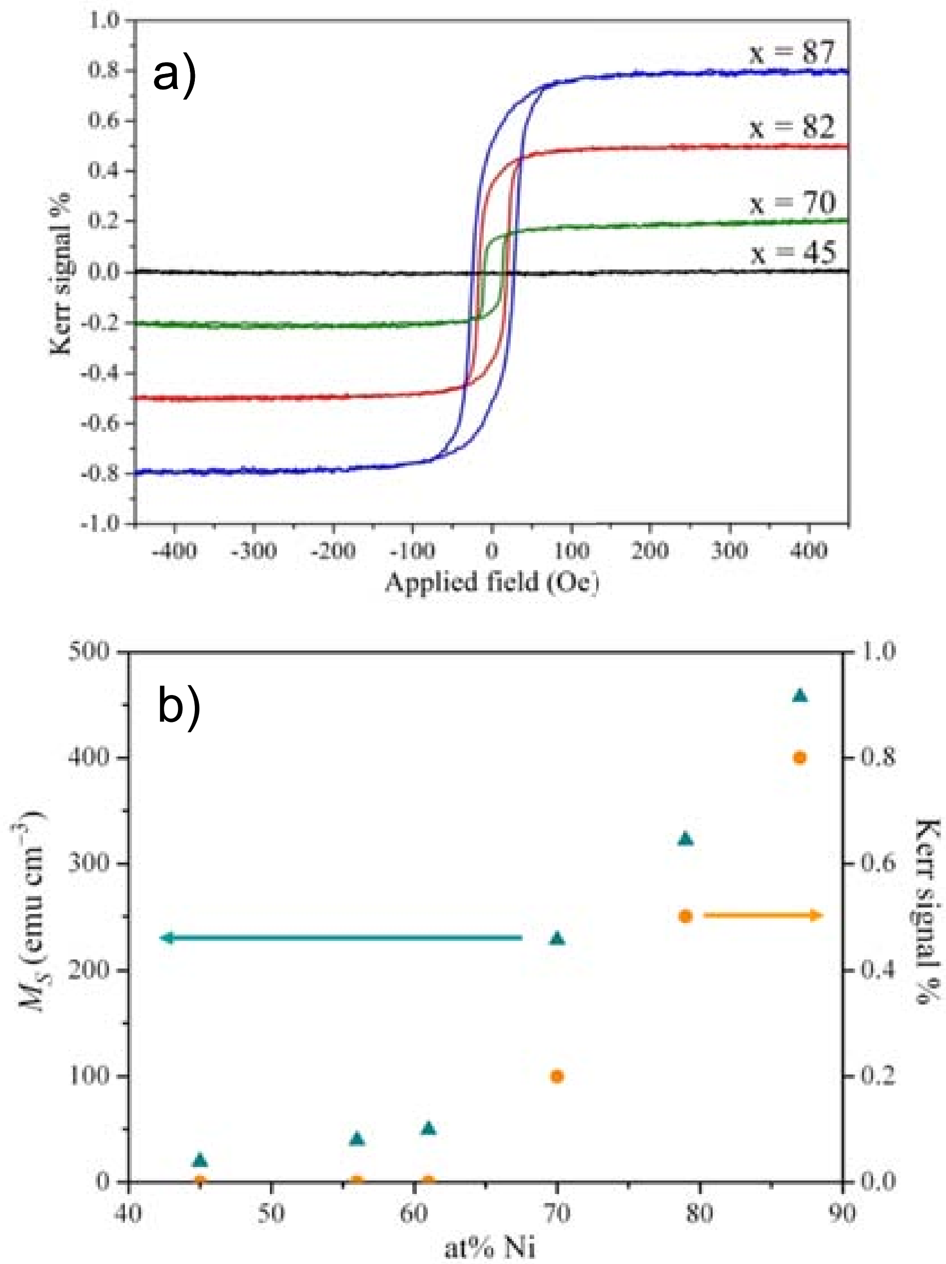

Figure 4.8: (a) MOKE hysteresis loops of various $Cu_{1-x}Ni_x$ films. (b) Dependence of the saturation magnetisation (M_S) (▲, left y-axis) and Kerr signal (○, right y-axis) on the Ni percentage in the films.

4.1.1. Conclusions

Metallic films with composition $Cu_{1-x}Ni_x$ ($0.45 \leq x \leq 0.87$) and 3 µm thickness have been prepared by electrodeposition using a saccharine-containing sulphate-based bath. A detailed structural characterisation by means of XRD, AFM and TEM showed that the films exhibit a nanocrystalline nature (with crystallite size around 30 nm) and revealed the occurrence of stacking faults involving the formation of intragranular nanotwins. Due to this nanocrystalline character, the Cu-Ni thin films are very smooth. Furthermore, from a mechanical viewpoint, these films combine an outstanding hardness (larger than for conventional coarse-grained metallic films) with large Young's modulus, both of which increase with the Ni percentage. Thin films with larger Ni amounts also exhibit higher elastic recovery and H/E_r ratios. Furthermore, these metallic films display tuneable magnetic properties. While alloys with $x \leq 0.61$ are paramagnetic, those with larger x show ferromagnetic behaviour, with saturation magnetisation and coercivity values that progressively increase with the Ni content. The results presented here will certainly contribute to pave the way for the use of nanocrystalline metallic thin films in widespread technological applications, such as surface coatings or magnetic NEMS.

References

1. **T. A. Green, A. E. Russel, S. Roy.** 1998, J. Electrochem. Soc., Vol. 145, p. 875.

2. **X. Cui, W. Chen.** 2008, J. Electrochem. Soc., Vol 155, p. K133.

3. **A. Ollivier, L. Muhr, S. Delbos, P. P. Grand, M. Matlosz, E. Chassaing**, 2009, J. Appl. Electrochem., p. 2337.

4. **A. R. Denton, N. W. Ashcroft.** 1991, Phys. Rev. A., Vol 43, p. 3161.

5. **B. E. Warren.** *X-ray Diffraction*, Massachusetts: Addison-Wesley, Reading, 1969.

6. **B. Y. C. Wu, P. J. Ferreira, C. A. Schuh,** Metall. Mater. Trans. A, Vol. 36, p. 1927.

7. **X. Shen, J. Lian, Z. Jiang, Q. Jian.** 2008, Adv. Eng. Mater. Vol. 10, p. 539.

8. **L. Lu, M. L. Sui, K. Lu.** 2000, Science, Vol. 287, p. 1463.

9. **J. Sort, A. Zhilyaev, M. Zielinska, J. Nogués, S. Suriñach, J. Thibault, M.D. Baró.** 2003, Acta Mater., Vol. 51, p. 6385.

10. **F. Sansoz, K.D. Stevenson, R. Govinthasamy, N.S. Murthy.** 2008, Scripta Mater., Vol. 59, p. 103.

11. **V. Darrort, M. Troyon, J. Ebothé, C. Bissieux, C. Nicollin.** 1995, Thin Solid Films, Vol. 265, p. 52.

12. **N. Eliaz, T.M. Sridhar, E. Gileadi.** 2005, Electrochim. Acta, Vol. 50, p. 2893.

13. **L. Qian, M. Li, Z. Zhou, H. Yang, X. Shi.** 2005, Surf. Coat. Technol., Vol. 195, p. 264.

14. **I. Manika, J. Maniks.** 2006, Acta Mater., Vol. 54, p. 2049.

15. **W. D. Nix, H. Gao.** 1998, J. Mech. Phys. Solids, Vol. 46, p. 411.

16. **M. Dao, L. Lu, R. J. Asaro, J. T. M. De Hosson, E. Ma.** 2007, Acta Mater., Vol. 55, p. 4041.

17. **G. V. Samsonov [ed.].** *Handbook of the physicochemical properties of the elements.* New York: IFI-Plenum, 1968.

18. **J. Lamovec, V. Jović, D. Randjelović, R. Aleksić, V. Radojević.** 2008, Thin Solid Films Vol. 516, p. 8646.

19. **L. P. Wang, Y. Gao, Q. J. Xue.** 2005, Appl. Suf. Sci. Vol. 242, p. 326.

20. **J. N. Balaraju, K. S. Rajam.** 2005, Surf. Coat. Technol., Vol. 195, p. 154.

21. **V. D. Papachristos, C. N. Panagopoulos. L. W. Christoffersen, A. Markaki.** 2001, Thin Solid Films, Vol. 396, p. 173.

22. **A. J. Detor, C. A. Schuh.** 2007, J. Mater. Res., Vol. 22, p. 3233.

23. **Y. Kaneko, Y. Mizuta, Y. Nishijima, S. Hashimoto.** 2005, J. Mater. Sci., Vol. 40, p. 3231.

24. **Y. Li, H. Jiang, W. Huang, H. Tian.** 2008, Appl. Surf. Sci., Vol. 254, p. 6865.

25. **E. Kelesoglu, C. Mitterer.** 1998, Surf. Coat. Technol., Vol. 98, p. 1483.

26. **K. Lu, L. Lu, S. Suresh**. 2009, Science Vol. 324, p. 349.

27. **X. Zhang, A. Misra, H. Wang, M. Nastasi, J. D. Embury, T. E. Mitchell, R. G. Hoagland, J. P. Hirth.** 2004, Appl. Phys. Lett., Vol. 84, p. 1096.

28. **A. R. Krauss, O. Auciello, D. M. Gruen, A. Jayatissa, A. Sumant, J. Tucek, D. C. Mancini, N. Moldovan, A. Erdemir, D. Ersoy, M. N. Gardos, H. G. Busmann, E. M. Meyer, M.Q. Ding.** 2001, Diam. Relat. Mater. Vol. 10, p. 1952.

29. **X. Li, G. Ding, T. Ando, M. Shikida, K. Sato.** 2008, Microsyst. Technol., Vol. 14, p. 131.

30. Mechanical Properties of nickel and its alloys. [Online] [accessed January, 2010] http://www.nickel-alloys.net/index.html

31. **T. Fritz, M. Griepentrog, W. Mokwa, U. Schnakenberg.** 2003, Electrochim. Acta, Vol. 48, p. 3029.

32. **Y. Shirakawa, K. Numakura.** 1955, J. Jpn. Inst. Met. Vol. 19, p. 546.

33. **A. Leyland, A. Matthews.** 2000, Wear, Vol. 246, p. 1.

34. **C. Rebholz, A. Leyland, J.M. Schneider, A. A. Voevodin, A. Matthews.** 1999, Surf. Coat. Technol., Vol. 120–121, p. 412.

35. **J. Musil, F. Kunc, H. Zeman, H. Poláková.** 2002, Surf. Coat. Technol., Vol. 154, p. 304.

36. **Y.-T. Cheng, C.-M. Cheng.** 1998, Appl. Phys. Lett. Vol. 73, p. 614.

37. **J. C. Ododo, B.R Coles.** 1977, J. Phys. F: Met. Phys. Vol. 7, p. 2393.

38. **S. A. Ahern, M. J. C. Martin W. Sucksmith.** 1958, Proc. R. Soc. Lond. A Vol. 248, p. 145.

39. **W. Olovsson, C. Göransson, L. V. Pourovskii, B. Johansson, I. A. Abrikosov,** 2005, Phys. Rev. B Vol. 72, 064203.

40. **N. Hamada,** 1981, J. Phys. Soc. Jpn., Vol. 50, p. 77.

41. **J. G. Booth, H. P. J. Wijn, G. Zibold.** *Landolt-Börnstein, Numerical Data and Functional Relationships in Science and Technology*, Vol. 19 Magnetic Properties of Metals, Subvol. b **(Ed.: H.P.J. Wijn)**, Berlin: Springer-Verlag, 1993.

42. **S. Baunack, W. Brückner.** 2000, Microchim. Acta, Vol. 133, p. 17.

Chapter 5 : Results and Discussion: Compilation of Articles

In the following, the results derived from the Thesis work are presented as a compilation of articles. An extended abstract is included before each of the three articles. A thorough discussion of the results can be found in the articles themselves.

5.1. A comparison between fine-grained and nanocrystalline electrodeposited Cu-Ni films. Insights on mechanical and corrosion performance.

In this article the effect of saccharine as a grain-refining agent in electrodeposited pure Ni and Cu-Ni alloys is investigated. For this purpose, four electrolytes have been used: saccharine-free and saccharine-containing Cu-Ni baths (denoted by SFB and SCB, respectively) and Ni baths (denoted by SFBN and SCBN, respectively), all having the same total metal concentration to keep the ionic strength constant. The effect of saccharine has been studied at different levels including surface morphology (by SEM and AFM), composition (by EDX), structure (by TEM and XRD), mechanical properties of the deposits (by nanoindentation) and corrosion behaviour (by potentiodynamic polarisation).

Compositional analyses performed by EDX reveal that composition is not much affected by the presence of saccharine in the bath and ranges from 43 at% Ni to 87 at% Ni in the obtained Cu-Ni alloy layers. Concerning surface morphology, smooth Cu-Ni deposits have been achieved (in the range of current densities from -10 to -40 mA/cm^2) from SCB while much rougher deposits with edged grains have been obtained from SFB. AFM image quantification analyses of RMS and peak-to-valley values confirm the decrease in surface roughness for deposits grown from SCB. The effect of saccharine on pure Ni deposits is less pronounced, suggesting a synergic effect of saccharine and the alloying of Ni with Cu on deposit's growth. XRD pattern analysis confirms the formation of fcc Cu-Ni solid solution in all cases. In addition, films obtained from the SCB feature much broader reflections, indicating smaller crystallite sizes (smaller than 30 nm). Pure Ni films plated from SCBN also display wider reflections compared to films deposited from SFBN, although truly nc-films are not achieved (~200 nm versus ~400 nm, respectively). The difference in the width of (111) and (200) reflections in all samples is indicative of the existence of stacking faults. Accordingly, HRTEM images show the presence of intergranular nanotwins in films obtained from SCB.

Regarding mechanical properties, Oliver and Pharr analysis of the recorded nanoindentation curves using a maximum applied load of 10 mN unambiguously reveal that nc-Cu-Ni (SCB) and ufg-Ni (SCBN) deposits are harder than fg-Cu-Ni (SFB) and fg-Ni (SFBN), respectively. From the chemical composition point of view, hardness increases with Ni content due to solid solution hardening. From the microstructural point of view,

the enhanced hardness in nc- Cu-Ni films with respect to fg-Cu-Ni, 6.7 – 8.2 GPa versus 4.2 – 5.4 GPa, has been ascribed to the decrease in crystallite size (from ~400 nm to ~30 nm), and the larger amount of intragranular nanotwins. Similar E_r values have been achieved in nc- and fg-Cu-Ni deposits (in the range of 164 - 192 GPa). The small variations in E_r can be attributed to the low porosity of the coatings. The H/E_r (related to wear resistance), H^3/E_r^2 (a good indicator of resistance to plastic deformation) and W_{el}/W_{tot} (related to elastic recovery) ratios have been also calculated. These values conclude that nc-films show improved elastic recovery and better wear resistance.

Finally E_{corr} and j_{corr} parameters determined from the potentiodynamic polarization curves in aerated 3.5 wt.% NaCl show that nc- Cu-Ni films exhibit more negative E_{corr} but lower j_{corr} than their fg counterparts. This trend can be ascribed to the formation of dense and pore-free nc-films by means of electrodeposition.

A comparison between fine-grained and nanocrystalline electrodeposited CuNi films. Insights on mechanical and corrosion performance.

Eva Pellicer,[*,†] Aïda Varea,*[†] Salvador Pané,*[‡] Kartik M. Sivaraman,*[‡] Bradley J. Nelson,*[‡]
Santiago Suriñach,[†] Maria Dolors Baró,*[†] and Jordi Sort*[§]

[†]Departament de Física, Facultat de Ciències, Universitat Autònoma de Barcelona, E-08193 Bellaterra, Spain.

[‡]Institute of Robotics and Intelligent Systems (IRIS), ETH Zurich, CH-8092 Zurich, Switzerland.

[§]Institució Catalana de Recerca i Estudis Avançats (ICREA) and Departament de Física, Universitat Autònoma de Barcelona, E-08193 Bellaterra, Spain.

*To whom correspondence should be addressed:

Dr. Eva Pellicer

E-mail: Eva.Pellicer.icn@uab.cat

ABSTRACT

Cu_{1-x}-Ni_x ($0.43 \leq x \leq 1.0$) films were electroplated from citrate-sulphate baths at different current densities onto Cu/Ti/Si (100) substrates with the addition of saccharine as a grain-refining agent. The Cu-Ni alloy films produced from saccharine-free baths were fine-grained (crystallite size of ~400 nm). The addition of saccharine to the electrolytic solution induced a dramatic decrease in crystal size (down to ~27 nm) along with a reduction in surface roughness. Although the effect of saccharine on pure Ni films was less obvious, significant changes were observed due to the presence of saccharine in the bath during the alloying of Cu with Ni. Compared to fine-grained Cu-Ni films, the nanocrystalline films exhibited lower microstrains and a larger amount of stacking faults as observed by X-ray diffraction. These features enhance the mechanical properties of the Cu-Ni alloys, making the nanocrystalline Cu-Ni films superior to both the corresponding fine-grained films and pure Ni films. In particular, hardness in fine-grained films varied from 4.2 (x = 0.43) to 6.7 GPa (x = 0.86), whereas hardness varied between 5.4 and 8.2 GPa for nanocrystalline films of similar composition. In addition, wear resistance and elastic recovery were enhanced. Nanostructuring did not significantly affect corrosion resistance of Cu-Ni alloys in chloride media. Although the corrosion potential shifted slightly towards more negative values, the corrosion current density decreased, thereby making the electrodeposition nanostructuring process an effective tool to improve the overall properties of the Cu-Ni system.

Keywords: electrodeposition, Cu-Ni, nanocrystalline, hardness, wear resistance, corrosion.

1. Introduction

Nanostructured materials benefit from improved, and sometimes novel, physical and chemical properties compared to conventional coarse-grained materials, thus creating opportunities for advanced technological applications. Amongst the material properties of metals that can be enhanced by nanostructuring, mechanical properties currently receive considerable attention from both fundamental and applied perspectives (1-3). Of the investigations that exist, the focus is either on understanding the mechanical behaviour of nanostructured materials from a fundamental perspective, or exploiting the new properties that result from nanostructuring. Compared to conventional coarse-grained materials, nanocrystalline metals with grain sizes typically smaller than 100 nm possess

lower elastic moduli, higher tensile strength and hardness, increased ductility and fatigue resistance, and, under certain conditions, superplastic behaviour (4-7). Some of these characteristics were theoretically predicted by Gleiter et al. two decades ago (8) and have since then been experimentally verified by a number of researchers. In addition, the measurement of the mechanical properties of nanostructured metallic materials greatly depends on the kind of sample considered, i.e. thin films, thick films or bulk specimens. Compared with nanostructured bulk materials, the assessment of the mechanical properties of nanocrystalline metallic thin films still remains a rather unexplored field (9).

Electrodeposition is one of the best techniques to prepare nanocrystalline metallic thin films with thicknesses ranging from hundreds of nanometers to tens of micrometres. This is an old yet versatile technique with several attributes that make it extremely well suited for micro- and nanotechnologies. The process can be scaled up or down, deposition can be performed on a wide variety of substrates, it can be performed near room temperature from water-based, environmentally friendly electrolytes, and it produces pore-free coatings at high rates. With the advent of nanotechnology, electrodeposition has gained many supporters within the scientific community largely because it is a simple, cost-effective technique and less time-consuming compared to physical methods such as sputtering or evaporation. Furthermore, physical methods are generally limited to thinner films (up to 1-2 μm), a restriction that can be a drawback for some micro- and nano-electromechanical systems where thicker films are desired. Due to these reasons, the development of electroplated films either by direct or pulse methods to produce nanocrystalline sheets of metals (such us Co, Ni and Cu) (10-12) and metallic alloys (e.g. Co-Pt, Co-Ni, Ni-W, Co-Fe-Ni) (13-16) is of increasing interest.

The first investigations of the electrodeposition of nickel films with fine grain sizes used saccharine and coumarin as additives (17). Since then, considerable effort has been directed towards the development of nanocrystalline nickel films plated in either re-formulated traditional or newly formulated baths (18-22). The Watts bath, with or without organic additives, remains the most commonly employed (23-26). To the basic Watts bath (nickel sulphate, nickel chloride and boric acid) saccharine is typically added as a grain refining and stress relieving agent. In fact, saccharine performs these functions well for many metals and alloys deposited from a variety of baths (27-29). Despite the numerous studies performed regarding the various strategies towards grain refinement, reported data is, in some cases, inconsistent across different investigations. It is, therefore, difficult to draw conclusions, especially when comparing the mechanical properties for a given metal in its nanocrystalline, fine- or coarse-grained forms. This lack of systemization

becomes even more evident when dealing with alloys, for which the literature is limited. This problem arises in part from the difficulty of explaining the extent to which various factors, both the ones inherent in the system considered (e.g. solution hardening effects, stacking fault energies of each metal), and the electrodeposition conditions (e.g. bath formulation, applied current density, bath temperature) contribute to the obtained properties. This work is aimed at providing a more comprehensive framework by a clear comparison between fine-grained and nanocrystalline Cu-Ni thin films. The Cu-Ni system has been chosen for several reasons; it can be electroplated from aqueous electrolytes (30, 31), it shows total miscibility over the complete composition range, its production is much less expensive compared to Co-based alloys or alloys containing metals like W and Mo. Moreover, the Cu-Ni alloys exhibit interesting functional properties such us good corrosion resistance in marine environments, anti-biofouling properties, and, depending on their composition, either paramagnetic or ferromagnetic behaviour (32-34). Nanostructuring has been reported to have either beneficial or detrimental effects on the corrosion performance of metallic materials depending on the system under study. Though the corrosion behaviour of bulk Cu-Ni alloys in several environments is well documented (35-38), the effects induced by nanostructuring on the corrosion resistance of electroplated Cu-Ni films still remains poorly understood.

In this study, Cu_{1-x}-Ni_x ($0.43 \leq x \leq 1.0$) films were electroplated from a sulphate-based bath containing citrate as a complexing agent, both with and without the addition of saccharine. The purpose of the present investigation is two-fold; the assessment of the effects of alloying copper with nickel, and a direct comparison between the properties of fine-grained and nanocrystalline Cu_{1-x}-Ni_x films with similar composition. The hardness, Young's modulus and wear characteristics of the films were evaluated by depth-sensing nanoindentation which is a particularly well-suited technique for coatings (39). Apart from the mechanical properties, the morphology, microstructure, surface roughness and corrosion performance of these films were studied in detail and key relationships between these properties outlined.

2. Experimental procedure

The metallic films were obtained by direct current electrodeposition in a one-compartment thermostatized three-electrode cell using a PGSTAT30 Autolab potentiostat/galvanostat (Ecochemie). Cu-Ni alloy films were deposited from an electrolyte containing 184 g/L $NiSO_4 \cdot 6H_2O$, 6.24 g/L $CuSO_4 \cdot 5H_2O$, 87 g/L $Na_3C_6H_5O_7 \cdot 2H_2O$,

0.2 g/L $NaC_{12}H_{25}SO_4$ (*saccharine-free bath, SFB*) and 0.5 g/L $C_7H_5NO_3S$ (*saccharine-containing bath, SCB*). Nickel films were obtained from an electrolyte containing 190 g/L $NiSO_4 \cdot 6H_2O$, 87 g/L $Na_3C_6H_5O_7 \cdot 2H_2O$, 0.2 g/L $NaC_{12}H_{25}SO_4$ (*saccharine free-bath, SFBN*) and 0.5 g/L $C_7H_5NO_3S$ (*saccharine-containing bath, SCBN*). The electrolyte volume was 100 ml. Analytical grade reagents and ultrapure water (18 MΩ cm) were used to prepare the electrolyte. For all solutions, the pH was fixed at 4.5 and the temperature at 30ºC. Silicon (100) substrates with e-beam evaporated Ti (100 nm)/Cu (500 nm) adhesion/seed layers were used as working electrodes (WE), which were positioned vertically within the electrolyte. The working area was 6 x 5 mm^2. A double junction Ag|AgCl (E = +0.210V/SHE) reference electrode (Metrohm AG) was used with 3M potassium chloride (KCl) inner solution and an interchangeable outer solution. The outer solution was made of 1M sodium sulphate. A platinum spiral served as counter electrode. Prior to deposition, the copper surface was first degreased with acetone followed by isopropyl alcohol and water and, finally, dipped in diluted sulphuric acid to remove any oxides and organic residues present on the copper surface. The backside of the silicon substrate was insulated by painting it with a nonconductive ink to ensure that only the copper surface was conductive. Before each experiment, the electrolyte was de-aerated with nitrogen gas for 10 min through a glass purge pipe which provides a vigorous stream of nitrogen. A blanket of nitrogen was maintained on top of the solution during the deposition. Deposition was conducted galvanostatically under mild stirring (200 rpm) using a magnetic stirrer bar. The electrical charge was adjusted across all depositions to attain similar film thicknesses. After deposition, the films were thoroughly rinsed in water and stored in air.

The chemical composition of the films was determined by energy dispersive X-ray spectroscopy (EDXS). Metal proportions are expressed in atomic percentage (at%). The morphology was examined by scanning electron microscopy (SEM) on a JEOL JSM-6300 microscope. The average film thickness was determined from four-point measurements over the entire surface by interferometric profilometry. The structure of the deposits was studied by X-ray diffraction (XRD) and transmission electron microscopy (TEM). X-ray diffraction patterns were recorded on a Philips X'Pert diffractometer using the Cu Kα radiation in the 38º-110º 2θ range (0.03º step size, 10s holding time). The global structural parameters, such as crystallite sizes, $\langle D \rangle$ (defined here as the average coherently diffracting domain sizes), and microstrains or atomic level deformations, $\langle \varepsilon^2 \rangle^{1/2}$, were evaluated by fitting the full XRD patterns using the Materials Analysis Using Diffraction (MAUD) Rietveld refinement program (40-42). This software includes a formalism to quantitatively evaluate the stacking fault probability, α_{SF} (41,43). TEM

characterisation was carried out on a JEOL JEM-2011 microscope operated at 200 kV. For the planar-view observations, the films were thinned by ion milling, which was performed on both sides of the film in order to remove any surface contamination. Roughness of the films was characterised by atomic force microscopy (AFM) using a Dual Scope™ C-26 system (Danish Micro Engineering) working in AC mode. A commercial silicon tip (50-100 KHz resonance frequency) was used to scan surface areas of 5 × 5 μm^2. Both the peak-to-valley distance and the root-mean-square (RMS) deviation values were extracted from the images.

The mechanical properties (hardness and reduced elastic modulus) were evaluated by nanoindentation operating in the load control mode using a UMIS device from Fischer-Cripps Laboratories equipped with a Berkovich pyramid-shaped diamond tip. The value of maximum applied force was chosen to be 10 mN to ensure that the maximum penetration depth during the tests was kept below one tenth of the overall film thickness. This is considered a necessary condition to avoid substrate influence on measured mechanical properties (44). The thermal drift during nanoindentation was kept below 0.05 nm/s. Corrections for the contact area (calibrated with a fused quartz specimen), instrument compliance, and initial penetration depth were applied. For nanoindentation testing the mechanical properties of the film can be extracted from the load–unload curve making direct measurements on the indentations unnecessary. The hardness (H) and reduced elastic modulus (E_r) values were derived from the load-displacement curves at the beginning of the unloading segment using the method of Oliver and Pharr (45). From the initial unloading slope the contact stiffness, S, was determined as:

$$S = \frac{dP}{dh} \qquad \text{(Equation 1)}$$

where P and h denote the applied load and penetration depth during nanoindentation, respectively. The elastic modulus was evaluated based on its relationship with the contact area, A, and contact stiffness:

$$S = \beta \frac{2}{\sqrt{\pi}} E_r \sqrt{A} \qquad \text{(Equation 2)}$$

Here, β is a constant that depends on the geometry of the indenter (β = 1.034 for a Berkovich indenter)(44), and E_r is the reduced Young's modulus, defined as:

$$\frac{1}{E_r} = \frac{1 - \nu^2}{E} + \frac{1 - \nu_i^2}{E_i} \qquad \text{(Equation 3)}$$

The reduced modulus takes into account the elastic displacements that occur in both the specimen, with Young's modulus E and Poisson's ratio ν, and the diamond indenter, with elastic constant E_i and Poisson's ratio ν_i. For diamond, E_i = 1140 GPa and ν_i = 0.07. Hardness (H) was calculated from:

$$H = \frac{P_{Max}}{A} \quad \text{(Equation 4)}$$

where P_{Max} is the maximum load applied during nanoindentation. Finally, the elastic recovery was evaluated as the ratio between the elastic (W_{el}) and the total (plastic + elastic) (W_{tot}) energies during nanoindentation. These energies were calculated from the nanoindentation experiments as the areas between the unloading curve and the x-axis (W_{el}) and between the loading curve and x-axis (W_{tot}) (44). The results presented here represent the statistical average of a set of 100 indentations for each sample.

The corrosion performance of the films was evaluated by electrochemical techniques in a conventional three-electrode cell. Corrosion tests were conducted in aerated 3.5 wt% NaCl solution under quiescent conditions at room temperature. The outer solution of the Ag|AgCl reference electrode was made of 1 mol dm^{-3} NaCl. A platinum spiral served as a counter electrode. After sample immersion in the 3.5 wt% NaCl solution, the steady state potential (E_{ss}) was measured until fluctuations less than 10 mV h^{-1} were observed. This process was usually complete within three to four hours. The electrochemical polarization was scanned from the steady-state potential to E_{ss} – 300 mV cathodically and then to E_{ss} + 300 mV anodically with a scan rate of 0.1 mV s^{-1}. The reproducibility of the data related to the corrosion potential (E_{corr}) and the corrosion current density (j_{corr}) was monitored using four samples per film (0.3 cm^2 exposed area), and average results are reported.

3. Results

3.1 Electrochemical preparation of the thin films

Figure 1 shows the E-t transients for Cu-Ni plated onto Cu/Ti/Si (100) substrates from saccharine-free and saccharine-containing baths at two different applied current densities, −10 and −40 $mAcm^{-2}$. For a given applied current density, the stabilized potential (E_S) slightly shifts towards more negative values with the addition of saccharine to the bath. The same trend was observed when recording cathodic linear sweep curves (not shown),

both for Ni and Cu-Ni systems. Since saccharine molecules adsorb onto the electrode and interfere with the normal metal deposition by blocking the attachment of ad-atoms, the cathodic overpotential increases (46, 47). In fact, the double layer capacitance is expected to decrease as a consequence of the blocking adsorption of saccharine. Also, the addition of saccharine changes the composition of the Helmholtz electrochemical double layer, thus variations in cathode polarization are expected (48). This shift is more pronounced at higher current densities, suggesting that, as observed for other metals and alloys, the inhibiting effect on ion discharge is enhanced.

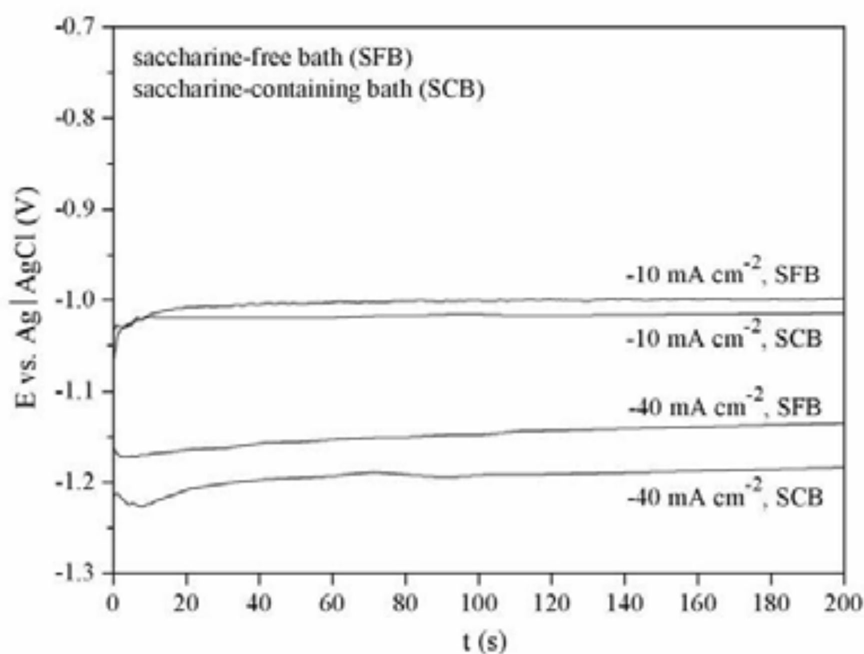

Figure 1. *E-t* transients for Cu-Ni deposition onto Cu/Ti/Si (100) substrates at the indicated current densities.

3.2 Morphological characterization

The morphology of the Cu-Ni films obtained galvanostatically from the SFB and SCB baths is shown in Figures 2a-2d. Charge density was tuned to obtain a film thickness of 3.0 ± 0.2 μm. Optimization was possible by combining Faraday's law with the current efficiency, which depends on both the bath composition and the applied current density. The deposits obtained from the SFB at −10 mA cm^{-2} displayed edged grains featuring cauliflower-like clusters in some regions (Figure 2a). At a higher current density, the grains became rounded and their size distribution narrowed (Figure 2c). Conversely, the SCB bath yielded smooth and almost featureless deposits irrespective of the applied

current density (Figures 2b and 2d), indicating a decrease in surface roughness. In all cases, deposits were crack-free and pitting was not observed, probably due to the anti-pitting effect brought by the sodium lauryl sulphate wetting agent (49).

Pure nickel deposits of a similar thickness were also prepared from a bath in which copper sulphate was replaced by nickel sulphate in order to maintain the same ionic strength. The morphology of the films, produced from either the saccharine-free bath (SFBN) or saccharine-containing bath (SCBN) at −40 mA cm^{-2}, was different from the films previously described. Unlike the Cu-Ni films, deposits obtained from the SFBN showed less rounded clustered grains (cf. Figures 2c and 2e). Most importantly, the morphology of the nickel deposits plated from the SCBN could be resolved, giving a cotton-like appearance (cf. Figures 2d and 2f). It is, therefore, clear that copper has some influence on the deposition of Ni which is observed in the deposit morphology.

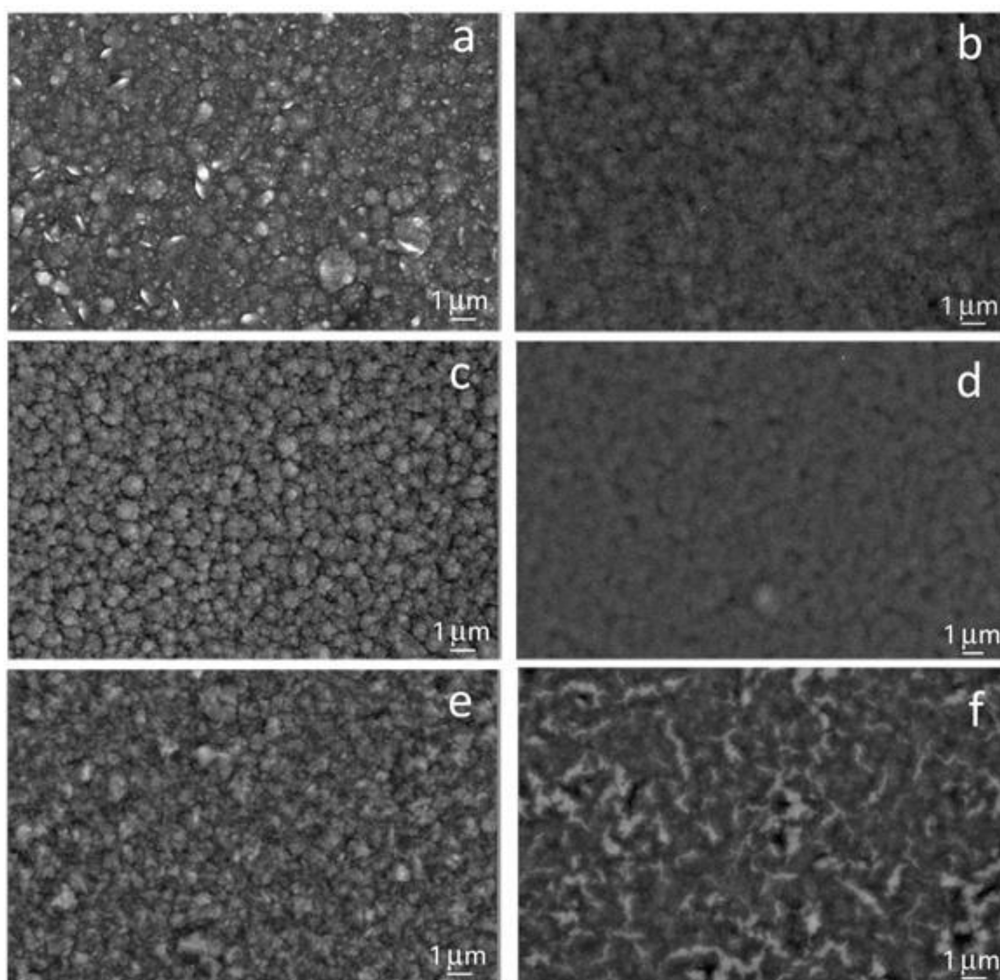

Figure 2. SEM images of Cu-Ni films deposited at *j* = −10 mA cm^{-2} from (a) saccharine-free bath (SFB) with 43 at% Ni and (b) saccharine-containing bath (SCB) with 45 at% Ni, and deposited at *j* = −40 mA cm^{-2} from (c) SFB with 86 at% Ni and (d) SCB with 87 at% Ni. SEM images of Ni films deposited at *j* = −40 mA cm^{-2} from (e) saccharine-free bath (SFBN) and (f) saccharine-containing bath (SCBN).

EDX analyses on the Cu-Ni films revealed that nickel content increased with current density. In the presence of citrate as a complexing agent, copper is typically discharged under mass-transport control, whereas nickel remains under activation control within a wide potential range (50, 51). Therefore, an increase in the overvoltage promotes nickel discharge and, ultimately, leads to deposits with higher nickel contents. At a given current density the composition remained nearly identical regardless of the presence of saccharine in the bath. Only a slight enrichment in Ni (at around 1-2 at%) was detected in the films obtained from the SCB, probably due to the greater overpotential. At j = –10 mA cm^{-2} the Ni content was 43-45 at% and increased to 86-87 at% at j = –40 mA cm^{-2}.

Although the smoothing effect induced by saccharine on the topography was visually apparent, quantitative measurements of surface roughness were carried out by AFM. Typical 2D topographical images of the Cu-Ni films obtained from the SFB and SCB are shown in Figure 3. The former featured rough surfaces with edged grains, while the latter displayed an almost perfectly flat surface. The root-mean-square deviation (RMS) and the peak-to-valley distance values for 5 x 5 μm^2 scanned areas are listed in Table 1. The AFM analyses corroborated visual observations, i.e. a loss of metallic sheen and, therefore, higher surface roughness (and larger peak-to-valley distances) in the Cu-Ni films prepared from the SFB compared to the SCB derived ones. Although smoother deposits were produced by increasing the current density in the SFB, a drastic reduction of surface roughness was accomplished with the addition of saccharine to the bath. Roughness decrease was less effective, yet noticeable, for pure Ni films.

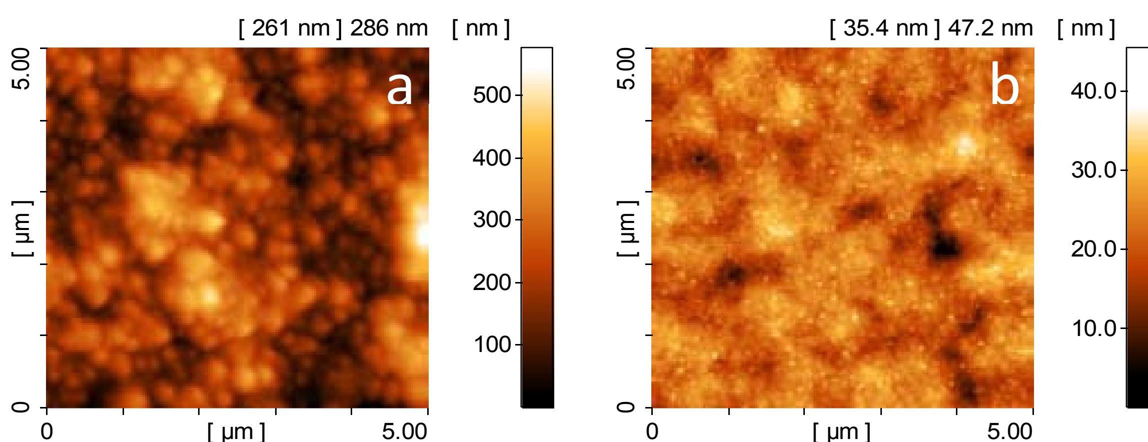

Figure 3. AFM topographical images of (a) $Cu_{0.57}Ni_{0.43}$ film obtained from the SFB and (b) $Cu_{0.55}Ni_{0.45}$ film obtained from the SCB. Note that the scale bar on the right side of the images indicates distance along the z-axis (i.e. depth).

Table 1. RMS and peak-to-valley distance values extracted from topographical AFM images of Cu-Ni and Ni films.

Bath*	$-j$ (mA cm^{-2})	Film	RMS (nm)	Peak-to-valley (nm)
SFB	10	$Cu_{0.57}Ni_{0.43}$	43	266
SCB	10	$Cu_{0.55}Ni_{0.45}$	5	36
SFB	40	$Cu_{0.14}Ni_{0.86}$	20	127
SCB	40	$Cu_{0.13}Ni_{0.87}$	4	30
SFBN	40	Ni	21	128
SCBN	40	Ni	17	111

*SFB: saccharine-free Cu-Ni bath, SCB: saccharine-containing bath, SFBN: saccharine-free Ni bath, SCBN: saccharine-containing Ni bath.

3.3 Structural characterization

The structural properties of the thin films were studied by XRD and TEM analyses. All films showed a face-centered cubic (fcc) structure, but the width of the fcc reflections greatly varied across the different samples. The XRD measurements confirmed the formation of Cu-Ni solid solution in all samples. The role of citrate is to reduce the large difference in the standard reduction potentials of copper (+0.34 V) and nickel (−0.25V), thus allowing their co-deposition (31). Figure 4 shows a detail of the (111) and (200) fcc reflections for Cu-Ni and pure Ni films. The narrow peaks located at around 2θ = 43.3º and 50.5º belong to the Cu seed-layer, which also displayed an fcc structure. As the alloy became enriched in Ni, a shift in the Cu-Ni peak positions towards higher angles was observed (see Figures 4a and 4b). For a given composition, the Cu-Ni films obtained from the SCB featured much broader reflections, indicating smaller grain sizes in agreement with previous morphological observations. The peaks were not precisely centered at the same 2θ, but at slightly higher angles corresponding to a richer Ni composition. Notice that the stabilized potential (E_S) of the galvanostatic curves shifted towards more negative values due to saccharine addition, thus favouring Ni discharge. The Ni films plated from the SCBN also displayed wider reflections (Figure 4c). On the other hand, the difference in

the width of the (111) and (200) peaks for all samples is indicative of the existence of stacking faults. To rationalize all these trends from quantitative structural factors, the full XRD patterns were Rietveld-refined. The extracted cell parameters, crystallite sizes, microstrains and stacking fault probabilities are listed in Table 2. As an example, Figure 4d shows the Rietveld fitting of the XRD pattern corresponding to the nanocrystalline $Cu_{0.13}Ni_{0.87}$ film in the 42-55° 2θ region.

The main trends regarding crystallite size (*i*), microstrains (*ii*) and stacking fault probabilities (*iii*) are summarized below:

(*i*) All samples plated from saccharine-free baths (SFB/SFBN) had crystallite sizes at approximately 400 nm, i.e. fine-grained. An increase of the current density made the crystallize size of the Cu-Ni alloy decrease slightly, as expected due to the higher deposition rate. The addition of saccharine to the plating solution induced a dramatic crystallite size reduction yielding nanocrystalline films. TEM images further corroborated these results (Figure 5). Moreover, the crystallite size remained nearly the same (26-29 nm) irrespective of the applied current density, which suggests that its value is mainly controlled by the saccharine additive in SCB. In contrast, though the crystallite size of pure Ni films also decreased with the addition of saccharine to the bath, it remained within the fine-grained regime. We denote the Ni films plated from the SFBN by *fine-grained nickel* and the ones plated from SCBN by *ultrafine-grained nickel*. Notice that when saccharine was absent from the bath, the alloying of Cu with Ni did not change the structure apart from the expected increase in the cell parameter (compare the fine-grained Ni with the $Cu_{0.14}Ni_{0.86}$ films in Table 2). TEM images were in accordance with these findings (see Figures 5a and 5b). Conversely, when saccharine was present in the electrolyte, alloying Cu with Ni did make a difference; the crystal size reduced by an order of magnitude, from 207 to 29 nm with just 13 at% of Cu being dissolved in the Ni lattice (compare the ultrafine-grained Ni with the nanocrystalline $Cu_{0.13}Ni_{0.87}$ films in Table 2, and TEM images of Figures 5a and 5c).

(*ii*) Saccharine is also responsible for the decrease in microstrain. Strain is common in electrodeposits (52). Macrostrain develops over large areas, arises from either tensile or compressive stresses, and leads to XRD peak shifting. Microstrains (non-uniform strains) develop over small distances and are a distribution of d-spacings thus leading to XRD peak broadening. The values reported in Table 2 refer to this class of strains. Saccharine is known to be an excellent tensile macrostress reducing agent. Recently, it has been reported that the coalescence of Ni grains in films electroplated from saccharine-free

sulfamate baths is a tensile stress controlled process, while films with compressive stress or low tensile stress are obtained in the presence of saccharine (53). In fact, the Ni films prepared from the SFBN were prone to peeling from the copper surface, mostly due to high tensile stress. The addition of saccharine to the bath led to properly adhering deposits owing to the compressive effect conferred by saccharine.

(*iii*) From Table 2, it is clear that the number of planar defects increases when the Cu-Ni alloy is nanocrystalline. The same is true for pure Ni films, i.e. the finer the grain size, the higher the stacking fault probability. This is in agreement with the large number of intragranular nanotwins detected by High Resolution TEM in the SCB plated films (Figure 5d). From a thermodynamic viewpoint, the formation of twins decreases the total interfacial energy (54). Because twins preferably nucleate at grain boundaries or triple junctions, one might expect that the stacking fault probability should be higher for larger amounts of grain boundaries (i.e. nanocrystalline films). However, the increased probability of twinning does not arise solely from the larger number of grain boundaries. The role of saccharine as an adsorbate creates physicochemical considerations that must also be taken into account. It has been reported for Ni electrodeposits that the presence of surface-active substances in the electrolytic solution clearly has an effect on stacking fault dislocations and twins (55). In the late 70's it was suggested that saccharine increases the probability of twinning in Ni electrodeposits because of its preferential adsorption onto (111) planes, which results in an increased amount of crystal mass in twin orientation (56). The same authors demonstrated that the probability of twinning is additive-dependent (for example, the butyne-2-diol, a typical brightener used in the galvanic industry, was reported to be inactive with respect to the formation of twin stacking faults). The addition of additives is not strictly necessary to generate nanotwins; an increase of current density is sufficient to enhance their formation. It is known that growth twins are frequently formed when electrodepositing metals with appropriate stacking fault energies (1). In particular, twins are easily formed in fcc metals with low stacking fault energies, as is the case with Cu and Ni (57). Moreover, faster deposition rates will, in principle, lead to higher twin densities since both metals have relatively large twin boundary energies (1). While the mechanism of twin formation in metal electroplating is not fully understood, it is generally accepted that it is a kinetically driven process in such a way that nucleation and growth rate of twins are controlled by the deposition conditions. Lu at al. have experimentally verified that nanotwining in electroplated Cu increases with deposition rate (i.e. with an increase of the applied current density) (54).

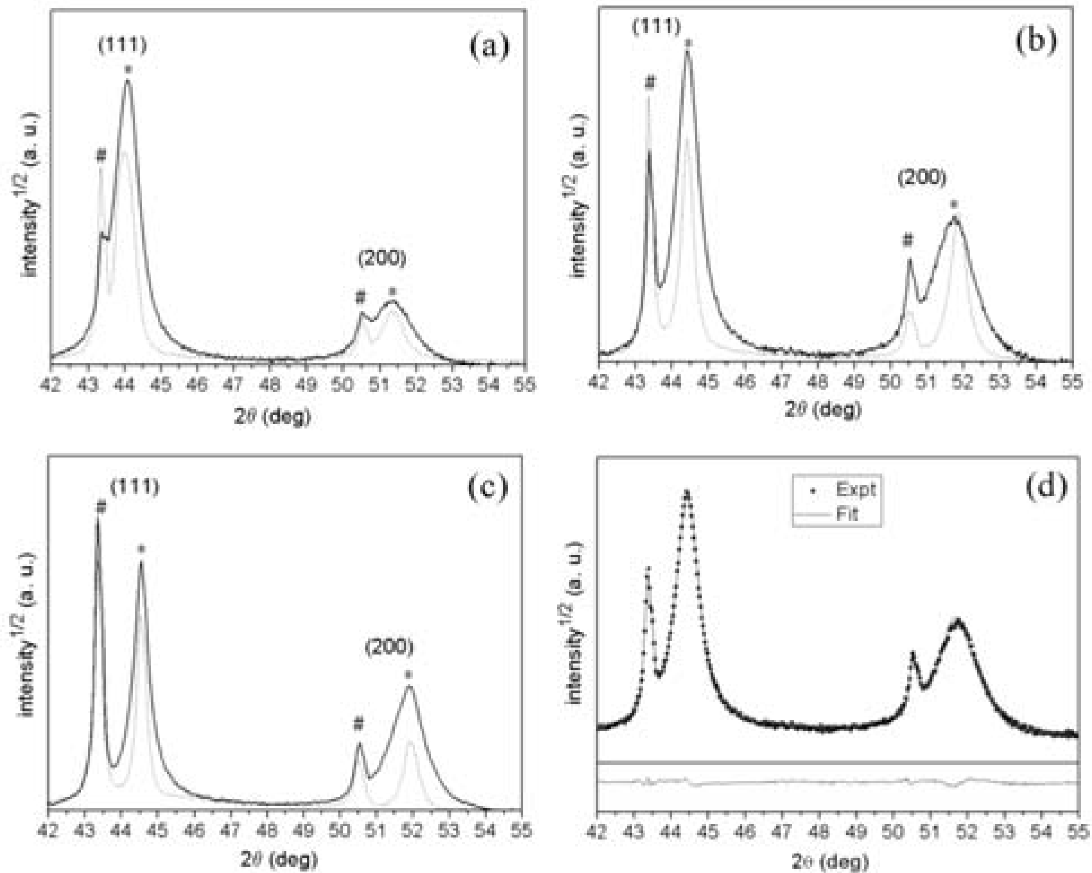

Figure 4. Detail of the (111) and (200) X-ray reflections for (a) Cu rich Cu-Ni, (b) Ni-rich Cu-Ni and (c) pure Ni films obtained from saccharine-containing (solid line) and saccharine-free (dotted line) baths. Peaks denoted by # and * belong to the Cu-seed layer and the electroplated film, respectively. d) Rietveld fitting of one of the spectra shown in (b) (nanocrystalline $Cu_{0.13}Ni_{0.87}$ film) and the corresponding difference between the experimental and the calculated profiles.

Figure 6 shows representative load-unload indentation curves of the electrodeposited films. For each composition, the penetration depth attained at the end of the unloading segment is lower for the film having smaller crystallite sizes. This indicates that the nanocrystalline Cu-Ni thin films are mechanically harder than the corresponding fine-grained films. For the Ni samples, grain refinement also accounts for the lower penetration depth observed in the SCBN plated films, again indicating enhanced hardness. Table 3 lists the hardness (H), reduced Young's modulus (E_r) together with H/E_r, H^3/E_r^2 and W_{el}/W_{tot} ratios for all films extracted from the corresponding indentation curves (where W_{el} and W_{tot} denote the elastic and total indentation energies, respectively).

Table 2. Global structural parameters obtained after Rietveld refinement of the full XRD patterns of Cu_{1-x}-Ni_x and Ni films.

Bath*	Film	Lattice cell parameter *a* (± 10^{-3} Å)	Crystallite size <*D*> (± 3 nm)	Microstrain $<\varepsilon^2>^{1/2}$ (±10^{-5})	Stacking fault probability α_{SF} (± $5x10^{-4}$)
SFB	$Cu_{0.57}Ni_{0.43}$	3.561	413	$3\cdot10^{-3}$	0.001
SCB	$Cu_{0.55}Ni_{0.45}$		26	$2\cdot10^{-4}$	0.007
SFB	$Cu_{0.14}Ni_{0.86}$	3.532	379	$8\cdot10^{-4}$	0.004
SCB	$Cu_{0.13}Ni_{0.87}$		29	$2\cdot10^{-4}$	0.007
SFBN	Ni	3.523	387	$3\cdot10^{-4}$	0.002
SCBN	Ni		207	$2\cdot10^{-5}$	0.008

*SFB: saccharine-free Cu-Ni bath, SCB: saccharine-containing bath, SFBN: saccharine-free Ni bath, SCBN: saccharine-containing Ni bath.

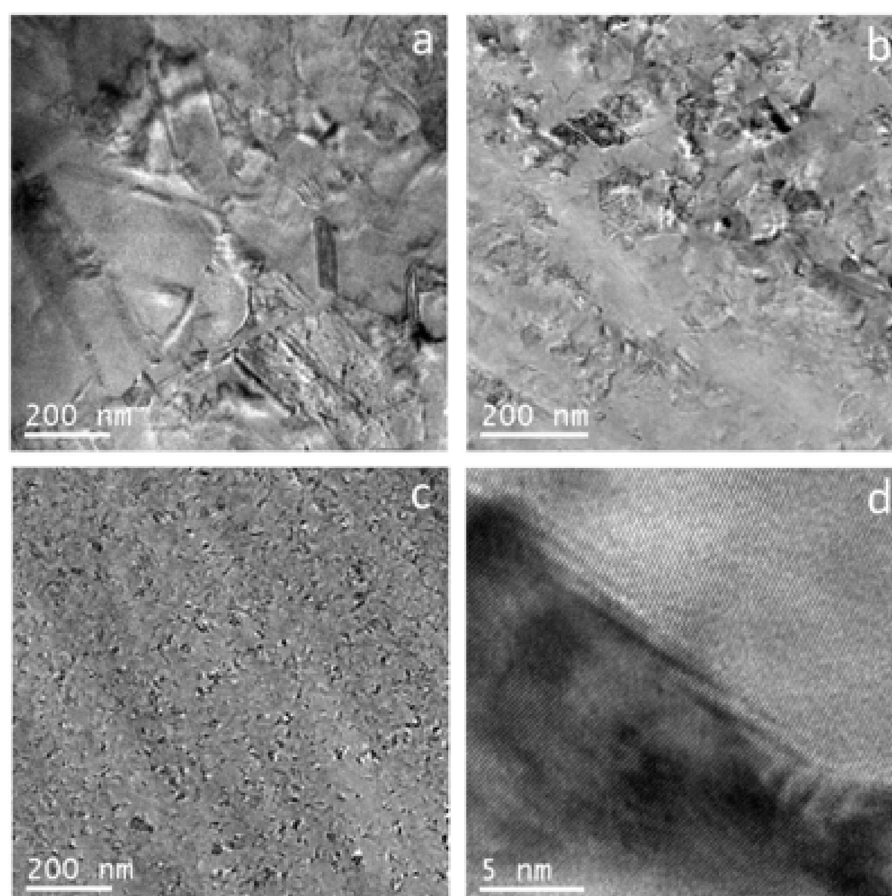

Figure 5. TEM images of (a) ultrafine-grained Ni, (b) fine-grained $Cu_{0.14}Ni_{0.86}$, and (c) nanocrystalline $Cu_{0.13}Ni_{0.87}$ films. (d) HRTEM image of a twinned region of the sample shown in (c).

3.4 Mechanical properties

Figure 6 shows representative load-unload indentation curves of the electrodeposited films. For each composition, the penetration depth attained at the end of the unloading segment is lower for the film having smaller crystallite sizes. This indicates that the nanocrystalline Cu-Ni thin films are mechanically harder than the corresponding fine-grained films. For the Ni samples, grain refinement also accounts for the lower penetration depth observed in the SCBN plated films, again indicating enhanced hardness. Table 3 lists the hardness (H), reduced Young's modulus (E_r) together with H/E_r, H^3/E_r^2 and W_{el}/W_{tot} ratios for all films extracted from the corresponding indentation curves (where W_{el} and W_{tot} denote the elastic and total indentation energies, respectively).

The increase of the Ni content in the alloy increased hardness both within the fine-grained (from 4.2 to 5.4 GPa) and nanocrystalline (from 6.7 to 8.2 GPa) domains, as expected due to solid solution hardening (58). Among the samples tested, the nanocrystalline $Cu_{0.13}Ni_{0.87}$ film was the hardest (H = 8.2 GPa), even harder than the two pure Ni samples. From the point of view of chemical composition alone, it would be expected that pure Ni would be mechanically harder than the Cu-Ni alloy since Cu is softer than Ni. However, the strength of a solid (i.e., its resistance against plastic deformation) is not only sensitive to the solid's chemical composition but also to its microstructure. In particular, larger hardness is expected for smaller crystallite sizes. Nanostructured metals have a larger density of grain boundaries than fine-grained or coarse-grained metals. Grain boundaries are efficient in disrupting the propagation of dislocations through a material. The enhanced hardness arising from the reduced crystallite sizes is explained by the Hall–Petch relationship (6). In addition, the presence of intragranular nanotwins contributes to material strength, since twin boundaries are able to block the propagation of slip bands (54). Coherent twin boundaries behave in a similar manner to grain boundaries by acting as obstacles to strain propagation.

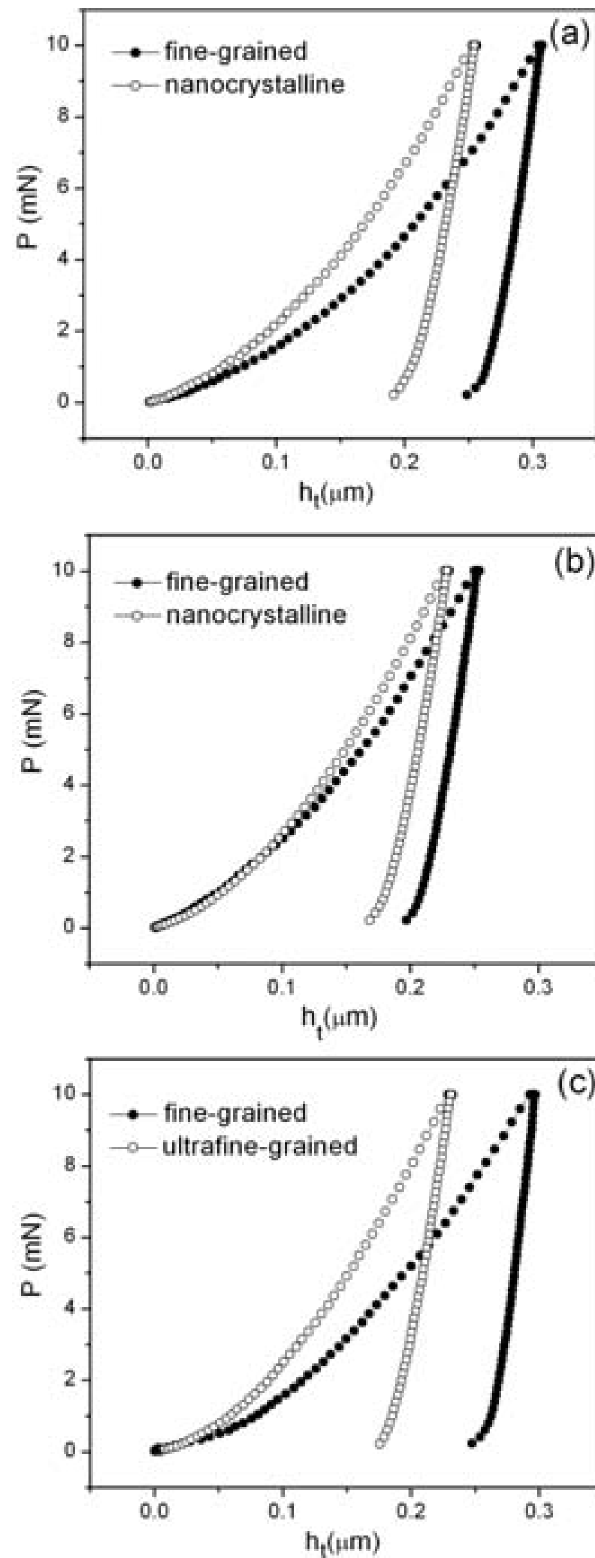

Figure 6. Representative load-unload nanoindentation curves for (a) fine-grained $Cu_{0.57}Ni_{0.43}$ and nanocrystalline $Cu_{0.55}Ni_{0.45}$, (b) fine-grained $Cu_{0.14}Ni_{0.86}$ and nanocrystalline $Cu_{0.13}Ni_{0.87}$ and (c) fine-grained and ultrafine-grained pure Ni films.

Table 3. Hardness (*H*), reduced Young's modulus (E_r) and H/E_r, H^3/E_r^2 and W_{el}/W_{tot} ratios extracted from the corresponding indentation curves of the listed thin films. W_{el} and W_{tot} denote the elastic and total indentation energies, respectively.

Film	*H* (GPa)	E_r (GPa)	H/E_r	H^3/E_r^2 (GPa)	W_{el}/W_{tot} (%)
fine-grained $Cu_{0.57}Ni_{0.43}$	4.2 ± 0.4	164 ± 4	0.0256 ±0.0016	0.0027 ± 0.0012	19.2 ± 0.7
nanocrystalline $Cu_{0.55}Ni_{0.45}$	6.7 ± 0.2	172 ± 3	0.0389 ± 0.0012	0.0102 ± 0.0008	27.1 ± 0.5
fine-grained $Cu_{0.14}Ni_{0.86}$	5.4 ± 0.3	195 ± 3	0.0277 ±0.0015	0.0041 ± 0.0010	20.1 ± 0.6
nanocrystalline $Cu_{0.13}Ni_{0.87}$	8.2 ± 0.2	192 ± 3	0.0427 ± 0.0012	0.0149 ± 0.0008	30.2 ± 0.5
fine-grained Ni	4.3 ± 0.3	196 ± 3	0.0219 ± 0.0015	0.0021 ± 0.0010	14.7 ± 0.6
ultrafine-grained Ni	8.0 ± 0.2	193 ± 3	0.0415 ± 0.0012	0.0137 ±0.0008	29.5 ± 0.5

E_r exhibited the same trend as *H* with regard to composition. Since the elastic modulus of Ni is higher than for Cu, E_r increased with the Ni content. For a given composition, E_r was slightly lower for the film with smaller crystallite sizes except for the Cu-rich Cu-Ni samples. Taking the Poisson's ratio for nickel (ν_i = 0.31) (59) into account, the Young's modulus is 214 and 210 GPa for fine-grained and ultrafine-grained nickel films, respectively. Similarly, if one assumes the Poisson's ratio of Cu-Ni alloy to be ν_i = 0.34 (60), the Young's modulus varies from 170 to 208 GPa within the fine-grained regime, and from 179 to 204 GPa within the nanocrystalline regime. The Young's modulus of nanocrystalline materials is usually lower than in coarse-grained materials by as much as 70% in some cases (61-63), due to the occurrence of porosity or the increased interatomic spacings in interface regions (61, 64). Regardless, our variations in the elastic modulus are rather small, probably because electrodeposition is known to produce pore-free coatings, which explains why similar E_r values were obtained for fine-grained and nanocrystalline Cu-Ni films. Our findings are in agreement with other works in which the reduction in the Young's modulus value was found to be less pronounced than expected. For instance, Legros *et al.* did not find any change in the Young's modulus in Ni and Cu films with grain sizes approaching 25 nm when evaluated by microsample tensile testing (65).

The hardness to elastic modulus ratio, H/E (or H/E_r if the reduced Young's modulus is used) is recognized to provide an indirect, yet reliable, assessment of the wear behaviour of a material (66). Notice that the H/E_r ratio for the nanocrystalline Cu-Ni (and ultrafine-grained Ni) films was higher than in fine-grained ones, indicating that the former displays enhanced wear resistance. The same factors account for the H^3/E_r^2 ratio, which is a good indicator of the resistance to plastic deformation (67, 68). The higher this index, the higher the energy absorbed by the material before fracture. Significantly, the nanocrystalline $Cu_{0.13}Ni_{0.87}$ film displayed higher H/E_r and H^3/E_r^2 ratios than the ultrafine-grained Ni sample. The singular microstructural attributes of nanocrystalline Ni-rich Cu_{1-x}-Ni_x films can again be used to explain this result. Finally, we evaluated the elastic recovery, expressed as W_{el}/W_{tot} in percentage, to gain information about the deformation degree recovered during unloading. The W_{el}/W_{tot} ratio correlated well with both H/E_r and H^3/E_r^2 (elastic recovery is closely related to H/E (67)). While W_{el}/W_{tot} increased with Ni content, smaller crystallite sizes also led to higher W_{el}/W_{tot} (69).

3.5 Corrosion behaviour

The corrosion performance of the films was evaluated in aerated 3.5 wt% NaCl. Because Cu-Ni alloys are commonly used in applications involving sea-water, a chloride-containing medium was chosen as a test solution. Typical potentiodynamic polarization curves are shown in Figure 7. While the cathodic branches did not reveal any special feature, the anodic branch displayed an oxidation peak followed by a passive region in some cases (see the grey curve). The oxidation peak is likely to be attributed to the formation of a passive oxide film that further protects the material. The presence of oxides as the primary corrosion products was identified in bulk Cu-Ni alloys exposed to chloride media (35, 36). Pure Ni films did not show an active-passive transition, but rather a monotonous increase in the anodic current. The E_{corr} and j_{corr} values were calculated using the Tafel extrapolation method and are listed in Table 4. Due to peeling of the fine-grained Ni films, only the results for ultrafine-grained Ni are reported. On comparing the behaviour of ultrafine-grained Ni with fine-grained $Cu_{0.14}Ni_{0.86}$ film, it can be seen that E_{corr} is nearly the same but j_{corr} decreases. Thus, the alloying of Cu with Ni clearly has a beneficial effect on corrosion performance, especially bearing in mind that the average crystallite size in the $Cu_{0.14}Ni_{0.86}$ film is higher than in ultrafine-grained nickel (379 nm vs. 207 nm). Rajasekaran and Mohan observed E_{corr} = –0.245 V vs. saturated calomel electrode (SCE) (i.e. –0.208 V vs. Ag | AgCl (3.5 M KCl)) in Ni-rich Cu-Ni films (15-50 nm crystallite size) brush plated

onto copper substrate (70). This value is close to the E_{corr} observed for nanoscrystalline $Cu_{0.13}Ni_{0.87}$ films electroplated. However, further Cu alloying did not seem to improve corrosion resistance, despite its higher nobility. Based on the electron configuration theory of passivity, it has been claimed that passive films formed on alloys with a Cu/Ni atomic ratio exceeding 1.6 are less stable (71).

One would intuitively expect corrosion to be initiated more easily at defects sites (e.g. grain boundaries and triple junctions in nanocrystalline metals). For a given Cu-Ni composition, nanostructuring caused a noticeable shift of E_{corr} towards more negative values, but resulted in a decrease in j_{corr}. These results are in agreement with the work by Troyon *et al.*, where it is reported that Ni/Cu multilayers prepared with saccharine showed more negative E_{corr} values but lower j_{corr} than the multilayers prepared without saccharine (i.e. with larger grain sizes) in 3.0 wt% NaCl solution (72). Similarly, the corrosion rate in 1M H_2SO_4 solution was also found to decrease in nanocrystalline Ni films electroplated from a saccharine-containing Watt's bath when the grain size was lowered from 28 to 8 nm (73). Due to the role of saccharine as a sulphur source, the inclusion of low amounts of sulphur in the nanocrystalline Cu_{1-x}-Ni_x films cannot be ruled out, and, as observed in other alloys, is partly responsible for the negative shift in E_{corr} (74).

Nanostructured materials prepared by mechanical methods are usually characterized by a large number of pores and microstrains, which are particularly susceptible to corrosion. Electrodeposition is known to provide dense and pore-free nanostructured metals, which make them less prone to certain types of corrosion such as pitting (75). In addition, the compact morphology and even surface of the nanocrystalline Cu-Ni alloys prepared help in lowering the dissolution rate, whereas the edged morphology of the fine-grained films allow an easier access of corrosive species (i.e. Cl^-) to the film/substrate interface. From the application point of view, the tradeoff between E_{corr} and j_{corr}, makes the nanocrystalline Cu-Ni films excellent candidates for protective coatings in marine environments.

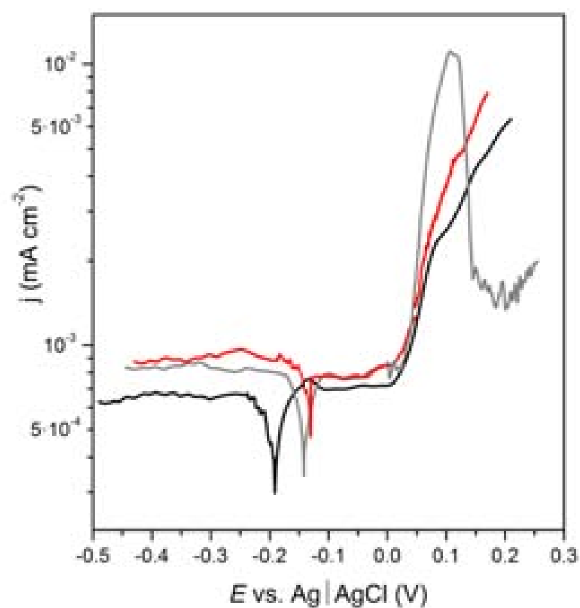

Figure 7. Typical potentiodynamic polarization curves of ultrafine-grained Ni (red curve), fine-grained $Cu_{0.14}Ni_{0.86}$ (grey curve) and nanocrystalline $Cu_{0.13}Ni_{0.87}$ (black curve) films onto Cu/Ti/Si (100) substrates.

Table 4. Corrosion data obtained from the polarization experiments in aerated 3.5 wt% NaCl

Film	E_{corr} (V)	j_{corr} (μA cm^{-2})	Active-passive transition
fine-grained $Cu_{0.57}Ni_{0.43}$	−0.163	6.3	yes
nanocrystalline $Cu_{0.55}Ni_{0.45}$	−0.200	5.8	yes
fine-grained $Cu_{0.14}Ni_{0.86}$	−0.140	6.5	yes
nanocrystalline $Cu_{0.13}Ni_{0.87}$	−0.197	5.8	no
ultrafine-grained Ni	−0.131	7.7	no

4. Conclusions

In situ growth of both fine-grained or nanocrystalline Cu-Ni films with variable composition was made possible by electrodeposition. The effects of a saccharine-assisted nanostructuring process on the morphology, structure, mechanical and corrosion properties of Cu-Ni films plated galvanostatically on silicon-based substrates has been discussed. Smooth films featuring much smaller crystallite sizes, lower microstrain, and larger numbers of stacking faults were obtained from saccharine-containing baths. The nanocrystalline films showed improved mechanical properties (larger hardness and elastic recovery and better wear resistance) compared to fine-grained films, while retaining good corrosion resistance in a chloride medium. These attributes surpassed those of pure Ni films obtained from a similar electrolytic bath. The present study clearly demonstrates that nanostructuring improves the properties of Cu-Ni alloys and thereby enables a wider range of applications for this system.

Acknowledgements

The authors wish to thank the Servei de Microscòpia of the Universitat Autònoma de Barcelona for the technical assistance during TEM characterization. This work has been partially financed by the 2009-SGR-1292 and MAT2007-61629 research projects. E.P. is indebted to the DURSI of the Generalitat de Catalunya for the Beatriu de Pinós postdoctoral fellowship. S.P. acknowledges a postdoctoral fellowship of Spanish MICINN. M.D.B. was partially supported by an ICREA ACADEMIA award.

References

(1) Lu, K.; Lu, L. Suresh, S. *Science* **2009**, *324*, 349.

(2) Chen, M.; Ma, E.; Hemker, K. J.; Sheng, H.; Wang, Y.; Cheng, X. *Science* **2003**, *23*, 1275.

(3) Lu, L.; Sui, M. L.; Lu, K. *Science* **2000**, *25*, 1463.

(4) Kumar, K. S.; Suresh, S.; Chisholm, M. F.; Horton, J. A.; Wang, P. *Acta Mater.* **2003**, *51*, 387.

(5) Kumar, K. S.; Van Swygenhoven, H.; Suresh, S. *Acta Mater.* **2003**, *51*, 5743.

(6) Dao, M.; Lu, L.; Asaro, R. J.; De Hosson, J. T. M.; Ma, E. *Acta Mater.* **2007**, *55*, 4041.

(7) Koch , C. C.; Youssef, K. M.; Scattergood, R. O.; Murty, K. L. *Adv. Eng. Mater.* **2005**, *7*, 787.

(8) Gleiter, H. *Prog. Mater. Sci.* **1989**, *33*, 223.

(9) Boé, A.; Safi, A.; Coulombier, M.; Fabrègue, D.; Pardoen, T.; Raskin, J.-P. *Smart Mater. Struct.* **2009**, *18*, 115018.

(10) Manhabosco, T. M.; Müller, I. L. *Surf. Coat. Technol.* **2008**, *202*, 3585.

(11) Subramanian, B.; Mohan, S.; Jayakrishnan, S.; Jayachandran, M. *Curr. Appl. Phys.* **2007**, *7*, 305.

(12) Tao, S.; Li, D. Y. *Nanotechnol.* **2006**, *17*, 65.

(13) Wang, F.; Hosoiri, K.; Doi, S.; Okamoto, N.; Kuzushima, T.; Totsuka, T.; Watanabe, T. *Electrochem. Commun.* **2004**, *6*, 1149.

(14) Park, D.-Y.; Song, R. Y.; Ko, J. M.; Yoo, B. Y.; Myung, N. V. *Electrochem. Sol. State Lett.* **2005**, *8*, C23.

(15) Klimenkov, M.; Haseeb, A. S. M. A.; Bade, K. *Thin Solid Films* **2009**, *517*, 6593.

(16) Zhang, Y.; Ivey, D. G. *Chem. Mater.* **2004**, *16*, 1189.

(17) Dennis, J. K.; Fuggle, J. J. *Electroplat. Met. Finish.* **1968**, *21*, 16.

(18) Cziráki, Á.; Fogarassy, B.; Geröcs, I.; Tóth-Kádár, E.; Bakonyi, I. *J. Mater. Sci.* **1994**, *29*, 4771.

(19) Natter, H.; Schmelzer, M.; Hempelmann, R. *J. Mater. Res.* **1998**, *13*, 1186.

(20) Qu, N. S.; Zhu, D.; Chan, K. C.; Lei, W. N. *Surf. Coat. Technol.* **2003**, *168*, 123.

(21) Shen, Y. F.; Xue, W. Y.; Wang, Y. D.; Liu, Z. Y.; Zuo, L. *Surf. Coat. Technol.* **2008**, *202*, 5140.

(22) Sansoz, F.; Stevenson, K. D.; Govinthasamy, R.; Murthy, N. S. *Scripta Mater.* **2008**, *59*, 103.

(23) Yong, P.; Shan, J.; Cui-ying, D.; Tian, T.; Zhao-feng, Z.; Yi-chun, Z. *Trans. Nonferrous Met. Soc. China* **2007**, *17*, 2770.

(24) Rashidi, A. M.; Amadeh, A. *Surf. Coat. Technol.* **2008**, *202*, 3772.

(25) Reddy, B. S. B.; Das, K.; Datta, A. K.; Das, S. *Nanotechnol.* **2008**, *19*, 115603.

(26) Rashidi, A. M.; Amadeh, A. *Surf. Coat. Technol.* **2009**, *204*, 353.

(27) Gómez, E.; Pellicer, E.; Vallés, E. *Electrochem. Commun.* **2004**, *6*, 853.

(28) Hassani, Sh.; Raeissi, K.; Golozar, M. A. *J. Appl. Electrochem.* **2008**, *38*, 689.

(29) Guan, S.; Nelson, B. J. *J. Magn. Magn. Mater.* **2005**, *292*, 49.

(30) Podlaha, E. J.; Bonhôte, Ch.; Landolt, D. *Electrochim. Acta* **1994**, *39*, 2649.

(31) Green, T. A.; Russel, A. E.; Roy, S. *J. Electrochem. Soc.* **1998**, *145*, 875.

(32) Beccaria, A. M.; Wang, Y. Z.; Poggi, G. *Surf. Interf. Anal.* **2004**, *21*, 442.

(33) Casella, I. G.; Gatta, M. *J. Electrochem. Soc.* **2002**, *149*, B465.

(34) Pellicer, E.; Varea, A.; Pané, S.; Nelson, B. J.; Menéndez, E.; Estrader, M.; Suriñach, S.; Baró, M. D.; Nogués, J.; Sort, J. *Adv. Funct. Mater.* **2010**, *20*, 983.

(35) Crousier, J.; Beccaria, A.-M. *Werks. Korr.* **1990**, *41*, 185.

(36) Milošev, I.; Metikoš-Huković, M. *Electrochim. Acta* **1997**, *42*, 1537.

(37) Badawy, W. A.; Ismail, K. M.; Fathi, A. M. *J. Appl. Electrochem.* **2005**, *35*, 879.

(38) Metikoš-Huković, M.; Škugor, I.; Grubač, Z.; Babić, R. *Electrohim. Acta* **2010**, *55*, 3123.

(39) Bull, S. J. *J. Phys. D: Appl. Phys.* **2005**, *38*, R393.

(40) The Rietveld Method (Ed: R. A. Young), Union of Crystallography, Oxford University Press, Oxford **1995**.

(41) Lutterotti, L.; Scardi, P. *J. Appl. Crystallogr.* **1990**, *23*, 246.

(42) Morales, M.; Chateigner, D.; Lutterotti, L. *Thin Solid Films* **2009**, *517*, 6264.

(43) Warren, B. E. in: X-ray Diffraction, Addison-Wesley, Reading, MA **1969**.

(44) Fischer-Cripps, A. C. in: Nanoindentation (Ed: F. F. Ling), Springer, New York **2004**.

(45) Oliver, W. C.; Pharr, G. M. *J. Mater. Res.* **1992**, *7*, 1564.

(46) Nakamura, Y.; Kaneko, N.; Watanabe, M.; Nezu, H. *J. Appl. Electrochem.* **1994**, *24*, 227.

(47) Moti', E.; Shariat, M. H.; Bahrololoom, M. E. *J. Appl. Electrochem.* **2008**, *38*, 605.

(48) Mockute, D.; Bernotiene, G.; Vilkaite, R. *Surf. Coat. Technol.* **2002**, *160*, 152.

(49) Mohanty, U. S.; Tripathy, B. C.; Das, S. C.; Singh, P.; Misra, V. N. *Hydrometallurgy* **2009**, *100*, 60.

(50) Rode, S.; Henninot, C.; Vallières, C.; Matlosz, M. *J. Electrochem. Soc.* **2004**, *151*, C405.

(51) Rode, S.; Henninot, C.; Matlosz, M. *J. Electrochem. Soc.* **2005**, *152*, C248.

(52) Weil, R. *Annu. Rev. Mater. Sci.* **1989**, *19*, 165.

(53) Bhandari, A.; Hearne, S. J.; Sheldon, B. W.; Soni, S. K. *J. Electrochem. Soc.* **2009**, *156*, D279.

(54) Lu, L.; Shen, Y.; Chen, X.; Qian, L.; Lu, K. *Science* **2004**, *304*, 422.

(55) Tochitskii, T. A.; Dmitrieva, A. E. *Russ. J. Electrochem.* **2003**, *39*, 305.

(56) Velinov, V.; Vitkova, S.; Pangarov, P. *Surf. Coat. Technol.* **1977**, *6*, 19.

(57) Randle, V. *Acta Mater.* **1999**, *47*, 4187.

(58) Wong, J.; Nixon, W. E.; Mitchell, J. W.; Laderman, S. S. *J. Appl. Phys.* **1992**, *71*, 150.

(59) J. R. Davis (ed), Nickel, cobalt, and their alloys. ASM International, USA **2000**, p. 4.

(60) http://www.nickel-alloys.net/index.html

(61) Gangfeng, W.; Xiqiao, F.; Shouwen, Y. *Chin. Sci. Bull.* **2002**, *47*, 1943.

(62) Sanders, P. G.; Eastman, J. A.; Weertman, J. R. *Acta Mater.* **1997**, *45*, 4019.

(63) Fougere, G. E.; Riester, L.; Ferber, M. *Mater. Sci. Eng. A* **1995**, *204*, 1.

(64) Kim, H. S.; Bush, M. B. *Nanostruc. Mater.* **1999**, *11*, 361.

(65) Legros, M.; Elliott, B. R.; Rittner, M. N. *Philos. Mag. A* **2000**, *80*, 1017.

(66) Leyland, A.; Matthews, A. *Wear* **2000**, *246*, 1.

(67) Musil, J.; Kunc, F.; Zeman, H.; Poláková, H. *Surf. Coat. Technol.* **2002**, *154*, 304.

(68) Mayrhofer, P. H.; Mitterer, C.; Musil, J. *Surf. Coat. Technol.* **2004**, *177–178*, 725.

(69) Levashov, E. A.; Shtansky, D. V. *Russ. Chem. Rev.* **2007**, *76*, 463.

(70) Rajasekaran, N.; Mohan, S. *J. Appl. Electrochem.* **2009**, *39*, 1911.

(71) Mansfeld, F.; Uhlig, H. H. *Corr. Sci.* **1969**, *9*, 377.

(72) Troyon, M.; Wang, L. *Appl. Surf. Sci.* **1996**, *103*, 517.

(73) Mishra, R.; Balasubramaniam, R. *Corr. Sci.* **2004**, *46*, 3019.

(74) George, J.; Rantschler, J.; Bae, S.-E.; Litvinov, D.; Brankovic, S. R. *J. Electrochem. Soc.* **2008**, *155*, D589.

(75) Ghosh, S. K.; Dey, G. K.; Dusane, R. O.; Grover, A. K. *J. Alloy Comp.* **2006**, *426*, 235.

Table of Contents Graphic (TOC)

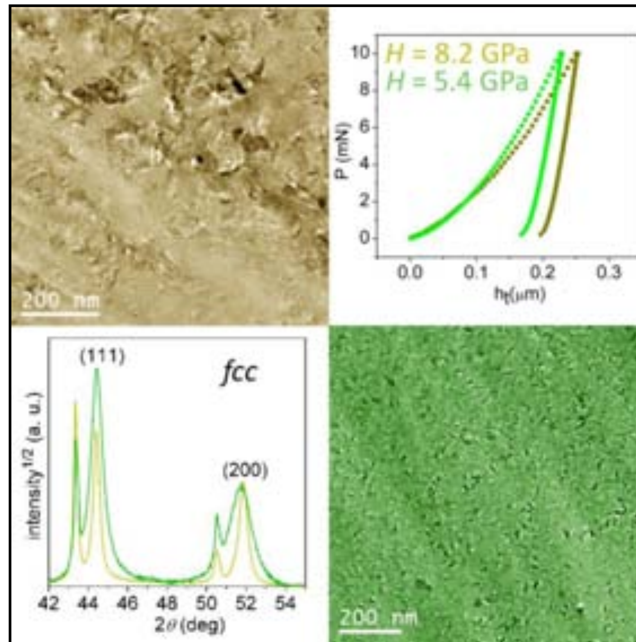

5.2. Grain boundary segregation and interdiffusion effects in nickel-copper alloys: an effective means to improve the thermal stability of nanocrystalline nickel.

In this article the thermal stability of nc-Ni and nc-Cu-Ni alloy films electrodeposited on Si/Ti/Cu substrates is compared. Changes observed in the mechanical and magnetic behaviour upon annealing at temperatures (T_{ANN}) ranging from 425 K to 625 K under high vacuum conditions are reported.

The nanocrystalline character is preserved up to 475 K for pure Ni, 525 K for $Ni_{0.88}Cu_{0.12}$ and 575 K for $Ni_{0.70}Cu_{0.30}$ and $Ni_{0.56}Cu_{0.44}$. These results reveal that alloying Ni with Cu is a good means to enhance the thermal stability of Ni. The higher the Cu content, the higher the annealing temperature before grain coarsening starts. Another interesting feature is the appearance of small reflections located between pure Cu and Cu-Ni peak positions upon annealings. These peaks suggest the formation of a Cu-rich phase when the temperature exceeds 525 K. The origin of this phase could be two-fold: i) it forms from the interdiffusion between the Cu seed-layer and the upper Cu-Ni films or ii) it arises from thermally induced segregation of Cu atoms at grain boundaries, a phenomenon one could expect because Cu and Ni have a positive enthalpy of mixing. With the aim to clarify the origin of this Cu-rich phase, in depth XRD, TEM and EELS analysis of Cu-Ni films are performed. For the Ni film, it is demonstrated that interdiffusion between the Cu seed-layer and the film takes place, at least at 625 K. For the Cu-Ni films, segregation of Cu atoms from the Cu-Ni grains also occurs, as demonstrated by the shift of Cu-Ni deposit XRD peaks toward higher 2θ angles, indicating Ni enrichment inside the grains for temperatures beyond 525 K. HRTEM, FFT and EELS techniques provide evidence for Cu segregation at grain boundaries in annealed Cu-Ni alloys.

The nanoindentation hardness of as deposited films decreases as Cu content increases, from 7.21 GPa to 6.15 GPa. However, the drop in hardness is shifted toward higher T_{ANN} as the Cu content in the deposit increases, thus confirming that segregation of Cu at Cu-Ni grain boundaries acts as a shielding layer against grain growth.

MOKE measurements reveal that the magnetic behavior of Cu-Ni films is markedly dependent on T_{ANN}. Hysteresis loops of the Ni-rich Cu-Ni films become progressively more tilted as T_{ANN} increase. Particularly noticeable is the reduction in remanence to saturation

magnetization ratio. The coercivity tends to increase for T_{ANN} ≥ 475 K. This effect is probably related to segregation of paramagnetic Cu-rich interfacial phase which reduces intergranular magnetic exchange interactions.

ACS APPLIED MATERIALS & INTERFACES

Grain Boundary Segregation and Interdiffusion Effects in Nickel-Copper Alloys: An Effective Means to Improve the Thermal Stability of Nanocrystalline Nickel

Eva Pellicer*[a], Aïda Varea[a], Kartik M. Sivaraman[b], Salvador Pané[b], Santiago Suriñach[a], Maria Dolors Baró[a], Josep Nogués[c], Bradley J. Nelson[b], Jordi Sort[#,d]

[a]Departament de Física, Facultat de Ciències, Universitat Autònoma de Barcelona, E-08193 Bellaterra, Spain.

[b]Institute of Robotics and Intelligent Systems (IRIS), ETH Zurich, CH-8092 Zurich, Switzerland.

[c]Institució Catalana de Recerca i Estudis Avançats (ICREA) and, Catalan Institute of Nanotechnology (ICN) and CIN2 and Universitat Autònoma de Barcelona, Campus UAB, E-08193 Bellaterra (Barcelona), Spain.

[d]Institució Catalana de Recerca i Estudis Avançats (ICREA) and Departament de Física, Universitat Autònoma de Barcelona, E-08193 Bellaterra, Spain.

Corresponding authors: Phone: +003493 5811401. Fax: +0034935812155. E-mails: *eva.pellicer.icn@uab.cat

#jordi.sort@uab.cat

Abstract

Nanocrystalline (nc) Ni films show pronounced grain growth and suffer from concomitant deterioration of their mechanical and magnetic properties after annealing at relatively low temperatures (T_{ANN} ≥ 475 K). This constitutes a drawback for their applicability as coatings or in components of miniaturized devices. This work reveals that the thermal stability of nc Ni is significantly improved by controllably alloying Ni with Cu to form a $Ni_{1-x}Cu_x$ solid solution. To tune the composition of such nc alloys, $Ni_{1-x}Cu_x$ films are obtained galvanostatically using an electrolytic bath containing Ni and Cu sulphate salts as electroactive species, saccharine as grain-refining agent, and applying current densities ranging from -10 to -40 mA cm^{-2}. The enhanced thermal stability is ascribed to segregation of a Cu-rich phase at the $Ni_{1-x}Cu_x$ grain boundaries, which acts as a shielding layer against grain growth. As a result, high values of hardness (in excess of 6 GPa) remain in nc $Ni_{1-x}Cu_x$ for x ≥ 0.3, even after annealing at T_{ANN} ≥ 575 K. From a magnetic point of view, $Ni_{1-x}Cu_x$ films possess lower coercivity values than pure nc Ni films, both in the as-prepared and annealed states, thus offering potential advantages for certain soft magnetic applications.

1. Introduction

Nanocrystalline (*nc*) metallic films are known to benefit from enhanced, and sometimes novel, physical and chemical properties as compared to conventional coarse-grained films.[1-4] Indeed, a reduction of the crystallite size towards the sub-100 nm scale results in larger hardness values, increased ductility and fatigue behaviour, better wear resistance, enhanced coercivity and, eventually, higher resistance to pitting corrosion. These properties make *nc* films technologically appealing for the implementation of a wide range of components in micro/nano-electro-mechanical systems (MEMS/NEMS) or to obtain mechanically hard, corrosion-resistant coatings.[5-7]

In spite of these outstanding properties, *nc* metals typically show relatively poor thermal stability.[8,9] Grain growth occurs in these materials at relatively low homologous temperatures (often less than 50% of the melting temperature), mainly because of the large amounts of metastable grain boundaries and defects, where enhanced atomic diffusivity is promoted. As a result, the use of *nc* materials in applications such as cutting and friction tools, thermal and diffusion barriers, high-temperature catalysts, emission and filter components, jet engines or stampers for compact disk manufacturing remains rather challenging. In particular, poor thermal stability constitutes a real technological

drawback in miniaturized devices, where temperature can locally raise significantly because heat dissipation is precluded as compared to bulk materials. In this case, grain coarsening can lead to loss of geometrical fidelity, in addition to the decrease in mechanical strength. Moreover, some lithographic methods used to fabricate small components in MEMS/NEMS also require a few heating steps, such as baking or thermal curing, which can easily deteriorate the properties of *nc* metallic films.

For all these reasons, several strategies have been designed in recent years to improve the thermal stability of *nc* metals. These include, among others, grain boundary pinning (using solute atoms, fine particles –oxide or nitride phases– or porosity), control of compressive residual stresses, induced interfacial phase transformations or tuning of the chemical ordering at grain boundaries.[1,8,9] Alloying with certain specific elements can have a beneficial effect on preserving the *nc* character of a material, particularly when segregation of one of the constituent elements to the grain boundaries occurs during annealing (such as in Ni-P, Fe-Zr, Pd-Zr, Ru-Al, Y-Fe or Ni-Mn), thus reducing the total Gibbs free energy of the system.[8,9,10-15] This effect is particularly exacerbated in alloys composed of elements with a large positive enthalpy of mixing, like Fe-Ag or Fe-Cu.[1,16,17] Due to grain boundary segregation, the *nc* structure can be either kinetically or thermodynamically stabilized. Kinetic stabilization is accomplished when the grain boundary velocity is reduced during thermal annealing (e.g., by solute drag mechanism).[9,11,14,18] Besides, in some systems (e.g., Fe-Zr, Ni-W), *nc* structures are thermodynamically favoured because alloying causes a significant reduction in the grain boundary energy and hence decreases the associated driving force for grain growth.[10,11,19]

Among the numerous techniques to grow metallic films, electrodeposition stands out from the rest because it relies on a simple, relatively low-cost and user friendly set-up, it allows fast deposition rates (thus being much less time-consuming than physical methods like sputtering or electron beam evaporation), it does not require vacuum technology and deposition can be performed onto a wide variety of substrate shapes, not necessarily flat.[20] It is noteworthy that conventional physical deposition methods are generally limited to the growth of thin films (up to 1-2 μm), a restriction that can be disadvantageous for some MEMS/NEMS, where thicker patterned features are required.

Remarkably, electrodeposition is particularly suitable to prepare *nc* metals virtually free of porosity. This can be achieved by adding grain-refining agents (e.g., saccharine, coumarine or polyethylenglycol) to the electrolytic bath or by depositing under pulse-plating mode.[21] Such direct growth of *nc* metallic material circumvents the problem of

other manufacturing techniques where the *nc* metals are obtained by high-temperature consolidation of *nc* powder precursors, during which a certain degree of grain coarsening unavoidably occurs. Furthermore, electrodeposition is not limited to the growth of films or sheets composed of single metallic elements. In fact, several alloys (e.g. Co-Pt, Co-Ni, Ni-W, Co-Fe-Ni, Co-Mo, Ca-P, etc.)[22-28] can be easily electroplated for assorted purposes and, as aforementioned, this can be advantageous in terms of enhancing the thermal stability of the obtained materials. There are various parameters that allow precise tuning of the alloy composition: bath formulation and temperature, applied current density/overpotential, hydrodynamic regime, etc. For instance, in citrate-containing electrolytic solutions, deposition of some metals (like Cu) is mass-transfer-controlled whereas that of other metals (like Ni) is charge-transfer-controlled. Hence, by decreasing the current density, Ni deposition can be enhanced while the concentration of electroactive Cu species at the electrolyte/working-electrode interface becomes depleted, thus providing a means to obtain Ni-Cu films with controllable composition.[29] It should be noted that Ni-Cu alloys with tunable stoichiometry have been prepared recently by means of alcohol-assisted chemical vapour deposition.[30]

Because of their soft magnetic character, Ni and some Ni alloys (like Co-Ni or $Ni_{19}Fe_{81}$, i.e. permalloy) are among the most widely used materials to manufacture remotely-actuated magnetic MEMS/NEMS.[31] In spite of their good magnetic properties, the mechanical behaviour of these films is typically worse than those of conventional materials employed in MEMS/NEMS (like Si, SiN or SiC). For this reason, it is important to grow these metallic films in *nc* form and to preserve the *nc* structure after remaining at intermediate temperatures (i.e., at the working conditions).

Herein, the effects of alloying Ni with Cu on the thermal stability (grain size, microstrains, cell parameter, stacking faults) and the resulting properties of electroplated $Ni_{1-x}Cu_x$ ($0 \leq x \leq 0.44$) *nc* films are investigated. The results show that, for sufficiently large x values, segregation of a Cu-rich phase at grain boundaries occurs during annealing, preceding grain coarsening. Since the enthalpy of mixing between Cu and Ni is positive, the Cu-rich phase acts as a pinning layer against thermally-activated grain growth, thus enhancing the thermal stability of these films and improving some of their mechanical and magnetic properties with respect to pure Ni.

2. Experimental methods

The metallic films were obtained by direct current electrodeposition in one-compartment thermostatized three-electrode cell using a PGSTAT30 Autolab potentiostat/galvanostat (Ecochemie). The electrolytic solutions were prepared from analytical grade reagents and Milipore MilliQ water. Ni films were obtained from an electrolyte containing 190 g/L $NiSO_4 \cdot 6H_2O$ (nickel sulphate), 87 g/L $Na_3C_6H_5O_7 \cdot 2H_2O$ (sodium citrate), 0.2 g/L $NaC_{12}H_{25}SO_4$ (sodium dodecylsulphate) and 0.5 g/L $C_7H_5NO_3S$ (saccharine*)*. Ni-Cu alloy films were deposited from an electrolyte containing the same chemicals except for the metal salts: 184 g/L $NiSO_4 \cdot 6H_2O$, 6.24 g/L $CuSO_4 \cdot 5H_2O$ (copper sulphate). Hence, both, pure Ni and Ni-Cu films were obtained using analogous bath formulation. The electrolyte volume was 100 ml. The pH was fixed at 4.5 and the temperature at 30ºC in all cases. Silicon (100) substrates with e-beam evaporated Ti (100 nm)/Cu (500 nm) adhesion/seed layers were used as working electrodes, which were positioned vertically within the electrolyte. The working area was 6 x 5 mm^2. A double junction Ag|AgCl (E = +0.210V/SHE) reference electrode (Metrohm AG) was used with 3M KCl inner solution and an interchangeable outer solution made of 1M Na_2SO_4. A platinum spiral served as counter electrode. Prior to deposition, the copper surface was first degreased with acetone followed by washing in isopropyl alcohol and water and, finally, dipped in diluted sulphuric acid to remove any oxides and organic residues present on the copper surface. The backside of the silicon substrate was insulated to ensure that only the copper surface was conductive. Before each deposition, the electrolyte was de-aerated with nitrogen gas and a blanket of nitrogen was maintained on top of the solution during the experiment. Deposition was conducted galvanostatically, by applying a constant current density in the range from -10 to -40 mA cm^{-2}, under mild stirring (200 rpm) using a magnetic stirrer bar. The electrical charge was adjusted across all depositions to attain similar film thicknesses. After deposition, the films were thoroughly rinsed in water and stored in air. The chemical composition of the films was determined by energy dispersive X-ray spectroscopy (EDXS). Metal proportions are expressed in atomic percentage (at%). From four-point measurements using interferometric profilometry, the average film thickness was determined to be around 3 μm for all the investigated electroplated alloys.

To prevent oxidation, annealing treatments of the as-deposited films were performed under high vacuum ($p < 10^{-5}$ mbar) at temperatures, T_{ANN}, ranging from 425 to 625 K. The samples were heated at 5 K/min and cooled down to room temperature after keeping them at T_{ANN} for 3 h. The structure of the deposits, both before and after annealing, was

studied by X-ray diffraction (XRD) and transmission electron microscopy (TEM). XRD patterns were recorded on a Philips X'Pert diffractometer using the Cu K_{α} radiation in the 40° - 55° 2θ range (0.03º step size, 10s holding time). The global structural parameters, such as cell parameter, *a*, crystallite size, <*D*> (defined here as the average coherently diffracting domain sizes), and microstrains or atomic level deformations, $<\varepsilon^2>^{1/2}$, were evaluated by fitting the full XRD patterns using the Materials Analysis Using Diffraction (MAUD) Rietveld refinement program.[32,33] This software includes an algorithm to quantitatively evaluate the stacking fault probability, α_{SF} (in which $1/\alpha_{SF}$ indicates the average number of atomic planes between two consecutive stacking faults).[34] TEM characterisation was carried out on a JEOL JEM-2011 microscope operated at 200 kV. For the TEM observations (planar views), the films were thinned by ion milling, which was performed from both sides of the film in order to remove the seed layer and any surface contamination. Electron energy loss spectroscopy (EELS) analysis was also carried out after annealing at 625 K in order to assess the Cu/Ni proportion both inside and across grain boundaries (i.e., to probe thermally-induced atomic segregation). The EELS experiments were performed using a JEOL JEM 2010F TEM, operated at 200 kV, with a spot size of 0.5 nm.

The hardness and reduced Young's modulus of the films, before and after annealing, were evaluated by nanoindentation, operating in the load control mode, using an UMIS device from Fischer-Cripps Laboratories equipped with a Berkovich pyramidal-shaped diamond tip. The value of maximum applied force was chosen to be 10 mN to ensure that the maximum penetration depth during the tests was kept below one tenth of the overall film thickness. This is considered as a necessary condition to avoid having an influence of the substrate on the measured mechanical properties of the film.[35] The thermal drift during nanoindentation was kept below 0.05 nm/s. Proper corrections for the contact area (calibrated with a fused quartz specimen), instrument compliance, and initial penetration depth were applied. The Berkovich indentation hardness values, H_B, were derived from the load-displacement curves at the beginning of the unloading segment using the method of Oliver and Pharr.[36] The room-temperature magnetic properties were locally assessed by magneto-optic Kerr effect (MOKE) magnetometry (Durham Magneto-Optics) with a maximum in-plane applied field of 400 Oe. Note that MOKE is a surface-sensitive technique, which senses penetration depths of the order of a few tens of nm. Hence, the obtained Kerr signal is proportional to the saturation magnetization of the sample surface.

3. Results and discussion

3.1. Structural evolution during thermal annealing

The X-ray diffraction (XRD) patterns of the $Ni_{1-x}Cu_x$ films, measured both in the as-deposited state and after annealing at T_{ANN} = 575 K and 625 K, are shown in Figure 1. Broad diffraction peaks are observed in the as-deposited films, matching the angular positions of face-centred cubic (fcc) copper (seed-layer) and fcc Cu-Ni phases. The Rietveld analysis of the XRD data evidences that, before annealing, the crystallite size, $\langle D \rangle$, ranges from 30 to 40 nm, irrespective of the exact film composition (see Figure 2). Values of microstrains, $\langle \varepsilon^2 \rangle^{1/2}$, around 10^{-3} are obtained, which are lower than in nc materials typically obtained by severe plastic deformation techniques.[37] The small values of $\langle D \rangle$ and $\langle \varepsilon^2 \rangle^{1/2}$ can be ascribed to the crystal size refinement and stress relieve activity promoted by the saccharine. Note that, in general, smaller crystallite sizes would be expected for higher current densities (i.e., smaller Cu contents). As this trend was not observed here, the effect of saccharine likely dominates over any possible influence of the current density.

As shown in Figure 2, the crystallite size remains below 100 nm in the entire compositional range for $T_{ANN} \leq 475$ K. Remarkably, pronounced grain coarsening occurs in Ni films at T_{ANN} = 525 K. This is in agreement with the onset temperature for grain growth observed in pure Ni electrodeposits subject to annealing. In fact, several works examined in the past the thermal behaviour of nc Ni films by different means, mainly by differential scanning calorimetry (DSC) and TEM analyses.[38-43] Abnormal grain growth (leading to the formation of bimodal grain structures) in nc Ni (with 10-30 nm grain size) was reported to occur through a quasi-nucleation growth process above 473 K.[44] A broad exothermic band at ca. 373-498 K followed by a peak at around 543 K ascribed to pronounced grain growth were determined by DSC measurements.[40] Conversely, the films with x = 0.30 and 0.44 do not exhibit obvious thermally-induced grain growth until TANN ≥ 625 K. This is already evident in Figure 1, where clear narrowing of the XRD peaks occurs for x = 0 and 0.12 at 575 K, whereas the width of the XRD peaks of $Ni_{1-x}Cu_x$ films with x = 0.30 and 0.44 at T_{ANN} = 575 K remains virtually the same as in the as-deposited state. These results reveal that, from a microstructural point of view, alloying Ni with Cu significantly enhances the thermal stability of nc Ni films. In turn, the microstrains tend to be progressively released as T_{ANN} is increased [see Figure 2 (b)], particularly for samples with low Cu percentages. Note that the reduction in $\langle \varepsilon^2 \rangle^{1/2}$ takes place already before the onset temperature for grain growth.

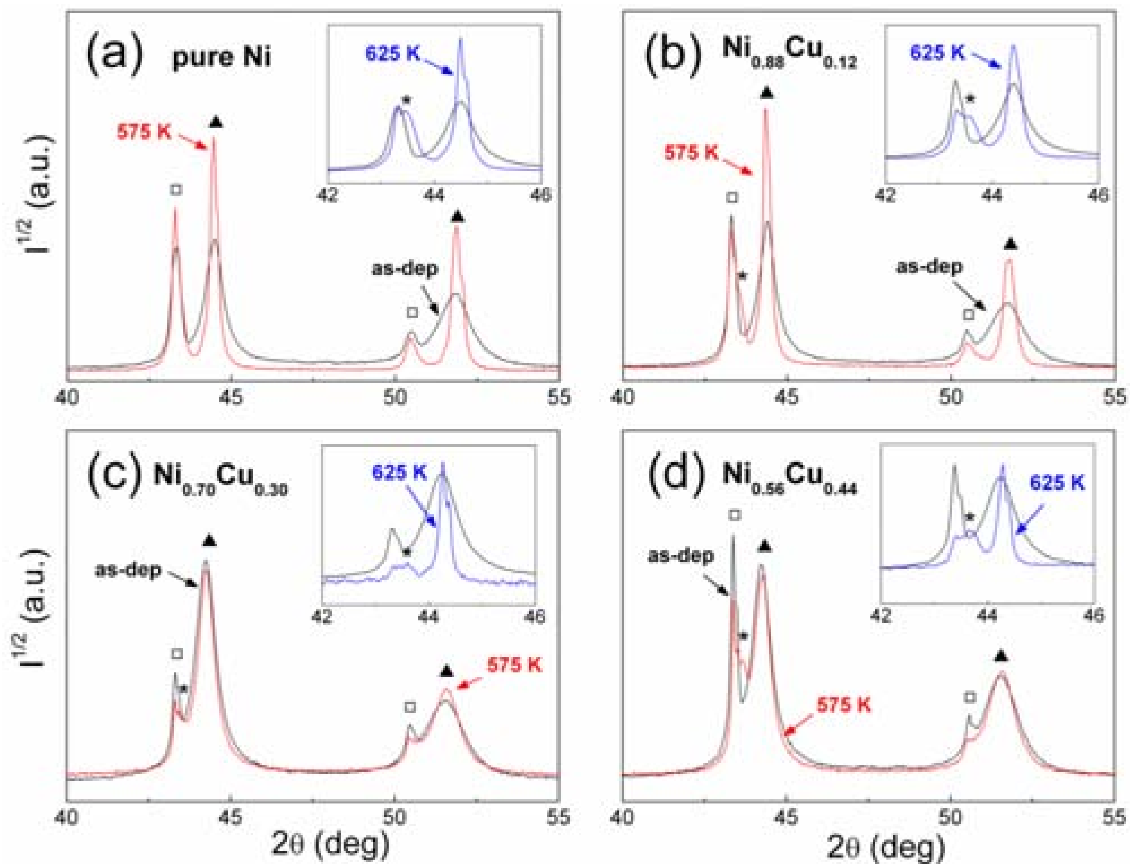

Figure 1: X-ray diffraction (XRD) patterns, in the 40-55° 2θ range, of (a) pure Ni, (b) $Ni_{0.88}Cu_{0.12}$, (c) $Ni_{0.70}Cu_{0.30}$ and (d) $Ni_{0.56}Cu_{0.44}$ films in the as-deposited states (in black) and after annealing at T_{ANN} = 575 K (in red). Indicated with the symbols □, ▲ and * are the XRD peaks corresponding to the Cu seed layer, the $Ni_{1-x}Cu_x$ film and a Cu-rich phase that forms during annealing. Shown in the insets are enlargements of the (111) XRD peaks of the as-deposited films (in black) and the films annealed at T_{ANN} = 625 K (in blue). Note that pronounced XRD peak narrowing (i.e., grain growth and microstrain release) occurs in pure Ni and $Ni_{0.88}Cu_{0.12}$ films already at T_{ANN} = 575 K. Conversely, for the films containing larger Cu percentages, a clear decrease in the peak width is only observed at higher temperatures (T_{ANN} = 625 K).

The 40°−55° 2θ range, displayed in Figure 1, covers the (111) and (200) XRD reflections, located for $Ni_{1-x}Cu_x$ around 44° and 52°, respectively. An obvious difference in the width of the (111) and (200) peaks of the as-prepared $Ni_{1-x}Cu_x$ films is observed. This is indicative of the existence of stacking faults.[34] The MAUD Rietveld refinement software allows deconvoluting the contributions from crystallite size, microstrains and stacking faults on the XRD peaks width. From the refinements, the stacking fault probability was found to be $\alpha_{SF} \sim 2 \times 10^{-3}$ for all as-deposited films, suggesting that intragranular growth nanotwins were formed during electroplating. As expected, the values of α_{SF} were also found to decrease with annealing temperature in the overall investigated compositional range.

Another interesting observation is that small peaks (indicated with an * in Figure 1), located at 2θ angles between those of Cu and $Ni_{1-x}Cu_x$ reflections, appear for $T_{ANN} \geq 525$ K.

The occurrence of these peaks suggests that a Cu-rich phase is formed when the annealing temperature exceeds 525 K. The origin of this phase could be two-fold: either it forms from interdiffusion between the Cu seed-layer and the upper $Ni_{1-x}Cu_x$ films or it arises from thermally-induced segregation of Cu atoms at the grain boundaries present in the $Ni_{1-x}Cu_x$ phase. Detailed investigations combining XRD and TEM results suggest that both effects occur simultaneously, although grain boundary segregation starts at a lower T_{ANN} than interlayer diffusion and is actually enhanced in samples with higher Cu contents. Indeed, as shown in Figure 1, a progressive decrease in the intensity of the Cu seed layer peaks is observed as T_{ANN} is increased. This is particularly obvious for T_{ANN} = 625 K. Moreover, although no additional peaks emerge at 575 K in the XRD pattern corresponding to pure Ni, a clear shoulder appears for this film at T_{ANN} = 625 K [see panel (a) in Figure 1], thus corroborating that interdiffusion between the seed-layer and the films unambiguously takes place, at least at 625 K. This progressive decrease in the intensity of the Cu XRD peaks (and not in the $Ni_{1-x}Cu_x$ reflections) is in agreement with other works which show that when a diffusion-induced recrystallization layer forms in NiCu/Cu couples during annealing, this layer grows mainly towards Cu, which progressively decreases in thickness.[45]

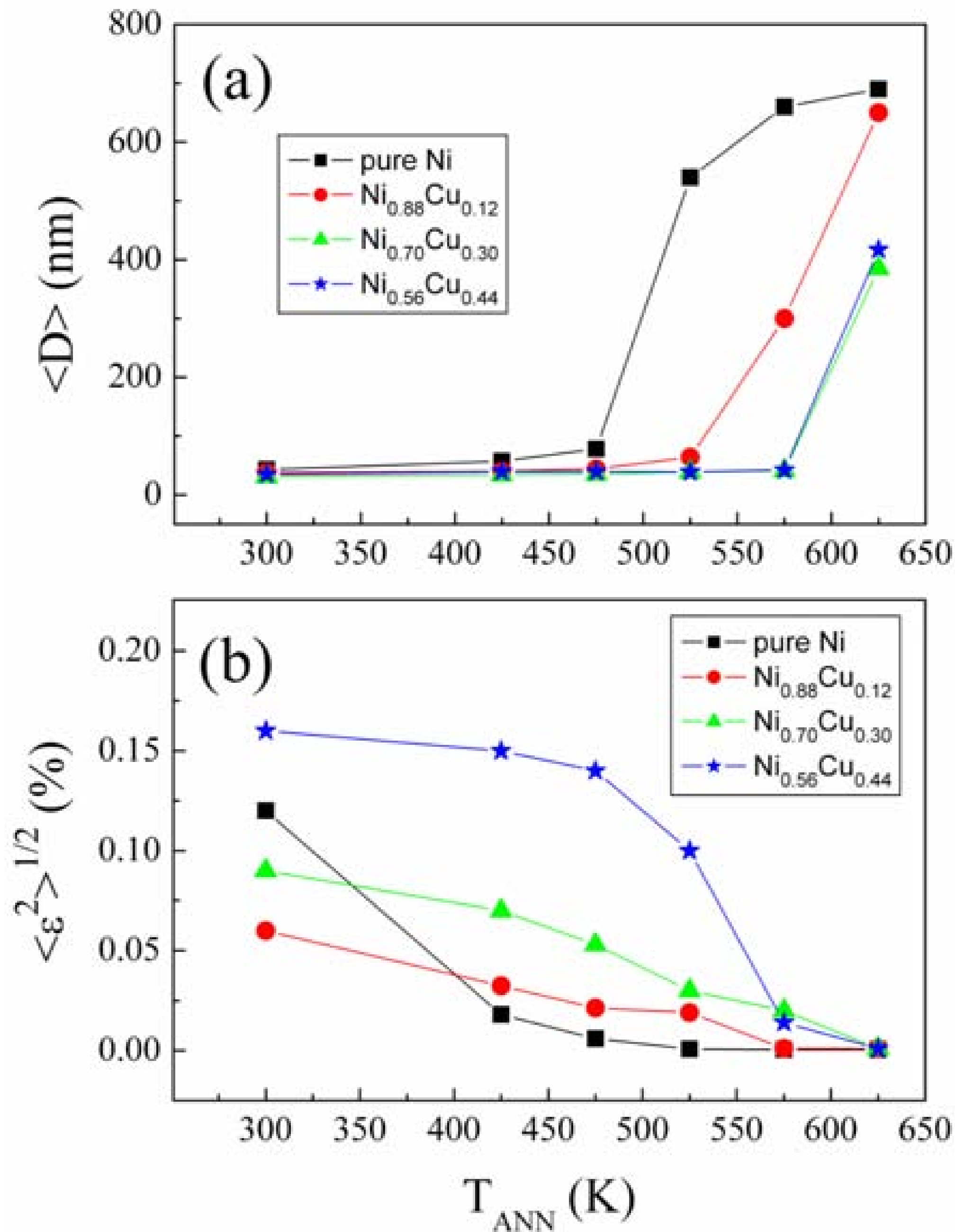

Figure 2: Dependence of (a) the crystallite size, <D>, and (b) the microstrains, $<\varepsilon^2>^{1/2}$, on the annealing temperature, T_{ANN}, for pure Ni (-■-), $Ni_{0.88}Cu_{0.12}$ (-●-), $Ni_{0.70}Cu_{0.30}$ (-▲-) and $Ni_{0.56}Cu_{0.44}$ (-★-) films. Pronounced grain growth occurs in pure Ni around T_{ANN} = 500 K, whereas for $Ni_{0.70}Cu_{0.30}$ and $Ni_{0.56}Cu_{0.44}$ films, significant grain coarsening occurs around T_{ANN} = 600 K. A progressive decrease of $<\varepsilon^2>^{1/2}$ with T_{ANN} is observed for all compositions, although $<\varepsilon^2>^{1/2}$ decreases earlier for pure Ni and the reduction seems to be delayed for the $Ni_{0.56}Cu_{0.44}$ film. Note that error bars would be included within the size of the symbols.

From our results, there is also clear evidence that, besides interlayer diffusion, Cu segregation towards grain boundaries occurs as well during thermal annealing. Figure 1 shows that the Ni-Cu reflections of as-deposited $Ni_{1-x}Cu_x$ films are progressively shifted

towards lower 2θ angles as the Cu percentage is increased, indicating a progressive increase in the cell parameter, *a* (see Figure 3). This is in agreement with the Vegard's law since a_{Ni} = 0.35238 nm is smaller than a_{Cu} = 0.36150 nm. Of course, the Cu seed-layer peaks are not shifted in angle. Upon annealing, the cell parameter of pure Ni films does not vary. Conversely, for $T_{ANN} \geq 525$ K, the cell parameter for all $Ni_{1-x}Cu_x$ films (except for x = 0) is found to decrease. This confirms that there is a tendency for grain boundary Cu segregation as annealing proceeds which, in turn, causes Ni enrichment inside the grains. Actually, Cu grain boundary segregation in Ni-Cu alloys is a well-documented effect and it can occur in bulk alloys, thin films or nanoparticles.[46-48] However, the role of this effect in stabilizing the *nc* character of Ni films has not been so far unravelled. It should be noted that, from the Rietveld refinement of the XRD data, the weight percentage of the Cu-rich phase formed upon annealing is around 15% and 25% in $Ni_{0.70}Cu_{0.30}$ after annealing at T_{ANN} = 575 and 625 K, respectively. For films with lower Cu percentage, the amount of Cu-rich phase is smaller (e.g., only 10% in $Ni_{0.88}Cu_{0.12}$ after annealing at T_{ANN} = 625 K).

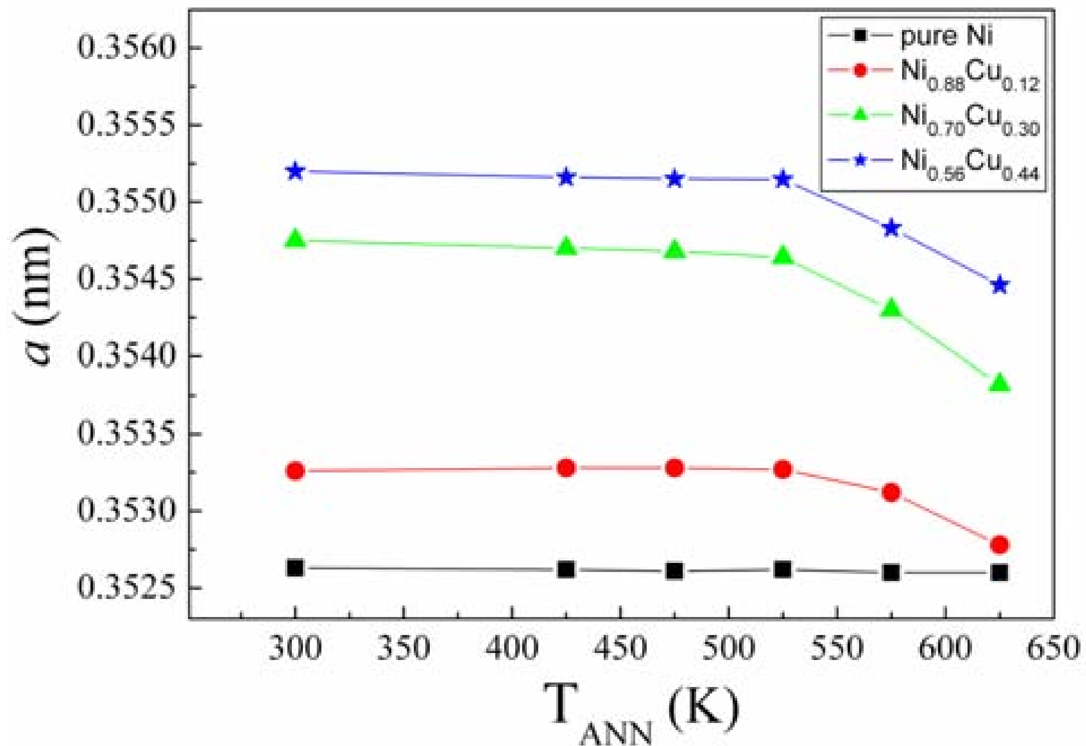

Figure 3: Dependence of the cell parameter, *a*, on the annealing temperature, T_{ANN}, for pure Ni (-■-), $Ni_{0.88}Cu_{0.12}$ (-●-), $Ni_{0.70}Cu_{0.30}$ (-▲-) and $Ni_{0.56}Cu_{0.44}$ (-★-) films. As expected, larger cell parameter is observed for the alloys containing larger Cu percentages (in agreement with Vegard's law). Remarkably, a decrease of *a* is observed in $Ni_{0.88}Cu_{0.12}$, $Ni_{0.70}Cu_{0.30}$ and $Ni_{0.56}Cu_{0.44}$ films for T_{ANN} > 525 K. This indicates that the $Ni_{1-x}Cu_x$ alloys become enriched in Ni as the Cu-rich phase segregates during the high-temperature annealing treatments. Note that error bars would be included within the size of the symbols.

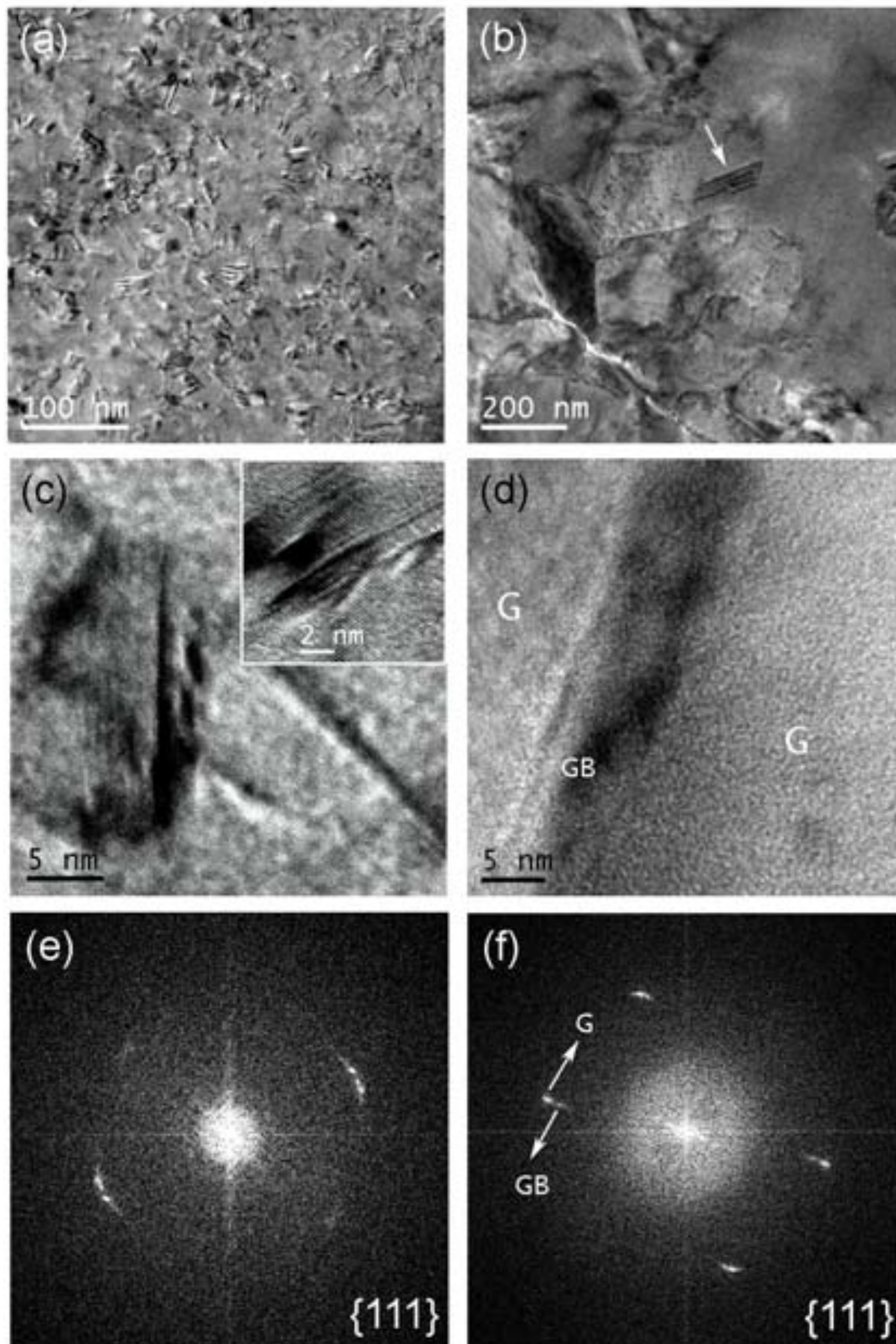

Figure 4: (a) Transmission electron microscopy (TEM) image of the as-deposited $Ni_{0.56}Cu_{0.44}$ alloy, revealing the nanocrystalline nature of the electroplated film; (b) TEM image of the same film after annealing at T_{ANN} = 625 K, where a pronounced increase in the average crystallite size is clearly observed (a few annealing twins are also observed, one of them is indicated with an arrow); (c) high resolution TEM image of the as-deposited $Ni_{0.56}Cu_{0.44}$ film, showing the presence of several intragranular nanotwins (as also evidenced in the inset, which corresponds to a different grain of the same film); (d) high-resolution TEM image of the $Ni_{0.56}Cu_{0.44}$ film annealed at T_{ANN} = 625 K, showing a detail of a grain boundary; (e) fast-Fourier transform (FFT) of the image displayed in panel (c) –the ring portion corresponds to the {111} planes–; (f) FFT of the image shown in panel (d). In the latter, a double peak is observed at the position of the {111} planes. The spots located at a slightly larger interplanar distance correspond to the grain boundary (GB) whereas the other spots correspond to the interplanar distances in the grains (G). This can be demonstrated by creating the inverse Fourier transform images from the FFT.

Further insight into the role of Cu on the thermally-driven structural changes of electroplated *nc* $Ni_{1-x}Cu_x$ films was obtained by TEM. As shown in Figure 4, pronounced grain coarsening occurs in $Ni_{0.56}Cu_{0.44}$ after annealing at 625 K [cf. panels (a) and (b)], in agreement with XRD results. Remarkably, although large amounts of intragranular nanotwins are observed in the as-deposited film [panel (c)], most of these nanotwins are annihilated during annealing. Just a few, but larger, twinned regions (the so-called annealing twins) are perceptible after the heat-treatments, like the one indicated with a white arrow in panel (b). The occurrence of growth nanotwins in *nc* Cu and *nc* Ni has been occasionally reported in the literature[49,50] and is mainly ascribed to the low stacking fault energy of these metals, which favours the presence of these planar defects, giving rise to the anomalous peak broadening of the XRD peaks. Indeed, it has been reported that the stacking fault energy of Ni decreases by alloying with Cu,[51] thus promoting the occurrence of planar defects. In addition, saccharine increases the probability of twinning in some electrodeposits (e.g. Ni) because of its preferential adsorption onto (111) planes, resulting in an increased amount of crystal mass in twin orientation.[52]

High-resolution TEM imaging also provides evidence for Cu segregation at the grain boundaries of annealed $Ni_{1-x}Cu_x$ films. Panel (d) in Figure 4 shows a detail of a grain boundary (and the two surrounding grains) of the $Ni_{0.56}Cu_{0.44}$ film after annealing at 625 K. Interestingly, the fast Fourier transform (FFT) of this micrograph [panel (f)] shows the occurrence of a double spot, with a slightly different interatomic spacing, at the position of the {111} ring. Note that double spots are not observed in the FFT image of the as-deposited film [panel (e)], where only one interatomic distance is distinguished. Detailed analysis using FFT of selected regions of panel (d) (see Figure 5) indicate that the double spot only appears in regions that include the grain boundary (GB1 and GB2), whereas single spots with $d_{111} \sim 0.2038$ nm are observed in the FFT of grains 1 and 2 (denoted as G1 and G2). The emerging small inner spots in FFT of the grain boundary correspond to a slightly larger interplanar distance ($d_{111} \sim 0.2085$ nm), indicating that the grain boundary region is enriched in Cu which, as previously stated, displays a larger cell parameter than Ni. In order to confirm the Cu segregation, EELS analysis was also carried out. Elemental Cu and Ni quantification was performed following a line crossing a grain boundary, as indicated with the white arrow in Figure 6 (a). The EELS results clearly show that an increase in the Cu percentage (up to 82 at% Cu) occurs at the grain boundaries during annealing of the $Ni_{0.56}Cu_{0.44}$ film. Concomitantly, the surrounding grains become overall depleted in Cu and a nominal composition around $Ni_{0.73}Cu_{0.27}$ is obtained inside the grains. This agrees rather well with the changes observed in the cell parameter during annealing

(Figure 3), where the *a* value of $Ni_{0.56}Cu_{0.44}$ after annealing at T_{ANN} = 625 K resembles that of as-deposited $Ni_{0.70}Cu_{0.30}$ film. Grain boundary segregation can be understood in terms of the cohesive energy of Ni and Cu. During annealing, more bonds are broken at the grain boundaries than in the interior of grains. Hence, elements with lower cohesive energy tend to concentrate/accumulate along the grain boundaries. Since the cohesive energy of Ni (4.44 eV) is larger than for Cu (3.49 eV)[53], Cu atoms are more likely to concentrate on grain boundaries than Ni atoms. This phenomenon is similar to what has been observed in the Fe-Cu system, where Cu atoms also accumulate at grain boundaries and cause an increase in the thermal stability of the alloy.[16] Such effect has also been observed in electrodeposited fcc Ni-Fe alloys, where alloying of Fe with Ni was reported to bring about changes in both grain boundary composition and structure, which were ultimately responsible for the higher thermal stability of Fe-Ni compared to pure Ni.[54,55] In the case of Ni-P alloys (either electrodeposited or electroless-plated), both grain boundary solute drag and Zener drag (Ni_3P precipitates) account for the enhanced thermal stability.[56,57] Nevertheless, sometimes the presence of impurities plays also a large effect on the thermal stability of the electrodeposits.[58]

It should be noted that atomic Cu interdiffusion from the seed layer towards the upper $Ni_{1-x}Cu_x$ films would also preferably occur by atomic motions through the grain boundaries since the atomic mobility at grain boundaries is larger than inside the grains. Indeed, the activation energy for bulk diffusion of Cu into Ni (297 kJ/mol)[59] is much larger than for Cu migration through Ni grain boundaries (124 kJ/mol).[60] Hence, interdiffusion from the Cu seed layer would also contribute to the observed Cu enrichment at the $Ni_{0.56}Cu_{0.44}$ grain boundaries.

The beneficial effect of Cu enrichment at grain boundaries on the thermal stability of the $Ni_{1-x}Cu_x$ system can be understood as follows. When temperature is sufficiently raised, grain growth is accompanied by an elimination of grain boundaries, implying that, to a certain extent, Cu atoms have to be re-dissolved into the Ni-rich $Ni_{1-x}Cu_x$ grains. However, this is energetically unfavourable because the enthalpy of mixing between Ni and Cu is positive (with maximum values ranging between +0.5 to +1.5 kJ/mol).[61-63] In pure Ni films, since Cu grain boundary segregation does not take place, grain growth readily occurs at T_{ANN} = 475 K. However, in $Ni_{1-x}Cu_x$ films, and for annealing temperatures beyond 475 K, there is a competition between thermally-driven Cu segregation and the tendency for grain coarsening and, as a result, grain growth is inhibited until enough energy is supplied to the system. Note that in pure Ni films, Cu diffusion from the seed-layer, which could also hinder grain coarsening, occurs only at higher annealing temperatures (T_{ANN} = 625K), once

the Ni grains have already grown. Since the enthalpy of mixing between Ni and Cu for Ni-rich alloys is only slightly positive, thermal annealing is not found to cause precipitation of Cu nanoparticles (at least for the investigated range of temperatures). This is opposite to what occurs in other systems, like Fe-Cu, where the large positive enthalpy of mixing (+13 kJ/mol) promotes annealing-induced phase separation.[16]

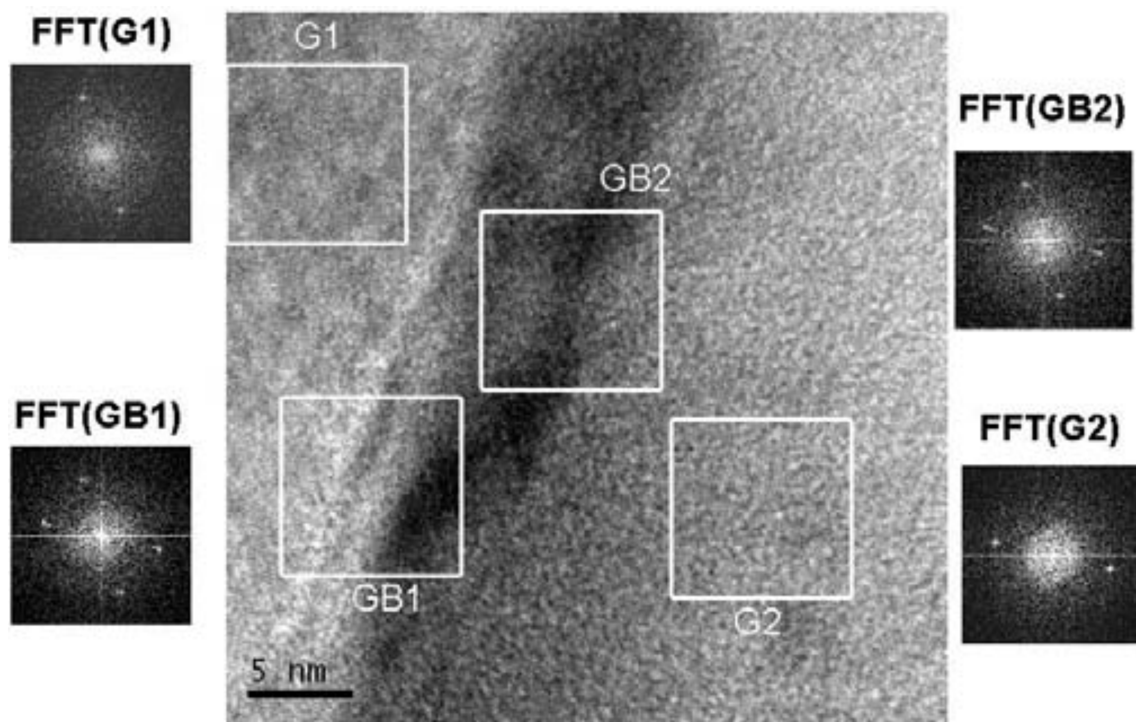

Figure 5: (a) Transmission electron microscopy (TEM) image of the $Ni_{0.56}Cu_{0.44}$ film annealed at T_{ANN} = 625 K, together with fast Fourier Transform (FFT) images of selected regions of the film. Remarkably, the FFT analyses corresponding to grain 1 (G1) and grain (G2) feature single spots located at the {111} interplanar distance (d_{111} ~ 0.2038 nm). Conversely, double-spots are clearly observed in FFT images GB1 and GB2, which correspond to the grain boundary region and include portions of grains 1 and 2. In particular, the emerging small inner spots in FFT(GB1) and FFT(GB2) correspond to a slightly larger interplanar distance, d_{111} ~0.2085 nm, indicating that the grain boundary region is enriched in Cu.

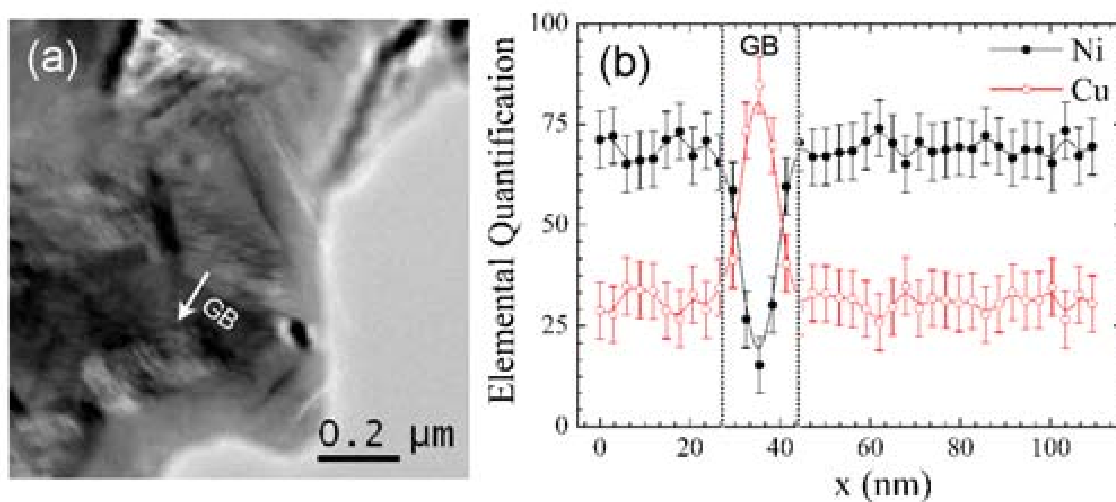

Figure 6: (a) Bright-field scanning transmission electron microscopy image of the $Ni_{0.56}Cu_{0.44}$ film annealed at T_{ANN} = 625 K; (b) elemental quantification (at% Ni and Cu), using electron energy loss spectroscopy EELS, following the white arrow highlighted in (a), which traverses a grain boundary (GB) region. The EELS analysis reveals that the GB region is a Cu-rich Ni-Cu solid solution, whereas the composition of the surrounding grains is concurrently depleted in Cu, indicating Cu grain boundary segregation.

3.2. Mechanical and magnetic properties of as-prepared and annealed films

The aforementioned thermally-induced structural changes occurring in $Ni_{1-x}Cu_x$ films cause a significant effect on the resulting mechanical and magnetic properties. The overall dependence of the Berkovich indentation hardness, H_B, on T_{ANN} for the different film compositions is plotted in Figure 7. The hardness of the as-deposited films decreases as the Cu content is increased, from 7.21 GPa (for x = 0) to 6.15 GPa (for x = 0.44). The hardness of pure Ni in the as-prepared state resembles the values reported in the literature for electrodeposited *nc* Ni when evaluated by nanoindentation,[64] but it is slightly larger than those obtained by conventional Vickers measurements.[65,66] This can be explained on the basis of the indentation size effect. Typically, due to strain gradient hardening, the hardness values estimated at low loads can be as much as 10 to 30% larger than the hardness that would be obtained for sufficiently large loads. In addition, even for comparable crystallize sizes, other effects such as impurity contents (e.g. sulphur), dissimilar degrees of porosity or residual stress can also affect the hardness, thus accounting for the dispersion in the values one can find in the literature.[67] It should be noted that the hardness values obtained in the *nc* $Ni_{1-x}Cu_x$ thin films investigated here are larger than those of microcrystalline or *nc* Cu thin films[68], which is not surprising bearing in mind that Ni is intrinsically harder than Cu.[69] However, the hardness of the *nc* $Ni_{1-x}Cu_x$ films is also considerably larger than the values in electrodeposited fine-grained pure Ni[70] as-deposited *nc* Ni-P or Ni-Cu-P films[71], coarse-grained Co-Ni alloys[72] or Ni-P-W

multilayered structures.[73] Hence, it is clear that not only the composition but also the microstructure plays a crucial role on the mechanical properties of the investigated materials. In particular, the main reason for the large H_B displayed by the electrodeposited $Ni_{1-x}Cu_x$ alloys is the saccharine-assisted crystallite size refinement during thin film growth. For small crystallite sizes, the role of grain boundaries in hindering dislocation motion is enhanced, resulting in an increase of stress concentration due to dislocation pile-up. This leads to the well-known Hall-Petch relationship, which postulates that the hardness is inversely proportional to the square root of grain size.[74] Intragranular nanotwins, like the ones shown in Figure 4 (c), also contribute to increase the hardness since twin boundaries can be considered analogous to high-angle grain boundaries in terms of disrupting dislocation motion.[75]

For certain applications of metallic thin films (e.g., wear resistant surface coatings or some MEMS/NEMS components like cantilevers, springs or microgears) it is desirable not only to prepare mechanically hard materials but also to be able to maintain these outstanding mechanical properties on usage and when eventually exposed to intermediate working temperatures. Figure 7 reveals that addition of Cu increases the temperature range within which *nc* $Ni_{1-x}Cu_x$ films exhibit large H_B values. Indeed, although H_B abruptly decreases in pure *nc* Ni films for T_{ANN} > 475 K, such a decrease occurs at much higher temperatures for $Ni_{1-x}Cu_x$ with x = 0.30 or 0.44. This can be mostly attributed to the different temperature interval where grain coarsening occurs in the series of investigated alloys (see Figure 2). The reduced Young's modulus, E_r, does not show pronounced variations as a function of temperature. The E_r values in as-deposited films range from 182 GPa (for x = 0) to 170 GPa (for x = 0.44) and slightly increase, by less than 10%, as T_{ANN} is raised.

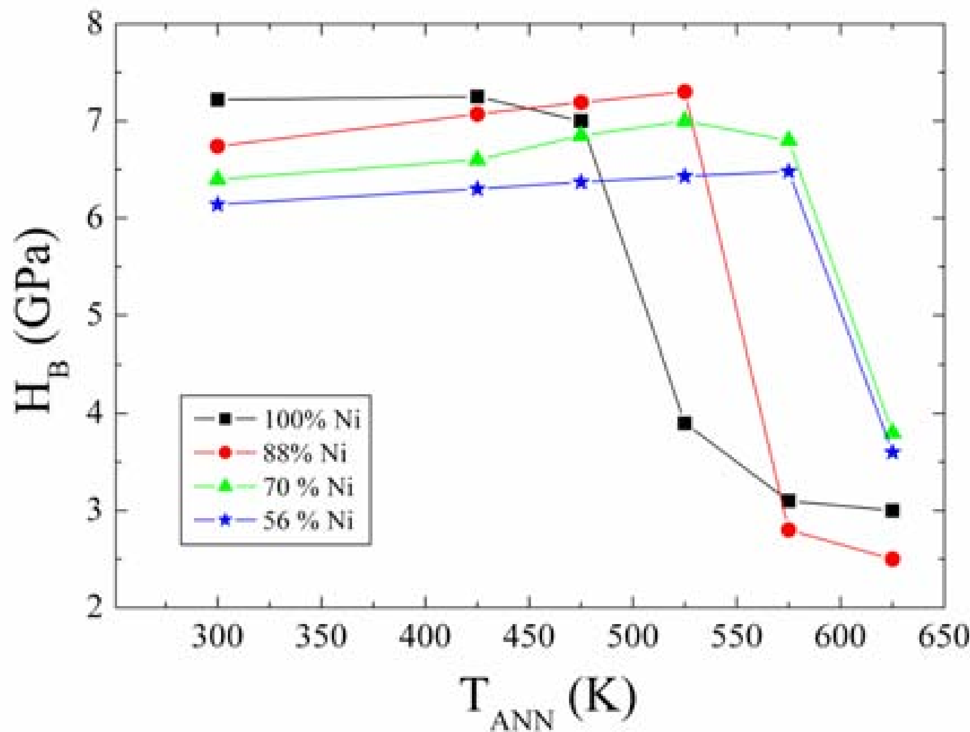

Figure 7: Dependence of Berkovich hardness, H_B, on the annealing temperature, T_{ANN}, for pure Ni (-■-), $Ni_{0.88}Cu_{0.12}$ (-●-), $Ni_{0.70}Cu_{0.30}$ (-▲-) and $Ni_{0.56}Cu_{0.44}$ (-★-) films. After annealing, H_B slightly increases for low annealing temperatures (due to the grain boundary relaxation). However, at sufficiently large T_{ANN} values, H_B significantly decreases owing to grain growth. Note that while for pure Ni H_B decreases already after heating to 525 K, for the $Ni_{0.70}Cu_{0.30}$ and $Ni_{0.56}Cu_{0.44}$ films H_B does not fall down until T_{ANN} = 625 K. Note that error bars would be included within the size of the symbols.

Another interesting observation, also from Figure 7, is that for all $Ni_{1-x}Cu_x$ films H_B slightly increases when the samples are annealed at relatively low temperatures. For example, H_B increases from 6.75 GPa to 7.30 GPa when the $Ni_{0.88}Cu_{0.22}$ alloy is annealed at 525 K, hence slightly surpassing the hardness of as-deposited *nc* Ni. Note that this behaviour is opposite to the one conventionally observed in metals, where annealing typically lowers material strength. However, an increase of hardness for low annealing temperatures has been occasionally encountered in some *nc* metallic systems prepared by electrodeposition or severe plastic deformation.[76-78] It has been argued that thermal annealing can lead to strengthening of *nc* metals due to structural relaxation of the non-equilibrium grain boundaries and a consequent depletion of available dislocation sources. Namely, as temperature is raised and the amount of microstrains decreases [see Figure 2(b)] it becomes progressively more difficult for such relaxed grain boundaries to emit dislocations under stress application, thus making the material more resistant to yielding. Thus, from our results it is clear that, in order to maximize hardness, it is ideal to achieve a *nc* material whose grain boundaries are virtually free from microstrains.

The magnetic behaviour of the $Ni_{1-x}Cu_x$ films is also markedly dependent on the annealing temperature. First, it is worth mentioning that only the samples with $x \leq 0.30$ are ferromagnetic at room temperature. Due to its large Cu content, the $Ni_{0.56}Cu_{0.44}$ alloy is paramagnetic, in agreement with the magnetic phase diagram reported in the literature for the Ni-Cu system.[79,80] As shown in Figure 8, the hysteresis loops of the remaining Ni-rich $Ni_{1-x}Cu_x$ films become progressively more tilted as T_{ANN} is increased. Remarkably, for the three compositions investigated here, a drastic variation in the shape of the loops occurs already at T_{ANN} = 425 K, even though the structural modifications at this low annealing temperature are scarce (see Figures 2 and 3). Particularly noticeable is the reduction in the remanence to saturation magnetization ratio, M_R/M_S, plotted in Figure 9(a) as a function of T_{ANN}. The rapid decrease of M_R/M_S with T_{ANN} is probably linked to the release of microstrains and the concomitant decrease of the domain wall energy, thus favouring self-demagnetizing effects, similar to what has been reported for permalloy annealed at intermediate temperatures.[81]

In turn, the coercivity, H_C, of the as-deposited films is lower for larger Cu contents. This cannot be attributed solely to variations in the crystallite size, as <D> is virtually independent of the composition of the films (Figure 2). Hence, changes in H_C are probably related to variations in the magnetocrystalline anisotropy. In fact, the magnetocrystalline anisotropy in the Ni-Cu system has been reported to increase with the Ni percentage.[82] Furthermore, for Ni contents around 70at% the Curie temperature should be close to room temperature,[80] which should further reduce the anisotropy. In any case, such reduced coercivity values, achieved by Cu alloying, are desirable in soft-magnetic micro-/nano-components. Figure 9(b) shows that H_C tends to increase for $T_{ANN} \geq 475$ K. This effect is probably related to the Cu grain boundary segregation since the emerging Cu-rich interfacial phase is paramagnetic at room temperature and, therefore, it tends to isolate the ferromagnetic $Ni_{1-x}Cu_x$ grains, thus reducing intergranular magnetic exchange interactions which are often detrimental in terms of coercivity. Finally, the overall Kerr signal, which is proportional to the surface saturation magnetization of the $Ni_{1-x}Cu_x$ films, does not show pronounced variations as a function of T_{ANN}, except for the $Ni_{0.70}Cu_{0.30}$ film, where an increase is observed for $T_{ANN} > 475$ K [see Figure 9(c)]. This has several implications. On the one hand, the result suggests that intermixing between the Cu seed layer and the $Ni_{1-x}Cu_x$ films does not extend throughout the overall film thickness (otherwise a reduction in the Kerr signal would be observed at high T_{ANN} values in pure Ni films). On the other hand, the increase of Kerr signal in the $Ni_{0.70}Cu_{0.30}$ film indicates that for this particular composition, the Ni-enrichment inside the grains, resulting from Cu

grain boundary segregation (as evidenced by EELS), surpasses the loss of magnetization which stems from the thermally-induced formation of the interfacial paramagnetic phase.

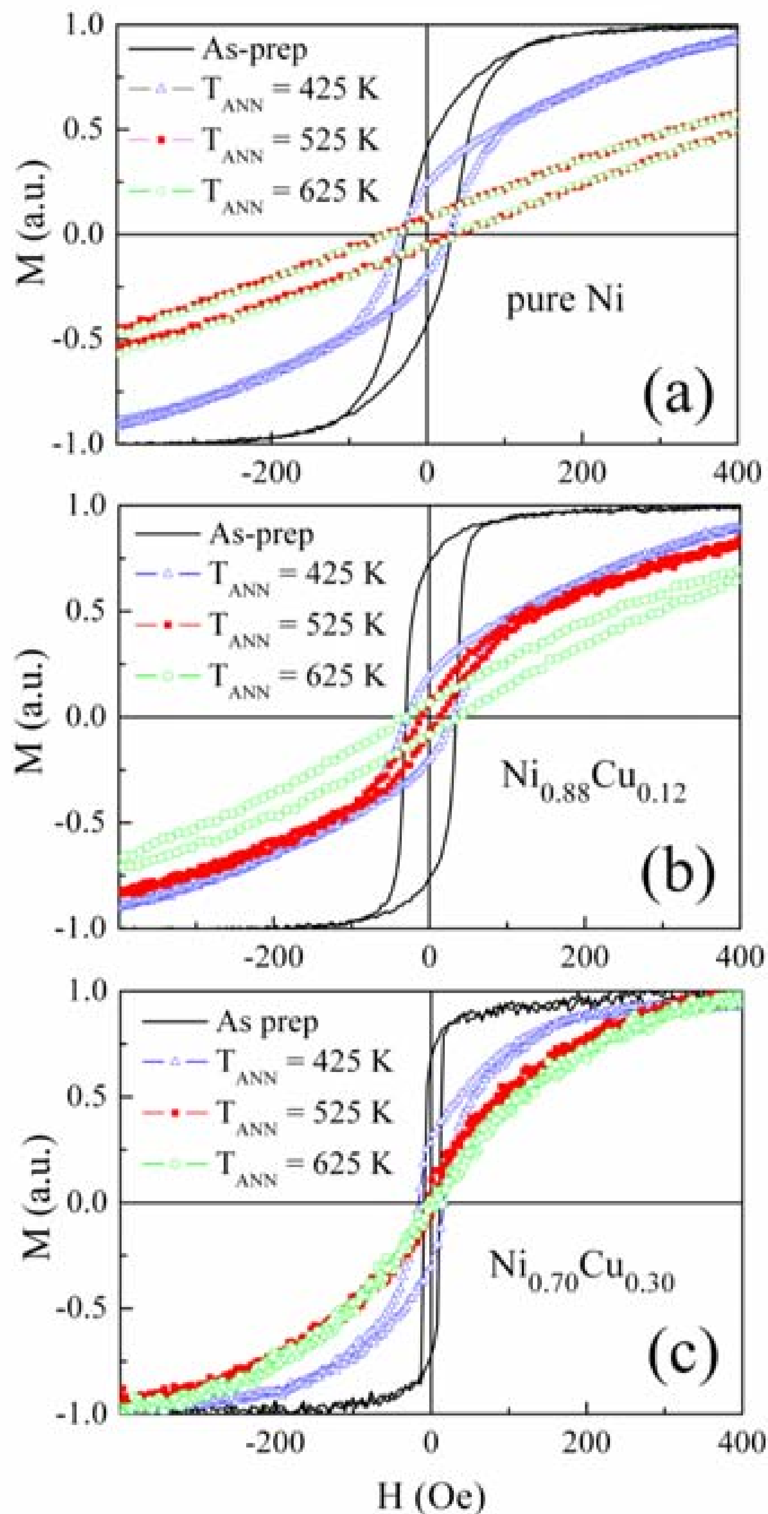

Figure 8: Hysteresis loops, measured in longitudinal configuration by magneto-optic Kerr effect, corresponding to (a) pure Ni, (b) $Ni_{0.88}Cu_{0.12}$ and (c) $Ni_{0.70}Cu_{0.30}$ films, in the as-deposited states (–) and after annealing at T_{ANN} = 425 K (-△-), T_{ANN} = 525 K (-■-) and T_{ANN} = 625 K (-○-). An obvious change in the magnetic properties is observed at relatively low annealing temperatures.

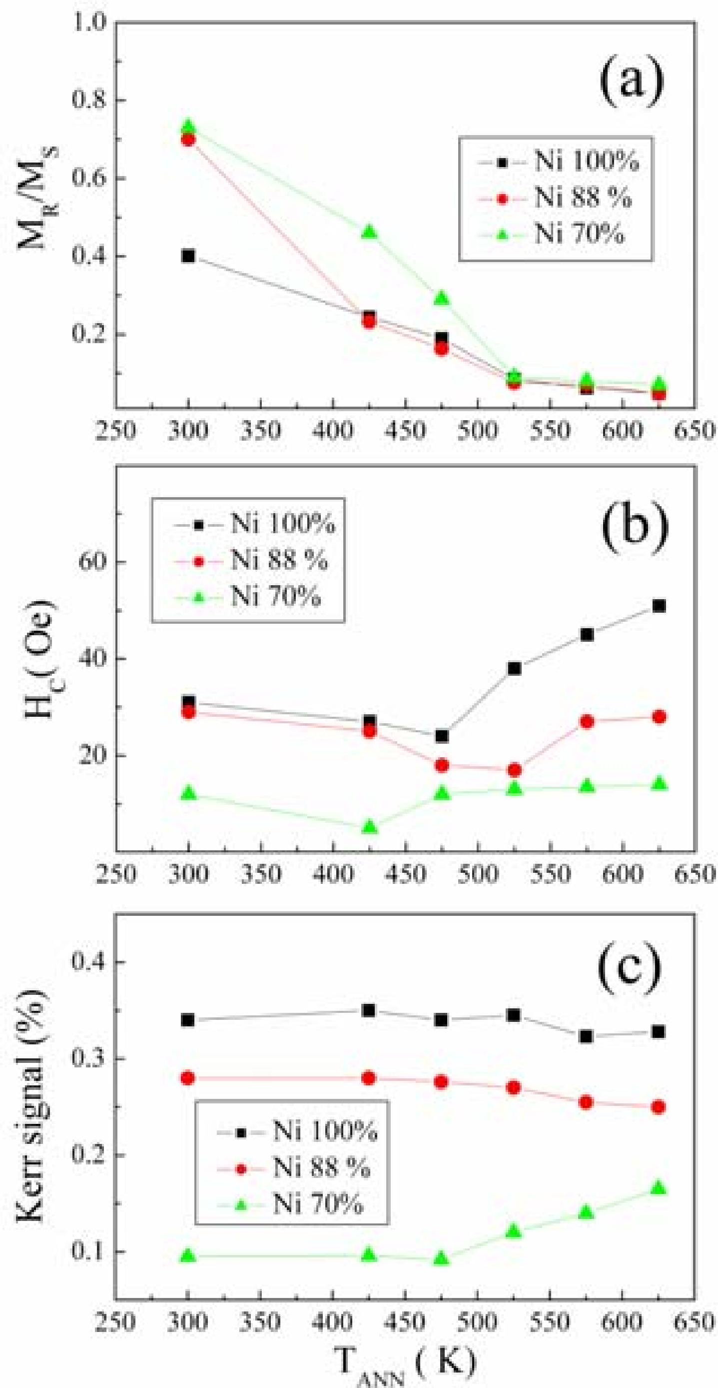

Figure 9: Dependence of (a) the remanence to saturation ratio, M_R/M_S, (b) the coercivity, H_C, and (c) the overall Kerr signal (proportional to the saturation magnetization) of pure Ni (-■-), $Ni_{0.88}Cu_{0.12}$ (-●-) and $Ni_{0.70}Cu_{0.30}$ (-▲-) films. Note that while M_R/M_S decreases with T_{ANN} (due to the decrease of microstrains), H_C tends to increase for T_{ANN} > 475 K, probably because of the grain coarsening and the formation of the non-magnetic Cu-rich phase, which tends to isolate ferromagnetic $Ni_{1-x}Cu_x$ grains, thus reducing magnetic dipolar interactions.

4. Conclusions

In summary, our work demonstrates that the thermal stability of electroplated *nc* Ni becomes considerably enhanced when Cu is added to the system to form a Ni-Cu solid solution. The composition of the Ni-Cu alloys can be precisely tailored by changing the applied current density during electrodeposition. The improved thermal stability is mainly ascribed to Cu grain boundary segregation that occurs during annealing. Since Ni and Cu have a positive enthalpy of mixing, the segregated Cu-rich layer stabilizes the *nc* structure against thermally-induced grain growth. As a consequence, the mechanical and some magnetic properties of $Ni_{1-x}Cu_x$ annealed films (for x = 0.30 or 0.44) are superior to those of annealed Ni. These results, apart from their fundamental interest, are also of technological relevance for the implementation of nanocrystalline metallic films in high-temperature applications. The electrochemically-controlled alloying of metallic species with positive enthalpy of mixing can pave the way to enhance the functionality of *nc* metallic films for a wide variety of assorted purposes.

Acknowledgements

The authors wish to thank the *Servei de Microscòpia* of the *Universitat Autònoma de Barcelona* and the *Serveis Científico-Tècnics* of the *Universitat de Barcelona* for the technical assistance during TEM and EELS characterization. We also acknowledge the Spanish MICINN (MAT2007-61629 and MAT2010-20616-C02) and the Catalan DGR (2009-SGR-1292) for partial financial support. E.P. is indebted to the Generalitat de Catalunya for the *Beatriu de Pinós* postdoctoral fellowship. M.D.B. acknowledges partial financial support from an ICREA-Academia Award.

References

[1] Gleiter, H. *Acta Mater*. **2000**, *48*, 1-29.

[2] McFadden, S. X.; Mishra, R. S.; Valiev, R. Z.; Zhilyaev, A. P.; Mukherjee, A. K. *Nature* **1999**, *398*, 684-686.

[3] Lu, K.; Lu, L; Suresh, S. *Science* **2009**, *324,* 349-352.

[4] Rajagopalan, J.; Han, J. H.; Saif, M. T. A. *Science* **2007,** *315*, 1831-1834.

[5] Zorman, C.A.; Mehregany, M. *Springer Handbook of Nanotechnology*, Part A. Chapter 11, Bhushan, B. (Ed.). Sringer-Verlag, Berlin-Heidelberg, 2010.

[6] Luber, E.; Mohammadi, R.; Ophus, C.; Lee, Z.; Nelson-Fitzpatrick, N.; Westra, K.; Evoy, S.; Dahmen, U.; Radmilovic, V.; Mitlin, D.; *Nanotechnol*. **2008**, *19*, 125705.

[7] Baghbanan, M.; Erb, U.; Palumbo, G. *Phys. Status Sol. (a)* **2006**, *203*, 1259-1264.

[8] Andrievski, R. A. *J. Mater Sci.* **2003**, *38*, 1367-1375.

[9] Krill, C. E.; Ehrhardt, H.; Birringer, R. *Z. Metallkund*. **2005**, *96*, 1134-1141.

[10] Kirchheim, R. *Acta Mater.* **2002**, *50*, 413-419.

[11] Darling, K. A.; VanLeeuwen, B. K.; Koch, C.C.; Scattergood, R. O. *Mater. Sci. Eng. A* **2010**, *527*, 3572-3580.

[12] Färber, B.; Cadel, E.; Menand, A.; Schmitz, G.; Kirchheim, R. *Acta Mater.* **2000**, *48*, 789-796.

[13] Weissmüller, J.; Krauss, W.; Haubold, T.; Birringer, R.; Gleiter, H. *Nanostruct. Mater.* **1992**, *1*, 439-447.

[14] VanLeeuwen, B. K.; Darling, K. A.; Koch, C. C.; Scattergood, R. O.; Butler, B. G. *Acta Mater.* **2010**, *58*, 4292-4297.

[15] Talin, A. A.; Marquis, E. A.; Goods, S. H.; Kelly, J. J.; Miller, M. K. *Acta Mater.* **2006**, *54*, 1935-1947.

[16] Eckert, J.; Holzer, J. C.; Johnson, W. L. *J. Appl. Phys.* **1993**, *73*, 131-141.

[17] Liu, F. *Mater. Lett.*, **2005**, *59*, 1458-1462.

[18] Michels, A.; Krill, C. E.; Ehrhardt, H.; Birringer, R.; Wu, D. T. *Acta Mater.* **1999**, *47*, 2143-2152.

[19] Detor, A. J.; Schuh, C. A. *Acta Mater.* **2007**, *55*, 4221-4232.

[20] Schlesinger, M.; Paunovic, M. *Modern Electroplating*. John Wiley & Sons, Pennington, 2000.

[21] Bicelli, L. P.; Bozzini, B.; Mele, C.; D'Urzo, L. *Int. J. Electrochem. Sci.* **2008**, *3*, 356-408.

[22] Wang, F.; Hosoiri, K.; Doi, S.; Okamoto, N.; Kuzushima, T.; Totsuka, T.; Watanabe T. *Electrochem. Commun.* **2004**, *6*, 1149-1152.

[23] Gómez, E.; Pellicer, E.; Duch, M.; Esteve, J.; Vallés, E. *Electrochim. Acta* **2006**, *51*, 3214-3222.

[24] Klimenkov, M.; Haseeb, A. S. M. A.; Bade, K. *Thin Solid Films* **2009**, *517*, 6593.

[25] Zhang, Y.; Ivey, D. G. *Chem. Mater.* **2004**, *16*, 1189-1194.

[26] Song, Y.; Zhang, S.; Li, J.; Zhao, C.; Zhang, X. *Acta Biomater.* **2010**, *6*, 1736-1742.

[27] Bartlett, P. N.; Ghanem, M. A.; El Hallag, I. S.; de Groot, P.; Zhukov, A. *J. Mater. Chem.* **2003**, *13*, 2596-2602.

[28] Younes, O.; Zhu, L.; Rosenberg, Y.; Shacham-Diamand, Y.; Gileadi, E. *Langmuir* **2001**, *17*, 8270-8275.

[29] Pellicer, E.; Varea, A.; Pané, S.; Nelson, B. J.; Menéndez, E.; Estrader, M.; Suriñach, S.; Baró, M. D.; Nogués, J.; Sort, J. *Adv. Funct. Mater.* **2010**, *20*, 983-991.

[30] Bahlawane, N.; Premkumar, P. A.; Tian, Z.; Hong, X.; Qi,; F.; Kohse-Höinghaus, K. *Chem. Mater.* **2010**, *22*, 92-100.

[31] Myung, N. V.; Park, D. Y.; Yoo, B. Y.; Sumodjo, P. T. A. *J. Magn. Magn. Mater.* **2003**, *265*, 189-198.

[32] Young, R. A. *The Rietveld Method*, Union of Crystallography. Oxford University Press, Oxford, 1995.

[33] Morales, M.; Chateigner, D.; Lutterotti, L. *Thin Solid Films* **2009**, *517*, 6264-6270.

[34] Warren, B. E. *X-ray Diffraction*, Addison-Wesley Reading, Massachusetts, 1969.

[35] Fischer-Cripps, A. C. *Nanoindentation*, Springer, New York, 2004.

[36] Oliver, W. C.; Pharr, G. M. *J. Mater. Res.* **1992**, *7*, 1564-1583.

[37] Sort, J.; Zhilyaev, A.; Zielinska, M.; Nogués, J.; Suriñach, S.; Thibault, J.; Baró, M. D. *Acta Mater.* **2003**, *51*, 6385-6393.

[38] Natter, H.; Schmelzer, M.; Hempelmann, R. *J. Mater. Res.* **1998**, *13,* 1186-1197.

[39] Boylan, K.; Ostrander, D.; Erb, U.; Palumbo, G.; Aust, K.T. *Scripta Metall. Mater.* **1991**, *25*, 2711-2716.

[40] Klement, U.; Erb, U.; El-Sherik, A.M.; Aust, K.T. *Mater. Sci. Eng. A* **1995**, *203*, 177-186.

[41] El-Sherik, A.M.; Boylan, K.; Erb, U.; Palumbo G.; Aust, K.T. *Mater. Res. Soc. Symp. Proc.* **1992**, *238*, 727-732.

[42] Cziráki, A.; Tonkovics, Zs.; Geröcs, I.; Fogarassy, B.; Groma, I.; Tóth-Kádar, E.; Tarnóczi, T.; Bakonyi, I. *Mater. Sci. Eng. A* **1994**, *179-180*, 531-535.

[43] Iordache, M.C.; Whang, S.H.; Jiao, Z.; Wang, Z.M. *Nanostruct. Mater.* **1999**, *11*, 1343-1349.

[44] Thuvander, M.; Abraham, M.; Cerezo A.; Smith, G.D.W. *Mater. Sci. Technol.* **2001**, *17*, 961–970.

[45] Yamamoto, Y.; Uemura, S.; Kajihara, M. *Mater. Sci. Eng. A* **2001**, *312*, 176-181.

[46] Wandelt, K.; Brundle, C. R. *Phys. Rev. Lett.* **1981**, *46*, 1529-1532.

[47] Abrikosov, I. A.; Skriver, H. L. *Phys. Rev. B* **1993**, *47*, 16532-16541.

[48] Ahmed, J.; Ramanujachary, K. V.; Lofland, S. E.; Furiato, A.; Gupta, G.; Shivaprasad, S. M.; Ganguli, A. K. *Colloid. Surf. A – Physicochem. Eng. Asp.* **2008**, *331*, 206-212.

[49] Randle, V. *Acta Mater.* **1999**, *47*, 4187-4196.

[50] Lu, L.; Chen, X.; Huang, X.; Lu, K. *Science* **2009**, *323,* 607-610.

[51] Ebrahimi, F.; Ahmed, Z.; Li, H. *Appl. Phys. Lett.* **2004**, *85*, 3749-3751.

[52] Velinov, V.; Vitkova, S.; Pangarov, P. *Surf. Technol.* **1977**, *6*, 19-29.

[53] Philipsen, P. H. T.; Baerends, E. J. *Phys. Rev. B* **1996**, *54*, 5326-5333.

[54] Czerwinski, F.; Li, H.; Megret, M.; Szpunar, J.A. *Scripta Mater.* **1997**, *37*, 1967-1972.

[55] Li, H.Q.; Ebrahimi, F. *Acta Mater.* **2003**, *51*, 3905-3913.

[56] Gonzalez, F.; Brennenstuhl, A.M.; Palumbo, G.; Erb, U.; Lichtenberger, P.C. *Mater. Sci. For.* **1996**, *83*, 225-227.

[57] Mehta, S.C.; Smith, D.A.; Erb, U. *Mater. Sci. Eng. A* **1995**, *204*, 227-232.

[58] Hibbard, G.D.; Aust, K.T.; Erb, U. *Mater. Sci. Eng. A* **2006**, *433*, 195-202.

[59] Rasuli, R.; Zad, A. I.; Ahadian M. M. *Vacuum* **2010**, *84*, 469-473.

[60] Kolobov, Y. R., Grabovetskaya, G. P.; Ivanov, M. B.; Zhilyaev, A. P.; Valiev, R. Z.; Scri*pta Mater*. **2001**, *44*, 873-878.

[61] Abrikosov, I. A.; Skriver, H. L. *Phys Rev B* **1993**, *47*, 16532-16541.

[62] Lee, B.J.; Shim, J. H. *Calphad* **2004**, *28*, 125-132.

[63] Turchanin, M. A.; Agraval, P. G.; Abdulov, A. R. *Powder Metall. Met. Ceram.* **2007**, *46*, 467-477.

[64] Schwaiger, R.; Moser, B.; Dao, M.; Chollacoop, N.; Suresh, S. *Acta Mater.* **2003**, *51*, 5159-5172.

[65] Hughes, G.D.; Smith, S.D.; Pande, C.S.; Johnson, H.R.; Armstrong, R.W. *Scripta Metall.* **1986**, *20*, 93-97.

[66] El-Sherik, A.M.; Erb, U.; Palumbo, G.; Aust, K.T. *Scripta Metall. Mater.* **1992**, *27*, 1185-1188.

[67] Koch, C.C.; Shen, T.D. in *Processing and Properties of Nanocrystalline Materials*, C. Suryanarayana et al., (eds), TMS, Warrendale, PA, **1996**.

[68] Dao, M.; Lu, L.; Asaro, R. J.; De Hosson, J. T. M.; Ma, E. *Acta Mater*. **2007**, *55*, 4041-4065.

[69] Samsonov, G. V. *Handbook of the physicochemical properties of the elements*, IFI-Plenum, New York, 1968.

[70] Lamovec, J.; Jović, V.; Randjelović, D.; Aleksić, R.; Radojević, V. *Thin Solid Films* 2008, 516, 8646-8654.

[71] Balaraju, J. N.; Rajam, K. S. *Surf. Coat. Technol.* **2005**, *195*, 154-161.

[72] Wang, L. P.; Gao, Y.; Xue, Q. J. *Appl. Suf. Sci.* **2005**, *242*, 326-332.

[73] Papachristos, V. D.; Panagopoulos, C. N.; Christoffersen, L. W.; Markaki, A. *Thin Solid Films* **2001**, *396*, 173-182.

[74] Dieter, G. E. *Mechanical Metallurgy*, 3rd Edition. McGraw-Hill Science/Engineering/Math, New York, 1986.

[75] Zhang, X.; Misra, A.; Wang, H.; Nastasi, M.; Embury, J. D.; Mitchell, T. E.; Hoagland, R. G.; Hirth J. P. *Appl. Phys. Lett.* **2004**, *84*, 1096-1098.

[76] Valiev, R. Z.; Sergueeva, A. V.; Mukherjee, A. K. *Scripta Mater.* **2003**, *49*, 669-674.

[77] Wang, Y. M.; Cheng, S.; Wei, Q. M.; Ma, E.; Nieh, T. G.; Hamza, A. *Scripta Mater.* **2004**, *51*, 1023-1028.

[78] Huang, X.; Hansen, N.; Tsuji, N. *Science* **2006**, *312*, 249-251.

[79] Ahern, S. A.; Martin, M. J. C.; Sucksmith, W. *Proc. R. Soc. Lond. A,* **1958**, *248*, 145-152.

[80] Ododo, J. C.; Coles, B. R. *J. Phys. F: Met. Phys.* **1977**, *7*, 2393-2400.

[81] Chikazumi, S. *Physics of Magnetism*, Chapter 12. R. E. Krieger Publishing Company, Malabar, 1978.

[82] Booth, J. G.; Wijn, H. P. J.; Zibold, G. (Landolt-Börnsteinin Wijn H. P. J. Ed.) *Numerical Data and Functional Relationships in Science and Technology*, Vol. 19 Magnetic Properties of Metals, Subvol. B. Springer-Verlag, Berlin, 1993.

5.3. Mechanical properties and corrosion behaviour of nanostructured Cu-rich CuNi electrodeposited films.

In this article, the mechanical properties and corrosion behaviour of nanocrystalline Cu-rich Cu-Ni alloy electrodeposited films have been investigated. To obtain Cu-Ni alloys with Cu contents ranging from 22 to 97 at% Cu, the bath used in the previous works has been reformulated. Namely, the [Ni(II)/Cu(II)] concentration ratio has been decreased to 11 while keeping the overall ion concentration (i.e., the ionic strength) constant.

For Cu contents below 70 at%, smooth and flat deposits are obtained. From the corresponding AFM images, PTV and RMS values confirm the role of saccharine as grain-refining agent while its action on deposits with Cu contents beyond 70 at% is limited at the used concentration (0.5 g/L). XRD patterns confirm the formation of a Cu-Ni solid solution. Rietveld analysis of XRD patterns shows that the crystallite size of the deposits is kept below 100 nm in all cases except for the Cu richest films. The calculated stacking fault probability decreases as Ni content increases, in agreement with the stacking fault energies of Cu and Ni metals (between 124 and 250 mJ/m^2 for Ni and between 55 and 78 mJ/m^2 for Cu).

Regarding mechanical properties, the values of H, E_r, and H/E_r and H^3/E_r^2 ratios of Cu-rich Cu-Ni deposits are shown together with the values of Ni-rich deposits presented in our previous articles. This allows us to depict the overall trend of mechanical properties for all range of compositions. The dependence of the normalized plastic energy, $(W_{tot} - W_{el})/W_{tot}$, on the H/E_r ratio has been found to follow a linear relationship in agreement with previous works from the literature.

Concerning corrosion performance in NaCl medium, it is observed that nc-Cu-rich Cu-Ni films display lower j_{corr} and more positive E_{corr} values than the bare substrate (Cu seed-layer), thus confirming the protective character of the here-prepared films. Interestingly, films with composition close to that of Constantan ($Cu_{0.55}Ni_{0.45}$) exhibit rather good corrosion resistance. The porosity of the films has been assessed in two different ways: i) from the E_r values determined by nanoindentation and ii) from the R_P values determined by potentiodynamic polarization. It is demonstrated that both evaluations lead to the same observation. Namely, porosity fraction (P) for Cu percentages lower than 70 at% is found to be negligible, whereas P is around 7% and 11% in deposits with Cu contents close to 90 at% and 97 at%, respectively.

International Journal of
ELECTROCHEMICAL
SCIENCE
www.electrochemsci.org

Mechanical properties and corrosion behaviour of nanostructured Cu-rich CuNi electrodeposited films

Aïda Varea [a], Eva Pellicer [a], Salvador Pané [b], Bradley J. Nelson [b], Santiago Suriñach [a], Maria Dolors Baró [a] and Jordi Sort [c]*

[a]Departament de Física, Facultat de Ciències, Universitat Autònoma de Barcelona, E-08193 Bellaterra, Spain.

[b]Institute of Robotics and Intelligent Systems (IRIS), ETH Zurich, CH-8092 Zurich, Switzerland.

[c]Institució Catalana de Recerca i Estudis Avançats (ICREA) and Departament de Física, Universitat Autònoma de Barcelona, E-08193 Bellaterra, Spain.

* Corresponding author: aida.varea.espelt@gmail.com

Phone: +0034 93 5811401. Fax: +0034 93 5812155

Abstract

Nanocrystalline Cu-rich CuNi alloy thin films (with copper contents ranging from 22 to 97 at%) have been grown by electrodeposition, using galvanostatic conditions, in an electrolytic bath containing Ni and Cu sulphates with a [Ni(II)]/[Cu(II)] molar ratio to 11. The Cu content is tuned by varying the applied current density during deposition. The nanoscrystalline nature of Cu-rich CuNi thin films has been achieved using saccharine as a grain refinement agent, although for the highest Cu contents (> 90 at%) the refinement effect is less pronounced. Due to nanocrystalline character of the films, low surface roughness, good compactness, and outstanding mechanical properties (e.g. nanoindentation hardness values around 7 GPa) are obtained, particularly for Cu percentages below 70 at%. The presence of stacking faults also contributes to the observed high strength. The films show good corrosion protective behaviour in 3.5 wt% NaCl medium, with corrosion potentials more positive than the bare substrate (pure-Cu) and lower corrosion current density values, ranging from 1.8 to 5.4 μA/cm^2.

Keywords: CuNi, electrodeposition, nanocrystalline, mechanical properties, corrosion.

1. INTRODUCTION

Owing to their outstanding properties, pure copper and copper-rich alloys are being extensively used in a wide range of technological and metallurgical applications. The combination of high electrical and thermal conductivities has prompted, for example, the utilization of these materials in microelectronic devices and integrated circuits [1]. Furthermore, Cu is mechanically softer and shows better ductility than many others metals. This is advantageous in terms of mechanical workability and permits the manufacture of microwires and a variety of devices with small lateral sizes. However, a large hardness may be desirable in certain applications, for example when Cu has to be subject to high tension in a welding. In principle, one can increase Cu strength by reducing the grain size (i.e., work hardening) or by alloying it with another metal. Depending on the alloying element, there are basically two mechanisms that cause mechanical hardening: (i) solid solution strengthening (Cu-Zn, Cu-Mn, Cu-Ni or Cu-Si) [1,2], and (ii) precipitation hardening (Cu-Be, Cu-Cr or Cu-Zr) [2].

The binary Cu-Ni system constitutes one of the most appealing Cu-based alloys due to its superior and tuneable mechanical properties together with an outstanding corrosion resistance. In particular, Cu-rich CuNi alloys have been used for many years in sea water environments, where they offer high resistance against bio-fouling [3]. Some CuNi alloys serve also as heat exchanger tube materials in coolant systems of nuclear power plants [4]. Additionally, Ni-rich CuNi deposits (i.e., for Ni contents larger than 70 at.%) are known to become ferromagnetic [5].

Nowadays, with the advent of nanotechnology, new applications are being developed which often require novel or improved properties that only nanostructured or nanocrystalline materials can provide [6-8]. Nanostructured CuNi alloys can be fabricated by different methods: sputtering, severe plastic deformation or electrodeposition (ED), among others. ED offers several advantages as compared to other deposition techniques: it consists of a rather simple and cost-effective setup that can work without the need of high vacuum or high temperature conditions, samples can be grown at high deposition rates, there are no limitations concerning the substrate geometry, and films of several hundreds of microns in thickness can be easily prepared [9]. In addition, ED also allows precise

tailoring of the alloy composition (and, consequently, of the resulting mechanical, magnetic and corrosion properties), simply by varying the working potential or the applied current density during film growth. Moreover, the deposition can be performed onto a wide variety of substrate shapes, including pre-patterned substrates, thus rendering ED an adequate technique to fabricate micro-/nano-electromechanical systems (MEMS/NEMS) with complex geometries.

In previous works we have reported the mechanical properties, corrosion resistance and thermal stability of nanocrystalline electrodeposited Ni-rich Cu_xNi_{1-x} alloys ($0.13 \leq x \leq 0.55$) [5,10,11]. In this article, instead, we explore the Cu-rich region of the phase diagram ($0.22 \leq x \leq 0.97$). One of the drawbacks usually encountered in the ED of CuNi alloys with high Cu content is that Cu tends to exhibit a dendritic growth and it is thus difficult to obtain flat surfaces. Nevertheless, the dendritic growth can be avoided to a certain extent if suitable complex bath formulations are employed [12-14]. The resulting films with flat surfaces, which would be appropriate for their implementation in MEMS/NEMS, show good wear resistance combined with excellent anti-corrosion properties.

2. EXPERIMENTAL

2.1. Instrumentation

A three-electrode cell connected to a PGSTAT120 Autolab potenciostat/galvanostat (Ecochemie) has been used. A double junction Ag|AgCl (E = +0.210V/SHE) acted as reference electrode (RE) (Metrohm AG) with 3M KCl as the inner solution and 1M Na_2SO_4 as the outer solution. A Pt sheet served as counter electrode (CE). A vitreous carbon cylindrical rod with $\pi \cdot 10^{-2}$ cm^2 surface area was used as working electrode (WE) for cyclic voltammetry (CV) studies, whereas silicon (100) substrates, with e-beam evaporated Ti (25 nm)/Cu (250 nm) adhesion/seed layers, were the WE for deposit growth. The working area ranged between (0.25 ± 0.01) cm^2 and (0.30 ± 0.01) cm^2.

2.2. Chemicals, Reagents and Solutions

The electrolytic solution (50 mL) was prepared based on a modification of Green's bath with Milipore MilliQ water (MQ-water). The solution contained 174g/L $NiSO_4 \cdot 6H_2O$, 16

g/L $CuSO_4·5H_2O$ (i.e., a [Ni(II)]/[Cu(II)] molar ratio of approximately 11), 87 g/L sodium citrate as a complexing agent, 0.2 g/L sodium dodecylsulfate as wetting agent and 0.5 g/L saccharine as refinement agent. The pH was fixed at 4.5 with addition of NaOH, and the working temperature was set at 303 K.

2.3. Electrode preparation

Before thin film deposition, substrates were degreased with acetone followed by isopropyl alcohol and MQ-water, and finally dipped in 1M H_2SO_4 to remove any oxides and organic residues. The electrolyte was de-aerated with argon gas before each experiment.

2.4. Procedure

An initial CV study was performed with the aim of establishing the current densities window suitable for the deposition of CuNi alloys with tuneable composition. A single cycle was run in each experiment, at a scan rate of 50 mV/s. The potential was swept from 0.25 V towards different cathodic limits and then the scan was reversed towards the positive direction. Galvanostatic electrodeposition was run with applied current densities between -12 and -44 mA/cm^2 under mild stirring (200 rpm) using a magnetic stirrer bar. The galvanostatic mode with variable values of current density allowed us to control the alloy composition, as well as the amount of charge (i.e., the thickness of the deposits). The thickness of CuNi layers was measured to be around 3 μm.

2.5. Characterization

Sample morphology and roughness of each sample were examined by scanning electron microscopy (SEM), using a Zeiss EVO® MA 10 microscope and a Zeiss MERLIN field emission scanning electron microscope (FE-SEM), and by atomic force microscopy (AFM) using a Dual Scope™ C-26 system (Danish Micro Engineering) operating in AC mode. The AFM scanned surface area was 5 x 5 $μm^2$. Chemical composition of the samples was determined by energy dispersive X-ray spectroscopy (EDXS). The structure of the deposits was studied by X-ray diffraction (XRD). XRD patterns were recorded on a Philips X'Pert diffractometer using $CuK_α$ radiation and θ-2θ configuration with 2θ in the range of 30 – 60º, 0.03º step size and 10 s holding time. Cell parameter, crystallite sizes, microstrains

and stacking fault probability were evaluated by fitting the XRD patterns using the Materials Analysis Using Diffraction (MAUD) Rietveld refinement program [15].

The mechanical properties of the films were evaluated by nanoindentation, operating in the load control mode, using an UMIS device from Fischer-Cripps Laboratories equipped with a Berkovich pyramidal-shaped diamond tip. The maximum applied force was 10 mN and the thermal drift was kept below 0.05 nm/s. Following data acquisition of the load-displacement curves, proper corrections were applied for the initial penetration depth, tip blunting and instrument compliance. Hardness, H, and reduced Young's modulus, E_r, were then evaluated using the method of Oliver and Pharr [16]. The ratios H/E_r and H^3/E_r^2, related to the wear resistance and the resistance to plastic deformation, were also calculated. The elastic indentation energy, W_{el}, was determined as the area between the unloading indentation segment and the displacement axis, whereas the total indentation energy, W_{tot}, was estimated from the area underneath the loading indentation segment. The plastic energy, W_{pl}, was then evaluated as the difference ($W_{tot} - W_{el}$).

Corrosion tests were performed in NaCl (3.5 wt%) solution at room temperature. Three-electrode cell configuration was used with a platinum sheet as CE and a Ag|AgCl RE containing 1M NaCl as outer solution. Once the sample was introduced into the solution, the open circuit potential, E_{OCP}, was achieved after 3 - 4 h of immersion. We consider that the system became stabilized when the potential fluctuations were smaller than 10 mV/h. Potentiodynamic polarization scans were performed from (E_{OCP} – 300) mV to (E_{OCP} + 300) mV with a scan rate of 0.1 mV/s, for an exposed area of 0.25 cm^2.

3. RESULTS AND DISCUSSION

3.1. CuNi thin film preparation

The CV curves recorded from the electrolytic solution are shown in Fig. 1a. One can observe that Cu discharge starts at more positive potentials (around -0.10 V) than nickel deposition (around -0.85 V), as expected due to the nobler character of Cu. Moreover, when the potential is sufficiently cathodic to permit the Ni discharge, the absolute value of the current density steeply increases, indicating that incorporation of significant amounts of Ni into the deposits occurs rapidly within a relatively narrow potential range. In the anodic scan, different oxidation responses are observed depending on the applied cathodic

limit. For the lowest cathodic limit, a single oxidation peak appears in the anodic sweep, probably related to the oxidation of previously deposited almost pure Cu. At larger cathodic limits a second oxidation peak, located at more positive potentials, develops. This feature is clearly related to the incorporation of Ni in the deposit formed during the cathodic sweep. The double-oxidation peak could indicate the formation of a two-phase deposit with dissimilar chemical composition. According to the results gleaned from the CV study, suitable range of working current densities are chosen for the subsequent deposition of Cu-rich CuNi alloys.

Galvanostatic curves for CuNi deposition at current densities between -12 mA/cm^2 and -44 mA/cm^2 are shown in Fig. 1b. The selected current densities yield CuNi deposits with different composition. EDX analysis reveals that Cu content is varied from 22 at% (at the lowest applied current density) to 97 at% (at the highest applied current density). Such a large variation can be ascribed to the different factors that limit the deposition of Cu and Ni. Namely, Cu discharge is diffusion-controlled, whereas deposition of Ni is charge transfer-controlled. Therefore, deposits with higher Ni contents are progressively obtained at higher overpotentials. Pure Cu deposits are not attained from this bath since very little amounts of Ni (1-3 at%) enter the deposits despite using very low current densities.

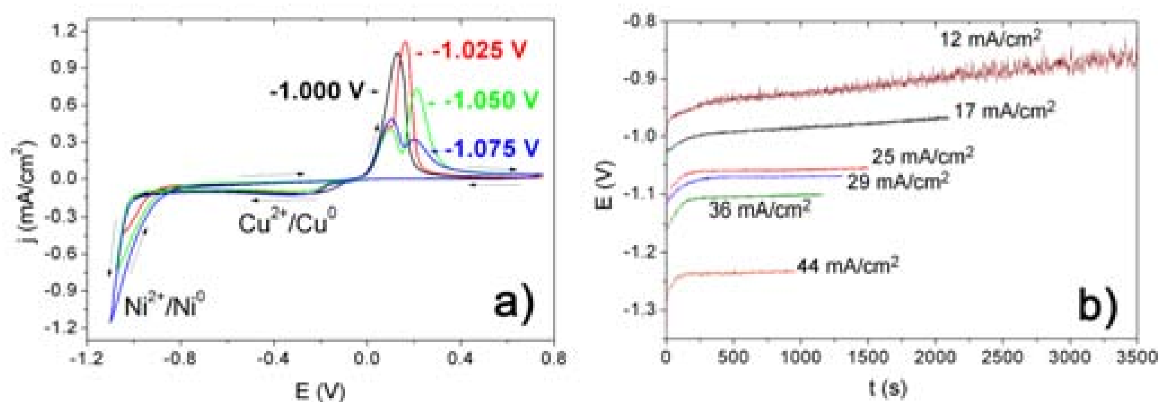

Figure 1: a) Cyclic voltammetry curves obtained at different cathodic limits between -1.000 and -1.075 V, at a scan rate of 50 mV/s. b) Galvanostatic curves for CuNi deposition at the indicated values of applied current densities.

3.2. Morphological and structural characterization

In our previous work [5,10,11] the effect of saccharine in reducing the surface roughness in Ni-rich Cu_xNi_{1-x} ($0.13 \leq x \leq 0.55$, atomic content) alloy films, obtained from an electrolytic solution with a [Ni(II)]/[Cu(II)] molar ratio of 29, was investigated. However, we failed in obtaining flat and smooth Cu-rich samples from that bath formulation. A decrease of the [Ni(II)]/[Cu(II)] molar ratio to 11 has permitted the growth of flat deposits with higher Cu contents, within the range $0.22 \leq x \leq 0.97$. SEM images (Fig. 2a-c) of film's surface indicate two different types of morphology depending on the Cu content. At very high Cu percentages (Fig. 2a) cauliflower-like deposits are obtained. For percentages below 70 at%, instead, the grain morphology cannot be resolved by conventional SEM imaging. An extremely fine-grained morphology was revealed using a FE-SEM microscope (Fig. 2c-inset). From the corresponding AFM images (Fig. 2d-f), the peak-to-valley (PTV) and root-mean-square (RMS) values were evaluated (Table 1). The PTV and RMS are around 300 nm and 50 nm, respectively, for the sample with $x = 0.97$, while a sharp decrease of both parameters is observed for lower Cu contents. Hence, we can conclude that the new bath formulation permits the fabrication of very smooth thin films with Cu contents $x \leq 70$ at%. It is well known that organic additives, such as saccharine, can change the microstructure of Cu/Ni multilayers, avoiding the grain growth and favouring grain refinement [17]. Similarly, saccharine causes surface smoothing in CuNi alloys prepared from the Ni-rich bath formulation [5,10,11]. The saccharine concentration used in the present study still works fine for deposits with $x \leq 70$ at% Cu but seems not appropriate to induce the deposition of flat deposits for higher Cu contents. Actually, deposits featuring Cu contents between 70 and 90 at% are not easy to obtain from this bath. Namely, while at low current densities Ni enters the deposits to a low extent (3 at% Cu for $j = -12$ mA/cm^2), just a little increase in the applied current density gives rise to a large incorporation of Ni into the deposits (30 at% Cu for $j = -22$ mA/cm^2). This result is in agreement with the rather sharp increase in the current density values attributed to Ni discharge observed in the CV experiments (Fig. 1a).

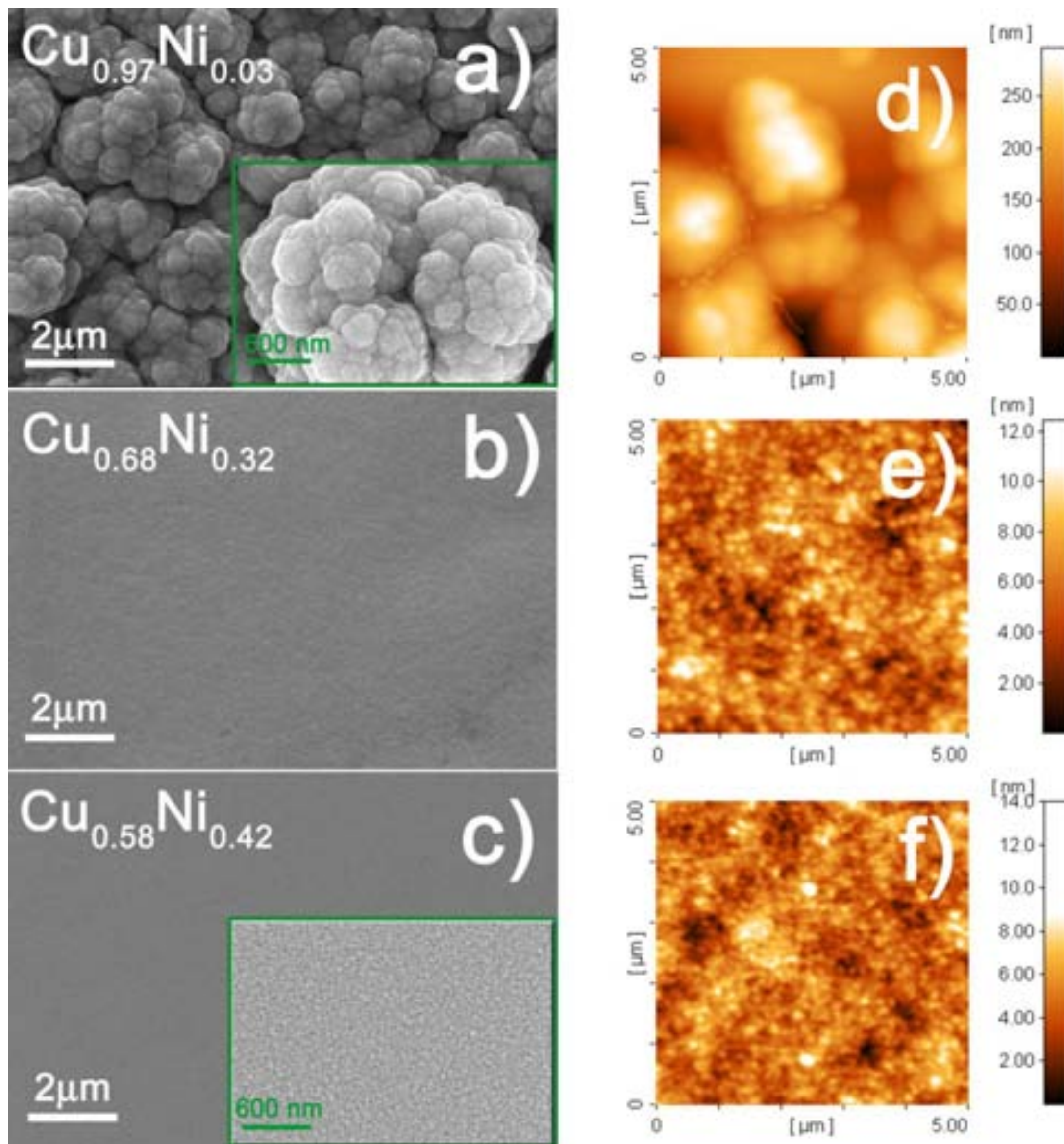

Figure 2: SEM (a-c) and corresponding AFM (d-f) images of CuNi alloys with different Ni content. Inset images in a) and c) show magnified details of sample surface obtained with a FE-SEM.

Fig. 3 shows the XRD patterns of CuNi films with dissimilar Cu content (97, 68 and 46 at%). Notice that (111) and (200) fcc reflections shift towards higher angles as Cu content is decreased, indicating an increase of the cell parameter, in agreement with the Vegard's law. Simultaneously, a peak located at the angular position corresponding to pure-Cu (2θ = 43.3º) is also observed. This reflection corresponds to the Cu seed layer, that for high Cu contents becomes masked by the (111) fcc CuNi alloy reflection. Another important feature is the difference in width between the (111) and (200) peaks, which is indicative of the presence of stacking faults. The cell parameter, a, crystallite size, <D>, microstrains, $<\varepsilon^2>^{1/2}$, and stacking fault probability, α_{SF}, evaluated by Rietveld fitting are listed in Table

1. Crystallite size is kept below 100 nm for the complete range of compositions. Films with the highest Cu content (≥ 90 at.%) show the largest crystallite sizes, while values at around 40 nm are observed in all the other films independently of Cu content. Such difference in crystallite sizes is in agreement with the morphological differences observed among the different samples. As aforementioned, for very large Cu contents, effective nanostructuring is not accomplished and therefore the crystallite size falls within the fine-grained regime.

The MAUD software used for the Rietveld refinement of the XRD patterns includes the Warren's formalism to evaluate the stacking fault (SF) probability, α_{SF} [18]. According to Warren's description of SF, $1/\alpha_{SF}$ designates the average number of planes between two consecutive SF. The α_{SF} values in the Cu-rich CuNi films are of the order of 0.01 – 0.015 (Table 1) hence, on average, one stacking fault should be present every each 60-100 atomic planes. Since the crystalline size of our samples is about 40 nm, this means that a large fraction of grains are likely to include one or even two intragranular stacking faults. In the Ni-rich films, values of α_{SF} around 0.007 and 0.008 were obtained [5], therefore lower than for the here-prepared Cu-rich CuNi films. The difference of α_{SF} with composition could be understood taking into account that the stacking fault energy (SFE) is higher for Ni than for Cu (i.e., it ranges between 124 and 250 mJ/m^2 for Ni [19, 20] and between 55 and 78 mJ/m^2 for Cu [20, 21]). Therefore, an increase of Ni content in CuNi deposits probably increases the SFE and, consequently, it would reduce the stacking fault probability, as experimentally observed. However, even for similar CuNi compositions α_{SF} is higher for the samples prepared in this work than in the Ni-rich samples fabricated in [5]. For example $Cu_{0.55}Ni_{0.45}$ and $Cu_{0.44}Ni_{0.56}$ in [5], showed α_{SF} values around 0.008, while for the $Cu_{0.46}Ni_{0.54}$ sample herein investigated α_{SF} is 0.013. Such a discrepancy could stem from the different values of applied current densities used in both studies. Namely, near-stoichiometric samples in [5] were grown at a lower current density (10 mA/cm^2) than the analogous samples fabricated in this work (36 mA/cm^2). Higher current density implies faster deposition rates and this could lead to higher density of intragranular nanotwins and other types of planar defects, as observed experimentally in electrodeposited Cu films [22].

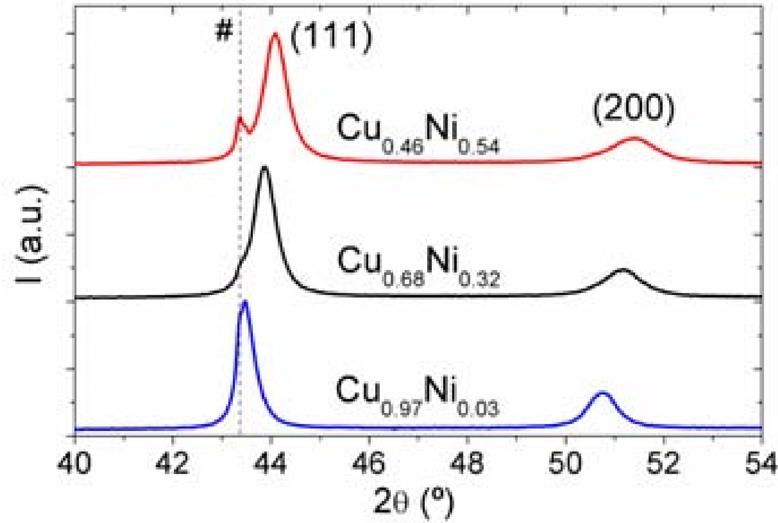

Figure 3: XRD patterns in the 40° – 54° 2θ region of CuNi samples with dissimilar copper content. The peak denoted by # belongs to the Cu seed layer.

Specimen composition	a (Å) [±10⁻⁴ Å]	<D> (nm)	$<\varepsilon^2>^{1/2}$ [±10⁻⁴]	α_{SF} [±5·10⁻³]	PTV (nm)	RMS (nm)
$Cu_{0.97}Ni_{0.03}$	3.5836	90 ± 7	0.0010	0.015	309	52
$Cu_{0.68}Ni_{0.32}$	3.5690	39 ± 3	0.0017	0.010	13	2
$Cu_{0.46}Ni_{0.54}$	3.5602	44 ± 3	0.0018	0.013	28	2

Table 1: Structural data obtained from XRD Rietveld refinement (lattice parameter a, crystallite size <D>, microstrains $<\varepsilon^2>^{1/2}$ and stacking fault probability α_{SF}) and AFM topological analysis (peak-to-valley value, PTV, and root-mean-square value, RMS).

3.3. Mechanical Properties

The mechanical properties of the films prepared in this work are plotted as a function of the Cu percentage in Fig. 4. For comparison, our previous results on Ni-rich CuNi films [5] are also included. Both the hardness, H, and the reduced Young's modulus, E_r, progressively decrease with an increase of the Cu content. The hardness varies from 7.9 GPa to 2.3 GPa and E_r from 198 GPa to 111 GPa as the Cu content is increased from 12 to 97 at%. The values of hardness in Cu-richest CuNi alloys are in rather good agreement with those obtained, for example, in Cu-based alloys reinforced with Ni particles [23] or in

fine-grained electroplated Cu films [24]. Remarkably, large hardness values are obtained for intermediate or low Cu percentages ($H \approx 7$ GPa), where the films exhibit a truly nanocrystalline microstructure. These films show comparable hardness values to those of electroplated nanocrystalline Ni-W alloys [25], nanocrystalline Ni-Co films [26] or nano-multilayered Cu-Ni films [27].

Several factors can have an influence on the observed hardness variations. First, except for very low strain rates, plastic deformation in nanocrystalline Cu is generally dominated by dislocation propagation inside the crystals rather than grain boundary sliding [28]. Consequently, larger H values are expected as the crystallite size is reduced towards the sub-100 nm range since in this case the amount of grain boundaries, which act as disruption sites for dislocation motion, becomes progressively higher (an effect often referred to as Hall-Petch) [29]. In this sense, the large amounts of stacking faults can also contribute to hardness because intragranular nanotwins hinder dislocation propagation in a similar way as high-angle grain boundaries [29,30]. Note that the decrease of H for Cu percentage larger than 90 at% can be thus attributed to the observed coarsening of the microstructure (Fig. 2). Besides grain size effects, it is well known that pure Ni exhibits higher yield stress, s_y, than Cu [31]. Hence, since $H \approx 3s_y$, the overall increase of H with de Ni percentage can be also ascribed to solution hardening [1,2].

Fig. 4b shows the variation of the reduced Young's modulus, E_r, on the Cu content. The reduced Young's modulus takes into account the elastic displacements that occur in both the specimen, with Young's modulus E and Poisson's ratio ν, and the diamond indenter, with elastic constants E_i and ν_i. The relationship between E_r and E can be expressed as follows [16]:

$$\frac{1}{E_r} = \frac{1-\nu^2}{E} + \frac{1-\nu_i^2}{E_i} \qquad \text{(Eq. 1)}$$

For diamond, E_i = 1140 GPa and n_i = 0.07. Note that, because of the high Young's modulus of the tip and its low Poisson's ratio, E_r is typically very similar to E for most metallic materials (for CuNi films E is about 1-2 GPa higher than E_r). Since the Young's modulus of electrodeposited polycrystalline Ni (200 GPa [32]) is higher than of Cu (130 GPa [33]), a progressive decrease of E_r could be actually anticipated as the Cu content becomes progressively larger, as indicated with the discontinuous line in Fig. 4b. The good agreement between the expected values of E_r (dotted line) and the experimental data, indicates that these samples do not exhibit appreciable porosity, particularly for Cu contents below 70 at%. Actually, it is well-known that even a low degree of porosity

typically leads to a drastic reduction in E [34, 35]. This can explain the pronounced decrease of E_r observed in Fig. 4b for Cu percentages higher than 70 at%. In a first approximation, the influence of porosity on the Young's modulus can be modelled using the approach of Ramakrishan and Arunachalam, which takes into account the intensification of pressure at the surface of spherical pores due to interactions between the pores and the surrounding bulk solid material [35]. For a given porosity fraction, P, the Young's modulus of the porous material, E_{porous}, is related to the Young's modulus of the fully dense material, E_{bulk}, according to [34, 35]:

$$\frac{E_{porous}}{E_{bulk}} = \frac{(1-P)^2}{1+2P-3\nu P} \qquad \text{(Eq. 2)}$$

where n is the Poisson's ratio of the bulk non-porous material (around 0.33 for CuNi in the investigated Cu-rich compositional range). Using Equations 1 and 2, the porosity level for Cu percentages lower than 70% is found to be virtually zero, whereas P attains values of around 7% and 11% for Cu contents of 90 and 97 at%, respectively.

From further analysis of the nanoindentation data, one can estimate additional mechanical parameters such as the H/E_r, which is related to the wear resistance [36,37] (Fig. 4c), or the H^3/E_r^2 ratio, related to the resistance against plastic deformation [38]. In most of the investigated films H/E_r tends to a constant value of around 0.04, except for Cu content beyond 90 at%, where H/E_r is clearly lower, mainly because of the larger crystallite size. However, as shown in Fig. 4d, H^3/E_r^2 increases with the increase in the Ni content, in a similar way as H. This is in agreement with the higher resistance against plastic deformation of Ni when compared to Cu, which typically shows better ductility.

From the analysis of the area of the load-unload nanoindentation curves, the total work of nanoindentation, W_{tot}, and the work recovered during unloading, W_{el}, can be also determined. The ratio W_{el}/W_{tot} gives an estimation of the elastic recovery of the films [39] and it is an important parameter for impact loading applications. This ratio indicates how much energy is released from the material after being loaded and it was found to decrease with the Cu percentage in the films. Although no direct correlation exists between the elastic recovery and hardness, finite element simulations of nanoindentation curves for a wide variety of elastic-plastic materials allowed to establish the following relationship [40,41]:

$$\frac{W_{tot}-W_{el}}{W_{tot}} \cong 1-5\frac{H}{E_r} \qquad \text{(Eq. 3)}$$

As shown in Fig. 5, if $\frac{W_{tot} - W_{el}}{W_{tot}}$ is plotted against H/E_r a linear relationship is obtained and the slope fits rather well with the expected value, in agreement with other results in electroplated Co-Ni films [42]. Note that $W_{tot} - W_{el}$ refers to the plastic energy during nanoindentation, W_{pl}, and it increases with the Cu content, indicating larger plasticity in the Cu-rich CuNi films than in the Ni-rich ones.

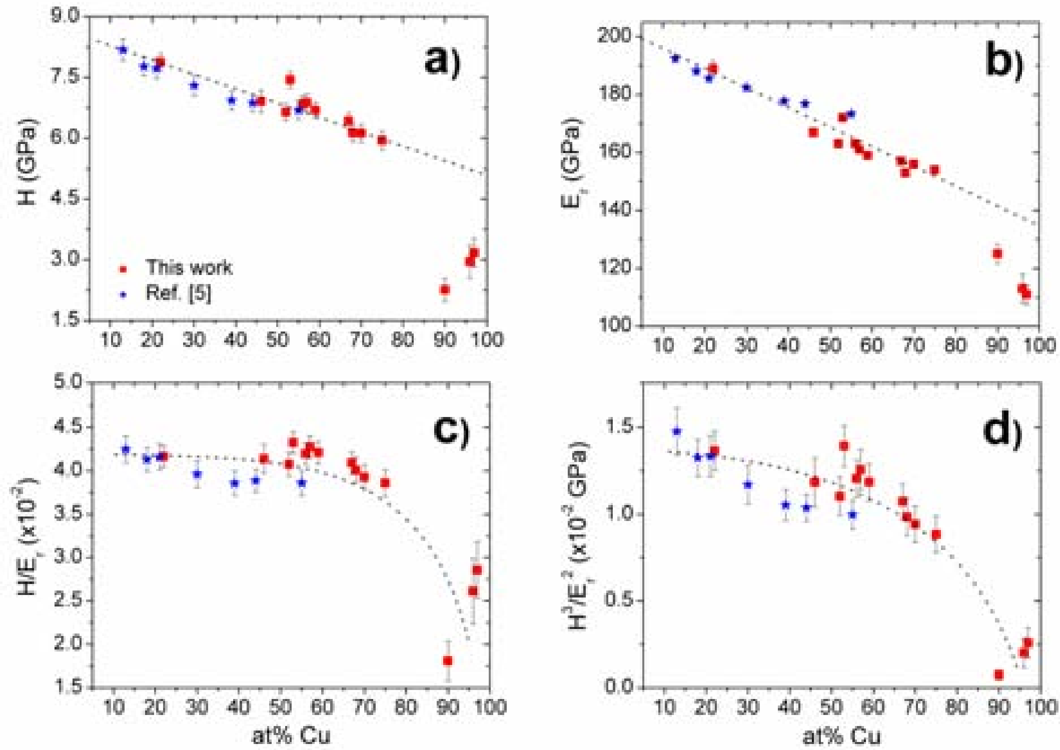

Figure 4: a) Hardness H, b) reduced Young's modulus E_r c) wear resistance H/E_r and d) resistance plastic deformation H^3/E_r^2 for the samples analysed in this work, i.e., grown using a [Ni(II)]/[Cu(II)] molar ratio of 11 (red-square spots), and data obtained from our previous work [5] where the [Ni(II)]/[Cu(II)] molar ratio in the electrolyte was 29 (blue-star spots). The discontinuous lines in panels (a) and (b) are linear fits of the experimental data for Cu contents lower than 70 at%, whereas the discontinuous lines in panels (c) and (d) are guides to the eye.

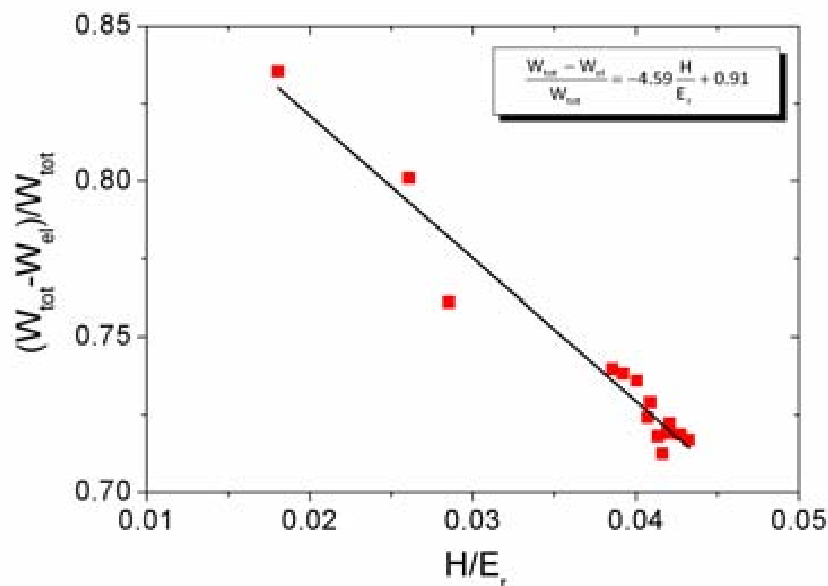

Figure 5: Dependence of the normalized plastic energy, $(W_{tot} - W_{el})/W_{tot}$, on the H/E_r ratio for the different investigated CuNi films. Note that the line is a linear fit of the experimental data.

3.4. Corrosion behaviour

The corrosion behaviour of CuNi films has been assessed in aerated 3.5 wt% NaCl because this material is commonly used in applications involving sea-water or chloride-containing media. Table 2 lists the E_{OCP} values of Cu_xNi_{1-x} (x = 0.97, 0.74, 0.58, 0.53, atomic content) samples and Cu/Ti/Si substrate (i.e., evaporated Cu seed layer). Compared to the substrate, the CuNi coatings show less negative E_{OCP} values except for x = 0.97. Representative potentiodynamic polarization curves are displayed in Fig. 6. While the cathodic branches do not reveal any special feature, in the anodic branch the current density monotonically increases up to a maximum and then either a plateau is observed or a smooth current decrease is detected, indicating a possible passive region. The initial oxidative current would correspond to the formation of a passive oxide film that further protects the sample surface from ongoing corrosion. It has been claimed that the structure of these passive films actually consists of two layers, an outer CuO layer and an inner Cu_2O layer containing Ni^{2+} and Ni^{3+} [43]. Using Tafel extrapolation analysis, the E_{corr} and j_{corr} values have been determined (Table 2). It can be seen that the films with x = 0.74, 0.58 and 0.53 display similar parameters, all E_{corr} values being more positive and all j_{corr} values being lower compared to both the substrate (pure-Cu) and the $Cu_{0.97}Ni_{0.03}$ film. Rajasekaran and Mohan also observed an increase of the corrosion resistance in CuNi alloys electrodeposited on Cu substrate when compared to pure-Cu films deposited onto Cu substrate [44]. These results demonstrate that alloying Cu with significant amounts of

Ni clearly improves the corrosion resistance of the material. This is in agreement with the well-known corrosion resistance of Constantan ($Cu_{55}Ni_{45}$) [2], a composition that has been used for many years as thermocouples. Actually, the films with x = 0.53 and 0.58 have a composition rather close to that of Constantan. Our values resemble those reported in the literature for CuNi coatings of similar composition and crystallite sizes. For example, E_{corr} values between -0.200 and -0.163 V vs. Ag|AgCl| 3M KCl were observed in $Cu_{0.55}Ni_{0.55}$ films with crystallize sizes ranging from 26 to 413 nm [10]. Interestingly, the films prepared in this work exhibit better anticorrosion properties in aerated NaCl medium than pulse-plated layers with higher Ni contents (70 at.%) but lower crystallite sizes (13 nm) [45]. It is important to stress that the rather good corrosion resistance of the here-prepared films can be partly ascribed to their compactness (i.e., absence of porosity). The porosity (P) of a film can be estimated from the potentyodinamic polarization tests according to the following equation [46]:

$$P = \frac{R_{P,S}}{R_P} 10^{-(\Delta\Delta_{corr}/\beta_a)} \qquad \text{(Eq. 4)}$$

where $R_{P,S}$ and R_P are the polarization resistances of the substrate and the deposited layer, respectively, ΔE_{corr} the potential difference between the bare substrate and the coated substrate, and β_a is the anodic Tafel coefficient of the substrate. The porosity values obtained from the linear potentiodynamic tests are in the range between 1.5% and 4.0% except for the film with the highest Cu content ($Cu_{0.97}Ni_{0.03}$) (Table 2). In this case, the porosity increases up to 9.4%, which makes sense taking into account the rough, cauliflower-like morphology shown by this electrodeposit (see Fig. 2a). Indeed, this sample shows the most negative E_{corr} value and the largest j_{corr} among the tested CuNi films. This could be partly ascribed to its intrinsic larger porosity, which would facilitate chlorine anion diffusion towards the film/substrate interface. Note that the obtained porosities fully agree with the values estimated from the Young's moduli (Eq. 2).

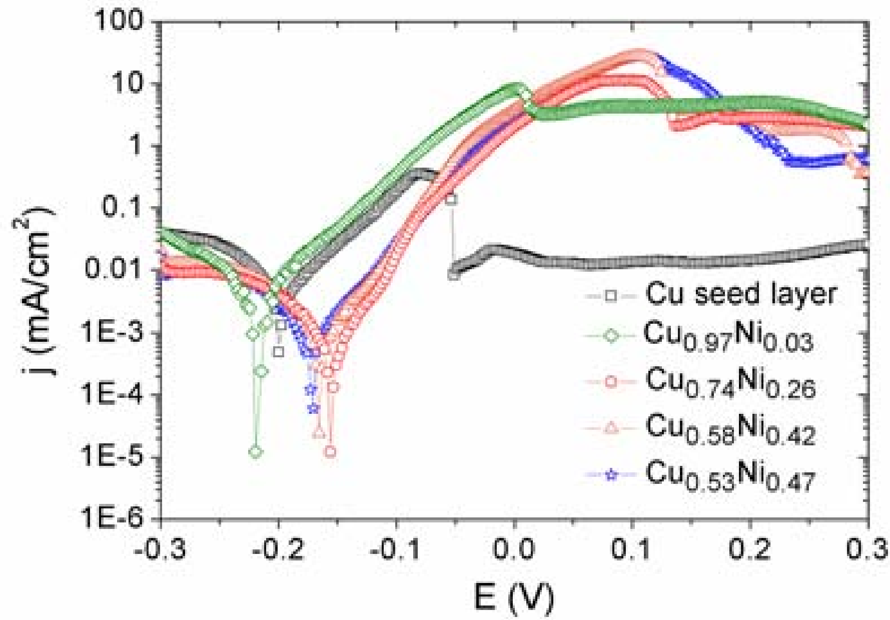

Figure 6: Representative potentiodynamic polarisation curves for various electrodeposited CuNi films and the bare substrate (i.e., evaporated Cu seed layer onto Ti/Si).

Specimen composition	E_{OCP} (V)	E_{corr} (V)	j_{corr} (μA/cm²)	P (%)
Cu/Ti/Si (substrate)	-0.218	-0.195	15.9	--
$Cu_{0.97}Ni_{0.03}$	-0.171	-0.211	5.4	9.4
$Cu_{0.74}Ni_{0.26}$	-0.160	-0.156	1.8	1.5
$Cu_{0.58}Ni_{0.42}$	-0.169	-0.164	3.6	2.9
$Cu_{0.53}Ni_{0.47}$	-0.175	-0.171	3.0	4.0

Table 2: Open-circuit potential (E_{OCP}), corrosion potential (E_{corr}), corrosion current density (j_{corr}) and porosity values (P) estimated using Equation 4 corresponding to the substrate and the different CuNi alloys.

4. CONCLUSIONS

Nanocrystalline Cu-rich CuNi alloy films have been prepared by electrodeposition from an electrolytic bath containing Ni and Cu sulphates with a [Ni(II)]/[Cu(II)] molar ratio to 11. The decrease of the [Ni(II)]/[Cu(II)] molar concentration ratio from 29 (as in our previous Ni-rich CuNi films) to 11 allows extending the compositional range of the newly prepared films up to 97 at% Cu. Remarkably, these Cu-rich films follow similar structural, morphological and mechanical trends as our previous Ni-rich samples despite the well-known difficulties in controlling the growth of nanocrystalline smooth Cu-rich films. For CuNi deposits with Cu contents lower than 70 at%, SEM and XRD analyses reveal the occurrence of very flat surfaces accompanied with crystallite size of around 40 nm. Such refined microstructure probably stems from the addition of saccharine in the electrolytic bath. The nanocrystalline character together with the high density of stacking faults, as evaluated from the XRD Rietveld refinements, are the main factors that contribute to the observed outstanding mechanical properties of these Cu-rich films. Actually, the mechanical properties (i.e., Young's modulus, hardness, wear resistance or resistance to plastic deformation) can be tailored by varying the deposit composition and are superior for intermediate or low Cu percentages. Concerning the corrosion performance in NaCl medium, the CuNi films display lower j_{corr} values and more positive E_{corr} values than the bare substrate, thus confirming the protective character of the here-prepared nanostructured, highly-dense CuNi alloys. For deposits with Cu content around 90-97 at% the crystallite size and the roughness are higher due to the occurrence of cauliflower-like surface morphologies and concomitant increased porosity, ascribed to the lower effectiveness of saccharine in refining the grain size. This kind of morphology is also responsible for the decrease of strength and wear resistance, as well as the worsening in the corrosion behaviour, presumably due to the enhanced chloride anion diffusion towards the film/substrate interface.

References

[1] D.R. Askeland, P.P. Fulay and W.J.Wright, *The Science and Engineering of Materials*, Cengage Learning, Stamford (2011).

[2] J.R. Davis, *Copper and Copper Alloys*, ASM International, United States of America (2001).

[3] M. Metikoš-Huković, R. Babić, I. Škugor Rončević and Z. Grubač, *Desalination*, 276 (2011) 228-232.

[4] V. Subramanian, P. Chandramohan, M.P. Srinivasan, S. Velmurugan and S.V. Narasimhan, *Corr. Sci.*, 49 (2007) 620-636.

[5] E. Pellicer, A. Varea, S. Pané, B.J. Nelson, E. Menéndez, M. Estrader, S. Suriñach, M.D. Baró, J. Nogués and J. Sort, *Adv. Funct. Mater.*, 20 (2010) 983-991.

[6] K. Lu, L. Lu and S. Suresh, *Science*, 324 (2009) 349-352.

[7] M. Chen, E. Ma, K. J. Hemker, H. Sheng, Y. Wang and X. Cheng, *Science*, 23 (2003) 1275-1277.

[8] L. Lu, M.L. Sui and K. Lu, *Science*, 25 (2000) 1463-1466.

[9] M. Schlesinger and M. Paunovic, *Modern Electroplating*, John Wiley & Sons, New York (2000).

[10] E. Pellicer, A. Varea, S. Pané, K.M. Sivaraman, B.J. Nelson, S. Suriñach, M.D. Baró, and J. Sort, *Surf. Coat. Technol.*, 205 (2011) 5285-5293.

[11] E. Pellicer, A. Varea, K.M. Sivaraman, S. Pané, S. Suriñach, M.D. Baró, J. Nogués, B.J. Nelson and J. Sort, *ACS Appl. Mater. Interf.*, 3 (2011) 2265-2274.

[12] E. Gómez, E. Pellicer and E. Vallés, *Electrochem. Commun.*, 6 (2004) 853-859.

[13] Sh. Hassani, K. Raeissi and M.A. Golozar, *J. Appl. Electrochem.*, 38 (2008) 689-694.

[14] S. Guan and B. J. Nelson, *J. Magn. Magn. Mater.*, 292 (2005) 49-58.

[15] J. Sort, J. Nogués, S. Suriñach and M.D. Baró, *Philos. Mag.*, 83 (2003) 439-455.

[16] W.C. Oliver and G.M. Pharr, *J. Mater. Res.*, 7 (1992) 1564-1583.

[17] M. Troyon and L. Wang, *Appl. Surf. Sci.*, 103 (1996), 517-523.

[18] B.E. Warren, *X-ray Diffraction*, Addison-Wesley, New York (1969).

[19] R. Meyer and L.J. Lewis, *Phys. Rev. B*, 66 (2002) 052106.

[20] F. Ebrahimi, A. Ahmed and H. Li, *Appl. Phys. Lett.*, 85 (2004) 3749-3751.

[21] K. Youssef, M. Sakaliyska, H. Bahmanpour, R. Scattergood and C. Koch, *Acta Mater.*, 59 (2011) 5758-5764.

[22] L. Lu, Y. Shen, X. Chen, L. Qian and K. Lu, *Science*, 304 (2004) 422-426.

[23] D. Gu, Y. Shen and Z. Lu, *Mater. & Design*, 30 (2009) 2099-2107.

[24] A. Ibáñez and E. Fatás, *Surf. Coat. Technol.*, 191 (2005) 7-16.

[25] A. J. Detor and C. A. Schuh, *J. Mater. Res.*, 22 (2007) 3233-3248.

[26] Y. Li, H. Jiang, W. Huang and H. Tian, *Appl. Surf. Sci.*, 254 (2008) 6865-6869.

[27] Y. Kaneko, Y. Mizuta, Y. Nishijima and S. Hashimoto, *J. Mater. Sci.*, 40 (2005) 3231-3236.

[28] H. Zhang, Z. Jiang and Y. Qiang, *Mater. Sci. Eng. A*, 517 (2009) 316-320.

[29] M. Dao, L. Lu, R.J. Asaro, J.T.M. De Hosson and E. Ma, *Acta Mater.*, 55 (2007) 4041–4065.

[30] X. Zhang, A. Misra, H. Wang, M. Nastasi, J. D. Embury, T. E. Mitchell, R. G. Hoagland and J. P. Hirth, *Appl. Phys. Lett.*, 84 (2004) 1096-1098.

[31] G. V. Samsonov, *Handbook of the Physicochemical properties of the Elements*, IDI-Plenum, New York (1968).

[32] T. Fritz, M. Griepentong, W. Mokwa and U. Schnakenberg, *Electrochim. Acta*, 48 (2003) 3029-3035.

[33] T. H. Fang and W. J. Chang, *Microelectr. Engineer.*, 65 (2003) 231–238.

[34] N. Chawla and X. Deng, *Mater. Sci. Eng. A*, 390 (2005) 98–112.

[35] N. Ramakrishnan and V.S. Arunachalam, *J. Am. Ceram. Soc.*, 76 (1993) 2745-2752.

[36] A. Leyland and A. Matthews, *Wear*, 246 (2000) 1-11.

[37] C. Rebholz, A. Leyland, J.M. Schneider, A.A. Voevodin and A. Matthews, *Surf. Coat. Technol.*, 412 (1999) 120-121.

[38] J. Musil, F. Kunc, H. Zeman and H. Poláková, *Surf. Coat. Technol.*, 154 (2002) 304-313.

[39] A.C. Fisher-Cripps, *Nanoindentation*, Springer, New York (2004).

[40] Y.-T. Cheng and C.-M. Cheng, *Appl. Phys. Lett.*, 73 (1998) 614-616.

[41] W.C. Oliver and G.M. Pharr, *J. Mater. Res.*, 19 (2004) 3-20.

[42] E. Pellicer, S. Pané, K.M. Sivaramen, O. Ergeneman, S. Suriñach, M.D. Baró, B.J. Nelson and J. Sort, *Mater. Chem. Phys.*, 130 (2011) 1380-1387.

[43] M. Metikoš-Huković, I. Škugor, Z. Grubač and R. Babić, *Electrochim. Acta*, 55 (2010) 3123-3129.

[44] N. Rajasekaran and S. Mohan, *J. Appl. Electrochem.*, 39 (2009) 1911-1916.

[45] S.K. Ghosh, G.K. Dey, R.O. Dusane and A.K. Grover, *J. Alloy Comp.*, 426 (2006) 235-243.

[46] J. Creus, H. Mazille and H. Idrissi, *Surf. Coat. Technol.,* 130 (2000) 224-232.

Acknowledgements

This work has been partially financed by the 2009-SGR-1292 and MAT2011-27380-C02-01 research projects. M.D.B. was partially supported by an ICREA Academia award.

Chapter 6 : Template-Assisted Electrodeposition of Cu-Ni Nanopillars

6.1. Introduction. Miniaturization of Cu-Ni layers

In Chapters 4 and 5 the electrodeposition of continuous nc-Cu-Ni alloy films with tuneable mechanical and magnetic behaviour, good thermal stability and corrosion performance has been demonstrated. As mentioned throughout this Thesis dissertation, one of the key applications of these alloys is in the MEMS/NEMS field. To this end, miniaturization of the continuous films is required. Such miniaturization is usually performed by electron beam lithography (EBL) combined with sputtering. However both techniques are rather expensive and good quality sputtered layers are limited to thicknesses up to 70 nm. For thicknesses beyond this value the layers lack structural homogeneity, which seriously precludes their use in MEMS. Another technique, which is often used to fabricate MEMS/NEMS, is focused ion beam (FIB) lithography (1). However, this technique also has some drawbacks: i) a long time is required to manufacture individual samples, which significantly reduces the output; ii) the minimum realistically attainable diameter for cylindrical-shaped objects is around 150 nm; and iii) Ga^{+} ions easily incorporate in the objects being fabricated, thus modifying their chemical composition and structure and, in turn, their physical properties (1).

To overcome all these issues, new cost-effective methods able to miniaturize nc-metallic films are being explored. Electrodeposition overcomes the drawbacks of the previously mentioned physical techniques (sputtering and FIB) in terms of cost, film growth rate and film thickness. The fabrication of large aspect ratio metallic nanowires in the cylindrical pores of membranes like anodized alumina, polycarbonate and polymethyl methacrylate (PMMA) is well documented in the literature (2, 3). The diameter of the nanowires obtained ranges from hundreds of micrometers down to tenths of nanometres depending on the pore size of the template. The application of these 1D nanostructures in sensors,

field-emission and magnetic devices often requires the nanostructures to be supported by a substrate (Si, glass, etc.) to ensure the robustness and mechanical stability of the device. For this reason the nanowires are kept embedded in the template to serve as high-performance platforms. In certain applications, however, the template needs to be removed because it can either interfere or hinder the nanowires response. In such a case, when the template is etched away the nanowires often bend and partially (or completely) collapse. For example, self-standing nanowires present an important disadvantage for magnetic applications as they tend to form disordered arrays due to partial collapse during the template removal step. It has been recently demonstrated that SiO_2 nanopillars, rather than nanowires, allows for highly localized fluorescence imaging and thereby serve as a chemical probes to address cellular events with high specificity (4).

Hence, there is currently an increasing demand for: i) obtaining metal alloy nanostructures that can offer improved properties compared to the pure constituent metals and ii) fabricating self-standing nanostructure arrays that are mechanically more stable than nanowires. In this sense, alloy nanopillars are proposed to overcome the limitations of free nanowires (mechanical instability and lack of robustness) and can be thus potentially used for a range of technological purposes. Combining EBL and electrodeposition can be a powerful approach to grow multifunctional alloy nanopillars. Up to now, a few pure metals (e.g. Co, In, Sn and Fe) have been prepared using this synthetic pathway (5–9). The diameter of the pillars typically ranges between 200 nm and 1 μm. Thinner pillars are scarcely reported. The preparation of alloy nanopillars has been even less exploited (NiFe is almost the only example available (10) mostly due to the difficulty in achieving the co-deposition of metals in nano-sized cavities). Herein the fabrication of Cu-Ni pillars by template-assisted electrodeposition and the characterization of their properties are presented. The contents are organized following the classical structure of a scientific article for ease of reading.

Self-standing, ordered and straight arrays of nanopillars are obtained in all cases after removing the e-beam resin used for patterning. It is demonstrated that alloy composition can be controllably tuned not only in conventional electrodeposition on flat substrates (11), but also when electroplating in nano-confined electrodes. The composition of the alloy nanopillars could be tuned between 34 and 70 at% of Ni by varying the applied potential. The obtained pillars, with diameters of 100 nm (300 nm pitch size) and 200 nm (600 nm pitch size), and aspect ratios of 4.5 and 2.25, respectively, exhibit a tuneable magnetic response as a function of the Cu/Ni atomic ratio. Coercivity values around 110 Oe, which are larger than for continuous films of similar composition, have been achieved.

6.2. Experimental conditions

6.2.1. Substrate fabrication and sample preparation

Electrodeposition has been performed onto pre-lithographed substrates (Figure 6.1). First, Ti (100 nm) / Au (400 nm) / Ti (15 nm) were successively evaporated onto Si (111) substrates. An electron sensitive resist (ZEP-520A) was then spin-coated onto the substrate and patterning was carried out by electron-beam lithography (EBL) with *CRESTEC CABL-9500C Nanolithography* equipment. 60 x 60 μm^2 arrays of cylindrical holes of 100 nm and 200 nm in diameter and pitch sizes of 300 nm and 600 nm, respectively, were patterned. Following the lithographic procedure, the resist was developed in anisol.

The upper 15 nm-thick Ti layer was used to protect the Au seed-layer during lithography. Before electrodeposition, all samples were submerged in HF solution during one minute to remove the 15 nm-thick Ti layer to allow the deposition of the metals directly onto the Au layer. Finally the substrates were dipped in diluted sulphuric acid to remove oxides and organic residues. Before deposition, the substrates were immersed in the electrolyte for 10 min, which had been previously deaerated with argon gas.

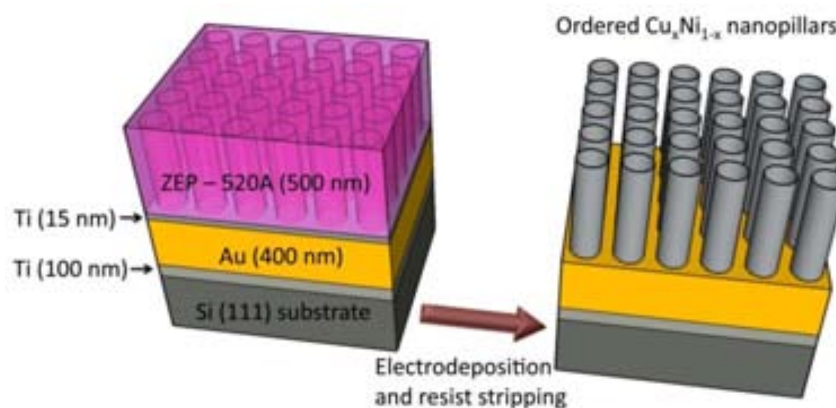

Figure 6.1: Layered structure of the substrates used for nanopillars electrodeposition.

6.2.2. Nanopillars electrodeposition

Cu, Ni and CuNi alloy materials nanopillars deposited by direct current electrodeposition in one-compartment thermostatized three-electrode cell using *PGSTAT30 Autolab potentiostat/galvanostat* (Ecochemie). The analytical solutions were prepared from analytical grade reagents and Milipore Milli-Q water (18 MΩ·cm). For Cu and Cu-Ni alloy a bath containing 6.24 g/L $CuSO_4 \cdot 5H_2O$, 624 g/L $NiSO_4 \cdot 6H_2O$ and 70 g/L $Na_3C_6H_5O_7 \cdot 2H_20$ (sodium citrate), 0.2 g/L $NaC_{12}H_{25}SO_4$ (sodium dodecyl sulphate) and 1.4 g/L $C_7H_5NO_3S$ (saccharine) was used. The electrolyte volume was 50 mL. The pH was fixed at 4.5 and the temperature at 30 ºC in all cases. Pure Ni was deposited from an electrolyte containing 630 g/L $NiSO_4 \cdot 6H_2O$ (nickel sulphate) and the same amount of the other chemicals (sodium citrate, sodium dodecyl sulphate and saccharine).

The Si (111)/Ti (100 nm)/Au (400 nm)/ZEP-520A layers were used as working electrodes, which were positioned vertically into the electrode. A double junction Ag|AgCl (E = +0.210 V/SHE) reference electrode was used with 3M KCl inner solution and 1M Na_2SO_4 outer solution. All the potentials are referred to this electrode. A Pt sheet was used as counter electrode.

Deposition was conducted potentiostatically, by applying a constant potential in the range of -0.900 to -1.150 V, under mild stirring (200 rpm) using a magnetic stirrer bar. It was found that the potentiostatic mode offers better control in filling the cylindrical holes than the galvanostatic mode previously used to electrodeposit continuous Cu-Ni films. After the deposition the samples were thoroughly rinsed in water and ZEP-520A resin was removed with dimethylacetamide (DMAC) at 35°C for 1 min to get self-standing nanopillars.

6.2.3. Characterization

SEM images of the nanopillars were obtained on *MERLIN SEM* microscope operated at 5 kV. The chemical composition was determined by EDXS at 15 kV. Metal proportions are expressed in atomic percentage (at%). Mapping analysis was carried out with the aim to clarify element distribution through the nanopillars length. Aspect-ratio values and nanopillar element distribution images were taken at 70° tilt angle. The magnetic properties of nanopillars were investigated acquiring hysteresis loops using magneto-optical Kerr effect

magnetometer (MOKE) in longitudinal and polar modes (perpendicular and parallel to the long axis of the structure, respectively) with a maximum field applied of 825 Oe under room temperature.

6.3. Results and discussion

6.3.1. Morphological characterization

Figure 6.1 shows the layered structure of the substrates used for electrodeposition (left image). The role of the upper 15 nm thick Ti layer was to protect the Au seed-layer during the lithography process and subsequent wafer slicing into single chips (substrates). This layer was selectively etched immediately before electrodeposition to ensure the adhesion of the nanopillars to the substrates after resin removal; otherwise the nanopillars become detached from the substrate due to the mismatch between the crystallographic structure of Ti (hexagonal closed packed, P63/mmc spatial group) and the $Cu_{1-x}Ni_x$ structures (face-centred cubic, Fm-m3 spatial group) (Figure 6.2.a). Nanopillars grown onto Au seed layer show good adherence to the substrate since their crystallographic structures are the same.

An electrolytic solution containing a [Ni(II)]/[Cu(II)] molar ratio of 29 and several additives to control metals co-deposition and grain size was initially used for electrodeposition. This bath was proven to be effective in achieving the deposition of nanocrystalline, smooth, continuous Ni-rich Cu-Ni films (up to 55 at% Cu) (11). However, it did not work as fine as it did for continuous films because nanopillars' composition could not be tuned as a function of the applied potential/current density. As a matter of fact, almost pure Cu nanopillars were obtained regardless of the applied potential/current density, likely because the overpotential is not sufficient to plate Ni within high-aspect ratio cavities. To overcome this issue, the bath was re-formulated by increasing the [Ni(II)]/[Cu(II)] molar ration in solution to 95.2, keeping the overall ion concentration constant. Also the concentration of additives was re-scaled as shown in Table 6.1. The next step was to choose the appropriate window of deposition potentials so as to obtain deposits with tuneable Cu/Ni ratios and, most importantly, to set the deposition time to avoid overplating

(Figure 6.2.b); otherwise, mushroom-like nanostructures are obtained upon stripping of the resin, as observed in other works (10) (inset of Figure 6.2.b). A fancy forest of nanotrees array is obtained when overplating takes too long (Figure 6.3.). For recording or magnetic sensor applications overplating must be avoided because it can induce undesirable exchange and dipolar magnetic interactions between nanopillars (12). Moreover the order of the magnetic nanostructures, organized in patterned arrays, becomes crucial as the mesoscopic effects produces by confinement and proximity can be controlled and modified by their geometrical configuration.

The optimized parameters for the deposition of non-overplated structures (namely, the concentration of metal salts and additives in solution, applied potential, deposition time, stirring rate and temperature) are shown in Table 6.1.

The potentiostatic curves for $Cu_{1-x}Ni_x$ deposition onto the lithographed substrates from the optimized bath are shown in Figure 6.4.a. It can be observed that the absolute value of current density increases as the applied potential is made more negative. The applied potentials (from E = -0.900 V to E = -1.150 V) allowed growing nanopillars with varying composition. The nickel percentage obtained from EDXS increased from 34 at% to 70 at% as E was made more negative (Figure 6.4.b), since greater overpotentials favour nickel discharge.

Pure Cu and Ni metals were also electrodeposited onto the lithographed substrates for the aim of comparison. Pure Cu nanopillars could be obtained from the same bath formulation provided that the applied potential was made more positive. In particular, for deposition potentials above -0.8 V, only Cu is electrochemically reduced. To deposit pure Ni, though, we had to modify bath composition since Ni deposition is always accompanied by some Cu deposition even at high overpotentials. Therefore, the Cu sulphate in solution was replaced by Ni sulphate while keeping the overall ion concentration constant.

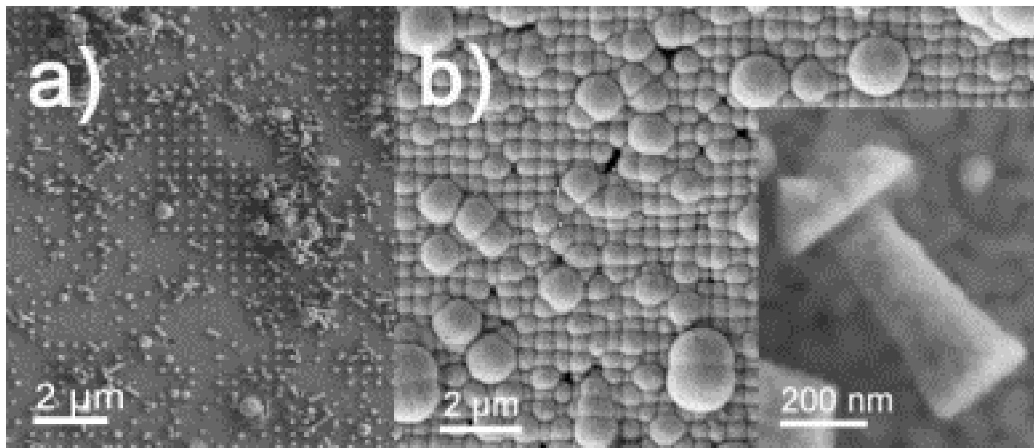

Figure 6.2: In-plane SEM image of a) Cu-Ni nanopillars electrodeposited directly onto 15 nm-thick upper Ti layer. As shown, most of the structures are detached from the substrate due to the poor adherence after the resin stripping; b) Overplated nanopillars. Inset: side-wide of one of these overplated entities featuring a mushroom-like appearance.

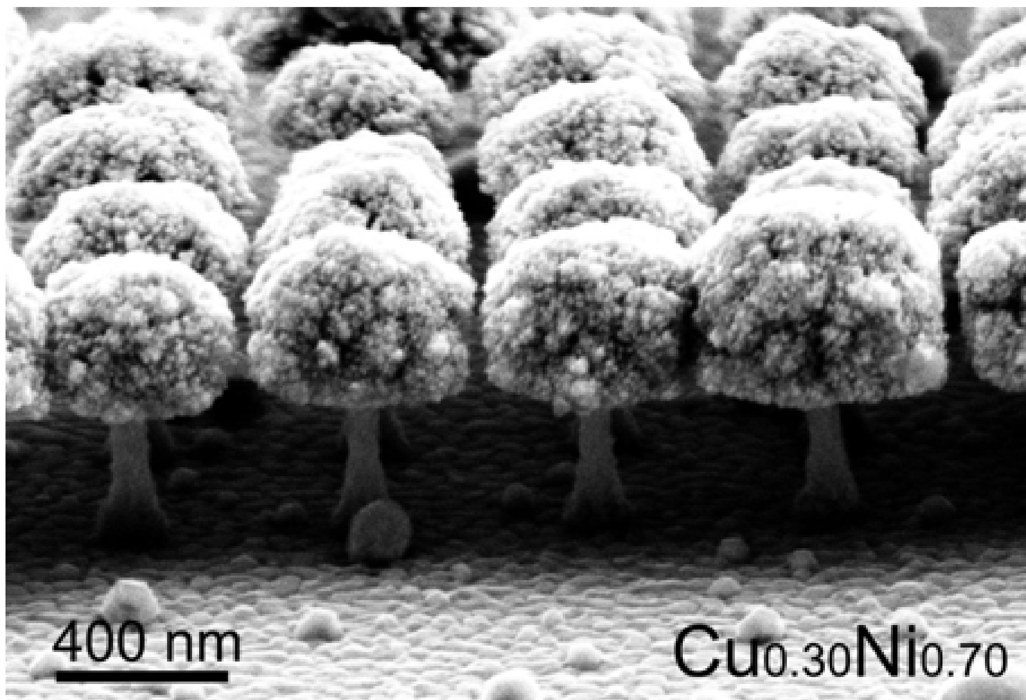

Figure 6.3: SEM image of a forest of nano-trees obtained due to exceedingly large overpotential and deposition time.

Table 6.1 Electrodeposition conditions for the deposition of pure Ni and Cu, and for Cu-Ni nanopillars (concentration of Ni and Cu salts and additives in solution, applied potential, time, stirring rate and temperature)

<table>
<tr><th colspan="2"></th><th>$NiSO_4$ (g/L)</th><th>$CuSO_4$ (g/L)</th><th>E (V)</th><th>t (s)</th><th rowspan="8">sodium citrate 70 g/L
sodium dodecylsulphate 0.4 g/L
saccharine 1.4 g/L
200 rpm
T = 30°C
pH =4.5</th></tr>
<tr><td colspan="2">Pure Ni</td><td>630</td><td>0</td><td>-0.900</td><td>30</td></tr>
<tr><td colspan="2">Pure Cu</td><td>624</td><td>6.24</td><td>-0.800</td><td>30</td></tr>
<tr><td rowspan="5">Cu-Ni alloy</td><td>34 at % Ni</td><td rowspan="5">624</td><td rowspan="5">6.24</td><td>-0.900</td><td>30</td></tr>
<tr><td>41 at % Ni</td><td>-1.000</td><td>30</td></tr>
<tr><td>45 at % Ni</td><td>-1.025</td><td>15</td></tr>
<tr><td>63 at % Ni</td><td>-1.100</td><td>7</td></tr>
<tr><td>70 at % Ni</td><td>-1.150</td><td>5</td></tr>
</table>

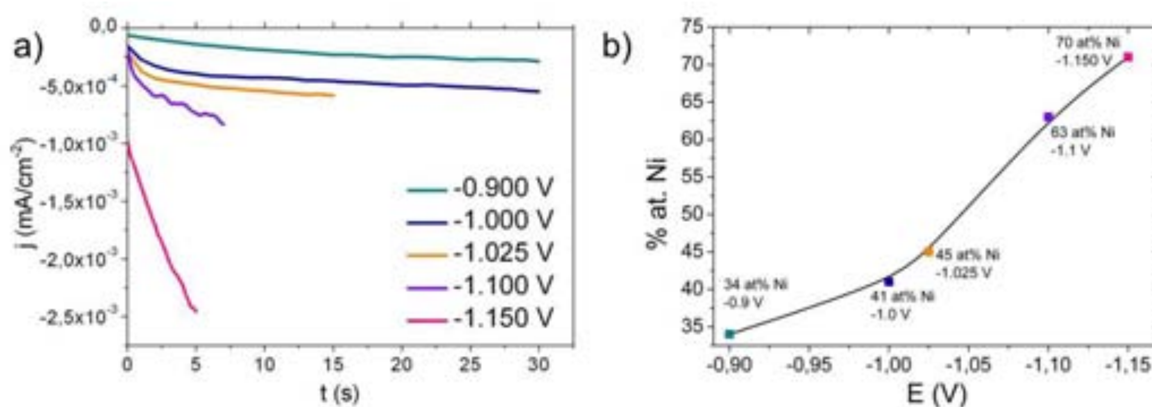

Figure 6.4: a) Potentiostatic curves for Cu-Ni alloy nanopillars deposition onto Au/Ti/Si substrates. b) Ni percentages in the nanopillars as a function of applied potential.

A representative field-emission scanning electron microscopy (FE-SEM) planar view of non-overplated $Cu_{1-x}Ni_x$ alloy nanopillars is shown in Figure 6.5.a. Likewise, 70° tilted (side-view) typical FESEM images of 200 nm and 100 nm-diameter nanopillars are displayed in Figure 6.5.b and c, respectively. Both images show well defined, periodically ordered nanopillars with a constant height of 450 nm. For the Cu-rich arrays, EDX mapping analysis of single entities revealed a graded composition along the nanopillar axis, with the Ni content being higher at the bottom of the nanopillar than at the top (Figure 6.6). This indicates that Cu is strongly depleted under these conditions, which makes sense considering the large [Ni(II)]/[Cu(II)] molar ratio in solution.

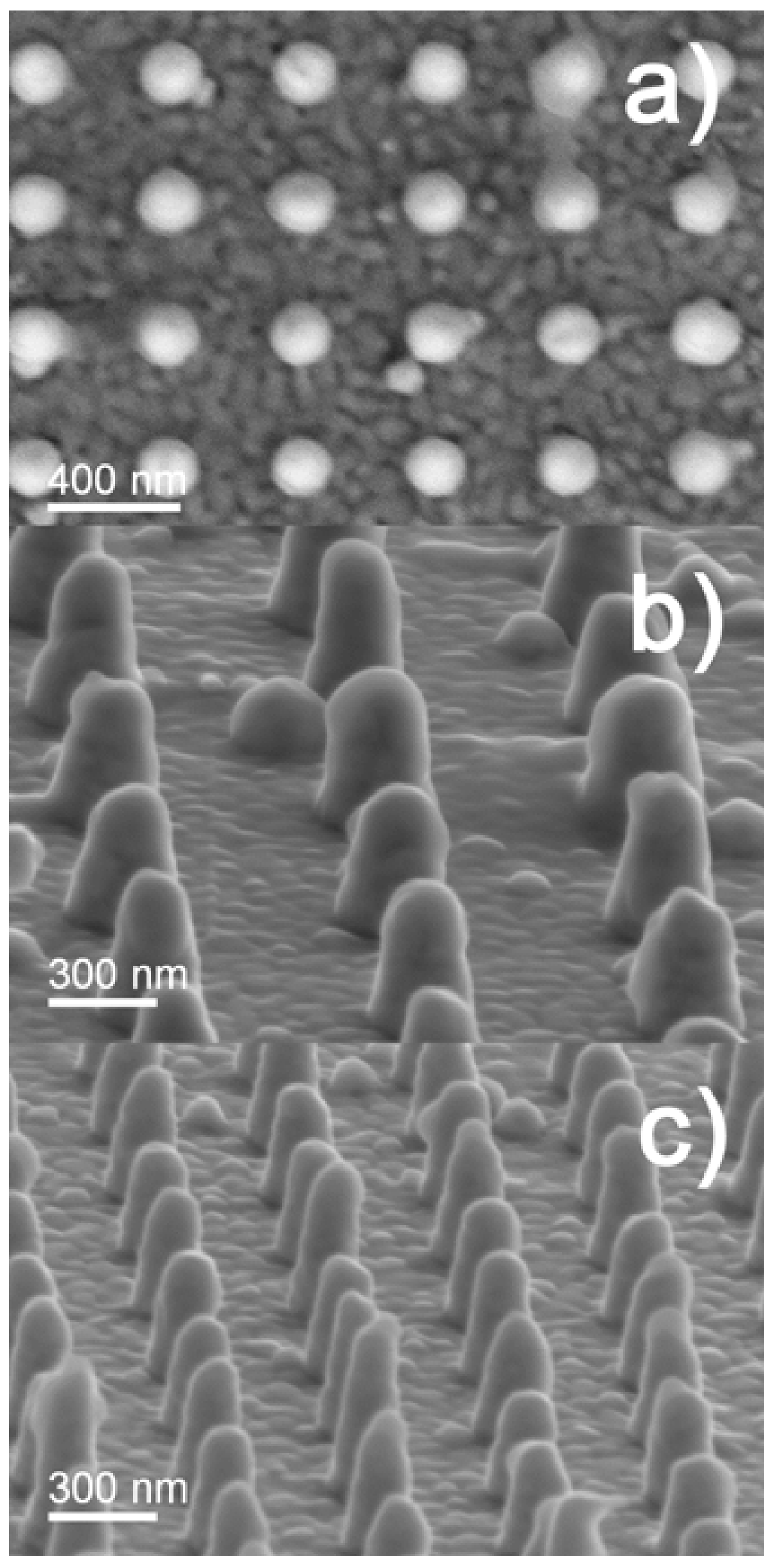

Figure 6.5: FE-SEM images of $Cu_{0.66}Ni_{0.34}$ nanopillars: a) planar view of 200 nm-diameter, and b-c) 70° tilted images in which the periodicity and uniformity of 200 and 100 nm-diameter nanopillars, respectively, can be appreciated.

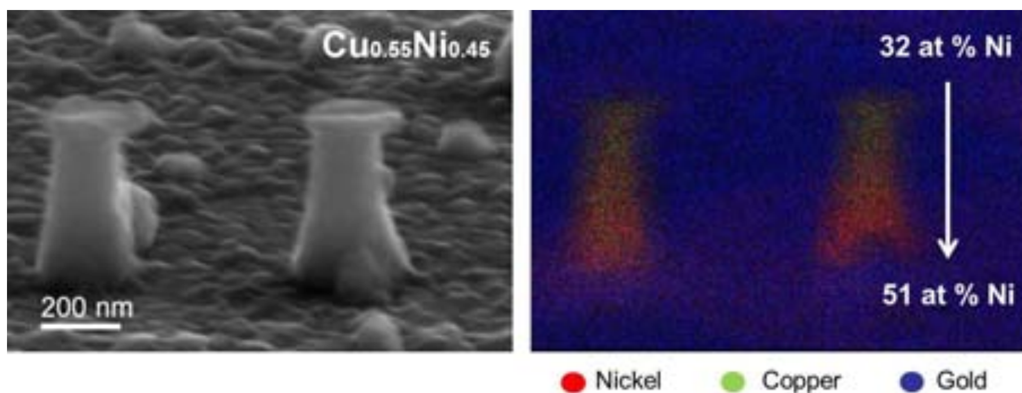

Figure 6.6: a) FESEM image of a couple of 200 nm-diameter nanopillars and b) the corresponding EDX mapping analysis along their length.

6.3.2. Magnetic behaviour

MOKE measurements indicate that the $Cu_{1-x}Ni_x$ nanopillars (diameter of 100 nm) are ferromagnetic at room temperature in the overall compositional range. The hysteresis loops measured in longitudinal configuration (with the magnetic field applied along the in-plane direction, i.e., perpendicular to the nanopillars axis) are rather square (except for the $Cu_{0.37}Ni_{0.63}$ composition) and exhibit coercivity values, H_C, around 100 - 150 Oe (Figure 6.7a) independently of the diameter size (100 nm or 200 nm). Similar loops were recorded for the nanopillars with diameter of 200 nm. Two ferromagnetic contributions seem to be present in the hysteresis loops corresponding to the $Cu_{0.37}Ni_{0.63}$ nanopillars. This could be due to the compositional gradation observed along the nanopillars axis, as evidenced from EDX-SEM analyses (Figure 6.6) or to the segregation of various Ni-rich regions with different Ni content. Actually, according to the Cu-Ni phase diagram, $Cu_{1-x}Ni_x$ alloys should only be ferromagnetic at room temperature for Ni percentages larger than 70 at% (13, 14). The occurrence of ferromagnetic behaviour in all the investigated $Cu_{1-x}Ni_x$ nanopillars (including $Cu_{0.66}Ni_{0.34}$ and $Cu_{0.55}Ni_{0.45}$) suggests that Ni (or Ni-rich $Cu_{1-x}Ni_x$) segregation indeed takes place during the electrodeposition. In this case, a single ferromagnetic contribution is observed in the hysteresis loops, indicating that the Ni or Ni-rich clusters that segregate during electroplating exhibit all similar composition.

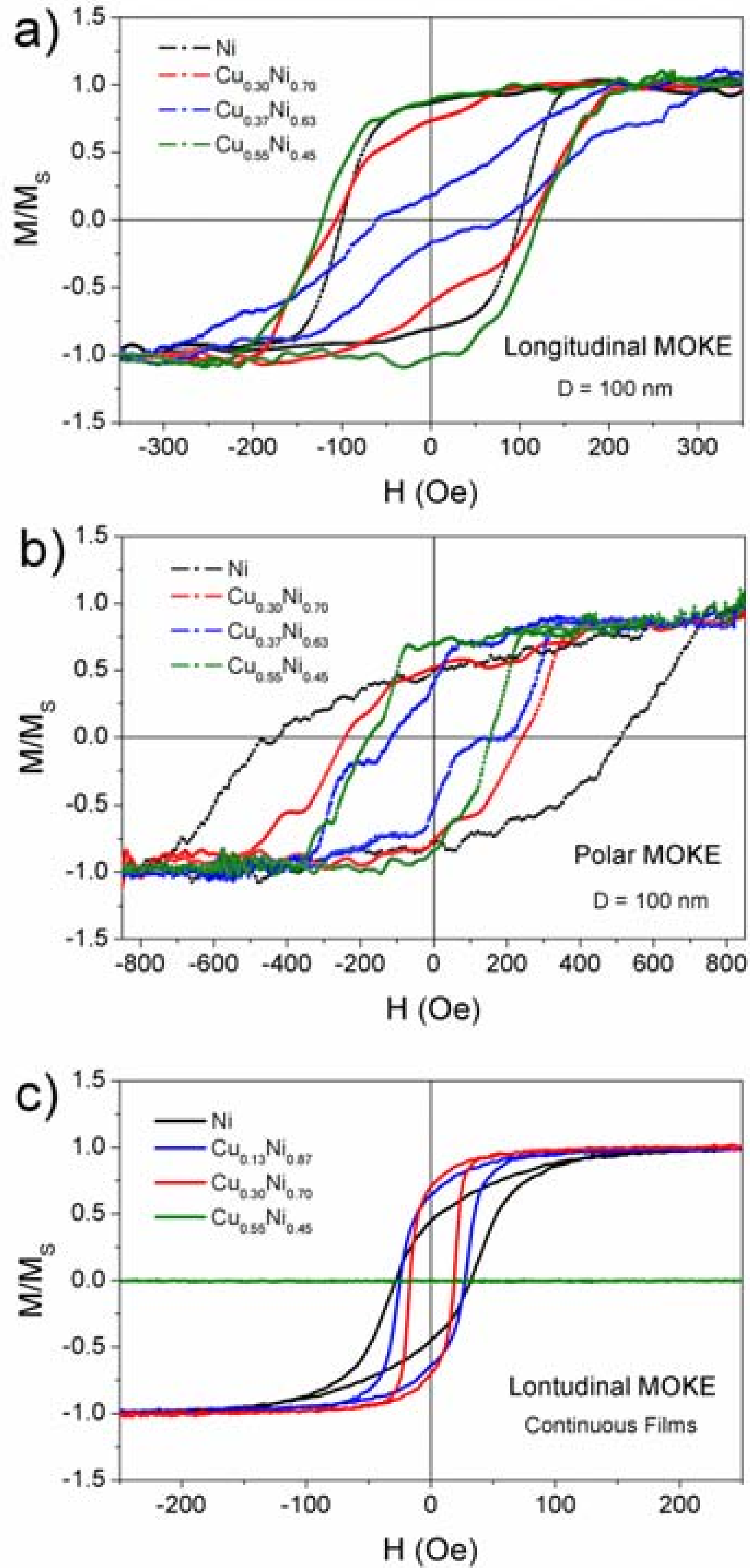

Figure 6.7: Room-temperature MOKE hysteresis loops for: (a) Cu-Ni nanopillar arrays with diameter of 100 nm, measured in longitudinal configuration, (b) Cu-Ni nanopillar arrays with diameter of 100 nm, measured in polar configuration and (c) continuous (unpatterned) films, measured in longitudinal configuration.

Remarkably, square hysteresis loops are also obtained by polar MOKE (i.e., applying the magnetic field along the nanopillars axis) both for pure Ni and $Cu_{0.29}Ni_{0.70}$ nanopillars with a diameter of 100 nm. In fact, the coercivity in this case (H_C ~ 500 Oe) is much larger than for the longitudinal hysteresis loops. Such an increase of H_C is probably due to the role of shape anisotropy, which is particularly pronounced for the nanopillars with smaller diameter (i.e., with larger aspect ratio). Again, two ferromagnetic contributions are observed by polar MOKE in the $Cu_{0.37}Ni_{0.63}$ and $Cu_{0.30}Ni_{0.70}$ nanopillars (Figure 6.7.b). Finally, no clear polar MOKE hysteresis loops could be recorded for the nanopillars with 200 nm in diameter, probably because the shape anisotropy is exceedingly low in this case.

The coercivity values obtained from the nanopillars are larger than those encountered in Cu-Ni thin films with the same Cu/Ni ratio (Figure 6.7.c). The increase in H_C can be ascribed to size effects, i.e., either to the formation of single domain states or the hindrances imposed by the limited lateral size of the nanopillars on the propagation of domain walls. Note that, as expected, continuous films with the $Cu_{0.55}Ni_{0.45}$ composition are not ferromagnetic.

6.4. Conclusions

Periodically ordered arrays of Cu-Ni nanopillars have been synthetized by template-assisted electrodeposition from aqueous solutions. Cylindrical cavities of 100 nm and 200 nm in diameter can be filled with Cu-Ni in a variable metal proportion that depends on the applied potential. The nanopillar arrays exhibit ferromagnetic behaviour at room temperature. This work paves the way for the controlled and cost-effective synthesis of arrays of 1D objects with potential applications in magnetic NEMS devices.

References

1. **M. D. Chic, D. M. Dimiduk.** 2005, Mater. Sci. Eng. A, Vols. 400-401, p. 268.

2. **M. Tian, J. Wang, J. Kurtz, T. E. Mallouk, M. H. W. Chan.** 2003, Nano Lett., Vol. 3, p. 919.

3. **M. A. Zeeshan, K. Shou, S. Pané, E. Pellicer, J. Sort, K. M. Sivaraman, M. D. Baró, B. J. Nelson.** 2011, Nanotechnol., Vol. 22, 275713.

4. **C. Xie, L. Hanson, Y. Cui, B. Cui.** 2011, PNAS, Vol. 108, p. 3894.

5. **S. Jin, M. J. Burek, R. D. Evans, Z. Jahed, M. C. Leung.** 2012, Mater. Sci. Eng. A, Vol. 552, p. 104.

6. **G. Lee, J.-Y. Kim, A. S. Budiman, N. Tamura, M. Kunz, K. Chen, M. J. Burek, J. R. Greer, T. Y. Tsui.** 2010, Acta Mater., Vol. 58, p. 1361.

7. **M. J. Burek, A. S. Budiman, Z. Jahed, N. Tamura, M. Kunz, S. Jin, S. M. J. Han, G. Lee, C. Zamecnik, T. Y. Tsiu.** 2011, Mater. Sci. Eng. A, Vol. 528, p. 5822.

8. **M. J. Burek, J. R. Greer.** 2010, Nano Lett., Vol. 10, p. 69.

9. **M. Zenger, W. Breuer, M. Zöfl, R. Pulwey, J. Raabe, D. Weiss.** 2001, IEEE Trans. Magn., Vol. 37, p. 2094.

10. **X. Jin, Y. Hu, Y. Wang, R. Shen, Y. Ye, L. Wu, S. Wang.** 2012, Appl. Surf. Sci., Vol. 258, p. 2977.

11. **E. Pellicer, A. Varea, S. Pané, B. J. Nelson, E. Menéndez, M. Estrader, S. Suriñach, M. D. Baró, J. Nogués, J. Sort.** 2010, Adv. Funct. Mater., Vol. 20, p. 983.

12. **J. I. Martín, J. Nogués, K. Liu, J. L. Vincent, I. K. Schuller.** 2003, J. Magn. Magn. Mater., Vol. 256, p. 449.

13. **J. C. Ododo, B. R. Coles.** 1977, J. Phys. F: Met. Phys., Vol. 7, p. 2393.

14. **S. A. Ahern, M. J. C. Martin, W. Sucksmith.** 1958, Proc. R. Soc. Lond. A, Vol. 248, p.145.

Chapter 7 : General Conclusions

1. Nanocrystalline Cu-Ni alloy films can be fabricated by direct current electrodeposition from saccharine-containing citrate+sulphate baths. Films with tuneable composition are achieved by applying variable current densities.

2. The addition of saccharine to the bath leads to nanocrystalline deposits (crystallite size ~30 nm). In its absence, fine-grained deposits are obtained (crystallite size ~400 nm).

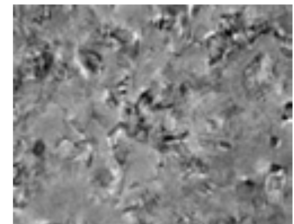

3. Regarding mechanical properties, an increase of hardness, wear resistance and elastic recovery can be achieved by: i) increasing the Ni content in the alloy, ii) reducing the crystallite size to nanoscale, and iii) inducing the formation of intergranular nanotwins in the deposit. The nanocrystalline $Cu_{0.13}Ni_{0.87}$ shows the largest value of hardness (8.2 GPa).

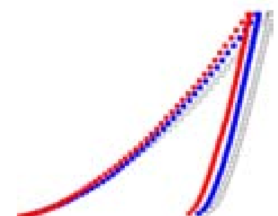

4. By varying the composition of the deposit, either paramagnetic or ferromagnetic behaviour can be obtained at room temperature. The threshold for ferromagnetism is ca. 70 at% Ni. Coercivity and saturation magnetization rise as Ni content increases in the deposits.

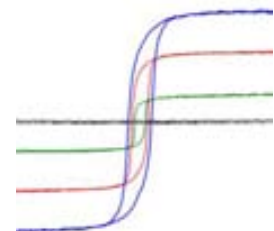

5. The thermal stability of nanocrystalline Cu-Ni alloy films is higher than that of pure Ni. Cu segregation at grain boundaries precludes grain coarsening and therefore the mechanical properties deteriorate at higher annealing temperatures. In turn, the coercivity increases for annealing temperatures above 475 K due to the formation of paramagnetic Cu-rich interfacial phase at grain boundaries that reduces the intergranular magnetic exchange interactions.

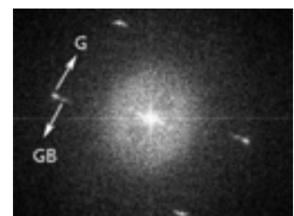

6. Alloying Cu with Ni improves the corrosion resistance of the deposits in NaCl environment. A shift toward more positive values of corrosion potential, and a decrease in corrosion current density is typically observed when the Ni content increases. Crystallite size refining does not significantly worsen the corrosion resistance of the material.

7. Miniaturization of Cu-Ni alloy films toward one-dimensional nanostructures can be performed by combining e-beam lithography with electrodeposition. Periodically distributed, ordered arrays of 100 nm and 200 nm-diameter nanopillars, with tuneable magnetic performance, have been successfully fabricated.

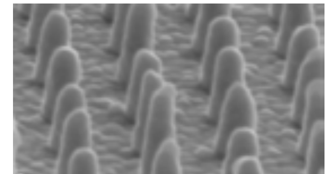

Chapter 8 : Future Perspectives

The work presented in this Thesis has shown the electrochemical fabrication of nanocrystalline Cu-Ni films using saccharine-containing citrate+sulphate baths. A comprehensive investigation of physical and chemical properties of the films has been carried out. This includes studies on the thermal stability, mechanical and magnetic behaviour, and corrosion performance, respectively. Also, the feasibility to fabricate Cu-Ni nanopillars combining e-beam lithography with electrodeposition has been demonstrated. The properties of these Cu-Ni alloys make them potentially suitable for their implementation in MEMS and NEMS devices. However, there is still room to explore new alternative possibilities in this field or clarify few issues that remain open.

Currently, an in-depth micro-structural characterization by means of HRTEM of the Cu-Ni nanopillars is under progress aimed at having a better understanding of the magnetic behaviour of these structures. In particular, we would like to reveal if the segregation of Ni-rich regions in nanopillars whose composition is below the threshold needed for ferromagnetism (ca. 70%) is responsible for the observed ferromagnetic signature.

The recent acquisition of a 4-point probe equipment intended for measuring the electrical properties of electrodeposited Cu-Ni films and nanopillars will allow us to investigate the resistivity dependence on crystallite size, chemical composition, etc. Also the relationship between electrical and magnetic properties will be explored.

On the other hand, alloying Cu-Ni with a third element might bring about an extra versatility and expand the range of metallurgical and technological applications of the material. For this reason the electrodeposition of nanocrystalline ternary alloys films and nanopillars will be studied using procedures similar to those presented in this Thesis. For example, Cu-Ni alloyed with Co emerges as a good candidate to improve the magnetic properties (e.g. coercivity or saturation magnetization)of Cu-Ni alloy.

Finally, since one of the advantages of electrodeposition lies in that complex geometries can be coated, other configurations like arrays of squares, stripes or rings will be prepared by template-assisted electrodeposition and their physical properties will be examined.

Scientific Curriculum

Aïda Varea Espelt

Physicist and Materials Science Engineer

Publications

1. E. Pellicer, A. Varea, S. Pané, B. J. Nelson, E. Menéndez, M. Estrader, S. Suriñach, M. D. Baró, J. Nogués, J. Sort

Nanocrystalline electroplated Cu-Ni: metallic thin films with enhanced mechanical properties and tuneable magnetic behaviour.

Advanced Functional Materials 20 (2010) 983

2. J. Sort, L. F. Bonavina, A. Varea, C. Souza, W. J. Botta, C. S. Kiminami, C. Bolframi, S. Suriñach, M. D. Baró, J. Nogués.

Out-of-plane Magnetic Patterning Based on Indentation-Induced Nanocrystallization of a Metallic Glass.

Small 6 (2010) 1543

3. A. Varea, E. Menéndez, J. Montserrat, E. Lora-Tamayo, A. Weber, L. J. Heyderman, S. C. Deevi, K. V. Rao, S. Suriñach, M. D. Baró, K. S. Buchanan, J. Nogués, J. Sort

Tuneable magnetic patterning of paramagnetic $Fe_{60}Al_{40}$ (at. %) by consecutive ion irradiation through pre-lithographed shadow masks.

Journal of Applied Physics 109 (2011) 093918.

4. E. Pellicer, A. Varea, S. Pané, K. M. Sivaraman, B. J. Nelson, S. Suriñach, M. D. Baró, J. Sort

A comparison between fine-grained and nanocrystalline electrodeposited Cu-Ni films. Insights on mechanical and corrosion performance

Surface and Coatings Technology 205 (2011) 5285.

5. E. Pellicer, A. Varea, S. Kartik, S. Pané, S. Suriñach, M.D. Baró, J. Nogués, B. Nelson, J. Sort

Grain boundary segregation and interdiffusion effects in nickel-copper alloys: an effective means to improve the thermal stability of nanocrystalline nickel

ACS Applied Materials and Interfaces 3 (2011) 2265

6. J. Fornell, N. Van Steenberge, A. Varea, E. Rossinyol, E. Pellicer, S. Suriñach, M. D. Baró, J. Sort

Enhanced mechanical properties and in-vitro corrosion behaviour of amorphous and devitrified $Ti_{40}Zr_{10}Cu_{38}Pd_{12}$ *metallic glass*

Journal of Mechanical Behavior of Biomedical Materials 4 (2011) 1709

7. A. Varea, E. Pellicer, S. Pané , B. J. Nelson, S. Suriñach, M. D. Baró, J. Sort

Mechanical Properties and Corrosion Behaviour of Nanostructured Cu-rich CuNi Electrodeposited Films

International Journal of Electrochemical Science 7 (2012) 1288 – 1302

8. E. Menéndez, J. Sort, A. Varea, A. Concustell, S. Suriñach, J. Montserrat, E. Lora-Tamayo, M. D. Baró, J. Nogués

Cuando el desorden genera magnetismo- When disorder generates magnetism

Revista de Física 26 (2012) 16-22